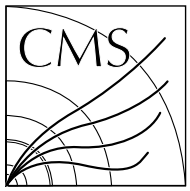

CERN-LHCC-2015-012
CMS-TDR-013
30 September 2015

CMS TECHNICAL DESIGN REPORT FOR THE MUON ENDCAP GEM UPGRADE

This report describes both the technical design and the expected performance of the Phase-II upgrade, using Gas Electron Multiplier (GEM) detectors, of the first endcap station of the CMS muon system. The upgrade is targeted for the second long shutdown of the CERN LHC and is designed to improve the muon trigger and tracking performance at high luminosity. The GEM detectors will add redundancy to the muon system in the $1.6 < |\eta| < 2.2$ pseudorapidity region, where the amount of detection layers is lowest while the background rates are highest and the bending of the muon trajectories due to the CMS magnetic field is small. GEM detectors have been identified as a suitable technology to operate in the high radiation environment present in that region. The first muon endcap station will be instrumented with a double layer of triple-GEM chambers in the $1.6 < |\eta| < 2.2$ region. The detector front-end electronics uses the custom designed VFAT3 chip to provide both fast input for the level-1 muon trigger and full granularity information for offline muon reconstruction. This document describes the design of detectors, electronics, and services. The expected performance of the upgraded muon system is discussed in the context of several benchmark physics channels. The document also presents the plan - including the project schedule, cost, and organization - for the detector construction, testing, and integration into the CMS detector.

ISBN 978-92-9083-396-3

Editors

A. Colaleo, A. Safonov, A. Sharma and M. Tytgat

Chapter Editors

P. Aspell, L. Benussi, O. Bouhali, A. Cimmino, A. Colaleo, G. De Lentdecker, J. Hauser, K. Hoepfner, M. Hohlmann, P. Karchin, M. Maggi, A. Marinov, A. Safonov, A. Sharma and M. Tytgat

Contributors

M. A. Akl, M. Abbrescia, O. Aboamer, N. Amapane, P. Aspell, S. Banerjee, S. Bally, A. Puig-Barnac, P. Barria, G. Bencze, N. Beni, L. Benussi, V. Bhopatkar, S. Bianco, O. Bouhali, C. Calabria, A. Castaneda, F. Cavallo, A. Cimmino, S. Colafranceschi, A. Colaleo, A. Conde Garcia, I. Crotty, M. Dabrowski, G. De Lentdecker, R. De Oliveira, G. De Robertis, S. Dildick, B. Dorney, A. Gaddi, P. Giacomelli, J. Gilmore, M. Hadjiiska, J. Hauser, K. Hoepfner, M. Hohlmann, T. Huang, A.K. Kalsi, T. Kamon, P. Karchin, V. Krutelyov, A. Lanaro, J. Lee, T. Lenzi, F. Loddo, A. Madorsky, T. Maerschalk, M. Maggi, A. Magnani, A. Marinov, J. Merlin, G. Mitselmakher, A. Mohapatra, P. Paolucci, R. Radogna, A. Ranieri, C. Riccardi, A. Safonov, M. Saleh, G. Saviano, A. Sharma, J. Sturdy, Z. Szillasi, J. Talvitie, S. Teruki, M. Tytgat, R. Venditti, E. Verhagen, P. Verwilligen, Y. Yang, F. Zenoni, A. Zhang

Language Editors

M. Hohlmann and P. Karchin

Cover Design

S. Cittolin

Acknowledgments

We would like to thank the technical staff from the various participating institutions for the design, R&D and testing of all components of this upgrade. We explicitly want to mention the Pisa/Totem group, namely S. Lami, G. Magazzu, A. Scribano, N. Turini, for their support during the R&D phase of the project. We wish to acknowledge the support received from the RD51 Collaboration during the early phase of the project. In addition, special thanks goes to Rui de Oliveira and his team at the CERN PCB Workshop for their continuous dedication to this upgrade project.

The important feedback from the following CMS internal reviewers greatly helped in the development of this technical design report: G. Apollinari, J. Butler, A. Charkiewicz, D. Contardo, K. Gill, G. Hall, M. Klute, N. Pastrone, E. Perez, L. Silvestris and J. Spalding. Furthermore, we are indebted to the CMS secretaries, K. Aspola, N. Barzaghini, A. Belova, Z. Garai, D. Hudson, T. Pardo and A. Yaneva, for their continuous support during all phases of the project. We also acknowledge the warm support received from the CMS management team and computing project.

The CMS Collaboration

Yerevan Physics Institute, Yerevan, Armenia
V. Khachatryan, A.M. Sirunyan, A. Tumasyan

Institut für Hochenergiephysik der OeAW, Wien, Austria
W. Adam, E. Asilar, T. Bergauer, J. Brandstetter, E. Brondolin, M. Dragicevic, J. Erö, M. Flechl, M. Friedl, R. Frühwirth[1], V.M. Ghete, C. Hartl, N. Hörmann, J. Hrubec, M. Jeitler[1], V. Knünz, A. König, M. Krammer[1], I. Krätschmer, D. Liko, T. Matsushita, I. Mikulec, D. Rabady[2], B. Rahbaran, H. Rohringer, J. Schieck[1], R. Schöfbeck, J. Strauss, W. Treberer-Treberspurg, W. Waltenberger, C.-E. Wulz[1]

National Centre for Particle and High Energy Physics, Minsk, Belarus
V. Mossolov, N. Shumeiko, J. Suarez Gonzalez

Universiteit Antwerpen, Antwerpen, Belgium
S. Alderweireldt, T. Cornelis, E.A. De Wolf, X. Janssen, A. Knutsson, J. Lauwers, S. Luyckx, S. Ochesanu, R. Rougny, M. Van De Klundert, H. Van Haevermaet, P. Van Mechelen, N. Van Remortel, A. Van Spilbeeck

Vrije Universiteit Brussel, Brussel, Belgium
S. Abu Zeid, F. Blekman, J. D'Hondt, N. Daci, I. De Bruyn, K. Deroover, N. Heracleous, J. Keaveney, S. Lowette, L. Moreels, A. Olbrechts, Q. Python, D. Strom, S. Tavernier, W. Van Doninck, P. Van Mulders, G.P. Van Onsem, I. Van Parijs

Université Libre de Bruxelles, Bruxelles, Belgium
P. Barria, C. Caillol, B. Clerbaux, G. De Lentdecker, H. Delannoy, D. Dobur, G. Fasanella, L. Favart, A.P.R. Gay, A. Grebenyuk, T. Lenzi, A. Léonard, T. Maerschalk, A. Mohammadi, L. Perniè, A. Randle-conde, T. Reis, T. Seva, L. Thomas, C. Vander Velde, P. Vanlaer, J. Wang, Y. Yang, R. Yonamine, F. Zenoni, F. Zhang[3]

Ghent University, Ghent, Belgium
K. Beernaert, L. Benucci, S. Cauwenbergh, A. Cimmino, S. Crucy, A. Fagot, G. Garcia, M. Gul, J. Mccartin, A.A. Ocampo Rios, D. Poyraz, D. Ryckbosch, S. Salva Diblen, M. Sigamani, N. Strobbe, M. Tytgat, W. Van Driessche, E. Yazgan, N. Zaganidis

Université Catholique de Louvain, Louvain-la-Neuve, Belgium
S. Basegmez, C. Beluffi[4], O. Bondu, G. Bruno, R. Castello, A. Caudron, L. Ceard, G.G. Da Silveira, C. Delaere, D. Favart, L. Forthomme, A. Giammanco[5], J. Hollar, A. Jafari, P. Jez, M. Komm, V. Lemaitre, A. Mertens, C. Nuttens, L. Perrini, A. Pin, K. Piotrzkowski, A. Popov[6], L. Quertenmont, M. Selvaggi, M. Vidal Marono

Université de Mons, Mons, Belgium
N. Beliy, T. Caebergs, G.H. Hammad

Centro Brasileiro de Pesquisas Fisicas, Rio de Janeiro, Brazil
W.L. Aldá Júnior, G.A. Alves, L. Brito, M. Correa Martins Junior, T. Dos Reis Martins, C. Hensel, C. Mora Herrera, A. Moraes, M.E. Pol, P. Rebello Teles

Universidade do Estado do Rio de Janeiro, Rio de Janeiro, Brazil
E. Belchior Batista Das Chagas, W. Carvalho, J. Chinellato[7], A. Custódio, E.M. Da Costa, D. De Jesus Damiao, C. De Oliveira Martins, S. Fonseca De Souza, L.M. Huertas Guativa, H. Malbouisson, D. Matos Figueiredo, L. Mundim, H. Nogima, W.L. Prado Da Silva, A. Santoro, A. Sznajder, E.J. Tonelli Manganote[7], A. Vilela Pereira

Universidade Estadual Paulista [a], Universidade Federal do ABC [b], S ao Paulo, Brazil
S. Ahuja[a], C.A. Bernardes[b], A. De Souza Santos[b], S. Dogra[a], T.R. Fernandez Perez Tomei[a], E.M. Gregores[b], P.G. Mercadante[b], C.S. Moon[a,8], S.F. Novaes[a], Sandra S. Padula[a], D. Romero Abad, J.C. Ruiz Vargas

Institute for Nuclear Research and Nuclear Energy, Sofia, Bulgaria
A. Aleksandrov, V. Genchev[2], R. Hadjiiska, P. Iaydjiev, A. Marinov, S. Piperov, M. Rodozov, S. Stoykova, G. Sultanov, M. Vutova

University of Sofia, Sofia, Bulgaria
A. Dimitrov, I. Glushkov, L. Litov, B. Pavlov, P. Petkov

Institute of High Energy Physics, Beijing, China
M. Ahmad, J.G. Bian, G.M. Chen, H.S. Chen, M. Chen, T. Cheng, R. Du, C.H. Jiang, R. Plestina[9], F. Romeo, S.M. Shaheen, J. Tao, C. Wang, Z. Wang, H. Zhang

State Key Laboratory of Nuclear Physics and Technology, Peking University, Beijing, China
C. Asawatangtrakuldee, Y. Ban, Q. Li, S. Liu, Y. Mao, S.J. Qian, D. Wang, Z. Xu, W. Zou

Universidad de Los Andes, Bogota, Colombia
C. Avila, A. Cabrera, L.F. Chaparro Sierra, C. Florez, J.P. Gomez, B. Gomez Moreno, J.C. Sanabria

University of Split, Faculty of Electrical Engineering, Mechanical Engineering and Naval Architecture, Split, Croatia
N. Godinovic, D. Lelas, D. Polic, I. Puljak

University of Split, Faculty of Science, Split, Croatia
Z. Antunovic, M. Kovac

Institute Rudjer Boskovic, Zagreb, Croatia
V. Brigljevic, K. Kadija, J. Luetic, L. Sudic

University of Cyprus, Nicosia, Cyprus
A. Attikis, G. Mavromanolakis, J. Mousa, C. Nicolaou, F. Ptochos, P.A. Razis, H. Rykaczewski

Charles University, Prague, Czech Republic
M. Bodlak, M. Finger[10], M. Finger Jr.[10]

Academy of Scientific Research and Technology of the Arab Republic of Egypt, Egyptian Network of High Energy Physics, Cairo, Egypt
A. Ali[11,12], R. Aly[13], S. Aly[13], Y. Assran[14], A. Ellithi Kamel[15], A. Lotfy[16], M.A. Mahmoud[16], R. Masod[11], A. Radi[12,11]

National Institute of Chemical Physics and Biophysics, Tallinn, Estonia
B. Calpas, M. Kadastik, M. Murumaa, M. Raidal, A. Tiko, C. Veelken

Department of Physics, University of Helsinki, Helsinki, Finland
P. Eerola, M. Voutilainen

Helsinki Institute of Physics, Helsinki, Finland
J. Härkönen, V. Karimäki, R. Kinnunen, T. Lampén, K. Lassila-Perini, S. Lehti, T. Lindén, P. Luukka, T. Mäenpää, J. Pekkanen, T. Peltola, E. Tuominen, J. Tuominiemi, E. Tuovinen, L. Wendland

Lappeenranta University of Technology, Lappeenranta, Finland
J. Talvitie, T. Tuuva

DSM/IRFU, CEA/Saclay, Gif-sur-Yvette, France
M. Besancon, F. Couderc, M. Dejardin, D. Denegri, B. Fabbro, J.L. Faure, C. Favaro, F. Ferri, S. Ganjour, A. Givernaud, P. Gras, G. Hamel de Monchenault, P. Jarry, E. Locci, M. Machet, J. Malcles, J. Rander, A. Rosowsky, M. Titov, A. Zghiche

Laboratoire Leprince-Ringuet, Ecole Polytechnique, IN2P3-CNRS, Palaiseau, France
S. Baffioni, F. Beaudette, P. Busson, L. Cadamuro, E. Chapon, C. Charlot, T. Dahms, O. Davignon, N. Filipovic, A. Florent, R. Granier de Cassagnac, S. Lisniak, L. Mastrolorenzo, P. Miné, I.N. Naranjo, M. Nguyen, C. Ochando, G. Ortona, P. Paganini, S. Regnard, R. Salerno, J.B. Sauvan, Y. Sirois, T. Strebler, Y. Yilmaz, A. Zabi

Institut Pluridisciplinaire Hubert Curien, Université de Strasbourg, Université de Haute Alsace Mulhouse, CNRS/IN2P3, Strasbourg, France
J.-L. Agram[17], J. Andrea, A. Aubin, D. Bloch, J.-M. Brom, M. Buttignol, E.C. Chabert, N. Chanon, C. Collard, E. Conte[17], J.-C. Fontaine[17], D. Gelé, U. Goerlach, C. Goetzmann, A.-C. Le Bihan, J.A. Merlin[2], K. Skovpen, P. Van Hove

Centre de Calcul de l'Institut National de Physique Nucleaire et de Physique des Particules, CNRS/IN2P3, Villeurbanne, France
S. Gadrat

Université de Lyon, Université Claude Bernard Lyon 1, CNRS-IN2P3, Institut de Physique Nucléaire de Lyon, Villeurbanne, France
S. Beauceron, C. Bernet[9], G. Boudoul, E. Bouvier, S. Brochet, C.A. Carrillo Montoya, J. Chasserat, R. Chierici, D. Contardo, B. Courbon, P. Depasse, H. El Mamouni, J. Fan, J. Fay, S. Gascon, M. Gouzevitch, B. Ille, I.B. Laktineh, M. Lethuillier, L. Mirabito, A.L. Pequegnot, S. Perries, J.D. Ruiz Alvarez, D. Sabes, L. Sgandurra, V. Sordini, M. Vander Donckt, P. Verdier, S. Viret, H. Xiao

Institute of High Energy Physics and Informatization, Tbilisi State University, Tbilisi, Georgia
Z. Tsamalaidze[10]

RWTH Aachen University, I. Physikalisches Institut, Aachen, Germany
C. Autermann, S. Beranek, M. Edelhoff, L. Feld, A. Heister, M.K. Kiesel, K. Klein, M. Lipinski, A. Ostapchuk, M. Preuten, F. Raupach, J. Sammet, S. Schael, J.F. Schulte, T. Verlage, H. Weber, B. Wittmer, V. Zhukov[6]

RWTH Aachen University, III. Physikalisches Institut A, Aachen, Germany
M. Ata, M. Brodski, E. Dietz-Laursonn, D. Duchardt, M. Endres, M. Erdmann, S. Erdweg, T. Esch, R. Fischer, A. Güth, T. Hebbeker, C. Heidemann, K. Hoepfner, D. Klingebiel, S. Knutzen, P. Kreuzer, M. Merschmeyer, A. Meyer, P. Millet, M. Olschewski, K. Padeken, P. Papacz, B. Philipps, T. Pook, M. Radziej, H. Reithler, M. Rieger, F. Scheuch, L. Sonnenschein, D. Teyssier, S. Thüer

RWTH Aachen University, III. Physikalisches Institut B, Aachen, Germany
V. Cherepanov, Y. Erdogan, G. Flügge, H. Geenen, M. Geisler, W. Haj Ahmad, F. Hoehle, B. Kargoll, T. Kress, Y. Kuessel, A. Künsken, J. Lingemann[2], A. Nehrkorn, A. Nowack, I.M. Nugent, C. Pistone, O. Pooth, A. Stahl

Deutsches Elektronen-Synchrotron, Hamburg, Germany
M. Aldaya Martin, I. Asin, N. Bartosik, O. Behnke, U. Behrens, A.J. Bell, K. Borras, A. Burgmeier, A. Cakir, L. Calligaris, A. Campbell, S. Choudhury, F. Costanza, C. Diez Pardos, G. Dolinska, S. Dooling, T. Dorland, G. Eckerlin, D. Eckstein, T. Eichhorn, G. Flucke, E. Gallo, J. Garay

Garcia, A. Geiser, A. Gizhko, P. Gunnellini, J. Hauk, M. Hempel[18], H. Jung, A. Kalogeropoulos, O. Karacheban[18], M. Kasemann, P. Katsas, J. Kieseler, C. Kleinwort, I. Korol, W. Lange, J. Leonard, K. Lipka, A. Lobanov, W. Lohmann[18], R. Mankel, I. Marfin[18], I.-A. Melzer-Pellmann, A.B. Meyer, G. Mittag, J. Mnich, A. Mussgiller, S. Naumann-Emme, A. Nayak, E. Ntomari, H. Perrey, D. Pitzl, R. Placakyte, A. Raspereza, P.M. Ribeiro Cipriano, B. Roland, M.Ö. Sahin, J. Salfeld-Nebgen, P. Saxena, T. Schoerner-Sadenius, M. Schröder, C. Seitz, S. Spannagel, K.D. Trippkewitz, C. Wissing

University of Hamburg, Hamburg, Germany
V. Blobel, M. Centis Vignali, A.R. Draeger, J. Erfle, E. Garutti, K. Goebel, D. Gonzalez, M. Görner, J. Haller, M. Hoffmann, R.S. Höing, A. Junkes, R. Klanner, R. Kogler, T. Lapsien, T. Lenz, I. Marchesini, D. Marconi, D. Nowatschin, J. Ott, F. Pantaleo[2], T. Peiffer, A. Perieanu, N. Pietsch, J. Poehlsen, D. Rathjens, C. Sander, H. Schettler, P. Schleper, E. Schlieckau, A. Schmidt, J. Schwandt, M. Seidel, V. Sola, H. Stadie, G. Steinbrück, H. Tholen, D. Troendle, E. Usai, L. Vanelderen, A. Vanhoefer

Institut für Experimentelle Kernphysik, Karlsruhe, Germany
M. Akbiyik, C. Barth, C. Baus, J. Berger, C. Böser, E. Butz, T. Chwalek, F. Colombo, W. De Boer, A. Descroix, A. Dierlamm, M. Feindt, F. Frensch, M. Giffels, A. Gilbert, F. Hartmann[2], U. Husemann, F. Kassel[2], I. Katkov[6], A. Kornmayer[2], P. Lobelle Pardo, M.U. Mozer, T. Müller, Th. Müller, M. Plagge, G. Quast, K. Rabbertz, S. Röcker, F. Roscher, H.J. Simonis, F.M. Stober, R. Ulrich, J. Wagner-Kuhr, S. Wayand, T. Weiler, C. Wöhrmann, R. Wolf

Institute of Nuclear and Particle Physics (INPP), NCSR Demokritos, Aghia Paraskevi, Greece
G. Anagnostou, G. Daskalakis, T. Geralis, V.A. Giakoumopoulou, A. Kyriakis, D. Loukas, A. Markou, A. Psallidas, I. Topsis-Giotis

University of Athens, Athens, Greece
A. Agapitos, S. Kesisoglou, A. Panagiotou, N. Saoulidou, E. Tziaferi

University of Ioánnina, Ioánnina, Greece
I. Evangelou, G. Flouris, C. Foudas, P. Kokkas, N. Loukas, N. Manthos, I. Papadopoulos, E. Paradas, J. Strologas

Wigner Research Centre for Physics, Budapest, Hungary
G. Bencze, C. Hajdu, A. Hazi, P. Hidas, D. Horvath[19], F. Sikler, V. Veszpremi, G. Vesztergombi[20], A.J. Zsigmond

Institute of Nuclear Research ATOMKI, Debrecen, Hungary
N. Beni, S. Czellar, J. Karancsi[21], J. Molnar, Z. Szillasi

University of Debrecen, Debrecen, Hungary
M. Bartók[22], A. Makovec, P. Raics, Z.L. Trocsanyi, B. Ujvari

National Institute of Science Education and Research, Bhubaneswar, India
P. Mal, K. Mandal, N. Sahoo, S.K. Swain

Panjab University, Chandigarh, India
S. Bansal, S.B. Beri, V. Bhatnagar, R. Chawla, R. Gupta, U.Bhawandeep, A.K. Kalsi, A. Kaur, M. Kaur, R. Kumar, A. Mehta, M. Mittal, N. Nishu, J.B. Singh, G. Walia

University of Delhi, Delhi, India
Ashok Kumar, Arun Kumar, A. Bhardwaj, B.C. Choudhary, R.B. Garg, A. Kumar, S. Malhotra, M. Naimuddin, K. Ranjan, R. Sharma, V. Sharma

Saha Institute of Nuclear Physics, Kolkata, India
S. Banerjee, S. Bhattacharya, K. Chatterjee, S. Dey, S. Dutta, Sa. Jain, Sh. Jain, R. Khurana, N. Majumdar, A. Modak, K. Mondal, S. Mukherjee, S. Mukhopadhyay, A. Roy, D. Roy, S. Roy Chowdhury, S. Sarkar, M. Sharan

Bhabha Atomic Research Centre, Mumbai, India
A. Abdulsalam, R. Chudasama, D. Dutta, V. Jha, V. Kumar, A.K. Mohanty[2], L.M. Pant, P. Shukla, A. Topkar

Tata Institute of Fundamental Research, Mumbai, India
T. Aziz, S. Banerjee, S. Bhowmik[23], R.M. Chatterjee, R.K. Dewanjee, S. Dugad, S. Ganguly, S. Ghosh, M. Guchait, A. Gurtu[24], G. Kole, S. Kumar, B. Mahakud, M. Maity[23], G. Majumder, K. Mazumdar, S. Mitra, G.B. Mohanty, B. Parida, T. Sarkar[23], K. Sudhakar, N. Sur, B. Sutar, N. Wickramage[25]

Indian Institute of Science Education and Research (IISER), Pune, India
S. Sharma

Institute for Research in Fundamental Sciences (IPM), Tehran, Iran
H. Bakhshiansohi, H. Behnamian, S.M. Etesami[26], A. Fahim[27], R. Goldouzian, M. Khakzad, M. Mohammadi Najafabadi, M. Naseri, S. Paktinat Mehdiabadi, F. Rezaei Hosseinabadi, B. Safarzadeh[28], M. Zeinali

University College Dublin, Dublin, Ireland
M. Felcini, M. Grunewald

INFN Sezione di Bari [a], Università di Bari [b], Politecnico di Bari [c], Bari, Italy
M. Abbrescia[a,b], C. Calabria[a,b], C. Caputo[a,b], S.S. Chhibra[a,b], A. Colaleo[a], D. Creanza[a,c], L. Cristella[a,b], N. De Filippis[a,c], M. De Palma[a,b], G. De Robertis[a], L. Fiore[a], G. Iaselli[a,c], F. Loddo[a], G. Maggi[a,c], M. Maggi[a], G. Miniello[a,b], S. My[a,c], S. Nuzzo[a,b], A. Pompili[a,b], G. Pugliese[a,c], R. Radogna[a,b], A. Ranieri[a], G. Selvaggi[a,b], A. Sharma[a], L. Silvestris[a,2], R. Venditti[a,b], P. Verwilligen[a]

INFN Sezione di Bologna [a], Università di Bologna [b], Bologna, Italy
G. Abbiendi[a], C. Battilana[2], A.C. Benvenuti[a], D. Bonacorsi[a,b], S. Braibant-Giacomelli[a,b], L. Brigliadori[a,b], R. Campanini[a,b], P. Capiluppi[a,b], A. Castro[a,b], F.R. Cavallo[a], G. Codispoti[a,b], M. Cuffiani[a,b], G.M. Dallavalle[a], F. Fabbri[a], A. Fanfani[a,b], D. Fasanella[a,b], P. Giacomelli[a], C. Grandi[a], L. Guiducci[a,b], S. Marcellini[a], G. Masetti[a], A. Montanari[a], F.L. Navarria[a,b], A. Perrotta[a], A.M. Rossi[a,b], T. Rovelli[a,b], G.P. Siroli[a,b], N. Tosi[a,b], R. Travaglini[a,b]

INFN Sezione di Catania [a], Università di Catania [b], CSFNSM [c], Catania, Italy
G. Cappello[a], M. Chiorboli[a,b], S. Costa[a,b], F. Giordano[a], R. Potenza[a,b], A. Tricomi[a,b], C. Tuve[a,b]

INFN Sezione di Firenze [a], Università di Firenze [b], Firenze, Italy
G. Barbagli[a], V. Ciulli[a,b], C. Civinini[a], R. D'Alessandro[a,b], E. Focardi[a,b], S. Gonzi[a,b], V. Gori[a,b], P. Lenzi[a,b], M. Meschini[a], S. Paoletti[a], G. Sguazzoni[a], A. Tropiano[a,b], L. Viliani[a,b]

INFN Laboratori Nazionali di Frascati, Frascati, Italy
L. Benussi, S. Bianco, F. Fabbri, D. Piccolo

INFN Sezione di Genova [a], Università di Genova [b], Genova, Italy
V. Calvelli[a,b], F. Ferro[a], M. Lo Vetere[a,b], E. Robutti[a], S. Tosi[a,b]

INFN Sezione di Milano-Bicocca [a], Università di Milano-Bicocca [b], Milano, Italy
M.E. Dinardo[a,b], S. Fiorendi[a,b], S. Gennai[a], R. Gerosa[a,b], A. Ghezzi[a,b], P. Govoni[a,b], S. Malvezzi[a],

R.A. Manzoni[a,b], B. Marzocchi[a,b,2], D. Menasce[a], L. Moroni[a], M. Paganoni[a,b], D. Pedrini[a], S. Ragazzi[a,b], N. Redaelli[a], T. Tabarelli de Fatis[a,b]

INFN Sezione di Napoli [a], Università di Napoli 'Federico II' [b], Napoli, Italy, Università della Basilicata [c], Potenza, Italy, Università G. Marconi [d], Roma, Italy
S. Buontempo[a], N. Cavallo[a,c], S. Di Guida[a,d,2], M. Esposito[a,b], F. Fabozzi[a,c], A.O.M. Iorio[a,b], G. Lanza[a], L. Lista[a], S. Meola[a,d,2], M. Merola[a], P. Paolucci[a,2], C. Sciacca[a,b], F. Thyssen

INFN Sezione di Padova [a], Università di Padova [b], Padova, Italy, Università di Trento [c], Trento, Italy
P. Azzi[a,2], N. Bacchetta[a], D. Bisello[a,b], A. Branca[a,b], R. Carlin[a,b], A. Carvalho Antunes De Oliveira[a,b], P. Checchia[a], M. Dall'Osso[a,b,2], T. Dorigo[a], U. Dosselli[a], F. Gasparini[a,b], U. Gasparini[a,b], A. Gozzelino[a], K. Kanishchev[a,c], S. Lacaprara[a], M. Margoni[a,b], A.T. Meneguzzo[a,b], J. Pazzini[a,b], N. Pozzobon[a,b], P. Ronchese[a,b], F. Simonetto[a,b], E. Torassa[a], M. Tosi[a,b], M. Zanetti, P. Zotto[a,b], A. Zucchetta[a,b,2], G. Zumerle[a,b]

INFN Sezione di Pavia [a], Università di Pavia [b], Pavia, Italy
A. Braghieri[a], M. Gabusi[a,b], A. Magnani[a], M. Manghisoni[a], P. Montagna[a,b], S.P. Ratti[a,b], V. Re[a], C. Riccardi[a,b], P. Salvini[a], I. Vai[a], P. Vitulo[a,b]

INFN Sezione di Perugia [a], Università di Perugia [b], Perugia, Italy
L. Alunni Solestizi[a,b], M. Biasini[a,b], G.M. Bilei[a], D. Ciangottini[a,b,2], L. Fanò[a,b], P. Lariccia[a,b], G. Mantovani[a,b], M. Menichelli[a], A. Saha[a], A. Santocchia[a,b], A. Spiezia[a,b]

INFN Sezione di Pisa [a], Università di Pisa [b], Scuola Normale Superiore di Pisa [c], Pisa, Italy
K. Androsov[a,29], P. Azzurri[a], G. Bagliesi[a], J. Bernardini[a], T. Boccali[a], G. Broccolo[a,c], R. Castaldi[a], M.A. Ciocci[a,29], R. Dell'Orso[a], S. Donato[a,c,2], G. Fedi, L. Foà[a,c†], A. Giassi[a], M.T. Grippo[a,29], F. Ligabue[a,c], T. Lomtadze[a], L. Martini[a,b], A. Messineo[a,b], F. Palla[a], A. Rizzi[a,b], A. Savoy-Navarro[a,30], A.T. Serban[a], P. Spagnolo[a], P. Squillacioti[a,29], R. Tenchini[a], G. Tonelli[a,b], A. Venturi[a], P.G. Verdini[a]

INFN Sezione di Roma [a], Università di Roma [b], Roma, Italy
L. Barone[a,b], F. Cavallari[a], G. D'imperio[a,b,2], D. Del Re[a,b], M. Diemoz[a], S. Gelli[a,b], C. Jorda[a], E. Longo[a,b], F. Margaroli[a,b], P. Meridiani[a], F. Micheli[a,b], G. Organtini[a,b], R. Paramatti[a], F. Preiato[a,b], S. Rahatlou[a,b], C. Rovelli[a], F. Santanastasio[a,b], P. Traczyk[a,b,2]

INFN Sezione di Torino [a], Università di Torino [b], Torino, Italy, Università del Piemonte Orientale [c], Novara, Italy
N. Amapane[a,b], R. Arcidiacono[a,c], S. Argiro[a,b], M. Arneodo[a,c], R. Bellan[a,b], C. Biino[a], N. Cartiglia[a], M. Costa[a,b], R. Covarelli[a,b], A. Degano[a,b], N. Demaria[a], L. Finco[a,b,2], B. Kiani[a,b], C. Mariotti[a], S. Maselli[a], E. Migliore[a,b], V. Monaco[a,b], E. Monteil[a,b], M. Musich[a], M.M. Obertino[a,b], L. Pacher[a,b], N. Pastrone[a], M. Pelliccioni[a], G.L. Pinna Angioni[a,b], F. Ravera[a,b], A. Romero[a,b], M. Ruspa[a,c], R. Sacchi[a,b], A. Solano[a,b], A. Staiano[a], U. Tamponi[a]

INFN Sezione di Trieste [a], Università di Trieste [b], Trieste, Italy
S. Belforte[a], V. Candelise[a,b,2], M. Casarsa[a], F. Cossutti[a], G. Della Ricca[a,b], B. Gobbo[a], C. La Licata[a,b], M. Marone[a,b], A. Schizzi[a,b], T. Umer[a,b], A. Zanetti[a]

Kangwon National University, Chunchon, Korea
S. Chang, A. Kropivnitskaya, S.K. Nam

Kyungpook National University, Daegu, Korea
D.H. Kim, G.N. Kim, M.S. Kim, D.J. Kong, S. Lee, Y.D. Oh, A. Sakharov, D.C. Son

Chonbuk National University, Jeonju, Korea
H. Kim, T.J. Kim, M.S. Ryu

Chonnam National University, Institute for Universe and Elementary Particles, Kwangju, Korea
S. Song

Korea University, Seoul, Korea
S. Choi, Y. Go, D. Gyun, B. Hong, M. Jo, H. Kim, Y. Kim, B. Lee, K. Lee, K.S. Lee, S. Lee, S.K. Park, Y. Roh

Seoul National University, Seoul, Korea
J. Almond, U. Yang, H.D. Yoo, G.B. Yu

University of Seoul, Seoul, Korea
M. Choi, J.H. Kim, J.S.H. Lee, I.C. Park, G. Ryu

Sungkyunkwan University, Suwon, Korea
Y. Choi, Y.K. Choi, J. Goh, D. Kim, E. Kwon, J. Lee, I. Yu

Vilnius University, Vilnius, Lithuania
A. Juodagalvis, J. Vaitkus

National Centre for Particle Physics, Universiti Malaya, Kuala Lumpur, Malaysia
Z.A. Ibrahim, J.R. Komaragiri, M.A.B. Md Ali[31], F. Mohamad Idris, W.A.T. Wan Abdullah

Centro de Investigacion y de Estudios Avanzados del IPN, Mexico City, Mexico
E. Casimiro Linares, H. Castilla-Valdez, E. De La Cruz-Burelo, I. Heredia-de La Cruz[32], A. Hernandez-Almada, R. Lopez-Fernandez, G. Ramirez Sanchez, A. Sanchez-Hernandez

Universidad Iberoamericana, Mexico City, Mexico
S. Carrillo Moreno, F. Vazquez Valencia

Benemerita Universidad Autonoma de Puebla, Puebla, Mexico
S. Carpinteyro, I. Pedraza, H.A. Salazar Ibarguen

Universidad Autónoma de San Luis Potosí, San Luis Potosí, Mexico
A. Morelos Pineda

University of Auckland, Auckland, New Zealand
D. Krofcheck

University of Canterbury, Christchurch, New Zealand
P.H. Butler, S. Reucroft

National Centre for Physics, Quaid-I-Azam University, Islamabad, Pakistan
A. Ahmad, M. Ahmad, Q. Hassan, H.R. Hoorani, W.A. Khan, T. Khurshid, M. Shoaib

National Centre for Nuclear Research, Swierk, Poland
H. Bialkowska, M. Bluj, B. Boimska, T. Frueboes, M. Górski, M. Kazana, K. Nawrocki, K. Romanowska-Rybinska, M. Szleper, P. Zalewski

Institute of Experimental Physics, Faculty of Physics, University of Warsaw, Warsaw, Poland
G. Brona, K. Bunkowski, K. Doroba, A. Kalinowski, M. Konecki, J. Krolikowski, M. Misiura, M. Olszewski, M. Walczak

Laboratório de Instrumentaç ao e Física Experimental de Partículas, Lisboa, Portugal
P. Bargassa, C. Beir ao Da Cruz E Silva, A. Di Francesco, P. Faccioli, P.G. Ferreira Parracho,

M. Gallinaro, L. Lloret Iglesias, F. Nguyen, J. Rodrigues Antunes, J. Seixas, O. Toldaiev, D. Vadruccio, J. Varela, P. Vischia

Joint Institute for Nuclear Research, Dubna, Russia
S. Afanasiev, P. Bunin, M. Gavrilenko, I. Golutvin, I. Gorbunov, A. Kamenev, V. Karjavin, V. Konoplyanikov, A. Lanev, A. Malakhov, V. Matveev[33], P. Moisenz, V. Palichik, V. Perelygin, S. Shmatov, S. Shulha, N. Skatchkov, V. Smirnov, T. Toriashvili[34], A. Zarubin

Petersburg Nuclear Physics Institute, Gatchina (St. Petersburg), Russia
V. Golovtsov, Y. Ivanov, V. Kim[35], E. Kuznetsova, P. Levchenko, V. Murzin, V. Oreshkin, I. Smirnov, V. Sulimov, L. Uvarov, S. Vavilov, A. Vorobyev

Institute for Nuclear Research, Moscow, Russia
Yu. Andreev, A. Dermenev, S. Gninenko, N. Golubev, A. Karneyeu, M. Kirsanov, N. Krasnikov, A. Pashenkov, D. Tlisov, A. Toropin

Institute for Theoretical and Experimental Physics, Moscow, Russia
V. Epshteyn, V. Gavrilov, N. Lychkovskaya, V. Popov, I. Pozdnyakov, G. Safronov, A. Spiridonov, E. Vlasov, A. Zhokin

P.N. Lebedev Physical Institute, Moscow, Russia
V. Andreev, M. Azarkin[36], I. Dremin[36], M. Kirakosyan, A. Leonidov[36], G. Mesyats, S.V. Rusakov, A. Vinogradov

Skobeltsyn Institute of Nuclear Physics, Lomonosov Moscow State University, Moscow, Russia
A. Baskakov, A. Belyaev, E. Boos, M. Dubinin[37], L. Dudko, A. Ershov, A. Gribushin, A. Kaminskiy[38], V. Klyukhin, O. Kodolova, I. Lokhtin, I. Myagkov, S. Obraztsov, S. Petrushanko, V. Savrin

State Research Center of Russian Federation, Institute for High Energy Physics, Protvino, Russia
I. Azhgirey, I. Bayshev, S. Bitioukov, V. Kachanov, A. Kalinin, D. Konstantinov, V. Krychkine, V. Petrov, R. Ryutin, A. Sobol, L. Tourtchanovitch, S. Troshin, N. Tyurin, A. Uzunian, A. Volkov

University of Belgrade, Faculty of Physics and Vinca Institute of Nuclear Sciences, Belgrade, Serbia
P. Adzic[39], M. Ekmedzic, J. Milosevic, V. Rekovic

Centro de Investigaciones Energéticas Medioambientales y Tecnológicas (CIEMAT), Madrid, Spain
J. Alcaraz Maestre, E. Calvo, M. Cerrada, M. Chamizo Llatas, N. Colino, B. De La Cruz, A. Delgado Peris, D. Domínguez Vázquez, A. Escalante Del Valle, C. Fernandez Bedoya, J.P. Fernández Ramos, J. Flix, M.C. Fouz, P. Garcia-Abia, O. Gonzalez Lopez, S. Goy Lopez, J.M. Hernandez, M.I. Josa, E. Navarro De Martino, A. Pérez-Calero Yzquierdo, J. Puerta Pelayo, A. Quintario Olmeda, I. Redondo, L. Romero, M.S. Soares

Universidad Autónoma de Madrid, Madrid, Spain
C. Albajar, J.F. de Trocóniz, M. Missiroli, D. Moran

Universidad de Oviedo, Oviedo, Spain
H. Brun, J. Cuevas, J. Fernandez Menendez, S. Folgueras, I. Gonzalez Caballero, E. Palencia Cortezon, J.M. Vizan Garcia

Instituto de Física de Cantabria (IFCA), CSIC-Universidad de Cantabria, Santander, Spain
J.A. Brochero Cifuentes, I.J. Cabrillo, A. Calderon, J.R. Casti neiras De Saa, J. Duarte Campderros, M. Fernandez, G. Gomez, A. Graziano, A. Lopez Virto, J. Marco, R. Marco, C. Martinez Rivero, F. Matorras, F.J. Munoz Sanchez, J. Piedra Gomez, T. Rodrigo, A.Y. Rodríguez-Marrero, A. Ruiz-Jimeno, L. Scodellaro, I. Vila, R. Vilar Cortabitarte

CERN, European Organization for Nuclear Research, Geneva, Switzerland
D. Abbaneo, E. Auffray, G. Auzinger, M. Bachtis, P. Baillon, A.H. Ball, S.L. Bally, D. Barney, A. Benaglia, J. Bendavid, L. Benhabib, J.F. Benitez, G.M. Berruti, P. Bloch, A. Bocci, A. Bonato, C. Botta, H. Breuker, T. Camporesi, G. Cerminara, S. Colafranceschi[40], A. Conde Garcia, M. D'Alfonso, D. d'Enterria, A. Dabrowski, V. Daponte, A. David, M. De Gruttola, F. De Guio, A. De Roeck, S. De Visscher, E. Di Marco, M. Dobson, M. Dordevic, B. Dorney, T. du Pree, N. Dupont-Sagorin, A. Elliott-Peisert, G. Franzoni, W. Funk, A. Gaddi, D. Gigi, K. Gill, D. Giordano, M. Girone, F. Glege, R. Guida, S. Gundacker, M. Guthoff, J. Hammer, M. Hansen, P. Harris, J. Hegeman, V. Innocente, P. Janot, H. Kirschenmann, M.J. Kortelainen, K. Kousouris, K. Krajczar, P. Lecoq, C. Lourenço, M.T. Lucchini, N. Magini, L. Malgeri, M. Mannelli, J. Marrouche, A. Martelli, L. Masetti, F. Meijers, S. Mersi, E. Meschi, F. Moortgat, S. Morovic, M. Mulders, M.V. Nemallapudi, H. Neugebauer, S. Orfanelli[41], L. Orsini, L. Pape, E. Perez, A. Petrilli, G. Petrucciani, A. Pfeiffer, D. Piparo, H. Postema, A. Racz, G. Rolandi[42], M. Rovere, M. Ruan, H. Sakulin, C. Schäfer, C. Schwick, A. Sharma, P. Silva, M. Simon, P. Sphicas[43], D. Spiga, J. Steggemann, B. Stieger, M. Stoye, Y. Takahashi, D. Treille, A. Tsirou, G.I. Veres[20], N. Wardle, H.K. Wöhri, A. Zagozdzinska[44], W.D. Zeuner

Paul Scherrer Institut, Villigen, Switzerland
W. Bertl, K. Deiters, W. Erdmann, R. Horisberger, Q. Ingram, H.C. Kaestli, D. Kotlinski, U. Langenegger, T. Rohe

Institute for Particle Physics, ETH Zurich, Zurich, Switzerland
F. Bachmair, L. Bäni, L. Bianchini, M.A. Buchmann, B. Casal, G. Dissertori, M. Dittmar, M. Donegà, M. Dünser, P. Eller, C. Grab, C. Heidegger, D. Hits, J. Hoss, G. Kasieczka, W. Lustermann, B. Mangano, A.C. Marini, M. Marionneau, P. Martinez Ruiz del Arbol, M. Masciovecchio, D. Meister, N. Mohr, P. Musella, F. Nessi-Tedaldi, F. Pandolfi, J. Pata, F. Pauss, L. Perrozzi, M. Peruzzi, M. Quittnat, M. Rossini, A. Starodumov[45], M. Takahashi, V.R. Tavolaro, K. Theofilatos, R. Wallny, H.A. Weber

Universität Zürich, Zurich, Switzerland
T.K. Aarrestad, C. Amsler[46], M.F. Canelli, V. Chiochia, A. De Cosa, C. Galloni, A. Hinzmann, T. Hreus, B. Kilminster, C. Lange, J. Ngadiuba, D. Pinna, P. Robmann, F.J. Ronga, D. Salerno, S. Taroni, Y. Yang

National Central University, Chung-Li, Taiwan
M. Cardaci, K.H. Chen, T.H. Doan, C. Ferro, M. Konyushikhin, C.M. Kuo, W. Lin, Y.J. Lu, R. Volpe, S.S. Yu

National Taiwan University (NTU), Taipei, Taiwan
P. Chang, Y.H. Chang, Y.W. Chang, Y. Chao, K.F. Chen, P.H. Chen, C. Dietz, F. Fiori, U. Grundler, W.-S. Hou, Y. Hsiung, Y.F. Liu, R.-S. Lu, M. Mi nano Moya, E. Petrakou, J.f. Tsai, Y.M. Tzeng, R. Wilken

Chulalongkorn University, Faculty of Science, Department of Physics, Bangkok, Thailand
B. Asavapibhop, K. Kovitanggoon, G. Singh, N. Srimanobhas, N. Suwonjandee

Cukurova University, Adana, Turkey
A. Adiguzel, S. Cerci[47], C. Dozen, S. Girgis, G. Gokbulut, Y. Guler, E. Gurpinar, I. Hos, E.E. Kangal[48], A. Kayis Topaksu, G. Onengut[49], K. Ozdemir[50], S. Ozturk[51], B. Tali[47], H. Topakli[51], M. Vergili, C. Zorbilmez

Middle East Technical University, Physics Department, Ankara, Turkey
I.V. Akin, B. Bilin, S. Bilmis, B. Isildak[52], G. Karapinar[53], U.E. Surat, M. Yalvac, M. Zeyrek

Bogazici University, Istanbul, Turkey
E.A. Albayrak[54], E. Gülmez, M. Kaya[55], O. Kaya[56], T. Yetkin[57]

Istanbul Technical University, Istanbul, Turkey
K. Cankocak, F.I. Vardarlı

Institute for Scintillation Materials of National Academy of Science of Ukraine, Kharkov, Ukraine
B. Grynyov

National Scientific Center, Kharkov Institute of Physics and Technology, Kharkov, Ukraine
L. Levchuk, P. Sorokin

University of Bristol, Bristol, United Kingdom
R. Aggleton, F. Ball, L. Beck, J.J. Brooke, E. Clement, D. Cussans, H. Flacher, J. Goldstein, M. Grimes, G.P. Heath, H.F. Heath, J. Jacob, L. Kreczko, C. Lucas, Z. Meng, D.M. Newbold[58], S. Paramesvaran, A. Poll, T. Sakuma, S. Seif El Nasr-storey, S. Senkin, D. Smith, V.J. Smith

Rutherford Appleton Laboratory, Didcot, United Kingdom
K.W. Bell, A. Belyaev[59], C. Brew, R.M. Brown, D.J.A. Cockerill, J.A. Coughlan, K. Harder, S. Harper, E. Olaiya, D. Petyt, C.H. Shepherd-Themistocleous, A. Thea, I.R. Tomalin, T. Williams, W.J. Womersley, S.D. Worm

Imperial College, London, United Kingdom
M. Baber, R. Bainbridge, O. Buchmuller, A. Bundock, D. Burton, S. Casasso, M. Citron, D. Colling, L. Corpe, N. Cripps, P. Dauncey, G. Davies, A. De Wit, M. Della Negra, P. Dunne, A. Elwood, W. Ferguson, J. Fulcher, D. Futyan, G. Hall, G. Iles, G. Karapostoli, M. Kenzie, R. Lane, R. Lucas[58], L. Lyons, A.-M. Magnan, S. Malik, J. Nash, A. Nikitenko[45], J. Pela, M. Pesaresi, K. Petridis, D.M. Raymond, A. Richards, A. Rose, C. Seez, P. Sharp†, A. Tapper, K. Uchida, M. Vazquez Acosta[60], T. Virdee, S.C. Zenz

Brunel University, Uxbridge, United Kingdom
J.E. Cole, P.R. Hobson, A. Khan, P. Kyberd, D. Leggat, D. Leslie, I.D. Reid, P. Symonds, L. Teodorescu, M. Turner

Baylor University, Waco, USA
A. Borzou, J. Dittmann, K. Hatakeyama, A. Kasmi, H. Liu, N. Pastika

The University of Alabama, Tuscaloosa, USA
O. Charaf, S.I. Cooper, C. Henderson, P. Rumerio

Boston University, Boston, USA
A. Avetisyan, T. Bose, C. Fantasia, D. Gastler, P. Lawson, D. Rankin, C. Richardson, J. Rohlf, J. St. John, L. Sulak, D. Zou

Brown University, Providence, USA
J. Alimena, E. Berry, S. Bhattacharya, D. Cutts, Z. Demiragli, N. Dhingra, A. Ferapontov, A. Garabedian, U. Heintz, E. Laird, G. Landsberg, Z. Mao, M. Narain, S. Sagir, T. Sinthuprasith

University of California, Davis, Davis, USA
R. Breedon, G. Breto, M. Calderon De La Barca Sanchez, S. Chauhan, M. Chertok, J. Conway, R. Conway, P.T. Cox, R. Erbacher, M. Gardner, W. Ko, R. Lander, M. Mulhearn, D. Pellett, J. Pilot, F. Ricci-Tam, S. Shalhout, J. Smith, M. Squires, D. Stolp, M. Tripathi, S. Wilbur, R. Yohay

University of California, Los Angeles, USA
R. Cousins, P. Everaerts, C. Farrell, J. Hauser, M. Ignatenko, G. Rakness, D. Saltzberg, E. Takasugi, V. Valuev, M. Weber

University of California, Riverside, Riverside, USA
K. Burt, R. Clare, J. Ellison, J.W. Gary, G. Hanson, J. Heilman, M. Ivova Rikova, P. Jandir, E. Kennedy, F. Lacroix, O.R. Long, A. Luthra, M. Malberti, M. Olmedo Negrete, A. Shrinivas, S. Sumowidagdo, H. Wei, S. Wimpenny

University of California, San Diego, La Jolla, USA
J.G. Branson, G.B. Cerati, S. Cittolin, R.T. D'Agnolo, A. Holzner, R. Kelley, D. Klein, J. Letts, I. Macneill, D. Olivito, S. Padhi, M. Pieri, M. Sani, V. Sharma, S. Simon, M. Tadel, Y. Tu, A. Vartak, S. Wasserbaech[61], C. Welke, F. Würthwein, A. Yagil, G. Zevi Della Porta

University of California, Santa Barbara, Santa Barbara, USA
D. Barge, J. Bradmiller-Feld, C. Campagnari, A. Dishaw, V. Dutta, K. Flowers, M. Franco Sevilla, P. Geffert, C. George, F. Golf, L. Gouskos, J. Gran, J. Incandela, C. Justus, N. Mccoll, S.D. Mullin, J. Richman, D. Stuart, I. Suarez, W. To, C. West, J. Yoo

California Institute of Technology, Pasadena, USA
D. Anderson, A. Apresyan, A. Bornheim, J. Bunn, Y. Chen, J. Duarte, A. Mott, H.B. Newman, C. Pena, M. Pierini, M. Spiropulu, J.R. Vlimant, S. Xie, R.Y. Zhu

Carnegie Mellon University, Pittsburgh, USA
V. Azzolini, A. Calamba, B. Carlson, T. Ferguson, Y. Iiyama, M. Paulini, J. Russ, M. Sun, H. Vogel, I. Vorobiev

University of Colorado at Boulder, Boulder, USA
J.P. Cumalat, W.T. Ford, A. Gaz, F. Jensen, A. Johnson, M. Krohn, T. Mulholland, U. Nauenberg, J.G. Smith, K. Stenson, S.R. Wagner

Cornell University, Ithaca, USA
J. Alexander, A. Chatterjee, J. Chaves, J. Chu, S. Dittmer, N. Eggert, N. Mirman, G. Nicolas Kaufman, J.R. Patterson, A. Rinkevicius, A. Ryd, L. Skinnari, L. Soffi, W. Sun, S.M. Tan, W.D. Teo, J. Thom, J. Thompson, J. Tucker, Y. Weng, P. Wittich

Fermi National Accelerator Laboratory, Batavia, USA
S. Abdullin, M. Albrow, J. Anderson, G. Apollinari, L.A.T. Bauerdick, A. Beretvas, J. Berryhill, P.C. Bhat, G. Bolla, K. Burkett, J.N. Butler, H.W.K. Cheung, F. Chlebana, S. Cihangir, V.D. Elvira, I. Fisk, J. Freeman, E. Gottschalk, L. Gray, D. Green, S. Grünendahl, O. Gutsche, J. Hanlon, D. Hare, R.M. Harris, J. Hirschauer, B. Hooberman, Z. Hu, S. Jindariani, M. Johnson, U. Joshi, A.W. Jung, B. Klima, B. Kreis, S. Kwan†, S. Lammel, J. Linacre, D. Lincoln, R. Lipton, T. Liu, R. Lopes De Sá, J. Lykken, K. Maeshima, J.M. Marraffino, V.I. Martinez Outschoorn, S. Maruyama, D. Mason, P. McBride, P. Merkel, K. Mishra, S. Mrenna, S. Nahn, C. Newman-Holmes, V. O'Dell, O. Prokofyev, E. Sexton-Kennedy, A. Soha, W.J. Spalding, L. Spiegel, L. Taylor, S. Tkaczyk, N.V. Tran, L. Uplegger, E.W. Vaandering, C. Vernieri, M. Verzocchi, R. Vidal, A. Whitbeck, F. Yang, H. Yin

University of Florida, Gainesville, USA
D. Acosta, P. Avery, P. Bortignon, D. Bourilkov, A. Carnes, M. Carver, D. Curry, S. Das, G.P. Di Giovanni, R.D. Field, M. Fisher, I.K. Furic, J. Hugon, J. Konigsberg, A. Korytov, J.F. Low, P. Ma, K. Matchev, H. Mei, P. Milenovic[62], G. Mitselmakher, L. Muniz, D. Rank, L. Shchutska, M. Snowball, D. Sperka, S.J. Wang, J. Yelton

Florida International University, Miami, USA
S. Hewamanage, S. Linn, P. Markowitz, G. Martinez, J.L. Rodriguez

Florida State University, Tallahassee, USA
A. Ackert, J.R. Adams, T. Adams, A. Askew, J. Bochenek, B. Diamond, J. Haas, S. Hagopian, V. Hagopian, K.F. Johnson, A. Khatiwada, H. Prosper, V. Veeraraghavan, M. Weinberg

Florida Institute of Technology, Melbourne, USA
V. Bhopatkar, M. Hohlmann, H. Kalakhety, D. Mareskas-palcek, T. Roy, F. Yumiceva, A. Zhang

University of Illinois at Chicago (UIC), Chicago, USA
M.R. Adams, L. Apanasevich, D. Berry, R.R. Betts, I. Bucinskaite, R. Cavanaugh, O. Evdokimov, L. Gauthier, C.E. Gerber, D.J. Hofman, P. Kurt, C. O'Brien, I.D. Sandoval Gonzalez, C. Silkworth, P. Turner, N. Varelas, Z. Wu, M. Zakaria

The University of Iowa, Iowa City, USA
B. Bilki[63], W. Clarida, K. Dilsiz, S. Durgut, R.P. Gandrajula, M. Haytmyradov, V. Khristenko, J.-P. Merlo, H. Mermerkaya[64], A. Mestvirishvili, A. Moeller, J. Nachtman, H. Ogul, Y. Onel, F. Ozok[54], A. Penzo, S. Sen[65], C. Snyder, P. Tan, E. Tiras, J. Wetzel, K. Yi

Johns Hopkins University, Baltimore, USA
I. Anderson, B.A. Barnett, B. Blumenfeld, D. Fehling, L. Feng, A.V. Gritsan, P. Maksimovic, C. Martin, K. Nash, M. Osherson, M. Swartz, M. Xiao, Y. Xin

The University of Kansas, Lawrence, USA
P. Baringer, A. Bean, G. Benelli, C. Bruner, J. Gray, R.P. Kenny III, D. Majumder, M. Malek, M. Murray, D. Noonan, S. Sanders, R. Stringer, Q. Wang, J.S. Wood

Kansas State University, Manhattan, USA
I. Chakaberia, A. Ivanov, K. Kaadze, S. Khalil, M. Makouski, Y. Maravin, L.K. Saini, N. Skhirtladze, I. Svintradze, S. Toda

Lawrence Livermore National Laboratory, Livermore, USA
D. Lange, F. Rebassoo, D. Wright

University of Maryland, College Park, USA
C. Anelli, A. Baden, O. Baron, A. Belloni, B. Calvert, S.C. Eno, C. Ferraioli, J.A. Gomez, N.J. Hadley, S. Jabeen, R.G. Kellogg, T. Kolberg, J. Kunkle, Y. Lu, A.C. Mignerey, K. Pedro, Y.H. Shin, A. Skuja, M.B. Tonjes, S.C. Tonwar

Massachusetts Institute of Technology, Cambridge, USA
A. Apyan, R. Barbieri, A. Baty, K. Bierwagen, S. Brandt, W. Busza, I.A. Cali, L. Di Matteo, G. Gomez Ceballos, M. Goncharov, D. Gulhan, G.M. Innocenti, M. Klute, D. Kovalskyi, Y.S. Lai, Y.-J. Lee, A. Levin, P.D. Luckey, C. Mcginn, X. Niu, C. Paus, D. Ralph, C. Roland, G. Roland, G.S.F. Stephans, K. Sumorok, M. Varma, D. Velicanu, J. Veverka, J. Wang, T.W. Wang, B. Wyslouch, M. Yang, V. Zhukova

University of Minnesota, Minneapolis, USA
B. Dahmes, A. Finkel, A. Gude, P. Hansen, S. Kalafut, S.C. Kao, K. Klapoetke, Y. Kubota, Z. Lesko, J. Mans, S. Nourbakhsh, N. Ruckstuhl, R. Rusack, N. Tambe, J. Turkewitz

University of Mississippi, Oxford, USA
J.G. Acosta, S. Oliveros

University of Nebraska-Lincoln, Lincoln, USA
E. Avdeeva, K. Bloom, S. Bose, D.R. Claes, A. Dominguez, C. Fangmeier, R. Gonzalez Suarez, R. Kamalieddin, J. Keller, D. Knowlton, I. Kravchenko, J. Lazo-Flores, F. Meier, J. Monroy, F. Ratnikov, J.E. Siado, G.R. Snow

State University of New York at Buffalo, Buffalo, USA
M. Alyari, J. Dolen, J. George, A. Godshalk, I. Iashvili, J. Kaisen, A. Kharchilava, A. Kumar, S. Rappoccio

Northeastern University, Boston, USA
G. Alverson, E. Barberis, D. Baumgartel, M. Chasco, A. Hortiangtham, A. Massironi, D.M. Morse, D. Nash, T. Orimoto, R. Teixeira De Lima, D. Trocino, R.-J. Wang, D. Wood, J. Zhang

Northwestern University, Evanston, USA
K.A. Hahn, A. Kubik, N. Mucia, N. Odell, B. Pollack, A. Pozdnyakov, M. Schmitt, S. Stoynev, K. Sung, M. Trovato, M. Velasco, S. Won

University of Notre Dame, Notre Dame, USA
A. Brinkerhoff, N. Dev, M. Hildreth, C. Jessop, D.J. Karmgard, N. Kellams, K. Lannon, S. Lynch, N. Marinelli, F. Meng, C. Mueller, Y. Musienko[33], T. Pearson, M. Planer, R. Ruchti, G. Smith, N. Valls, M. Wayne, M. Wolf, A. Woodard

The Ohio State University, Columbus, USA
L. Antonelli, J. Brinson, B. Bylsma, L.S. Durkin, S. Flowers, A. Hart, C. Hill, R. Hughes, K. Kotov, T.Y. Ling, B. Liu, W. Luo, D. Puigh, M. Rodenburg, B.L. Winer, H.W. Wulsin

Princeton University, Princeton, USA
O. Driga, P. Elmer, J. Hardenbrook, P. Hebda, S.A. Koay, P. Lujan, D. Marlow, T. Medvedeva, M. Mooney, J. Olsen, C. Palmer, P. Piroué, X. Quan, H. Saka, D. Stickland, C. Tully, J.S. Werner, A. Zuranski

Purdue University, West Lafayette, USA
V.E. Barnes, D. Benedetti, D. Bortoletto, L. Gutay, M.K. Jha, M. Jones, K. Jung, M. Kress, N. Leonardo, D.H. Miller, N. Neumeister, F. Primavera, B.C. Radburn-Smith, X. Shi, I. Shipsey, D. Silvers, J. Sun, A. Svyatkovskiy, F. Wang, W. Xie, L. Xu, J. Zablocki

Purdue University Calumet, Hammond, USA
N. Parashar, J. Stupak

Rice University, Houston, USA
A. Adair, B. Akgun, Z. Chen, K.M. Ecklund, F.J.M. Geurts, M. Guilbaud, W. Li, B. Michlin, M. Northup, B.P. Padley, R. Redjimi, J. Roberts, J. Rorie, Z. Tu, J. Zabel

University of Rochester, Rochester, USA
B. Betchart, A. Bodek, P. de Barbaro, R. Demina, Y. Eshaq, T. Ferbel, M. Galanti, A. Garcia-Bellido, P. Goldenzweig, J. Han, A. Harel, O. Hindrichs, A. Khukhunaishvili, G. Petrillo, M. Verzetti

The Rockefeller University, New York, USA
L. Demortier

Rutgers, The State University of New Jersey, Piscataway, USA
S. Arora, A. Barker, J.P. Chou, C. Contreras-Campana, E. Contreras-Campana, D. Duggan, D. Ferencek, Y. Gershtein, R. Gray, E. Halkiadakis, D. Hidas, E. Hughes, S. Kaplan, R. Kunnawalkam Elayavalli, A. Lath, S. Panwalkar, M. Park, S. Salur, S. Schnetzer, D. Sheffield, S. Somalwar, R. Stone, S. Thomas, P. Thomassen, M. Walker

University of Tennessee, Knoxville, USA
M. Foerster, G. Riley, K. Rose, S. Spanier, A. York

Texas A&M University, College Station, USA
M. Abi Akl, O. Bouhali[66], A. Castaneda Hernandez, A. Celik, M. Dalchenko, M. De Mattia, A. Delgado, S. Dildick, R. Eusebi, W. Flanagan, J. Gilmore, T. Huang, T. Kamon[67], V. Krutelyov, R. Montalvo, R. Mueller, I. Osipenkov, Y. Pakhotin, R. Patel, A. Perloff, J. Roe, A. Rose, A. Safonov, A. Tatarinov, K.A. Ulmer[2]

Texas Tech University, Lubbock, USA
N. Akchurin, C. Cowden, J. Damgov, C. Dragoiu, P.R. Dudero, J. Faulkner, S. Kunori, K. Lamichhane, S.W. Lee, T. Libeiro, S. Undleeb, I. Volobouev

Vanderbilt University, Nashville, USA
E. Appelt, A.G. Delannoy, S. Greene, A. Gurrola, R. Janjam, W. Johns, C. Maguire, Y. Mao, A. Melo, P. Sheldon, B. Snook, S. Tuo, J. Velkovska, Q. Xu

University of Virginia, Charlottesville, USA
M.W. Arenton, S. Boutle, B. Cox, B. Francis, J. Goodell, R. Hirosky, A. Ledovskoy, H. Li, C. Lin, C. Neu, E. Wolfe, J. Wood, F. Xia

Wayne State University, Detroit, USA
C. Clarke, R. Harr, P.E. Karchin, C. Kottachchi Kankanamge Don, P. Lamichhane, J. Sturdy

University of Wisconsin, Madison, USA
D.A. Belknap, D. Carlsmith, M. Cepeda, A. Christian, S. Dasu, L. Dodd, S. Duric, E. Friis, B. Gomber, R. Hall-Wilton, M. Herndon, A. Hervé, P. Klabbers, A. Lanaro, A. Levine, K. Long, R. Loveless, A. Mohapatra, I. Ojalvo, T. Perry, G.A. Pierro, G. Polese, I. Ross, T. Ruggles, T. Sarangi, A. Savin, N. Smith, W.H. Smith, D. Taylor, N. Woods

†: Deceased
1: Also at Vienna University of Technology, Vienna, Austria
2: Also at CERN, European Organization for Nuclear Research, Geneva, Switzerland
3: Also at State Key Laboratory of Nuclear Physics and Technology, Peking University, Beijing, China
4: Also at Institut Pluridisciplinaire Hubert Curien, Université de Strasbourg, Université de Haute Alsace Mulhouse, CNRS/IN2P3, Strasbourg, France
5: Also at National Institute of Chemical Physics and Biophysics, Tallinn, Estonia
6: Also at Skobeltsyn Institute of Nuclear Physics, Lomonosov Moscow State University, Moscow, Russia
7: Also at Universidade Estadual de Campinas, Campinas, Brazil
8: Also at Centre National de la Recherche Scientifique (CNRS) - IN2P3, Paris, France
9: Also at Laboratoire Leprince-Ringuet, Ecole Polytechnique, IN2P3-CNRS, Palaiseau, France
10: Also at Joint Institute for Nuclear Research, Dubna, Russia
11: Also at Ain Shams University, Cairo, Egypt

12: Now at British University in Egypt, Cairo, Egypt
13: Now at Helwan University, Cairo, Egypt
14: Also at Suez University, Suez, Egypt
15: Also at Cairo University, Cairo, Egypt
16: Now at Fayoum University, El-Fayoum, Egypt
17: Also at Université de Haute Alsace, Mulhouse, France
18: Also at Brandenburg University of Technology, Cottbus, Germany
19: Also at Institute of Nuclear Research ATOMKI, Debrecen, Hungary
20: Also at Eötvös Loránd University, Budapest, Hungary
21: Also at University of Debrecen, Debrecen, Hungary
22: Also at Wigner Research Centre for Physics, Budapest, Hungary
23: Also at University of Visva-Bharati, Santiniketan, India
24: Now at King Abdulaziz University, Jeddah, Saudi Arabia
25: Also at University of Ruhuna, Matara, Sri Lanka
26: Also at Isfahan University of Technology, Isfahan, Iran
27: Also at University of Tehran, Department of Engineering Science, Tehran, Iran
28: Also at Plasma Physics Research Center, Science and Research Branch, Islamic Azad University, Tehran, Iran
29: Also at Università degli Studi di Siena, Siena, Italy
30: Also at Purdue University, West Lafayette, USA
31: Also at International Islamic University of Malaysia, Kuala Lumpur, Malaysia
32: Also at CONSEJO NATIONAL DE CIENCIA Y TECNOLOGIA, MEXICO, Mexico
33: Also at Institute for Nuclear Research, Moscow, Russia
34: Also at Institute of High Energy Physics and Informatization, Tbilisi State University, Tbilisi, Georgia
35: Also at St. Petersburg State Polytechnical University, St. Petersburg, Russia
36: Also at National Research Nuclear University 'Moscow Engineering Physics Institute' (MEPhI), Moscow, Russia
37: Also at California Institute of Technology, Pasadena, USA
38: Also at INFN Sezione di Padova; Università di Padova; Università di Trento (Trento), Padova, Italy
39: Also at Faculty of Physics, University of Belgrade, Belgrade, Serbia
40: Also at Facoltà Ingegneria, Università di Roma, Roma, Italy
41: Also at National Technical University of Athens, Athens, Greece
42: Also at Scuola Normale e Sezione dell'INFN, Pisa, Italy
43: Also at University of Athens, Athens, Greece
44: Also at Warsaw University of Technology, Institute of Electronic Systems, Warsaw, Poland
45: Also at Institute for Theoretical and Experimental Physics, Moscow, Russia
46: Also at Albert Einstein Center for Fundamental Physics, Bern, Switzerland
47: Also at Adiyaman University, Adiyaman, Turkey
48: Also at Mersin University, Mersin, Turkey
49: Also at Cag University, Mersin, Turkey
50: Also at Piri Reis University, Istanbul, Turkey
51: Also at Gaziosmanpasa University, Tokat, Turkey
52: Also at Ozyegin University, Istanbul, Turkey
53: Also at Izmir Institute of Technology, Izmir, Turkey
54: Also at Mimar Sinan University, Istanbul, Istanbul, Turkey
55: Also at Marmara University, Istanbul, Turkey
56: Also at Kafkas University, Kars, Turkey

57: Also at Yildiz Technical University, Istanbul, Turkey
58: Also at Rutherford Appleton Laboratory, Didcot, United Kingdom
59: Also at School of Physics and Astronomy, University of Southampton, Southampton, United Kingdom
60: Also at Instituto de Astrofísica de Canarias, La Laguna, Spain
61: Also at Utah Valley University, Orem, USA
62: Also at University of Belgrade, Faculty of Physics and Vinca Institute of Nuclear Sciences, Belgrade, Serbia
63: Also at Argonne National Laboratory, Argonne, USA
64: Also at Erzincan University, Erzincan, Turkey
65: Also at Hacettepe University, Ankara, Turkey
66: Also at Texas A&M University at Qatar, Doha, Qatar
67: Also at Kyungpook National University, Daegu, Korea

Contents

Chapter 1

Introduction

1.1 Motivations for the GE1/1 muon detector upgrade

After the upgrade of the LHC injector chain during the second Long Shutdown (LS2), which is currently planned to take place around 2019, the instantaneous luminosity ($\mathcal{L}$) will approach or exceed 2×10^{34} cm^{-2}s^{-1}. The LHC Phase 1 operation is currently expected to end at around 2022 with the total integrated luminosity (L) $\sim$ 300 fb^{-1}. A high-luminosity upgrade of the LHC interaction regions is foreseen during a third long shutdown (LS3) to further increase the instantaneous luminosity to 5×10^{34} cm^{-2}s^{-1}.

The CMS muon system must be able to substain a physics program after the LS2 shutdown that maintains sensitivity for electroweak scale physics and for TeV scale searches similar to what was achieved before LS1.

The CMS muon subdetector was originally designed as a highly hermetic and redundant system that employs three detection technologies [1]. Precision measurements and Level 1 (L1) triggering are provided by drift tubes (DT) in the barrel, covering acceptances up to $|\eta| < 1.2$, and cathode strip chambers (CSC) in the endcaps covering $1.0 < |\eta| < 2.4$. Additionally, resistive plate chambers (RPC) provide redundant trigger and coarse position measurement in both barrel and endcap regions, but were not implemented beyond $|\eta| > 1.6$ due to concerns about their capability to handle the high background particle rates.

Muon trigger studies for the CMS Phase 1 Upgrade in [2] show that achieving an acceptable L1 trigger rate for muons with $p_T < 25$ GeV after LS2 is not possible without substantial additional efficiency losses in the endcap region, representing over a half of the overall CMS muon coverage.

CMS is producing a Phase 2 Upgrade Technical Proposal that describes the motivations and plans for improvements to the muon system that will be necessary to maintain the high level of performance achieved during Run 1 in the challenging environment of the high luminosity LHC collider (HL-LHC).

One of these improvements is the installation of an additional set of muon detectors, GE1/1, that use gas electron multiplier (GEM) technology in the first endcap muon station in order to maintain or even improve the forward muon triggering and reconstruction in the region $1.6 < |\eta| < 2.2$ in the face of high luminosity. This TDR describes the GE1/1 project which is already in well-advanced state and proposed for an early stage installation in LS2 (approx 2018-19).

The GE1/1 muon detector station is shown in the quadrant cross-section of CMS in Figure 1.1. Since forward RPCs were envisioned in the original conception of the CMS muon system, there is space available within CMS for installation of a sufficiently compact (thin) detector to respect

the tight geometrical limitations. The proposed GE1/1 detector utilizing GEM technology is an excellent choice for this region due to its thin profile and the ability of operating well at particle fluxes far above those expected in the forward region under HL-LHC conditions.. (In CMS terminology, this muon station is designated GE1/1, where the letter G indicates the GEM technology, the letter E indicates this is an endcap muon station, the first "1" indicates that it is part of the first muon station encountered by particles from the interaction point, and the second "1" indicates that it is the first ring of muon chambers going outward in radius from the beam line.)

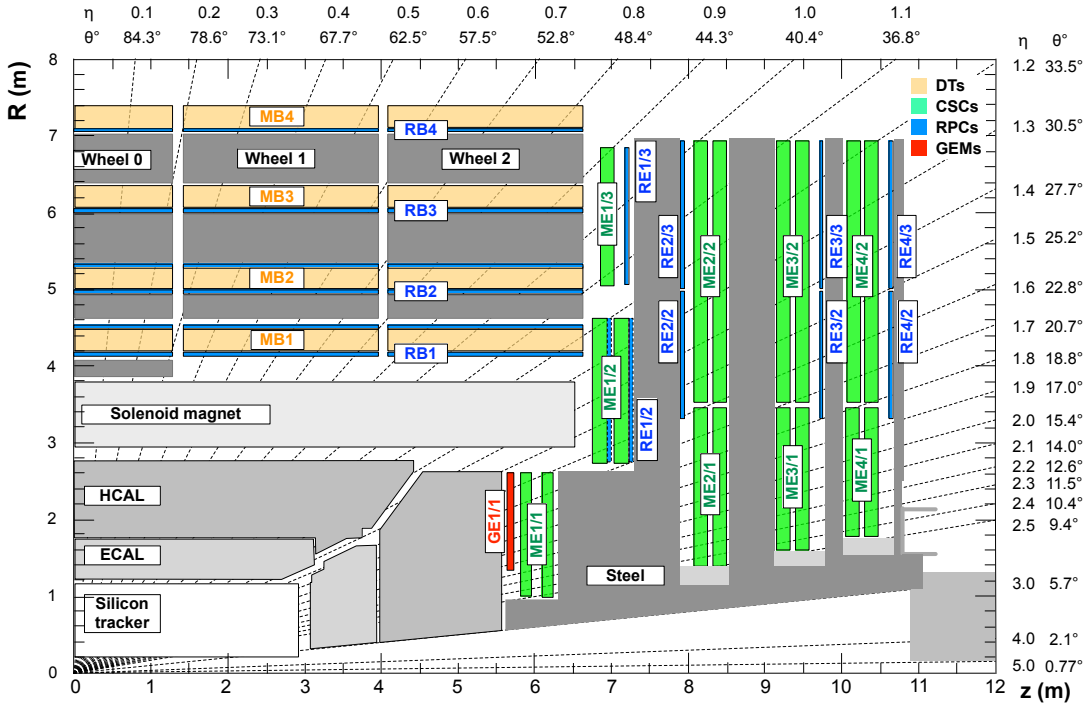

Figure 1.1: A quadrant of the $R-z$ cross-section of the CMS detector, highlighting in red the location of the proposed GE1/1 detector within the CMS muon system.

The greatest benefit of the early installation of the GE1/1 muon station is to improve the L1 muon trigger during LHC running before the installation of a new silicon tracker and its associated track trigger [3] in LS3.

The bending of muons within the CMS solenoid is largest at the position of the first muon station; the bending is much less at subsequent muon stations because the magnetic field lines bend around in the endcap flux return. Because of the reduction in the magnetic field and higher background rates with increasing η, the contribution to the trigger rate within the GE1/1 coverage of $1.6 < |\eta| < 2.2$ is particularly large and difficult to control. At this critical position, the GE1/1 chambers in conjunction with the existing CSC station ME1/1 effectively multiply by a factor of 2.4–3.5 the path length traversed by muons within the first muon station over that of the 6 layers of the ME1/1 CSC chambers alone (11.7 cm). The increased path length, in turn, significantly improves the L1 stand-alone muon trigger momentum resolution and drastically reduces its disproportionately large contribution to the overall L1 muon trigger rate. The single muon trigger rate curves before and after the GE1/1 upgrade for the region $1.6 < |\eta| < 2.2$ are shown in Figure 1.2. With the upgrade, the L1 muon trigger thresholds can be maintained at low p_{T} values, so that the efficiency for capturing interesting physics processes featuring soft leptons can be kept high. On the example of a single muon trigger, the upgrade will allow

preserving the L1 threshold at 12-14 GeV providing nearly full efficiency for offline muons with $p_T > 18 - 20$ GeV.

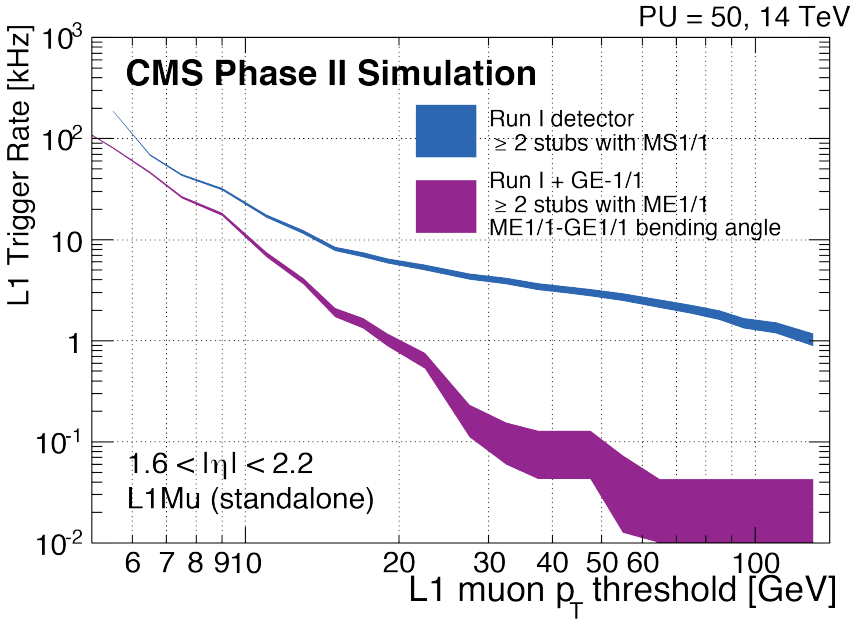

Figure 1.2: Level 1 muon trigger rates before and after the GE1/1 upgrade at a luminosity of 2×10^{34} cm^{-2} s^{-1}, for constant efficiency of 94%. MS1/1 denotes the first endcap muon station Level 1 trigger in both cases, i.e. with CSC-only or with the combination CSC and GEM trigger information. With the addition of GE1/1, the bending angle between the two stations can be used and the trigger rate is greatly reduced.

Maintaining low muon trigger p_{T} thresholds is important for a broad spectrum of physics studies ranging from new physics searches to the measurements in the Higgs sector. Some of the striking examples are scenarios in the context of split [4, 5] and anomaly mediated [6, 7] SUSY, sensitivity to which is often dependent on the ability to trigger on soft leptons, particularly in the difficult for the LHC scenarios with "compressed" mass spectra. Other examples include studies of the Higgs coupling to the third generation leptons via $H \to \tau\tau$ and searches for extended Higgs sectors appearing in various new physics scenarios [8] and which could hold the key to the electroweak baryogenesis [9]. As an illustration, we consider the $H \to \tau^+\tau^-$ case. Among the various decay channels, the semileptonic $\tau\tau \to \mu\tau_h + X$ channel is of special importance due to its relatively large branching fraction and clean signal, provided these events can actually be triggered efficiently given the low average lepton p_{T}. Simulation studies show an increase in the kinematic acceptance for $H \to \tau^+\tau^-$ signal events in this channel by as much as 35% if the muon p_{T} threshold is lowered by just 5 GeV, e.g. from 25 GeV to 20 GeV. In addition to the inclusive muon trigger, all other trigger paths that rely on muon selections at L1 will benefit from lower thresholds. The latter includes multi-object triggers such as μ+jet, $\mu + H_T^{miss}$ or $e/\gamma + \mu$, which is relevant for studies of the bosonic Higgs decays, $H \to VV$, such as $H \to W^+W^- \to e\mu\, 2\nu$. Additional justification for a low-p$_T$ muon trigger may derive from the B-physics program of CMS.

After the new silicon tracker and the track trigger for CMS will have been commissioned in LS3, they will be used in coincidence with the L1 muon trigger to form a "combined muon trigger," where the momentum resolution for most muons from the primary event vertex will be set by the very high resolution achieved by the track trigger. The GE1/1 and other planned

new muon stations will be used to maintain excellent position matching with the track trigger, and the stand-alone muon trigger will run in parallel with the combined muon trigger but at a higher p_T threshold. The stand-alone muon trigger will provide high efficiency for displaced muons and exotic particles as well as a backup for the combined muon trigger to maintain highest overall muon trigger efficiency.

Besides GE1/1, the CMS Phase 2 muon upgrade plans include later installation, during LS3, of a second station of GEM detectors (GE2/1), and third (RE3/1) and fourth (RE4/1) stations of improved RPC (iRPC) detectors. The additional forward muon detectors will increase the average number of muon hits along a forward track up to about the same level that is already present in the barrel muon region of CMS. This is a minimal requirement for handling HL-LHC conditions, given that in the forward region the background particle rates are higher and magnetic bending power is much reduced. The new forward muon stations provide additional redundancy that will be important for continued good operation of the forward muon system if any of the forward muon detectors suffer degradation due to the high particle rates and large radiation doses from the HL-LHC luminosity, or the long passage of time during the HL-LHC era. In such scenarios, the redundancy provided with the deployment of the GE1/1 detector allows mitigating a potentially large degradation in muon trigger performance. The latter is true not only for the L1 performance, but also for the standalone muon reconstruction used both in the offline and in the High Level Trigger (HLT). The added redundancy improves the quality of standalone muon reconstruction and can avert a deterioration in standalone muon momentum resolution if the performance of the aging ME1/1 system degrades.

In summary, the proposed GE1/1 upgrade targets the following improvements:

- The combined CSC-GEM operation allows measuring the bending angle at trigger level, thus strongly reducing the rate of mis-measured muons driving the trigger rate.
- Improve tracking performance in the high-rate environment where the background rates of all types are highest and the magnetic bending power is reduced.
- As part of the overall Phase 2 forward muon improvement plan, establish sufficient redundancy in the difficult region $1.6 < |\eta| < 2.2$, by adding detector planes using the space originally foreseen for RPC detectors which were not built due to concerns about hit rate capability.

1.2 GEM technology and GE1/1 system overview

In the Station GE1/1 we propose to install 72 ten-degree chambers per endcap of CMS. For charged-particle detection, the GE1/1 muon upgrade employs gas electron multipliers [10] (GEMs). GEMs exploit electron amplification that occurs within a gas medium inside narrow holes that perforate a thin polyimide foil in a hexagonal pattern. The GEM foil is clad on both sides with thin conductive layers of copper. A voltage of a few hundred volts is applied across the two layers which creates a strong electric field (60-100 kV/cm) inside the holes that causes electron-ion avalanches in the gas. An arrangement of three cascaded GEM foils, commonly known as a "Triple-GEM detector" (see Figure 1.3), allows for modest high voltage and gas amplification across each individual foil to avoid electrical breakdown problems, yet provides a high total charge amplification factor (up to 10^5). This is because the gains of the individual foils multiply to produce the total gain. The amplified charge induces a signal on the electrodes that are finely segmented in the muon bending direction (ϕ) to make the detector position-sensitive; the induced charges are read out by sensitive electronics. The chambers are segmented in 384

strips in ϕ, over 10 degree which means that each strip cover 450 μrad.

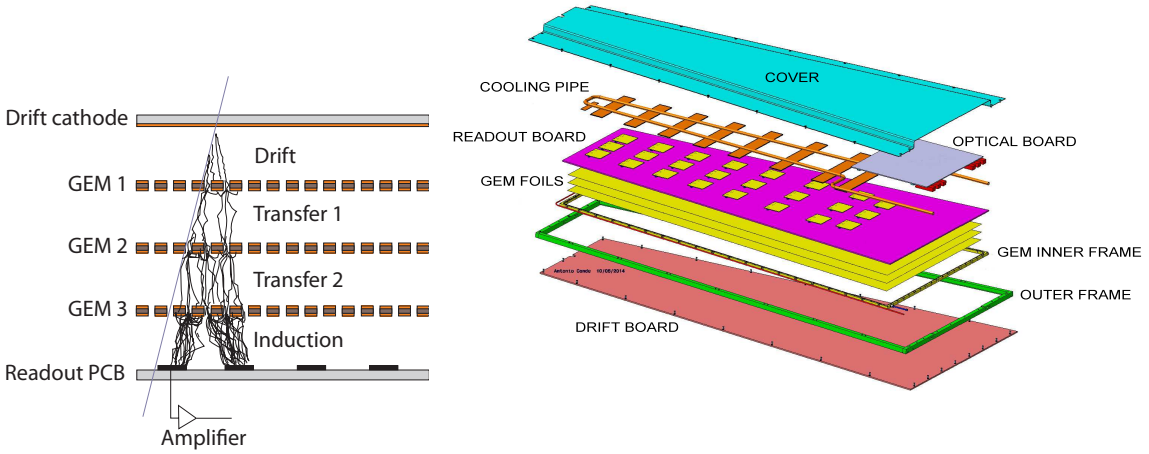

Figure 1.3: *Left:* By cascading three GEM foils, the amplification per stage can be kept modest to avoid electric breakdown problems. *Right:* Exploded view of the mechanical design of a Triple-GEM chamber.

In the GE1/1 muon system, a pair of such Triple-GEM chambers is combined to form a "super-chamber" (see Figure 1.4 left) that provides two measurement planes in the muon endcap that complement the existing ME1/1 detectors and maximizes the detection efficiency. Each super-chamber covers a $\approx 10^o$ sector, so that 72 superchambers are required (36 in each endcap) to form a ring of superchambers that gives full azimuthal coverage. The superchambers alternate in ϕ between long ($1.55 < |\eta| < 2.18$) and short ($1.61 < |\eta| < 2.18$) versions, as dictated by the mechanical envelope of the existing endcap. These η ranges maximize the GE1/1 coverage within the limits of that envelope. In most cases in this document, the coverage of GE1/1 will be quoted approximately as $1.6 < |\eta| < 2.2$. Each endcap holds 18 long and 18 short super-chambers. One endcap is depicted in Figure 1.4 (right). The superchambers will be installed in slots originally foreseen for RPC chambers, in the gap between the hadron calorimeter and the CSC ME1/1 chambers in the YE1 "nose" (see Figure 1.5). This geometry is also implemented in detector simulations used for various performance studies.

The performances of several generations of GE1/1 prototypes were studied in great detail in a series of beam tests at CERN and Fermilab and with x-ray sources over a five-year R&D period [11–13]. Figure 1.6 shows the most recent prototype, which is essentially equivalent to the proposed final production chamber. It was demonstrated that the detector response varies not more than 15% across the entire chamber. At the same time, detection efficiencies of 97-98% were achieved, depending on gas mixture and type of readout. With binary-output readout, an acceptable angular resolution of 131 μrad has been measured, which is close to the intrinsic resolution expected for the binary readout. Timing measurements of a prototype operated with $Ar/CO_2/CF_4$ 45:15:40 demonstrate that 97% of all hits are attributed to the correct 25 ns bunch crossing.

The small charge signals on the GE1/1 electrodes are amplified, digitized, and further processed by custom designed 128-channel ASIC circuits. A new front-end ASIC design based on the previous success of the binary-readout VFAT2 chip was developed to match the required particle rates and trigger precision. The transport of data between the GEM on-detector electronics and the off-detector DAQ system will be via optical fibres. CERN-based common design

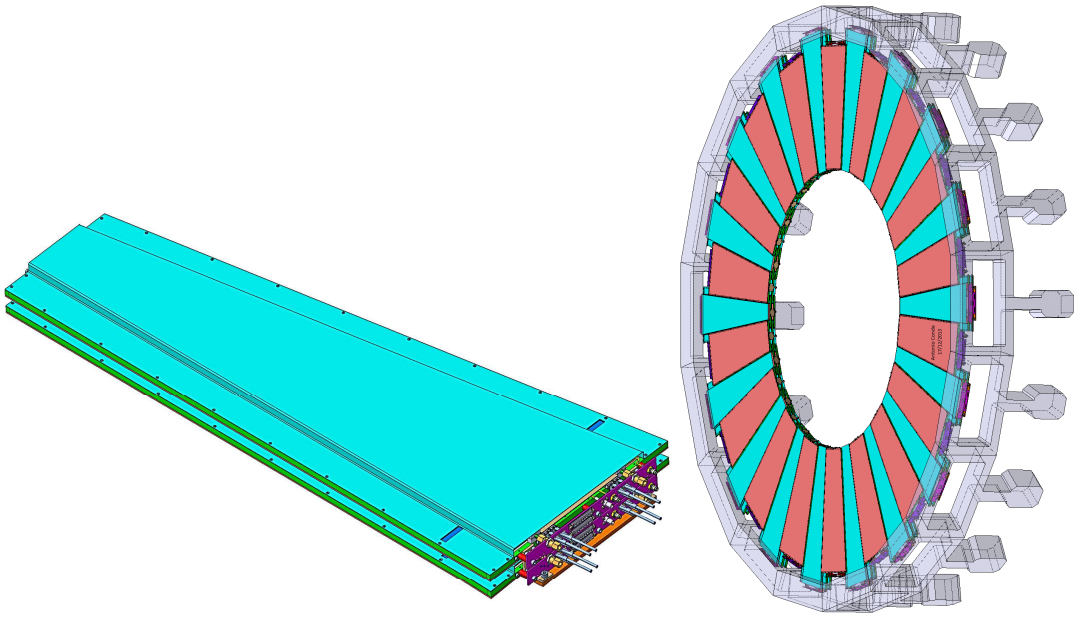

Figure 1.4: *Left:* A pair of GEM chambers form a superchamber. *Right:* Long and short chambers are combined to maximize the instrumentation within given mechanical constraints in the endcap.

projects such as the GBT chip set, Versatile link and GLIB/MP7 μTCA systems can provide the radiation tolerant optical communication system required.

Each single GEM chamber is treated as an individual unit from an electronics system point of view. The GEM chamber is segmented in both ϕ and η; the baseline for LS2 is segmentation of three in ϕ and eight in η creating a maximum of 24 individual detector segments. Each of these segments is further subdivided into 128 strips and read out by one 128-channel front-end chip. Each GEM chamber consequently has up to 24 front-end chips and channels organised in three columns. The system is designed such that one optical fibre can read out the tracking data from one GEM column, while all trigger data are carried out by a dedicated additional fibre. A single GEM chamber has three optical fibres to take the tracking and trigger data to and from the CMS GEM DAQ system. The data from the VFAT chips are sent to the GEB which delivers power and communication signals to and from the VFAT hybrid as well as providing the connection to the GEM strips. From the GEB, data are transmitted to one FPGA board, called the GEM OptoHybrid (OH), located on the wide end of the GEM module. One of the main components of the OH is a Xilinx Virtex 6 FPGA, which has been shown to be radiation-hard to levels at least two orders of magnitude higher than the expected radiation dosage.

The GEM trigger data will be sent to the CSC Trigger Mother Board (TMB) located in the experimental cavern (UXC55) while the trigger and the tracking data will be sent to the GEM off-detector electronics located in the service cavern (USC55). In the CSC TMB, the GEM trigger data will be combined with the CSC data to make combined local muon stubs, which will improve the endcap muon L1 trigger efficiency. In the GEM off-detector electronics, the tracking data will be transferred to the CMS DAQ system, and trigger data will be processed by a trigger algorithm and transferred to the L1 endcap muon track finder. The GEB and the OH boards have been designed and are undergoing tests in the laboratory and a test beam, while

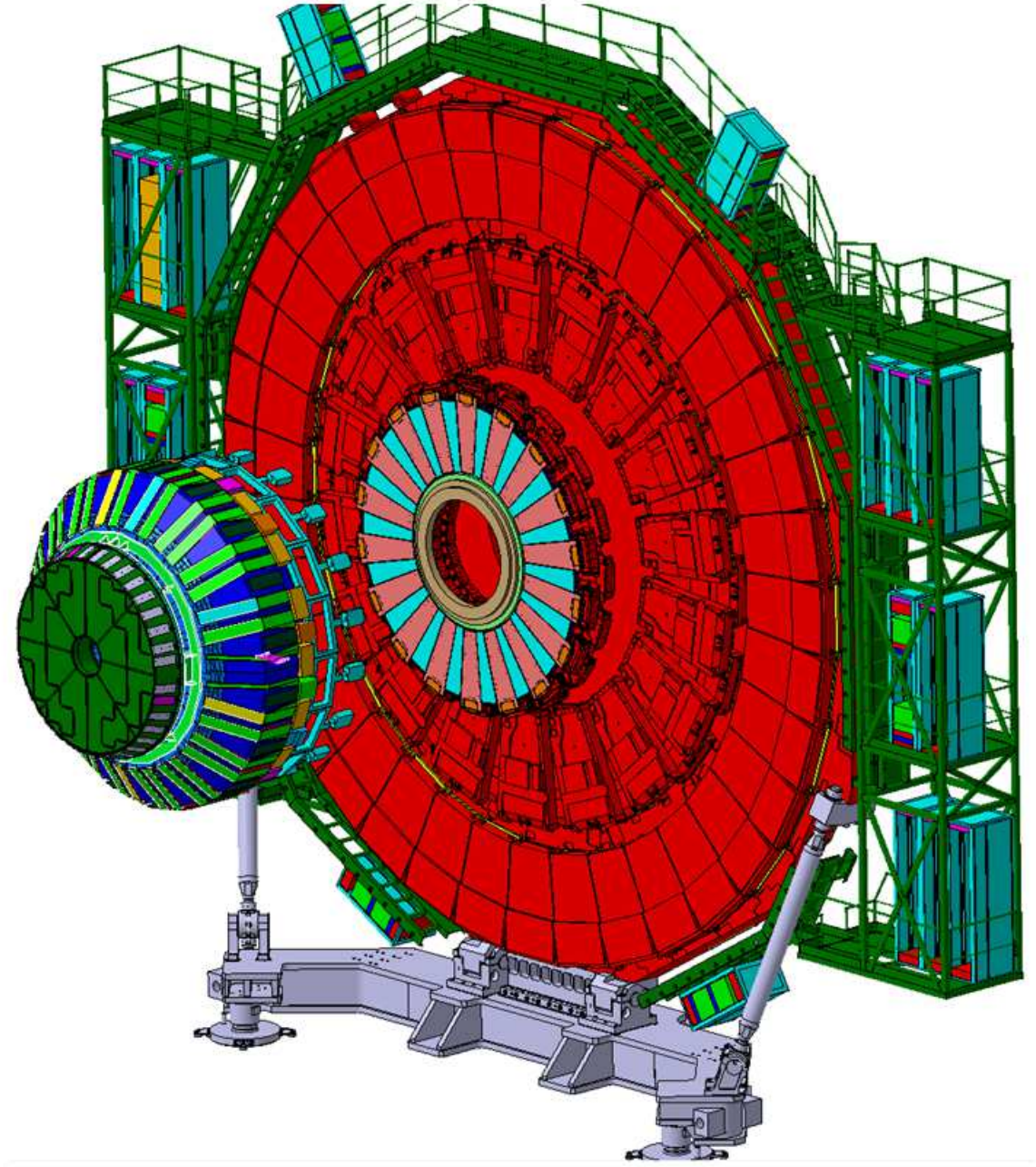

Figure 1.5: First CMS muon endcap station where the inner ring is equipped with 18 long and 18 short triple GEM superchambers.

Figure 1.6: Most recent GE1/1 chamber prototypes (top left) in the uniformity test stand, (top right) ready for CSC-GEM integration tests and (bottom) latest version of Optohybrid mounted on detector.

all off-detector electronics devices are commercial off-the-shelf components.

The GE1/1 front-end electronics is well advanced in its design cycle. Improvements are being made to the existing 128-channel VFAT2 ASIC chip, and the resulting VFAT3 design, detailed in Chapter 3, is expected to be submitted for a first fabrication near the end of 2015. A second submission is foreseen in 2016 if necessary. The full VFAT3 production is expected to be launched by early 2017.

The first prototype versions of the GEM Electronics Board (GEB) shown in Figure 1.3 and the OptoHybrid (OH) board detailed in Chapter 3 have already been designed, manufactured and tested. These are the first of a three step prototyping plan. The second step is currently in its design phase and expected to be complete by early 2015. Prototyping steps one and two use the VFAT2 chip which already exists and is readily available. The third prototyping step will incorporate the VFAT3 chip and the GigaBit Transceiver (GBT). The GBT is expected to be available for initial prototype tests in 2015. The design of the OptoHybrid and GEB boards for the third prototype step is expected to start during 2015.

For the off-detector electronics, we will use the μTCA standard and the CMS MP7 and AMC13 μTCA boards. Data will be transmitted between the on- and off-detector electronics through optical fibers using the CERN GBT protocol. In 2014 the first prototypes of the Opto-hybrid and GEB have already been successfully read out with a μTCA GLIB board together with an AMC13. In 2015 the system will be tested with the MP7 board replacing the GLIB.

1.3 Readiness for production and installation

Small GEM detectors have demonstrated excellent rate capability and robustness in the past. To cover the much larger areas that are required for CMS, new technologies for production of

large-size GEM detectors had to be developed. Within the CMS GEM R&D effort, cost-effective production of large GEM foils over 1m long was demonstrated and the resulting chambers have been extensively tested in beams. A novel technique has recently been developed where three foils are mounted into a single stack under tension, keeping a constant inter-GEM spacing. Since no gluing is involved, a large-size chamber can be quickly assembled by two people in about two to three hours; it can also be easily re-opened for maintenance.

Chamber production can be launched as soon as the project is approved. Six chamber production and testing sites (BARC, INFN Bari, CERN, FIT, UGent, and INFN LNF) have been under preparation for a couple of years. Building 186 at CERN is being developed as a center for GE1/1 chamber quality control, integration, and final testing. A cosmic-ray test stand has been built there which allows testing of up to 10 superchambers in terms of long-term HV stability; it will also allow for scans of gain, efficiency, and angular resolution over a large area of the chambers. It is estimated that the production of the 72 superchambers for the first muon endcap station will easily be completed within two years. In LS2 the full GE1/1 station with detectors, electronics, and full DAQ chain would be installed and fully integrated into CMS.

The slots for insertion into the endcap nose already exist and integration and installation studies for the existing CMS muon high-η envelope have been performed in order to ensure smooth installation. The needed technical services have been studied and detailed understanding of cooling, cabling, and gas distribution has been worked out. Several trials with mechanical demonstrators were successfully completed within this envelope. Figure 1.7 shows the most recent installation of an assembly of one long and two short GE1/1 superchambers in CMS. The routing of services, gas pipes and cables was also successfully demonstrated.

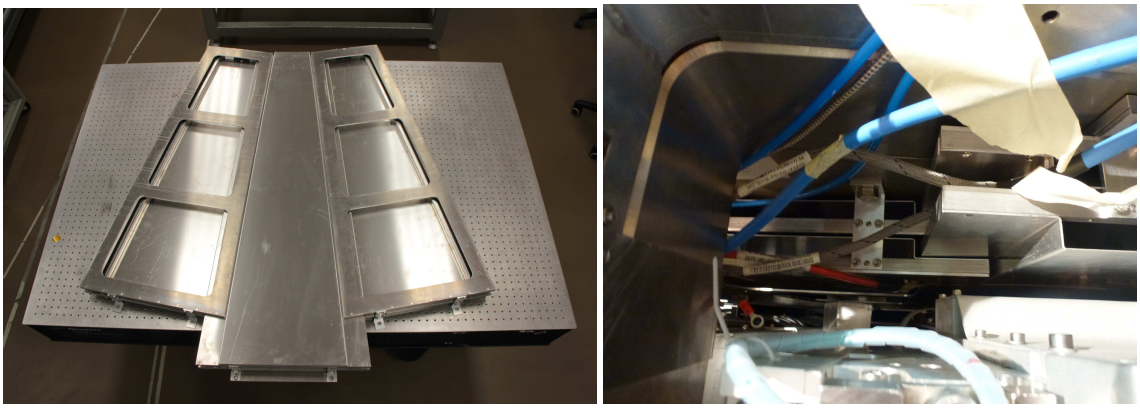

Figure 1.7: Installation test with an assembly of real-sized long and short dummy chambers.

In summary,

- R&D to build large-size triple GEM chambers is completed. Integration into CMS has been worked out and tested successfully with dummy chambers.
- Several chamber production sites are being prepared and provide sufficient capacity to produce the necessary 72 superchambers plus spares within two years.
- Design of the electronics for readout, trigger, and DAQ is in an advanced stage. First prototypes of various components are being integrated with the latest chamber prototypes.
- The objective for LS2 is to be ready with the full GE1/1 station and integrate it into CMS.

1.4 Structure of the TDR

The organization of this TDR is as follows.

Chapters 2–5 cover details of the chambers and their associated electronics. Details of the GEM chambers and their measured performance are described in Chapter 2. The front-end on-chamber electronics and the trigger path to the CSC are described in Chapter 3. In Chapter 4, the data flow and the DAQ system are discussed. Chapter 5 covers the detailed aspects of chamber production and quality assurance.

Chapter 6 presents in detail the challenging conditions expected during HL-LHC operation, the expected performance of the forward muon detector and the beneficial aspects of the GE1/1 upgrade, based on simulation studies.

Chapters 7–9 discuss "practical" matters: Chapter 7 presents various issues that will arise in integrating the GE1/1 detectors in CMS, such as installation procedures, power, gas and cooling systems. Chapter 8 discusses controls and monitoring that are needed for the proper operation of this detector. Chapter 9 discusses the project organization, schedules, and estimated costs.

Four appendices are included: Appendix A discusses a Slice Test consisting of 4 superchambers that are expected to be installed in CMS at the end of 2016, while Appendix B contains details of the estimated charge per unit area that is expected to be accumulated on the GE1/1 chamber electrodes during the lifetime of the HL-LHC. Engineering drawings for the GE1/1 Project are added in Appendix C as a reference. A glossary of some acronyms used is documented in Appendix D.

Chapter 2

GE1/1 GEM Chambers

2.1 Technology overview

A Gas Electron Multiplier [10] is a thin metal-clad polymer foil chemically perforated by a high density of microscopic holes. The polyimide (Kapton by DUPONT Co. or Apical by KANEKA Co.) used as the bulk material of the foil is 50 μm thick and has a dielectric constant of 3.5; it is clad on both sides with 5 μm of copper. As shown in Figure 2.1 (left), the GEM holes are truncated double cones with the larger (outer) diameters around 70 μm and the smaller (inner) diameter around 50 μm; they are spaced with a pitch of 140 μm in a hexagonal pattern.

A triple-GEM chamber consists of a stack of three GEM foils placed at a relative distance of a few mm and immersed in a counting gas mixture. The voltage applied between the two copper-clad surfaces of a foil produces an electric field as high as ~ 80 kV/cm in the GEM hole as seen in Figure 2.1 (right). The electrons produced by a charged particle passing through the chamber due to ionization of the counting gas drift towards the holes and once they start to experience the very intense electric field in the holes, they acquire enough kinetic energy to produce secondary ionization in the gas. This produces an electron avalanche process, which induces an electrical signal on the readout strips. A schematic view of this operation principle is given in Figure 2.2, which also defines the drift region, two transfer regions, and induction region within the triple-GEM chamber.

Typical dimensions of the different regions in a triple-GEM detector are: Drift region of 3 mm between drift cathode and first GEM, spaces of 1 mm and 2 mm in the electron transfer gaps between GEM foils, and a 1 mm space in the signal induction region (see Figure 2.2). A standard gas mixture for operating a triple-GEM detector is Ar/CO_2 70:30. For CMS, we have also evaluated $Ar/CO_2/CF_4$ 45:15:40, which is the gas that was used by LHCb for triple-GEMs during the data taking period in 2010-2012 [14].

2.1.1 Requirements on GE1/1 chamber performances and design specifications

The desired trigger and physics performances outlined in the introduction and detailed in Chapter 6 impose the following fundamental requirements on the detection performance of the GE1/1 chambers:

- Maximum geometric acceptance within the given CMS envelope.
- Rate capability of 10 kHz/cm^2 or better.
- Single-chamber efficiency of 97% or better for detecting minimum ionizing particles.
- Angular resolution of 300 μrad or better on $\Delta\phi = \phi_{GE1/1} - \phi_{ME1/1}$
- Timing resolution of 10 ns or better for a single chamber.
- Gain uniformity of 15% or better across a chamber and between chambers.

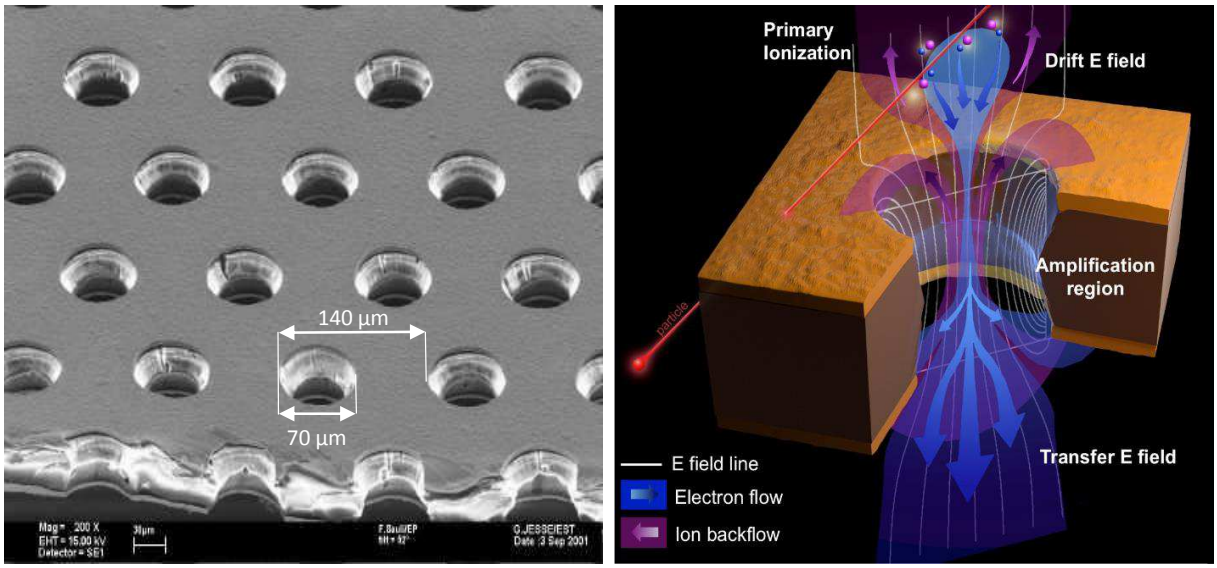

Figure 2.1: Scanning Electron Microscope (SEM) picture of a GEM foil (left) [10] and schematic view of the electric field lines (white), electron flow (blue), and ion flow (purple) through a bi-conical GEM hole (right). The outer diameters of the hole are 70 μm and the inner diameter is 50 μm; the hole pitch is 140 μm.

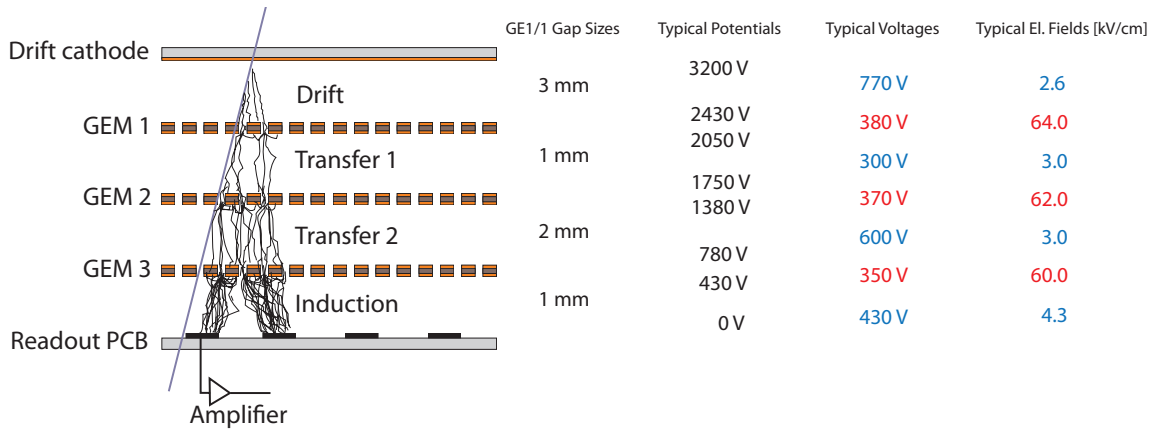

Figure 2.2: Principle of operation of a generic triple-GEM chamber and definition of drift, transfer, and signal induction gap regions within the detector [10]. The columns on the right give the actual gap sizes in the GE1/1. They also list typical values for electric potentials on the seven electrodes and typical values for voltages and electric fields across the four gaps (blue) and the three foils (red) if the nominal potential of 3200 V for operation in Ar/CO_2 70:30 is applied to the drift cathode.

- No gain loss due to aging effects after 200 mC/cm^2 of integrated charge.

We briefly review the rationale for these requirements. Clearly, maximum acceptance will yield maximum physics yield. The maximum expected hit rate within the GE1/1 acceptance is about 5 kHz/cm^2 for HL-LHC running at 14 TeV and 5 $\times 10^{34}$ cm^{-2}s^{-1}. Multiplying with a safety factor of two then requires a hit-rate cabability of 10 kHz/cm^2. With 97.0% individual chamber efficiency, a "superchamber" that contains two chambers will have an efficiency above 99.9% when the signals from the two chambers are combined as a logical OR. A precision of 300 μrad or better on the difference $\Delta\phi = \phi_{GE1/1} - \phi_{ME1/1}$ of the angular muon positions measured in GE1/1 and ME1/1 will enable the trigger to discriminate high-p$_T$ muons from low-p$_T$ muons reliably. At the outer radius (r = 2.6 m) of the GE1/1 chambers, this azimuthal precision of 300 μrad corresponds to a 0.8 mm resolution in the azimuthal $\hat{\phi}$ direction. Since two chambers can provide independent timing information that can also be combined with timing provided by the CSCs, a time resolution of 10 ns or better for a single chamber is sufficient to reliably match GE1/1 hits to ME1/1 stubs in time when running with a 25 ns bunch crossing time at the LHC. A uniform chamber response will ensure that there are no geometrical trigger or reconstruction biases. The gain of a single GEM foil typically varies across the foil surface by 5-8% due to intrinsic variations in hole diameters that stem from the production process [15]. The corresponding typical gain variation in a triple-GEM detector is $\sqrt{3}$ times larger, i.e. about 10-15%. The chambers should not incur significant additional response non-uniformities due to any other factors. The chambers must be able to integrate a charge of 200 mC/cm^2 over their lifetime without any gain loss or other loss in reponse. The charge expected to be integrated in the GE1/1 sector at highest η over 20 years of operation at the HL-LHC is about 100 mC/cm^2. A calculation of this estimated integrated charge value is given in Appendix B. The stated requirement of 200 mC/cm^2 includes an additional safety factor of two.

In addition, several technical constraints and requirements need to be taken into account in the chamber design. As a baseline, it must be possible to operate the chambers using only counting gases that have low global warming impact. The material budget must be low enough so that multiple scattering within the GE1/1 itself will not affect the muon track measurement in the GE1/1–CSC trigger. Sufficiently small readout segmentation in η, i.e. along the readout strips, is needed so that the GE1/1–CSC trigger can remove CSC ghosts effectively when reconstructing events with multiple muon hits in a CSC chamber. The chambers must be designed so that a superchamber is less than 10 cm thick and will easily fit into the available slot in the muon endcap nose. This constraint basically excludes the employment of bulkier standard wire-chamber technology such as CSCs for this application. The on-chamber service interfaces must be laid out so that pre-exisiting cabling and tubing infrastructure can be used effectively.

The resulting basic parameters and specifications for the construction of the GE1/1 triple-GEM chambers and their operation in CMS are compiled in Table 2.1.

2.1.2 Electron transport in GE1/1 gas mixtures

We briefly discuss the intrinsic electron transport parameters of Ar/CO_2/CF_4 45:15:40 and Ar/CO_2 70:30 gas mixtures. Triple-GEM detectors have been operated successfully in high-rate environments using Ar/CO_2/CF_4 45:15:40 in the LHCb experiment [14] and Ar/CO_2 70:30 in the TOTEM experiment [16]. These two gas mixtures have also been used extensively during the GE1/1 R&D phase and consequently are candidate gas mixtures for operating the GE1/1 in CMS. The Ar/CO_2/CF_4 45:15:40 mixture combines a high drift velocity due to its high CF_4 content with a small Lorentz angle, similar to that of Ar/CO_2. Since CMS has a magnetic field of 3 T at the location of the GE1/1 chambers, we review the effect of a magnetic field and the

Table 2.1: Main specifications and parameters for the design and operation of the GE1/1 chambers.

Specification / Parameter	**GE1/1**
Detector technology	Gaseous detector; micro-pattern gas detector (MPGD)
Charge amplification element	GEM foil (triple, cascaded, tensioned at $\approx$ 5 N/cm)
Number of chambers in overall system	144 (72 in each endcap)
Chamber shape (active readout area)	Trapezoidal; opening angle 10.15^o
Active area overlap in adjacent chambers	2.6 mrad (corresponds to 5.7 readout strip pitches)
Short chamber dimensions (active vol.)	L: 106.1 cm (center line), W: (23.1 - 42.0) cm, D: 0.7 cm
Long chamber dimensions (active vol.)	L: 120.9 cm (center line), W: (23.1 - 44.6) cm, D: 0.7 cm
Total chamber thickness	D: 3.5 cm
Active readout area	0.345 m^2 (short ch.); 0.409 m^2 (long ch.)
Active chamber volume	2.6 liters (short ch.); 3 liters (long ch.)
Radial distance from beam line	130.2 cm (at inner edge of active readout area)
Geometric acceptance in η	1.61 - 2.18 (short ch.); 1.55 - 2.18 (long ch.)
Signal readout structure	Truly radial readout strips
Readout strip dimensions	230 μrad angular strip width; 463 μrad angular pitch
Number of η-segments in readout	8
Number of readout strips per η-segment	384
Number of readout strips per chamber	3,072
Counting gas mixtures	Ar/CO_2 70:30 or $Ar/CO_2/CF_4$ 45:15:40
Nominal operational gas flow	1 chamber volume per hour
Number of gas inlets	1
Number of gas outlets	1
Nominal HV applied to drift electrode	3200 V (Ar/CO_2); 4000 V ($Ar/CO_2/CF_4$)
Nominal operational gas gain	1-2 $\times$ 10^4
Demonstrated rate capability	100 MHz/cm^2

effect of the angle between the E-field and B-field on the charge transport.

A general discussion of transport properties in gaseous detectors can be found, for example, in Ref. [17]. When electrons and ions in a gas are subjected to an electric field, they drift along the electric field lines on the average, but individual electrons can deviate from that average due to scattering in collisions with atoms and molecules in the gas. This leads to longitudinal diffusion of the drifting electron cloud along the field lines and to its transverse diffusion across the field lines. The scattering process in each direction is approximately Gaussian on a microscopic scale. An electric field affects the transverse and longitudinal diffusion differently and so two diffusion coefficients σ_L and σ_T are used to quantify the diffusions. In cold gases such as carbon dioxide, the diffusion is small and the drift velocity is low and unsaturated at electric field strengths that are typically used in gaseous detectors. Warm gases such as argon have stronger diffusion and slower drift velocities, but when they are mixed with polyatomic/organic gases with vibrational and rotational modes, the diffusion is reduced in most cases and the drift velocity is increased.

In the presence of both an electric field and a magnetic field, the Lorentz force deflects electrons between collisions so that they drift effectively at an angle, called the Lorentz angle, relative to the electric field (see Figure 2.3). The diffusion transverse to the drift direction is reduced in this case, while the longitudinal diffusion is basically unchanged (see Figure 2.4). Too large a Lorentz angle worsens the spatial resolution; however, a small Lorentz angle may improve the spatial resolution due to enhanced charge sharing among the readout strips. Knowledge of the Lorentz angle is important so that the spatial resolution can be optimized by correcting for this effect.

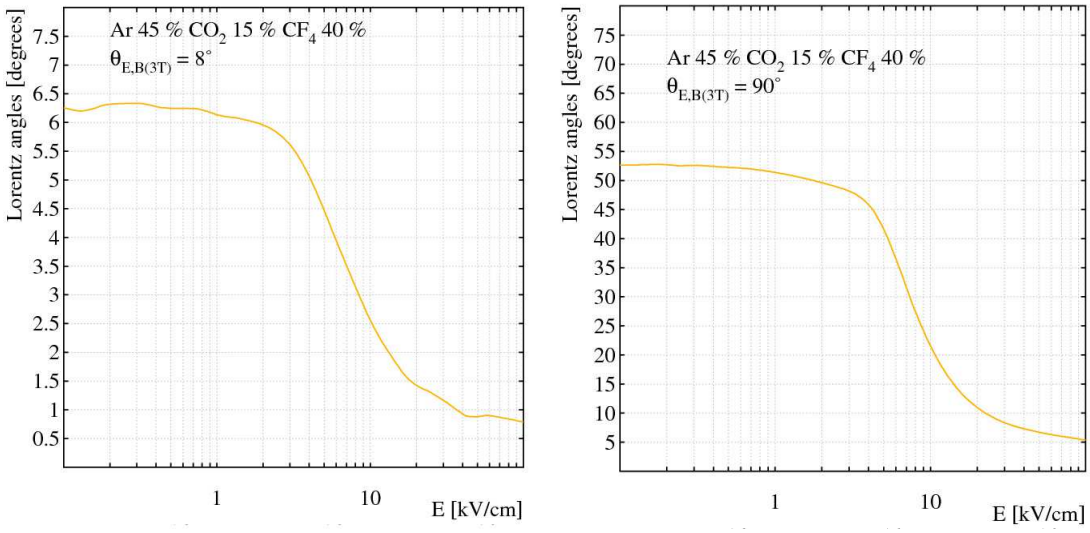

Figure 2.3: Lorentz angles as a function of electric field for $Ar/CO_2/CF_4$ 45:15:40 at B=3T obtained with the GARFIELD simulation suite [18]. The angles are shown for $\angle(\vec{E},\vec{B}) = 8°$ (left) as given in the GE1/1 and for a maximum angle $\angle(\vec{E},\vec{B}) = 90°$ (right).

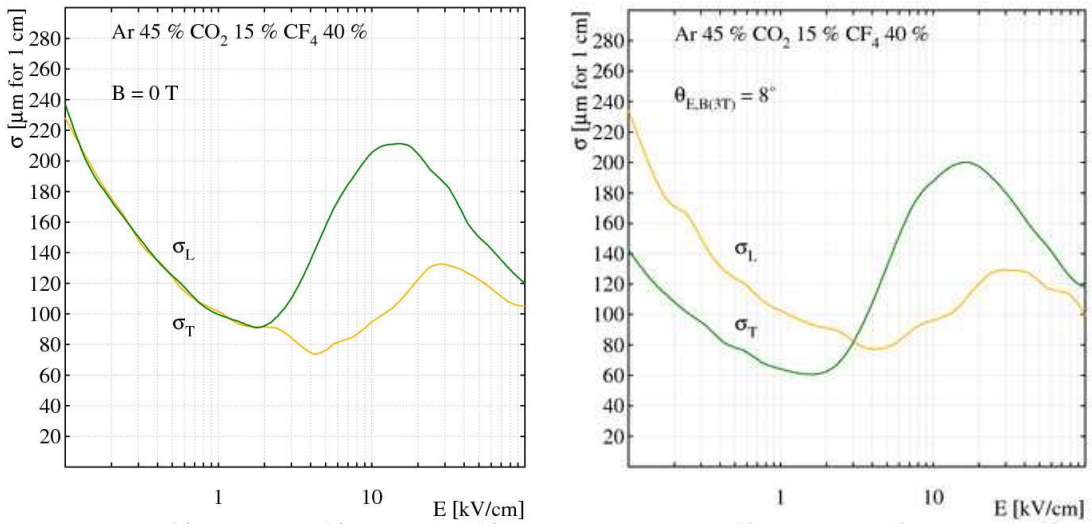

Figure 2.4: Longitudinal (σ_L) and transverse (σ_T) diffusion coefficients in $Ar/CO_2/CF_4$ 45:15:40 without magnetic field (left) and at B=3T with $\angle(\vec{E},\vec{B}) = 8°$ (right) obtained with GARFIELD.

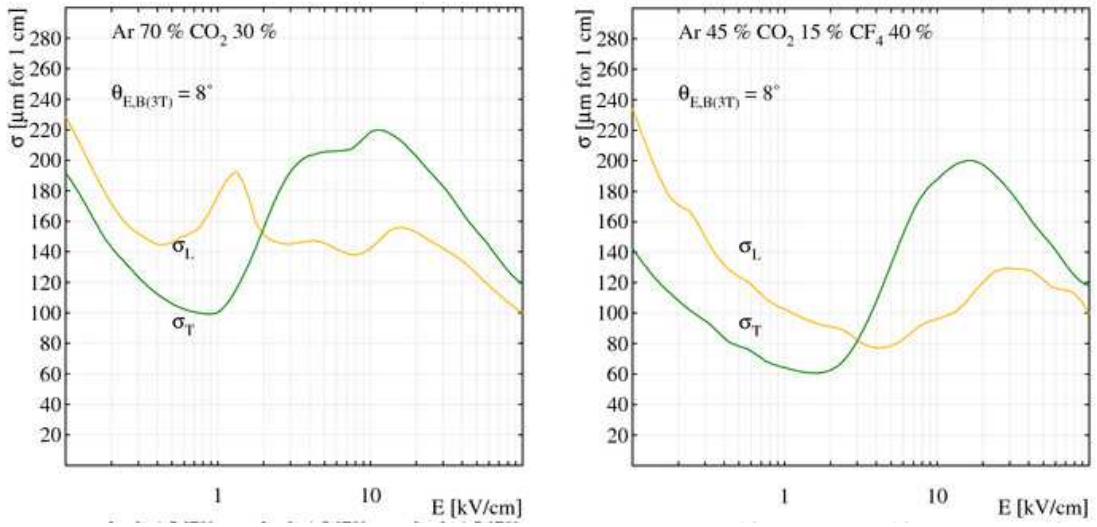

Figure 2.5: Longitudinal (σ_L) and transverse (σ_T) diffusion coefficients for the two gas mixtures of interest for GE1/1 operation at B=3T and with angle $\angle(\vec{E}, \vec{B}) = 8°$.

Figure 2.5 shows the diffusion coefficients for the two gas mixtures of interest as a function of the electric field for the specific angle $\angle(\vec{E}, \vec{B}) = 8°$. This is the maximum angle between electric drift field lines in the GEM and magnetic field lines produced by the CMS solenoid at the location of the GE1/1. The diffusion in $Ar/CO_2/CF_4$ is lower, as expected, due to higher polyatomic gas content; both CF_4 and CO_2 have vibrational modes which lower the diffusion. Simulation studies done by LHCb [14] for different gas mixtures show that the $Ar/CO_2/CF_4$ 45:15:40 mixture is a significantly faster gas due to the addition of the CF_4 gas (see Figure 2.6). CF_4 is advantageous in a high-rate environment because it enables high-rate capability due to its high drift velocity but it suffers from electron attachment. CO_2 is added to "cool" the electrons which reduces the electron attachment that occurs with CF_4.

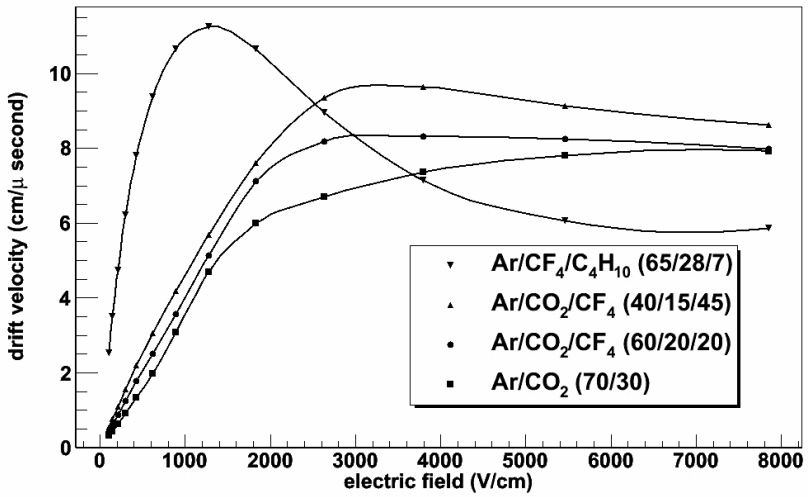

Figure 2.6: Electron drift velocities as a function of electric field from simulation studies by LHCb for various gas mixtures including the GE1/1 candidate gas mixtures.

2.1.3 Choice of GEM technology for GE1/1 as motivated by other experiments

We briefly review the experience with GEM technology that exists within the community. GEM detectors have been successfully operated long-term in several major high energy and nuclear physics experiments, i.e. COMPASS, PHENIX, STAR, TOTEM, and LHC-b. The main features of the GEM applications in those experiments are highlighted below.

- **COMPASS:** This is the pioneering experiment for GEM technology. It is the first high-rate experiment to use GEM detectors [19]. Running at the CERN SPS, COMPASS has been employing 22 medium-size ($30 \times 30\,\mathrm{cm}^2$) triple-GEM detectors with 3/2/2/2 mm gap sizes in 11 inner tracking stations. The detectors are operated with Ar/CO_2 70:30 at a gas gain around 8000 and are read out with two-dimensional Cartesian strips and APV25 chips [20]. The GEMs operate at rates up to $2.5\,\mathrm{MHz/cm}^2$, which corresponds to roughly 1000 times the expected rate for the CMS GE1/1. Operating with two OR'ed GEM trackers, each tracking station has an efficiency of 97.5%. A single COMPASS GEM achieves about 70 μm spatial resolution and 12 ns time resolution. During the 2002-2007 running period the detectors accumulated total charges around $200\,\mathrm{mC/cm}^2$ without any gain drop while in earlier bench tests with x-rays $700\,\mathrm{mC/cm}^2$ had been collected without any observed gain loss. COMPASS also operated five small-size GEM trackers with $1\,\mathrm{mm}^2$ pixel readout [21] that were exposed to muon rates up to $12\,\mathrm{MHz/cm}^2$ in the 2008/09 COMPASS runs and achieved 7 ns time resolution.
- **PHENIX:** This experiment operated 20 medium-size triple-GEM detectors at RHIC as a "hadron-blind" detector system [22] for electron identification. A special feature of this system was a reverse bias of the HV between drift mesh and first GEM, which desensitized the GEM to charged particles, while a CsI coating on the first GEM made the detector sensitve to Cherenkov radiation from electrons. The detector was operated in pure CF_4 and achieved a hadron rejection factor of 50 in the 2010 PHENIX run.
- **STAR:** Since late 2012, STAR has been operating 24 medium-size triple-GEM detectors read out with r-ϕ strips and APV25 chips as a forward tracker [23] at RHIC. GEM foils are shaped as circular quadrants and were produced industrially in the USA.
- **TOTEM:** This experiment employs 20 medium-size triple-GEM detectors of semicircular shape that are read out with concentric strips and radial pads and VFAT2 chips [24]. These detectors form two T2 telescopes for charged-particle tracking and triggering in the very forward region at the LHC. They were exposed to a total fluence of a few $10^{13}/\mathrm{cm}^2$ particles during the 2012 LHC run and had sustained a total ionizing dose of about 5×10^4 Gy by the end of the 2012 LHC run while performing as expected [16].
- **LHCb:** The LHCb experiment employs 12 pairs of medium-size triple-GEM detectors with 3/1/2/1 mm gap sizes as the inner section of the LHCb M1 muon station, which is located in immediate vicinity of the beam pipe. Using a pad readout, this GEM system produces input for the LHCb L0 muon trigger. Unusual for a muon station, this subdetector is located in front of the calorimeters rather than behind them. Consequently, it sustains rather high rates for a muon detector of up to 500 $\mathrm{kHz/cm}^2$. It operates with an $Ar/CO_2/CF_4$ 45:15:40 gas mixture that is one of the mixtures being considered for the CMS GE1/1. Read out with TDCs and running at a gain around 4,300, the GEMs have a time resolution of 4 ns when the signals

from two paired detectors are logically OR'ed and an efficiency of 97-99% in a 20ns time window. The most irradiated LHCb GEM detector has integrated about 120 mC/cm^2 during the 2010-12 LHC running period without signs of aging [14]. This value happens to correspond closely to the GE1/1 requirement for 20 years of running at the HL-LHC (see Section 2.1.1).

This strong track record for GEMs in high-rate applications for HEP and NP experiments demonstrates that GEMs represent a mature and robust technology for high-rate experiments. The CMS GE1/1 project represents the next major step in the evolution of GEM detector systems by going from systems with a small number of medium-size detectors to a large number of large-size detectors; it builds mainly upon the more recent experiences with the LHCb and TOTEM GEMs.

2.2 GE1/1 prototyping results

2.2.1 R&D program on full-size GE1/1 prototypes

The crucial first step in the 5-year R&D program that led to this design report was a demonstration that large-area GEM foils can indeed be manufactured reliably and that triple-GEM detectors built with such foils can satisfy the performance requirements listed in Section 2.1.1. Five generations of prototype detectors (see Figure 2.7) were built and tested in 2010-14 with one generation being developed every year based on the experience with the previous generation [11–13, 25]. Since the GE1/1 prototype performances discussed below are obtained from tests of different prototype generations, we briefly review the evolution of the GE1/1 detector prototypes.

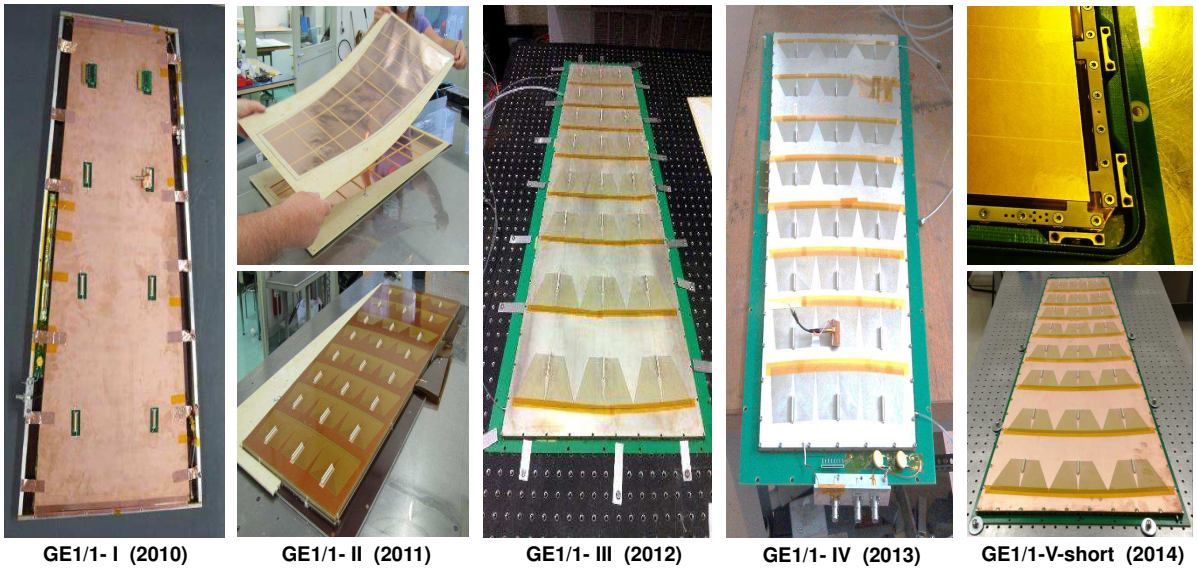

Figure 2.7: Five generations of GE1/1 prototype chambers constructed and tested by the GEM collaboration in 2010-2014. The split figures for GE1/1-II and GE1/1-V demonstrate the evolution from construction using spacer frames to purely mechanical stretching of GEM foils without any spacers.

The GE1/1-I prototype was the first 1m-class GEM detector ever constructed and operated [25]. Components were glued together and spacer ribs were used to keep the GEM foils apart; it had

only 8 readout sectors total. In the GE1/1-II the readout segmentation was increased to 24 sectors arranged in eight η-partitions and three columns. Each η-partition comprised 384 radial strips with 455 μrad angular pitch. The foil gap configuration was changed from 3/2/2/2 mm to 3/1/2/1 mm to speed up the signal [11]. The GE1/1-III prototype was the first detector in which foils were stretched purely mechanically against the outer detector frame, but this frame was made from several pieces and was glued to the drift board [12]. This generation was also the first prototype to use a miniaturized ceramic high voltage divider for powering. When bolting the readout board onto the outer frame in this design, the O-ring acted as a fulcrum creating a torque on the board as the bolts were tightened. This caused the readout board to deform slightly after assembly, which in turn caused a response non-uniformity across that chamber prototype as the foil gap sizes were not kept uniform enough. In the GE1/1-IV prototype, before assembly both readout and drift boards were pre-bent in the direction opposite to the bowing observed in the GE1/1-III in an attempt to compensate for the bending that occurs after assembly. They were bolted to the outer frames and sealed with O-rings making the GE1/1-IV the first large-area GEM detector produced without gluing any components. Consequently, it could be assembled in a few hours [26]. While the pre-bending technique works in principle, it is not deemed reliable enough for future mass production purposes and it is a time-consuming production step. Instead, the problem has been rectified in the GE1/1-V prototype design by tensioning the foils against independent "pull-out" pieces (see Figure 2.7 top right). The drift and readout boards are now bolted onto the pull-out pieces. The outer frame is made from a single piece and only serves as a wall for the gas volume; it is sealed against readout and drift boards with O-rings. This final prototype design with a few improvements of details is being adopted as the final design of the GE1/1 triple-GEM chambers, which is described in detail in this report (see Section 2.3).

2.2.2 Performance measurements and simulation studies

The performances of the different generations of GE1/1 prototypes were studied in a series of beam tests at CERN in 2010 [25], 2011 [11], and 2012 [12], and at Fermilab in 2013 [13]. The beam tests at CERN focused on measuring the performance when the chambers were operated with the $Ar/CO_2/CF_4$ 45:15:40 gas mixture and read out with binary-output VFAT2 front-end chips [24], whereas in the Fermilab beam test the chambers were operated with Ar/CO_2 70:30 and read out with analog APV25 front-end chips [20] that produce full pulse height information. The APV25 chips are mounted on small hybrid boards for use with the scalable readout system [27, 28] developed by the RD51 collaboration.

In addition to this multi-year experimental effort, the GEM collaboration has mounted an extensive GEM simulation effort, which is described below in Section 2.2.2.6.

2.2.2.1 Measurements of detector gain and response uniformity

Gas gain:

The gas gain was measured for each GE1/1 prototype generation. Typically, for this measurement a high-rate X-ray generator is used to irradiate the GEM chamber. The gas gain can then be calculated from measured hit rates and anode currents. For example, gain measurements performed at CERN for a GE1/1-IV operated at different high voltages applied to the drift electrode are shown in Figure 2.8 for both Ar/CO_2 70:30 and $Ar/CO_2/CF_4$ 45:15:40 counting gases. The typical exponential dependence of the gas gain on HV is evident. The plot also shows the hit rates observed in the GE1/1-IV for a fixed rate of incident X-rays, which feature the beginnings of rate plateaus where the chamber starts operating with full efficiency.

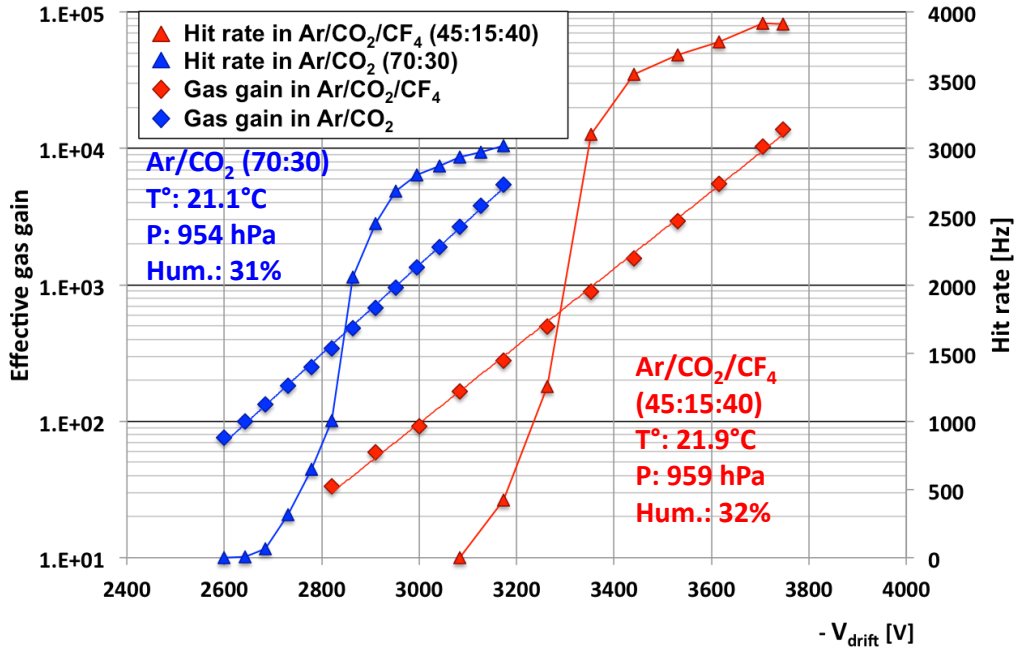

Figure 2.8: Measured gas gains (diamonds) and hit rates (triangles) as a function of high voltage applied to the drift electrode of a GE1/1-IV. Measurements with Ar/CO_2 70:30 (blue) and with $Ar/CO_2/CF_4$ 45:15:40 (red) gas mixtures are displayed. The log scale (left) applies to the gain whereas the rates are plotted on a linear scale (right).

Response uniformity:

An X-ray generator is also employed to study the response uniformity across the detector [26]. Figure 2.9 shows results from a GE1/1-III scan as an example. The variation of the peak position in the pulse charge distributions is taken as a measure of the response uniformity. From the data shown in Figure 2.9 (right) we conclude that the response varies not more than 15% across the detector in this slice. Corresponding measurements for the GE1/1-V are currently in progress.

2.2.2.2 Measurements of detection efficiency, angular resolution, and timing resolution

Detection efficiency:

Figure 2.10 shows GE1/1 efficiency measurements for charged particles from two separate beam tests at CERN and Fermilab. A GE1/1-IV prototype reaches a plateau efficiency of 98% for pions when operated with $Ar/CO_2/CF_4$ 45:15:40 and read out with VFAT2 chips. When a GE1/1-III is operated with Ar/CO_2 70:30 and offline cuts are placed on the strip charge measured by the APV to emulate VFAT2 thresholds, the plateau efficiency is 97%. When full APV pulse height information is used, the hit threshold can alternatively be set individually for each strip as a multiple of the pedestal width. For example, with a 5σ pedestal width cut the efficiency is measured slightly higher at 97.8% [13].

Angular resolution:

The required angular resolution of 300 μrad mentioned in Sec.2.1.1 is an upper limit imposed by the trigger. It is the minimal precision with which the difference $\Delta\phi = \phi_{GE1/1} - \phi_{ME1/1}$ of the angular muon positions measured in GE1/1 and ME1/1 must be determined to achieve the intended trigger rate reductions. In addition to the intrinsic GEM resolution, the intrinsic

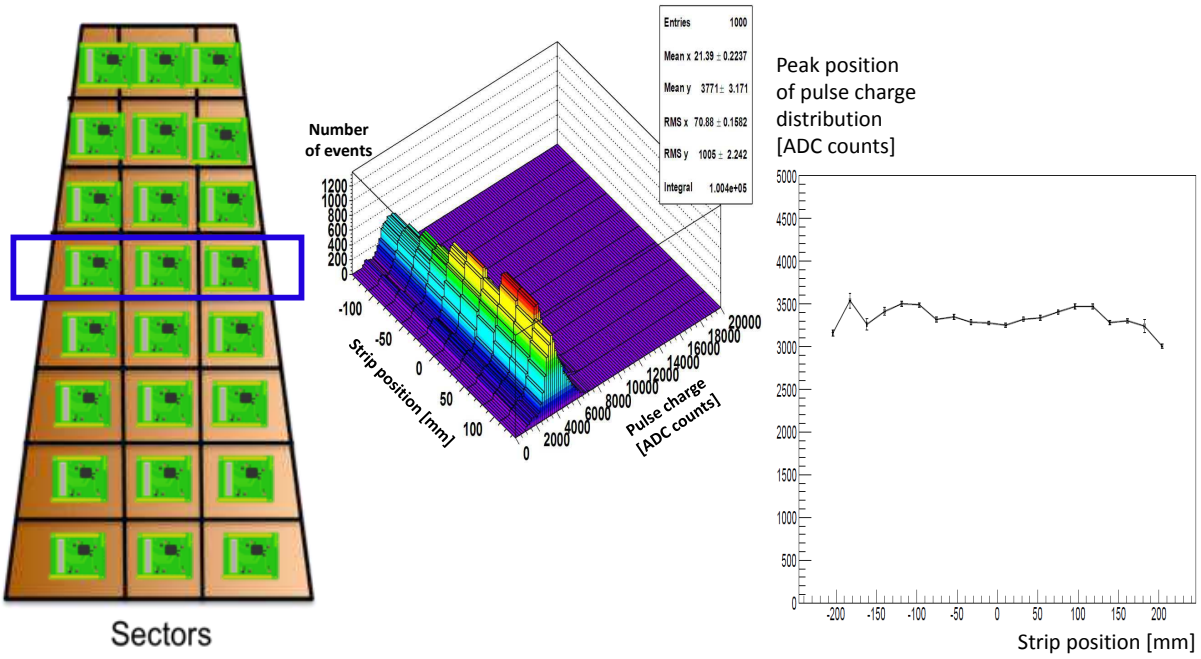

Figure 2.9: Results from a response scan across three sectors (left) of a GE1/1-III with an X-ray generator. The pulse charges measured on several adjacent strips are grouped together and histogrammed (center). The peak position of the pulse charge distributions for these strip groups are plotted vs. their positions across the chamber (right).

ME1/1 resolution as well as the ME1/1 and GE1/1 chamber alignments will contribute to the uncertainty in the $\Delta\phi$ measurement. Consequently, the intrinsic GE1/1 resolution must be significantly better than 300 μrad to provide a comfortable safety margin for this crucial performance parameter. As detailed below, the angular resolution for GE1/1 prototypes with an angular strip pitch of 455 μrad and binary signal readout was measured to be 137$\pm$1 μrad. As this is an appropriate performance, the final GE1/1 design adopts an angular strip pitch very close to that value. The actual strip pitch of 463 μrad in the final GE1/1 design is slightly larger because the azimuthal coverage of the chamber was expanded from 10.0^o to 10.15^o.

Results from independent GE1/1 angular resolution measurements obtained in two test beam campaigns are shown in Figures 2.11-2.13. In the 2012 CERN beam test conducted with a $Ar/CO_2/CF_4$ 45:15:40 counting gas and binary-output VFAT2 chips, the distribution of the residuals, i.e. the differences between the measured hit positions and the points where the fitted track impacts the chamber, in the azimuthal $\hat{\phi}$ directions shows a width of 268$\pm$2 μm when the GE1/1 is excluded from the track fit, which we refer to as an "exclusive residual" (see Figure 2.11 (top)). This width represents an upper limit on the intrinsic chamber resolution because the exclusive residual width overestimates the intrinsic resolution as the residual width is due to a convolution of intrinsic hit resolution and uncertainty in extrapolated track position. This result is obtained from sector 6 of the chamber at radius r $\approx$ 1.95 m, where the strip pitch in azimuthal direction is 0.88 mm. Consequently, this residual in the $\hat{\phi}$ direction corresponds to an exclusive angular residual of 137$\pm$1 μrad. This measured upper limit on the angular resolution in ϕ is close to the expected intrinsic resolution for a binary readout, which is given by:

$$\text{angular strip pitch}/\sqrt{12} = 455\ \mu\text{rad}/\sqrt{12} = 131\ \mu\text{rad}. \tag{2.1}$$

This performance exceeds the minimum requirement of 300 μrad with a comfortable perfor-

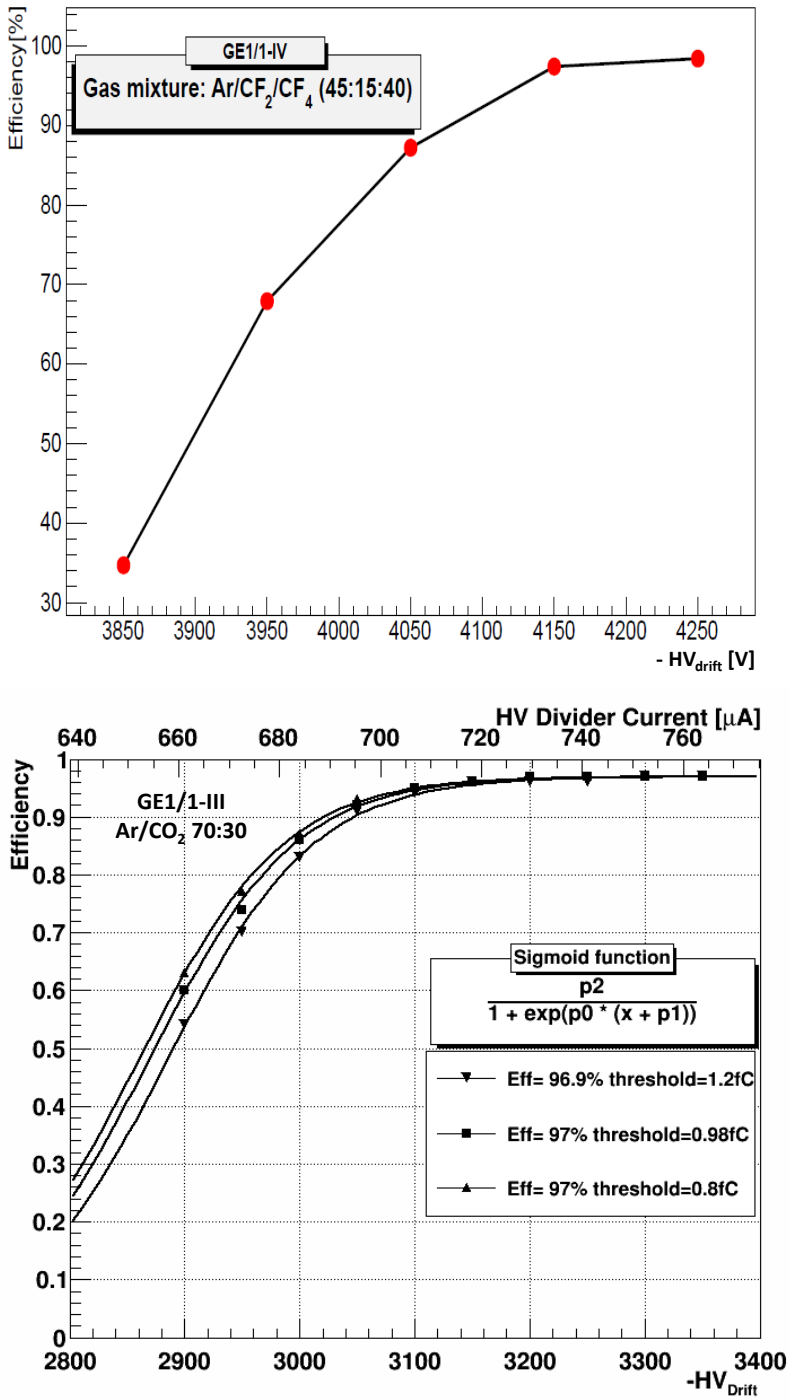

Figure 2.10: Measured detection efficiencies of GE1/1 prototypes for charged particles. *Top:* Eff. vs. HV applied to drift electrode when GE1/1-IV is operated with $Ar/CO_2/CF_4$ 45:15:40 and read out with VFAT2 chips configured with 0.8 - 1.2 fC strip-hit thresholds. *Bottom:* Eff. vs. HV applied to the drift electrode measured in central sector 5 of a GE1/1-III operated with Ar/CO_2 70:30 and read out with APV chips. Three different cuts are applied offline to the strip charges to simulate VFAT2 threshold behavior and the resulting efficiency curves are fitted to sigmoid functions.

mance margin.

For the 2013 Fermilab beam test data obtained with Ar/CO_2 70:30 counting gas and analog-output APV chips, the measured strip charges can be used to determine the hit position in the GE1/1 from the barycenter of the strip charges (centroid). For these data, exclusive residuals and "inclusive" residuals were calculated. For the latter, the GE1/1 hit is included in the track fit. Measurement of both residual types are shown at the center and bottom of Figure 2.11. The inclusive residual underestimates the intrinsic resolution of the chamber because including the hit of the probed chamber biases the track towards that hit. However, the intrinsic resolution can be obtained to good approximation from the geometric mean of the widths of the inclusive and exclusive residuals [29, 30]. At a radius r $\approx$ 1.85 m (sector 5), we then find an angular resolution

$$\sigma_{resolution} = \sqrt{\sigma_{incl.residual} \times \sigma_{excl.residual}} = 132\ \mu\text{rad}, \tag{2.2}$$

which is similar to the upper limit on the resolution obtained abive with VFAT2 chips and $Ar/CO_2/CF_4$ 45:15:40 at a similar radial position. We note that this result is still a slight overestimate for the resolution because multiple scattering of the tracked particles in the material of the ten chambers ($\approx$ 14% of a rad. length) placed in the beam is not taken into account, yet. Corresponding residuals and angular resolutions measured for other η-sectors using the centroid method are shown in Figure 2.12 (left). The measured angular resolution varies over a range of 100 - 160 μrad in sectors 2-7. The resolution could not be measured for the outer sectors 1 and 8 of the prototype due to geometric constraints in the test beam setup. Figure 2.12 (right) shows residual widths and angular resolution as a function of drift voltage. As expected, the resolution improves with increasing drift voltage, i.e. gas gain, reaching $\approx$ 125 μrad on the efficiency plateau.

The number of strips in a strip cluster is observed to increase with high voltage (see Figure 2.13 left) because the lateral size of the electron avalanche in the triple-GEM increases as the gain increases. At the start of the efficiency plateau around 3200 V in Ar/CO_2 70:30, two-strip clusters dominate; these also produce the best angular resolutions of $\approx$ 115 μrad (see Figure 2.13 right) when the centroid method is used for calculating the hit position.

Timing resolution:

The timing performance measured with a 10 cm $\times$ 10 cm triple-GEM equipped with standard double-mask GEM foils is shown in Figure 2.14. The timing resolution for Ar/CO_2 70:30 and a 3/2/2/2 mm gap configuration is compared with the timing resolution for $Ar/CO_2/CF_4$ 45:15:40 and a 3/1/2/1 mm gap configuration. With the faster gas and the shorter drift distances, the timing resolution improves by a factor of two from 8 ns to 4 ns.

The timing performance of an actual GE1/1-III prototype operated with $Ar/CO_2/CF_4$ 45:15:40 and read out with VFAT2 chips in the 2012 test beam at CERN [12] is shown in Figure 2.15. Dedicated timing hardware selects events within a 2 ns time window from the asynchronous SPS beam. Rather than performing direct TDC measurements, here the relative fraction of GEM hits in adjacent 25 ns time bins is measured (see Figure 2.15 left). For the configuration used, 97% of all hits occur within the correct 25 ns clock cycle.

One can then ask what value of a Gaussian width σ would produce that plot when a close to perfect ($\delta(t)$-like) input time distribution is smeared with that Gaussian and binned in 25 ns bins. We take the width σ of the Gaussian that best reproduces the timing fraction histogram of Figure 2.15 (left) as our measurement of the GE1/1 timing resolution. The GE1/1 time resolution measured with this method is shown as a function of current in the HV divider in Figure 2.15 (right). On the efficiency plateau, the GE1/1-III has a timing resolution of 6 ns. For

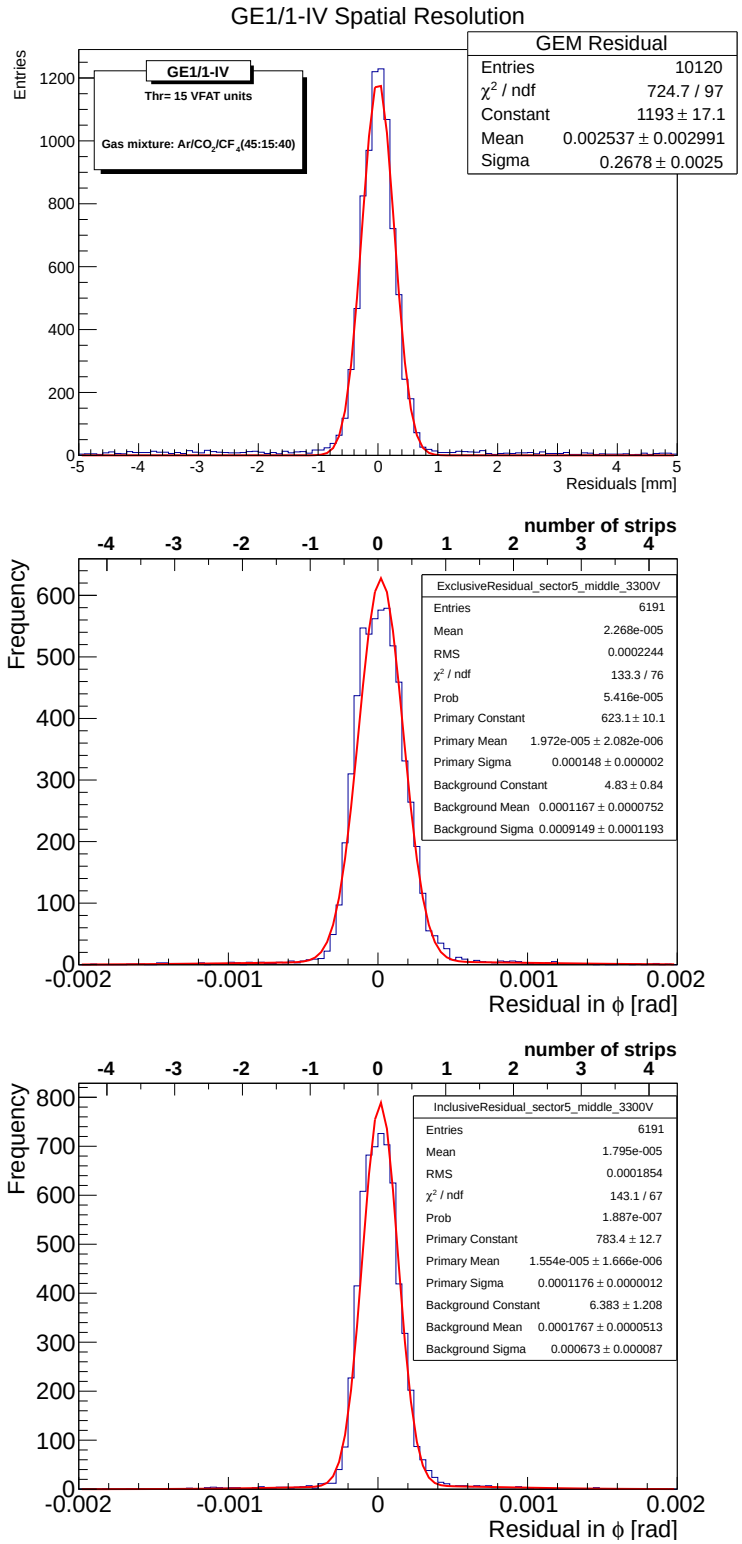

Figure 2.11: Track-hit residuals measured in central sectors of GE1/1 prototypes at r $\approx$ 1.9 m. *Top:* Exclusive residuals in azimuthal $\hat{\phi}$-direction measured with a pion beam at CERN when a GE1/1-IV is operated with $Ar/CO_2/CF_4$ 45:15:40 and read out with binary-output VFAT2 chips. *Center:* Exclusive angular residuals measured with a mixed pion and kaon beam at Fermilab when a GE1/1-III is operated with Ar/CO_2 70:30 at 3300 V and read out with APV chips. Here the barycenter of the strip cluster charge (centroid) is used to determine the hit position. The residuals are fitted with a double Gaussian function. *Bottom:* Corresponding inclusive angular residuals for same measurement as center plot.

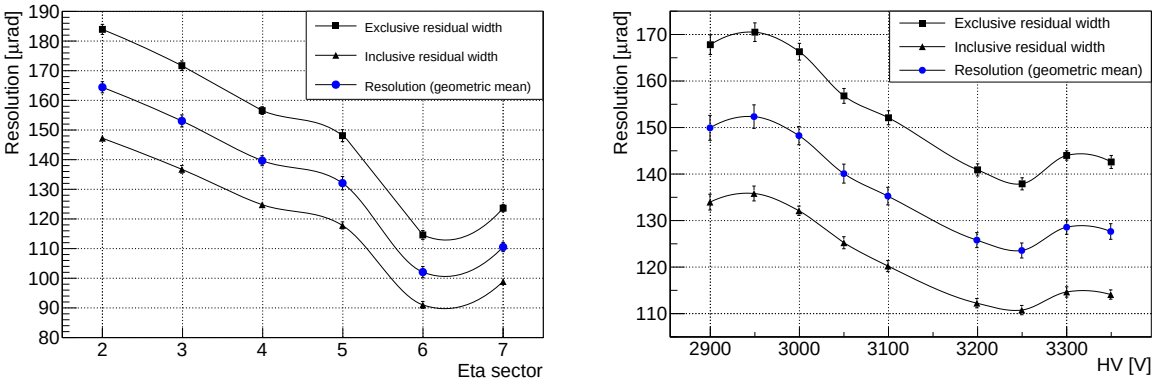

Figure 2.12: Measured exclusive and inclusive residual widths and angular resolutions (blue) of a GE1/1-III operated with Ar/CO_2 70:30 and read out with APV chips. *Left:* As a function of η-sector for six of the eight η-sectors at V_{drift} = 3300 V. Sector numbers increase with increasing radius and decreasing η. *Right:* As a function of voltage V_{drift} applied to the drift electrode in central sector 5.

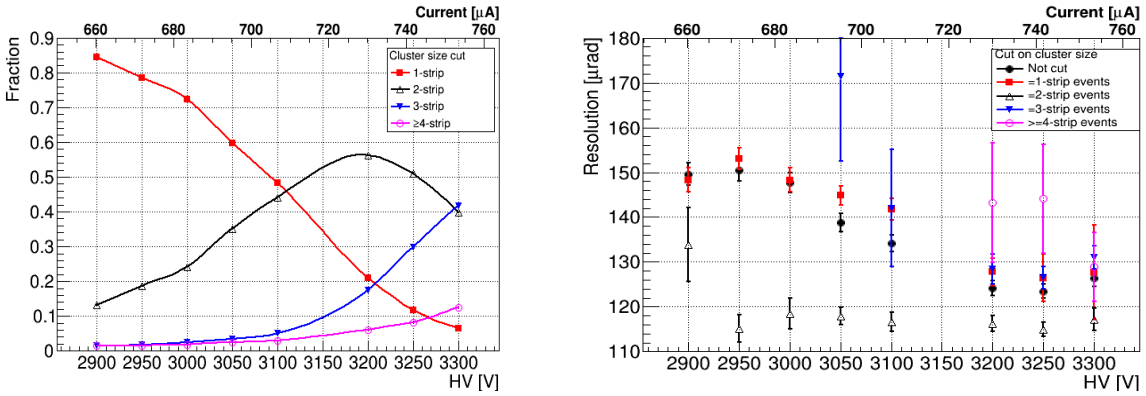

Figure 2.13: *Left:* Relative fractions of strip multiplicities observed for strip clusters in sector 5 of a GE1/1-III operated with Ar/CO_2 70:30 and read out with APV chips as a function of high voltage applied to drift electrode. *Right:* Corresponding measured angular resolutions for different strip multiplicities of strip clusters vs. high voltage.

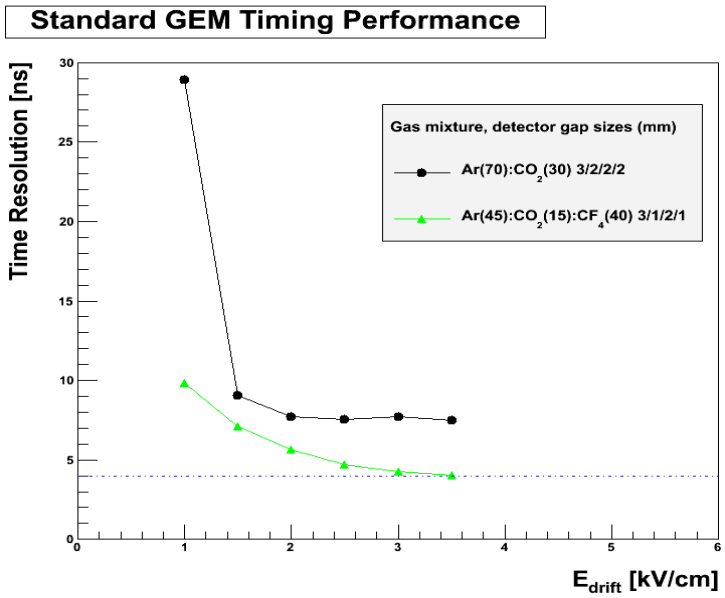

Figure 2.14: Timing resolutions measured with a TDC for a small triple-GEM detector equipped with GEM foils produced with the standard double-mask technique as a function of drift field for the counting gases under consideration.

two GE1/1 chambers in one superchamber operated with $Ar/CO_2/CF_4$ 45:15:40, we would expect a timing resolution of 6 ns $/\sqrt{2}$ = 4 ns. Based on the results in Figure 2.14, we then expect an overall timing resolution of 8 ns for a superchamber operated with Ar/CO_2 70:30.

2.2.2.3 Discharge probability

We have measured the discharge probability using an ^{241}Am α-source in a GE1/1 chamber operated with Ar/CO_2 70:30. To observe discharges at all it was necessary to operate the detector at rather high gains in the range of 4-6 $\times 10^5$. In that range, the discharge probability was measured to be on the order of 10^{-5} to 10^{-3} per ionizing particle (see Figure 2.16). However, these operating conditions are well beyond those that will be used in CMS (see Figure 2.8). Extrapolating these experimental data down to reasonable CMS operating conditions at gains around 5×10^3, the discharge probability is found to be approximately 9×10^{-10}. However, the alphas from the ^{241}Am source produce about a hundred times more primaries than a minimum ionizing particle (MIP). Consequently, the discharge probability for MIPs should be divided by this factor, i.e. it is expected to be approximately 10^{-12} to 10^{-11}. If a discharge does occur in a GEM detector, it will typically lead only to a short dead time of a few milliseconds. Once the overcurrent situation has passed, the detector will resume normal operation with full efficiency and nominal performance.

2.2.2.4 Rate capability measurement

In order to confirm the high-rate capability of the GE1/1 that is expected of such a triple-GEM detector, we measure the gain vs. incident rate using a medium-intensity 22 keV Ag X-ray source and a high-intensity 8 keV Cu X-ray source. A GE1/1-III detector, operated with Ar/CO_2 70:30, was illuminated with the Cu source and the gas gain was measured via the anode current produced in the chamber during this irradiation. The same measurement was also done with a more recent GE1/1-IV prototype, but operated with an $Ar/CO_2/CF_4$ 45:15:40 gas mixture and illuminated with the Ag X-ray source. The gain G can be calculated with the formula $G = \frac{I}{eNR}$, where I is the measured anode current in the GE1/1 chamber, N is the

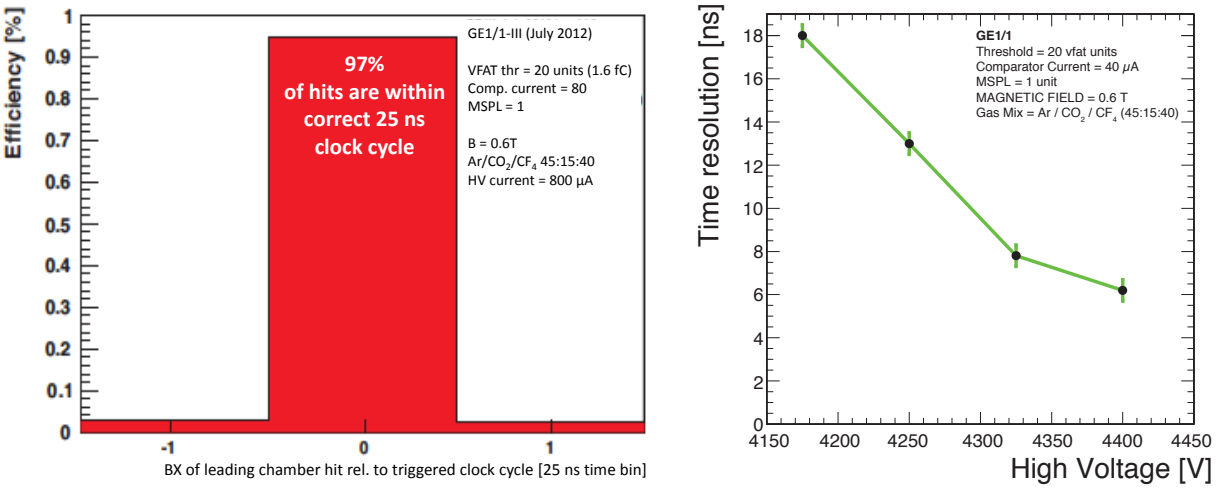

Figure 2.15: Timing measurements for a GE1/1-III prototype with VFAT2 readout in a beam with 25 ns bunch crossing time. *Left:* Fraction of hits measured in bunch crossings relative to the trigger clock cycle. *Right:* Timing resolution vs. drift voltage derived from plots as shown on the left assuming a Gaussian time resolution.

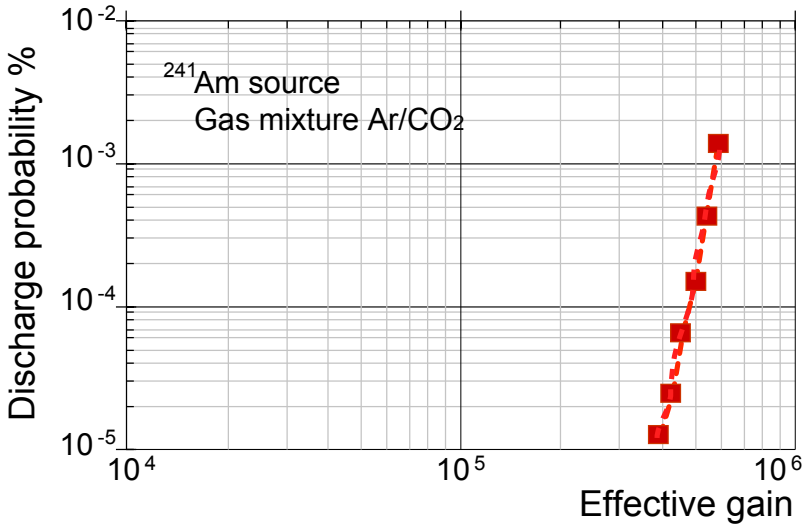

Figure 2.16: Discharge probability as a function of effective gas gain in a GE1/1-III detector operated with Ar/CO_2 70:30 counting gas and irradiated with a ^{241}Am alpha source.

total number of electrons produced in each X-ray conversion, e is the electron charge, and R is the measured rate of incident particles. The results in Figures 2.17 and 2.18 show that the gas gain is observed to be constant over four orders of magnitude of incident particle rate up to 100 MHz/cm^2. The gain begins to drop only above that value. This result confirms that the GE1/1 chambers will easily operate in the $1.6 < |\eta| < 2.2$ forward muon region of CMS, where a maximum rate on the order of 10 kHz/cm^2 is expected, i.e. four orders of magnitude lower than the rate that the GE1/1 detector can operate at while maintaining constant gain.

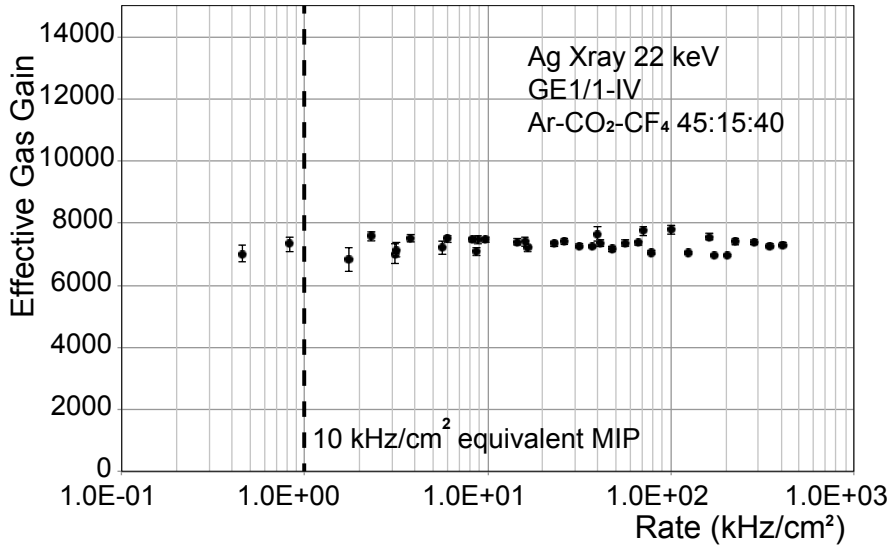

Figure 2.17: Effective gas gain as a function of the incident photon rate measured in a GE1/1-IV detector operated with $Ar/CO_2/CF_4$ 45:15:40 and irradiated with a 22 keV X-ray source with Ag anode.

2.2.2.5 Performance in magnetic field

Figure 2.19 shows a map of the magnetic field expected in the CMS muon endcap region during LHC Phase 2. In the location of the GE1/1, we expect a magnetic field strength of about 3T and a maximum polar angle of 8-9^o between the magnetic field lines and the CMS z-coordinate, which is also the direction of the internal electric field lines in the drift region of the GE1/1. This demonstrates that the GE1/1 will be operated in a substantial magnetic field. Consequently, we have tested the performance of GE1/1 prototypes also in magnetic fields.

During a test with 150 GeV muon and pion beams in the SPS H2 beam line at CERN, a GE1/1-II prototype was operated in a magnetic field up to 1.5 T provided by the CMS M1 superconducting magnet [11, 31]. The GE1/1-II was placed between the two magnet coils to validate the detector performance in a magnetic environment similar to that in the high-η region of the CMS muon endcap. For example, the Lorentz angle for the drifting electrons at 1.5 T and $\angle(\vec{E}, \vec{B}) = 90^\circ$ is comparable to the Lorentz angle at 3.8 T and $\angle(\vec{E}, \vec{B}) = 8^\circ$ that will be encountered by the GE1/1 in CMS (see Figure 2.19).

Figure 2.20 gives the measured strip multiplicity distribution for strip clusters in presence of a 0.6T magnetic field. Figure 2.21 shows the mean strip multiplicity of strip clusters and the cluster displacements as a function of magnetic field up to 1.5 T. The cluster size does not appear to be affected much by the magnetic field while the cluster position is displaced due to the presence of the magnetic field. The measurement of this displacement is in good agreement with simulations performed with GARFIELD. The timing performance was also measured with and without magnetic field as shown in Figure 2.22. The overall conclusion from these tests is that the magnetic field does not influence the performance of the GE1/1 detector in any way that would invalidate the conclusions from the measurements without field.

2.2.2.6 GEM performance simulations

The simulation comprises basic single-GEM simulations and a full triple-GEM simulation that includes signal generation and electronics. To simulate the detector response, one first has to calculate the electric field map, then simulate the electron transport in the gas, the avalanche

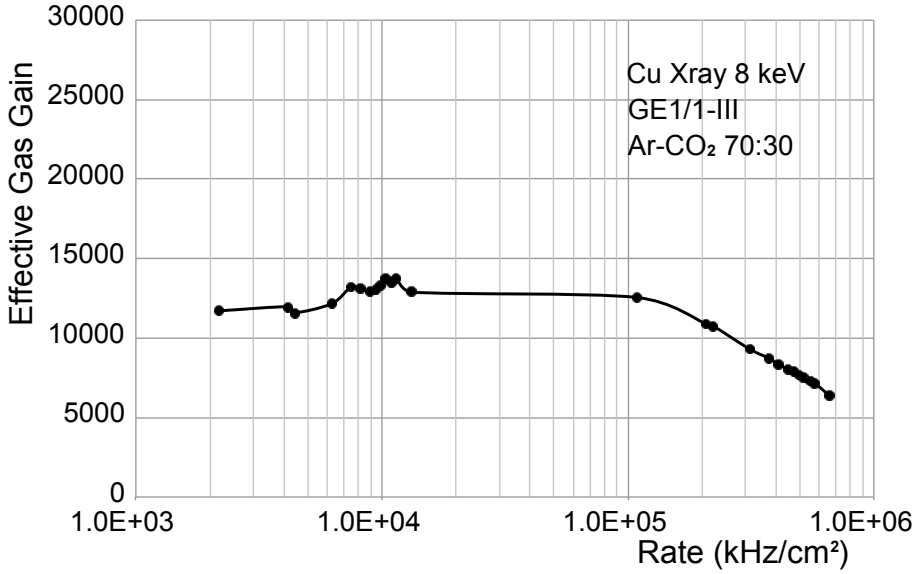

Figure 2.18: Effective gas gain as a function of the incident photon rate measured in a GE1/1-III detector operated with Ar/CO_2 70:30 and irradiated with an 8 keV X-ray source with Cu anode.

production, and signal formation and induction. A simulation flowchart is presented in Figure 2.23.

For the electric field simulation, the physical detector geometry (see Figure 2.24) is implemented in ANSYS, a simulation package for computational fluid dynamics applications [32]. Appropriate electrical potentials are assigned to each electrode. The field map is then generated in both 2D and 3D formats and loaded as an input to the GARFIELD++ suite [33], which simulates and computes electron transport in the gas medium, avalanche production (see Figure 2.25), and signal formation. Each simulation point consists of at least 5,000 electrons randomly distributed in X and Y and generated at a fixed 0.25 mm on the Z-axis (see Figure 2.25), i.e. just below the drift cathode. The gain uniformity as a function of the readout strip pitch, signal formation, and timing resolution are studied with this simulation.

Uniformity: An important GE1/1 performance parameter is the uniformity of the gain across the strips. Due to the trapezoidal shape, it is important to check the gain variations across the active area of the chamber. Figure 2.26 shows the effective gain as a function of the readout pitch in $Ar/CO_2/CF_4$ 45:15:40 for different values of the Penning effect parameterized by r_P. The simulated readout pitches 0.6 mm, 0.8 mm, 1.0 mm, and 1.2 mm represent the strip pitch variation in the GE1/1 going from higher to lower pseudorapidity. We observe some increase of the effective gain with pitch size, but the range of gains due to that effect does not exceed the maximum of 15% gain variation across the chamber that we require.

Timing resolution: In a triple-GEM detector, the signal on the readout strips is induced by the electrons amplified in the last of the three stages of multiplication. All electron production, transport, and amplification processes have statistical fluctuations which lead to fluctuations in the shape of the induced signal. The most important fluctuation occurs in the primary ionization process in the drift gap due to the clustering of the primary ionization; it dominates because of the small number of primary electrons. In the $Ar/CO_2/CF_4$ 45:15:40 gas mixture, the drift velocity is about 80 μm/ns (see Figure 2.6), so for a charged particle with perpendicular incidence, the primary electrons need up to 38 ns to completely clear the 3 mm drift gap.

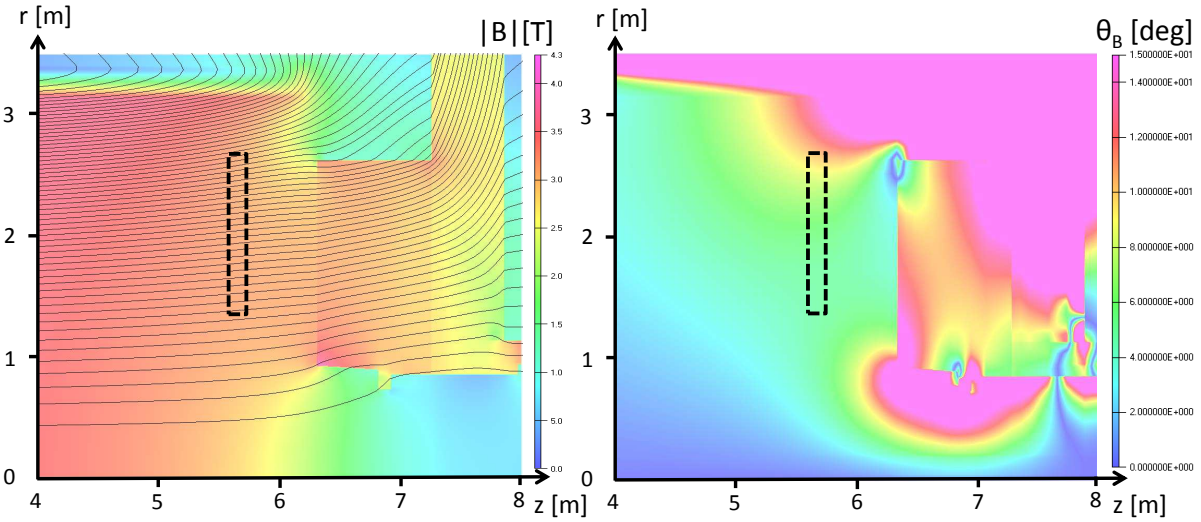

Figure 2.19: Map of the magnetic field expected in the CMS muon endcap region near the solenoid in LHC Phase 2 produced by OPERA simulation. Shown are field strength and field lines (left) and polar angle θ_B of the magnetic field vector (right), i.e. the angle between magnetic field and the z-axis of CMS. The dashed rectangles indicate the location of the GE1/1. Note that regions with $\theta_B \geq 15^o$ are colored pink.

These effects are reflected in the duration and structure of the charge signals induced in the readout strips as demonstrated by the simulation results (see Figure 2.27).

In order to fully estimate the performance of the triple-GEM detector such as time resolution, efficiency, etc., one has to include the response of the VFAT3 front-end electronics (see Ch.3) to the induced signals in the simulation. We convolute the induced signal given by the GARFIELD simulation, with the VFAT3 transfer function given by: $F(t) = (\frac{t}{\tau})^n \exp(-n\frac{t}{\tau})$, where t is the time, τ is the peaking time (25 ns, 50 ns, 75 ns, 100 ns, 200 ns or 400 ns) and n is the filter order (n = 3 for VFAT3). In the VFAT3 electronics, the output signal of the shaper is sent to a Constant Fraction Discriminator (CFD), which identifies the arrival time of the signal. We apply the CFD method with 5 different peaking times (25 ns, 50 ns, 75 ns, 100 ns and 200 ns). For each peaking time, we use 500 events simulated with GARFIELD. The time resolution as a function of the VFAT3 peaking time is better than 5 ns for peaking times longer than 50 ns (see Figure 2.28). This result makes sense since it takes at least 30 ns for the fully amplified electrons from the drift gap to induce a signal; it is also consistent with the good time resolution of the CMS triple-GEM detector with $Ar/CO_2/CF_4$ 45:15:40 measured in the test beam experiments.

2.2.3 Considerations for environmentally-friendly counting gas mixtures

Recently, a general discussion started within the gaseous detector community about the high environmental impact of several gases used during detector operation. Many gas mixtures commonly use gas components with extremely high Global Warming Potential (GWP). For example, GEM detectors often use gas mixture with CF_4 that has a GWP of 6500 (over 100 yrs) which makes this gas one of the most aggressive in terms of green house effects, the GWP of CO_2 being 1. The environmental policy (280/2004/EC) of the EU dictates that gases with high GWP must be phased out over the next several years. Moreover, and importantly, high GWP gases will not be produced anymore, with consequently expected rise of the gas price and difficulties with stock supplies.

The CMS GEM collaboration has started a campaign of studies to find potential alternatives to

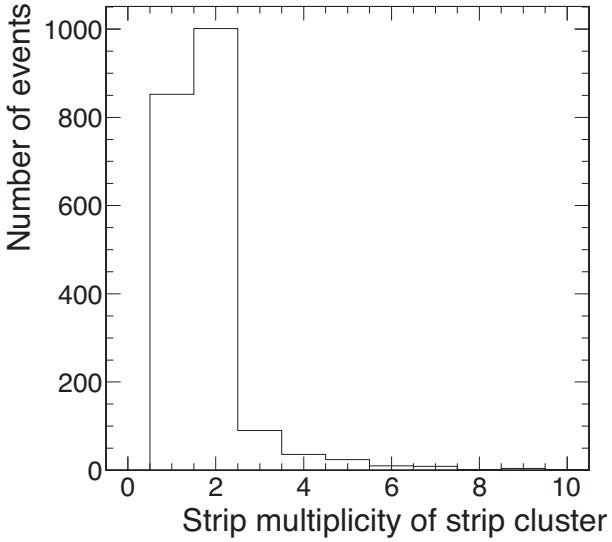

Figure 2.20: Strip multiplicity distribution for strip clusters at B=0.6 T when operating GE1/1-II chamber on the efficiency plateau.

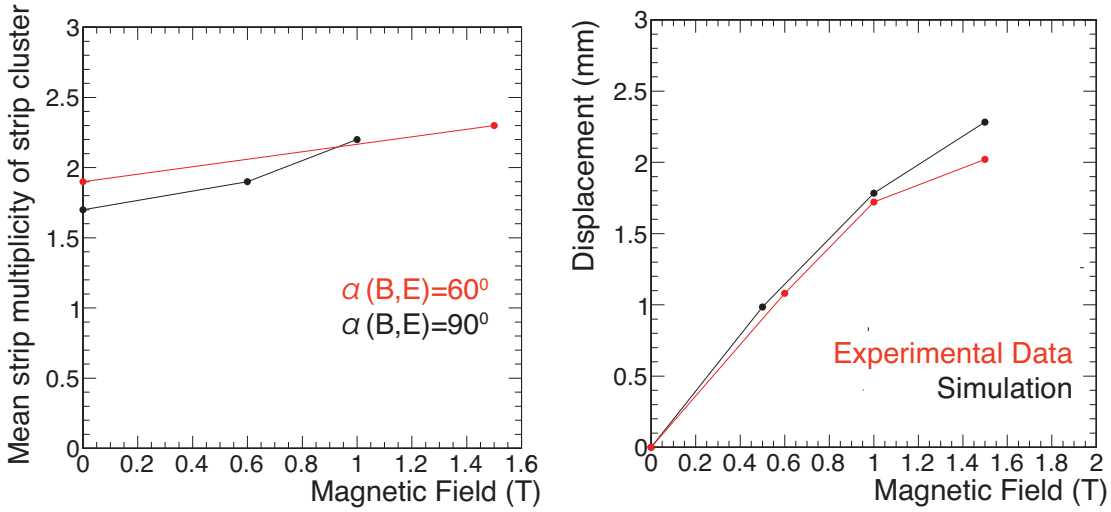

Figure 2.21: GE1/1-II performance inside a strong magnetic field. *Left:* Mean strip multiplicity of strip cluster. *Right:* Strip cluster displacement due to the magnetic field.

CF_4. As described above, the addition of CF_4 to the counting gas mixture improves the time response of the detector while maintaining a high detection efficiency. Obviously, the alternative to CF_4 must ensure similar performance in terms of time response, detection efficiency, and aging resistance. INFN Frascati, INFN Bari, INFN Bologna, and Ghent University are collaborating in this search for a replacement gas. Results are expected by the end of 2015. While the tests on alternative gases are ongoing, it must be stressed that Ar/CO_2 70:30 is a reasonably eco-friendly gas mixture that provides time and efficiency performances within the CMS requirements and is considered the current baseline gas for operation. This ensures that, even if a CF_4 candidate will not be found, the GE1/1 detector will be able to reach the expected performances.

One might consider a gas mixture that contains CH_4 instead of CF_4 as an alternative for an environmentally-friendly counting gas because it is well known that CH_4 is a good quencher

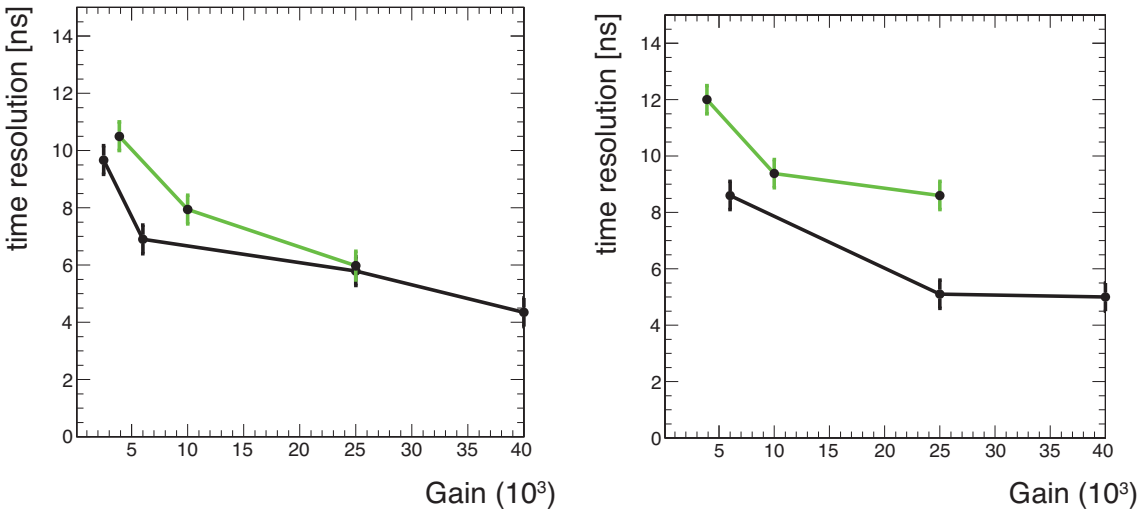

Figure 2.22: Detector time resolution as a function of gas gain without (left) and with (right) magnetic field equal to 1.5 T. The green curves are for the GE1/1-II while the black curves are for a small-size GEM prototype.

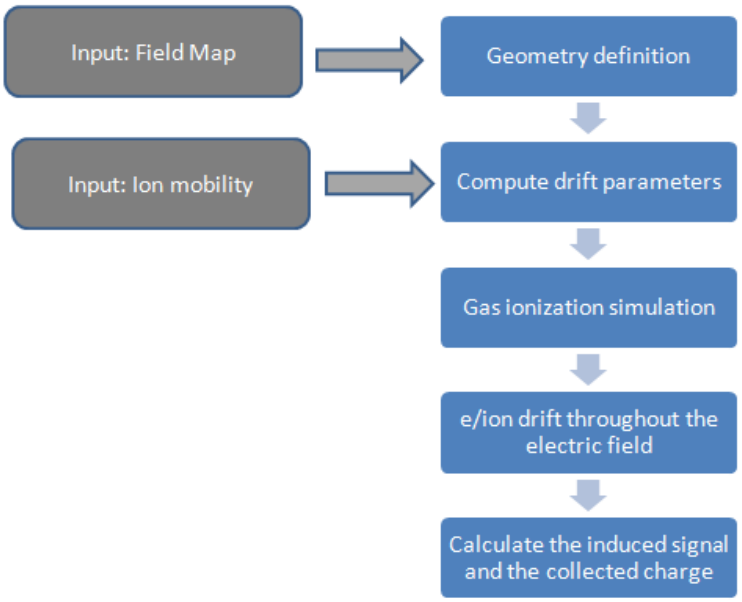

Figure 2.23: Flowchart of the simulation workflow.

and quite fast. However, in the literature it is also well documented that CH_4 contributes to the aging of gaseous detectors such as wire chambers and SWPC. For example, Kadyk's paper [34] demonstrates that Ar/CH_4 80:20 gives an approximate gain loss of about 10% per C/cm in wire chambers while Ar/CO_2 80:20 produces no gain loss. CH_4 polymerizes more easily than CF_4 because the typical bond strength of C-H (C-F) is 4.3 (5.4) eV and the energy required to destroy these bonds in CH_4 (CF_4) is 4.5-4.6 (5.2-7.8) eV depending on the reaction process [35]. While GEMs are intrinsically more aging tolerant than wire chambers because the gas avalanche and production of polymerizable molecules takes place in "empty space," i.e. in the holes, rather than near a wire, the use of CH_4 would still pose a substantial risk to the longevity of the detector due to this potential for easy polymerization.

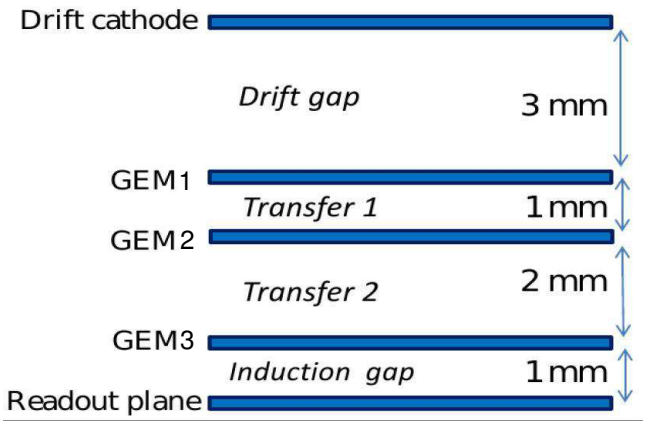

Figure 2.24: Cross section of the triple-GEM detector geometry as implemented in the simulation.

In addition, the CERN gas group prefers to avoid all use of flammable gases for obvious safety reasons. Even if the gas mixture itself is not flammable due to a low concentration of CH_4, the gas group would still have to provide pure CH_4 in a mixing station.

So far, three potential candidate gases are being considered and a campaign of measuring gas characteristics and chamber performance with different gas mixtures based on these gases is ongoing. Table 2.2 summarises their main characteristics in terms of GWP. Results from these studies are expected by the end of 2015.

Table 2.2: Summary of the Global Warming Potential (GWP) over 100 yrs for different gases under study as possible CF_4 replacement candidates. CF_4 is also listed as reference.

Chemical name (IUPAC)	Formula	CAS number	Type	GWP (100 yrs)
Tetrafluoromethane	CF_4	75-73-0	R14	6500
3,3,3-tetrafluoropropene	$C_3H_2F_4$	754-12-1	HFO-1234YF	4
1,3,3,3-tetrafluoropropene	$C_3H_2F_4$	29118-24-9	HFO-1234ZE	6
Trifluoroiodomethane	CF_3I	2314-97-8	R13I1	0.4

2.3 Technical design of GE1/1 chambers for CMS

2.3.1 GEM foil design and production technology

The three trapezoidal GEM foils used in one GE1/1 triple-GEM detector are basically identical. However, two different foil versions need to be designed, one for the short chamber type GE1/1-S and one for the long chamber type GE1/1-L. Shape and dimensions of the active foil areas are shown in Figure 2.29. The GEM foil surfaces oriented towards the readout board are a single contiguous conductor whereas the GEM foil surfaces oriented towards the drift board are segmented into 40 strips for the short chamber and 47 strips for the long chamber. The strips run across the width of the trapezoid (see Figure 2.30). Their width narrows when going from the short end of the trapezoid to the wide end so that each strip has an approximately equal area of about 100 cm^2. This segmentation restricts the amount of charge that can flow from one foil during a discharge to roughly 100 nC and, consequently, limits the total energy of a discharge. This protects the GEM foil against destruction due to discharges, which are inevitable even if they occur at very low rates under standard operating conditions. In the worst case, if a destructive discharge were to occur in an HV segment, it would only destroy that one HV segment instead of rendering the entire chamber unusable.

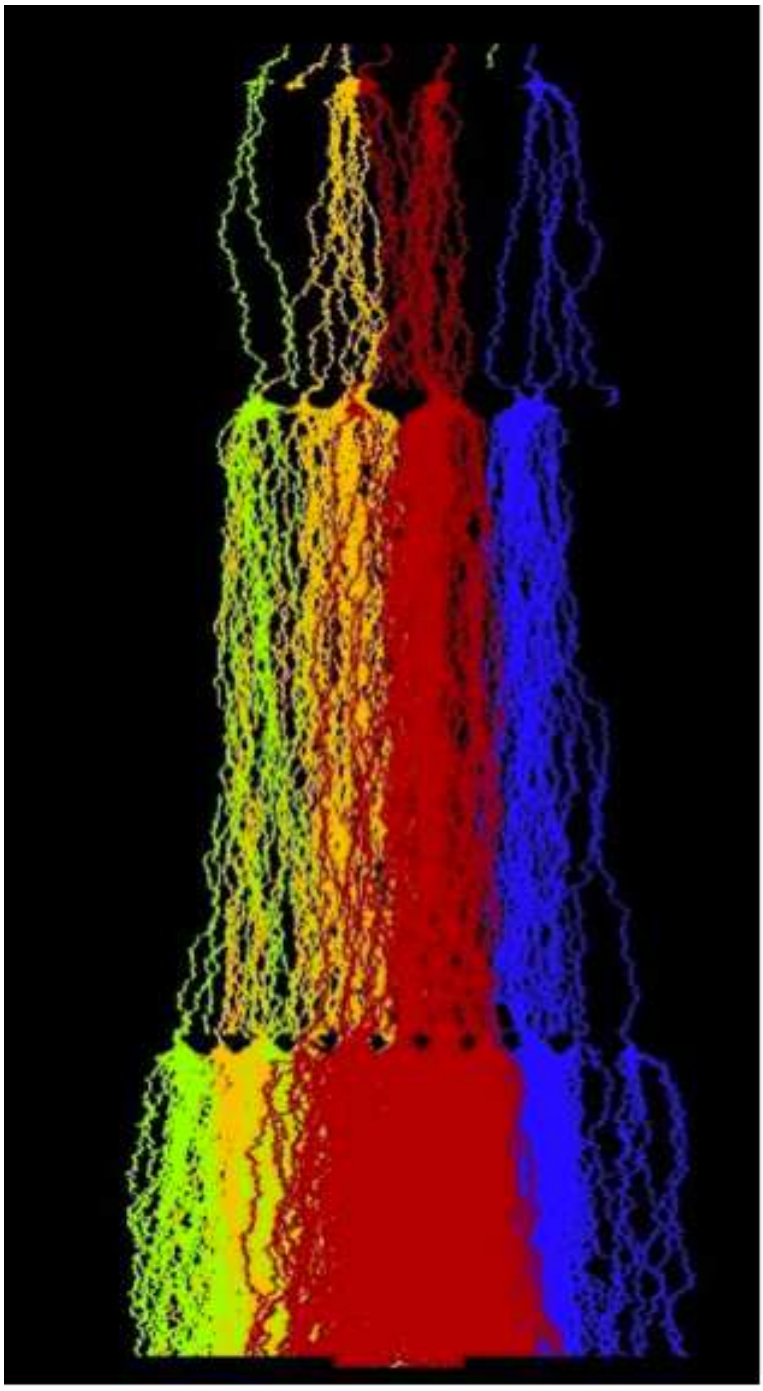

Figure 2.25: Visualization of the simulated avalanche development for seven primary electrons in a triple-GEM chamber starting from the drift volume.

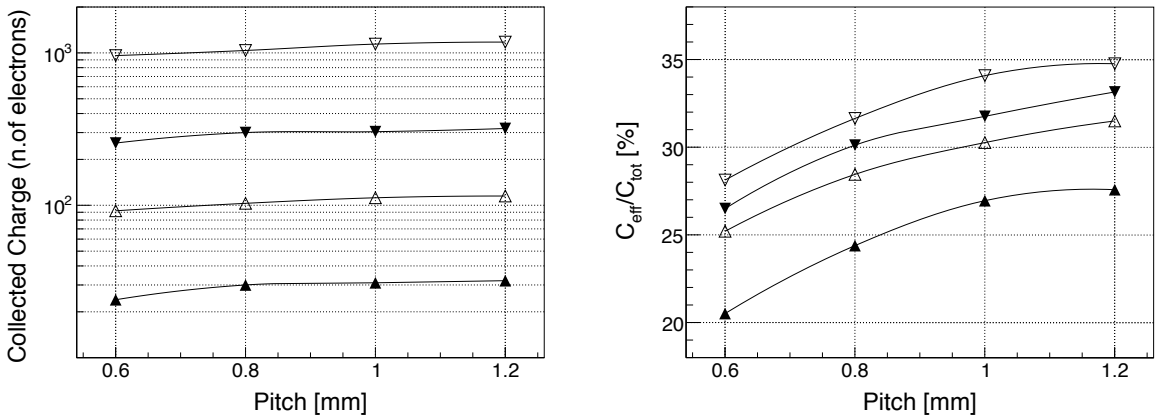

Figure 2.26: Simulation results for number of electrons collected on the anode strips (left) and ratio of effective and total charge collected (right) in $Ar/CO_2/CF_4$ 45:15:40 for 3650, 3850, 4050 and 4250 V (from bottom to top) as a function of readout strip pitch for V_{drift} = 4050 V and r_P = 0.4.

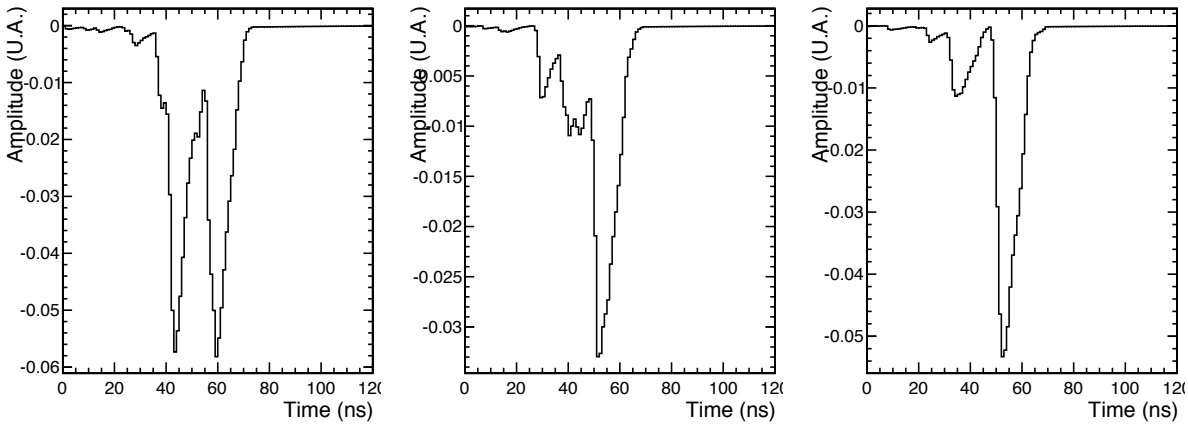

Figure 2.27: Examples for simulated signals that are induced in the readout electrodes.

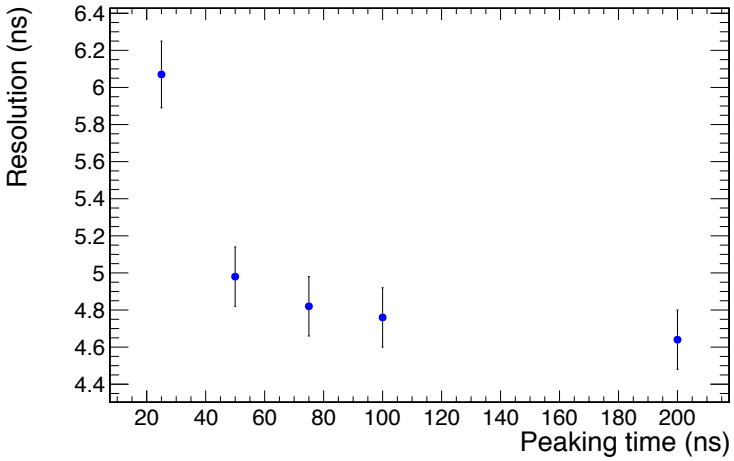

Figure 2.28: Simulated GE1/1 time resolution as a function of the VFAT3 peaking time.

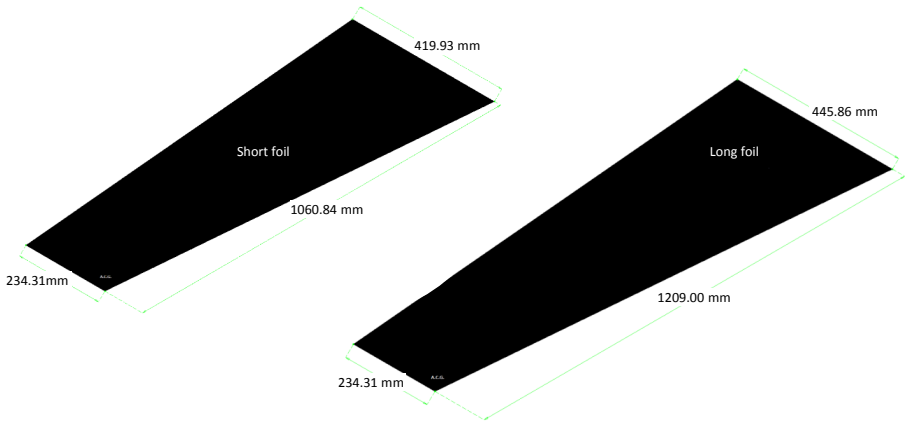

Figure 2.29: Shapes and dimensions of the active areas of short (left) and long (right) trapezoidal GEM foils for GE1/1. The trapezoids subtend an opening angle of 10^{o}.

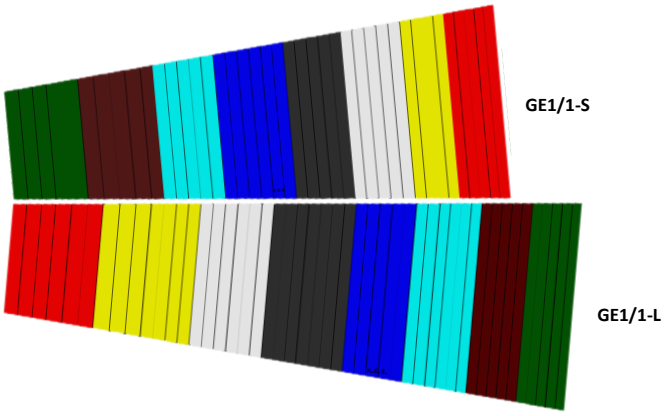

Figure 2.30: Schematic HV segmentation of short (top) and long (bottom) GE1/1 GEM foils into 40 and 47 strips, respectively, on the foil side oriented towards the drift board. The color scheme indicates which HV segments correspond to the eight η-sectors of the detector.

The design requires that each of the HV segments is supplied individually with HV. This is done by routing a trace around the edge of the GEM foil from a common connection point where the external HV potential is applied to the foil (see Figure 2.31). The HV trace is connected through 10 MΩ surface-mounted protection resistors to each HV segment (see Figure 2.31). The potential of the other side of the foil is provided by a single connection point. The common connection points are located at the wide end of the foil (see Figure 2.31). An additional trace is routed from HV segments to dedicated test points that facilitate fast continuity and leakage current tests during chamber assembly. Both long and short chambers have eight η-sectors, which are physically implemented on the readout board. The color scheme in Figure 2.30 indicates which HV segments correspond to which of the eight η-sectors of the detector.

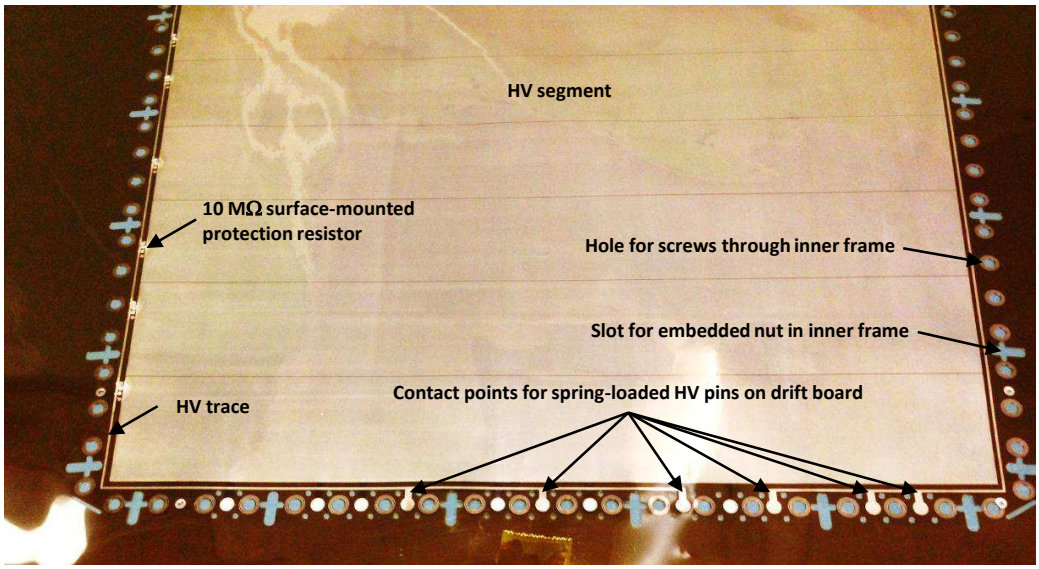

Figure 2.31: GE1/1 GEM foil with traces along the active area that route HV to the HV segments via 10 MΩ protection resistors.

The production of GEM foils is based on photolithographic techniques commonly used by the printed circuit industry. The copper-clad polyimide substrate (kapton or apical brands) gets coated on both sides with solid photoresist of 15 μm thickness that the GEM hole pattern is transferred onto by UV exposure through flexible masks. In order to get good homogeneity of the hole geometry across the foil, it is very important to keep the alignment error between the masks on the two GEM foil sides within 10 μm. However, since both the raw material and the two masks are made from flexible material, the manual alignment procedure becomes extremely cumbersome when the linear dimensions of the GEM exceed 40 cm.

A way of overcoming this alignment problem for larger foils is the use of single-mask photolithography. In this technique, the GEM pattern is transferred only to one side of the raw material, thus removing any need for alignment. The exposed photoresist is developed and the hole pattern is used as a mask to chemically etch holes in the top copper electrode of the GEM foil. After stripping the photoresist, the holes in the top copper electrode are in turn used as a mask to etch the polyimide (see Figure 2.32). This technique has been proven to be a valid manufacturing technique for making GEMs. It was initially used to build a prototype detector for a possible upgrade of the TOTEM T1 detector. More recently, the production process has been further refined, giving greater control over the dimensions of the GEM holes and the size of the hole rims during the production process. All GE1/1 prototypes mentioned above comprise GEM foils produced with this technique at CERN. Effects of the hole shape are also being

explored in simulation studies (see below). Production issues have been studied and single-mask GEMs are compatible with industrial production using roll-to-roll equipment, which is a very important aspect of this technique. Consequently, a price reduction for GEM foils is expected from large-scale industrial production.

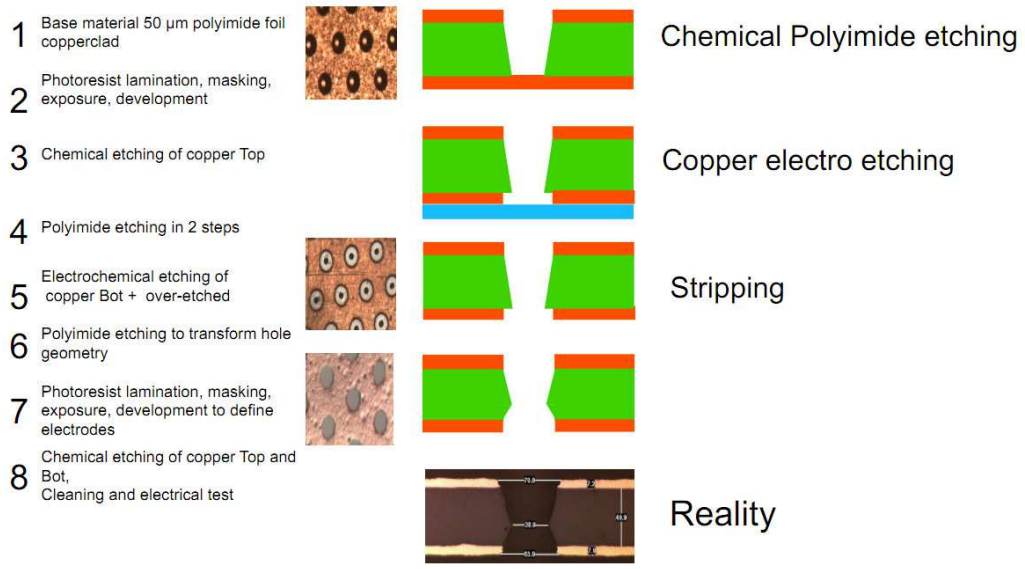

Figure 2.32: Overview of steps in the single-mask etching process for GEM foils.

2.3.2 Validation of chamber materials

Even though GEM detectors have been proven to perform well in high-rate environments and to intrinsically resist typical aging phenomena that can occur in gaseous detectors [36], it is still of paramount importance to carefully validate all materials actually used in the construction of the GE1/1 detectors. Specifically, materials used in GE1/1 construction need to be tested for potentially harmful outgassing and radiation hardness. Other system properties that could affect GE1/1 performance over long time periods, such as interactions with the gas mixture and gas system components and fluids need similar scrutiny. In addition, standard procedures for proper quality control of all materials and assembly procedure are needed to ensure uniform system performance.

We have adressed three aspects of material and system validation: 1) impact of water absorption and desorption on the tensile properties of GEM foils, 2) outgassing of chamber components, and 3) a long-term aging test of full-size GE1/1 prototypes.

Impact of water absorption on GEM tensile properties: The materials studied were pure kapton foils and GEM foils. Unused samples of kapton and GEM foils were analyzed to provide reference data for subsequent comparison with samples irradiated at the GIF. The state of the reference samples was determined by means of FTIR (Fourier Transform Infra-Red) analysis, optical microscopy, and SEM-EDS (Scanning Electron Microscopy - Energy Dispersive Spectrometry) characterization (see Figure 2.33).

GEM foils interact with humidity both before assembly because of cleaning procedures with deionized water and during operation via atmospheric air intake due to leaks in gas piping. It is important to characterize the GEM foil behaviour as a function of humidity as the amount of water contained in the chambers during the activity of detector can vary. Water content is expected to affect both electrical and mechanical GEM foil properties. Diffusion of water in the

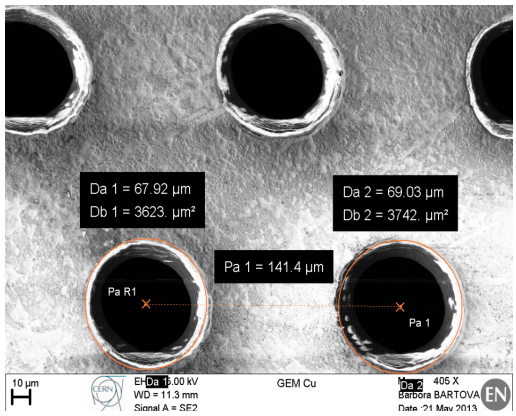

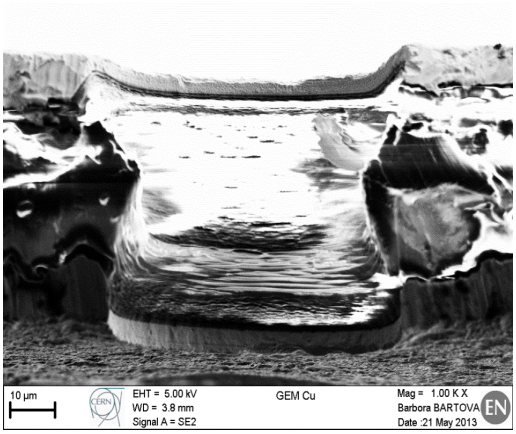

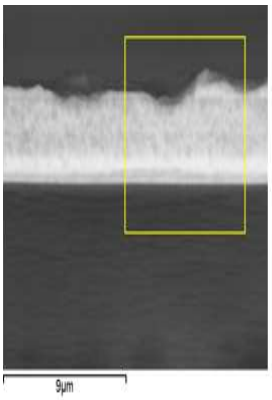

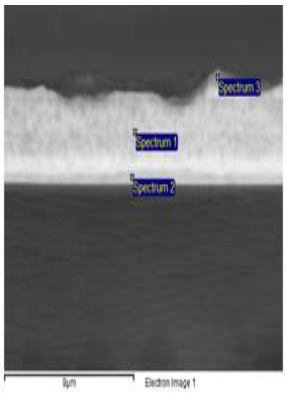

Spectrum	C	O	Cu	Total
wt.%				
Spectrum1	9.6	0.7	89.0	100.0
Spectrum2	35.7	3.2	61.1	100.0
Spectrum3	5.8	1.0	93.2	100.0

Figure 2.33: Reference microscopy images of the actual geometry of GEM holes to validate shapes and to confirm the absence of anomalous deposits (top left); cross-sectional view of GEM holes showing biconical shape (bottom left). Cross-sectional SEM-EDS analysis of GEM (top right). The table (bottom right) shows SEM-EDS analysis results for an unused sample in the cross-section spots shown in the top right picture. Such analyses provide information on composition of material, thickness and shape of copper coating, which are relevant factors for characterisation and detection of possible aging effects of the GEM foil.

GEM foil as a function of time was parameterized according to this formula

$$\frac{M(t)}{M(\infty)} = 1 - \frac{8}{\pi^2} e^{-\frac{D\pi^2 t}{4\ell^2}} \tag{2.3}$$

where $M(t)$ is the mass of water adsorbed on the polyimide surface and diffusing at time t, $M(\infty)$ is the mass of water at equilibrium (saturation), D is the diffusion coefficient and ℓ is the half-thickness of the polyimide layer. Two GEM samples with dimensions 10 mm $\times$ 15 mm and approximate weight 1080 mg were dried out in an oven at 110^{o}C for 36 hours. Samples were then placed into a vessel with controlled humidity obtained using potassium carbonate saturated solution (45% RH) along with a standard hygrometer to monitor internal conditions. The test was conducted in this controlled environment at $T = (20 - 22)^o$C and $RH = (45 - 50)\%$. The constant of diffusion of water in the GEM foils D_{GEM} was determined by a best fit of Eq.2.3 to the data. Preliminary results yield $D_{GEM} = (3.3 \pm 0.1) \times 10^{-10}$ cm^{2}s^{-1}, corresponding to an 8.5 hours saturation time.

The mechanical response of materials was analysed by uniaxial tensile tests [37–39] for samples of kapton and GEM foils in both dry and wet conditions. Four samples of GEM foils [10 mm $\times$ 110 mm $\times$60 μm (50 kapton + 5 Cu + 5 Cu)] and four samples of kapton (10 mm $\times$ 100 mm $\times$ 50 μm) were dried at 100^{o}C for 36 hours and tested using standard industrial procedures [40, 41]. For the test in humidity, the samples were humidified at 99.5% RH at room temperature for 7 days prior to measurement. Figure 2.34 shows preliminary results of the tensile tests. As expected, the GEM foil shows a slight increase of its Young's modulus compared to the kapton foil, due to the presence of Cu coating. However, the holes for the electronic multiplication affect the mechanical resistance of the structure, behaving as defects and amplifying local stress. Humidity has a larger effect on kapton foils than on GEM foils. The tensile properties of GEM foils also depend on the extrusion direction. The tension typically applied to a GEM foil in a GE1/1 is on the order of 5 N/cm, which is well within the elastic regime of the GEM foil material. Ongoing characterization of mechanical properties of GEM foils before and after irradiation will provide specific guidelines for proper tensioning of GEM foils in the GE1/1 chambers and information on their long-term mechanical stability.

Results from outgassing studies: Outgassing tests at room temperature and at 50^{o}C are being performed on all chamber materials in contact with the counting gas. The setup for the outgassing test consists of an outgassing box of 1,500 cm^3 equipped with a heating layer and temperature sensors. The gas flows through the box that contains the materials to be tested and is then sent to a Single-Wire Proportional Counter (SWPC) and a 10$\times$10 cm^2 triple-GEM detector. A gas chromatograph can be connected to the input or the output of the gas line to identify possible impurities. The test procedure has two steps. Each material is first flushed with the standard gas mixture $Ar/CO_2/CF_4$ 45:15:40 at room temperature for two weeks and then for two more weeks at 50°C to enhance any outgassing. During this period, the relative gain of both SWPC and triple-GEM detector are monitored every ten minutes using a ^{109}Cd energy spectrum. Once a gas gain drop of 5% is observed, the test ends and the material is rejected.

So far, two different polyurethane varnishes used for coating the inner and outer GE1/1 frames and the Viton o-ring material have been tested (see Figure 2.35). While the Cellpack polyurethane fails the test due to strong outgassing at 50^{o}C, the other polyurethane (Nuvoverne) and the Viton material pass the test and are validated for use in GE1/1 construction. Further outgassing tests will be conducted with the kapton material of the washers used for sealing the drift and readout board screws, pcb material used for drift and readout boards, glass-epoxy frame material, SM resistors mounted directly on GEM foils, and solder used to mount the resistors.

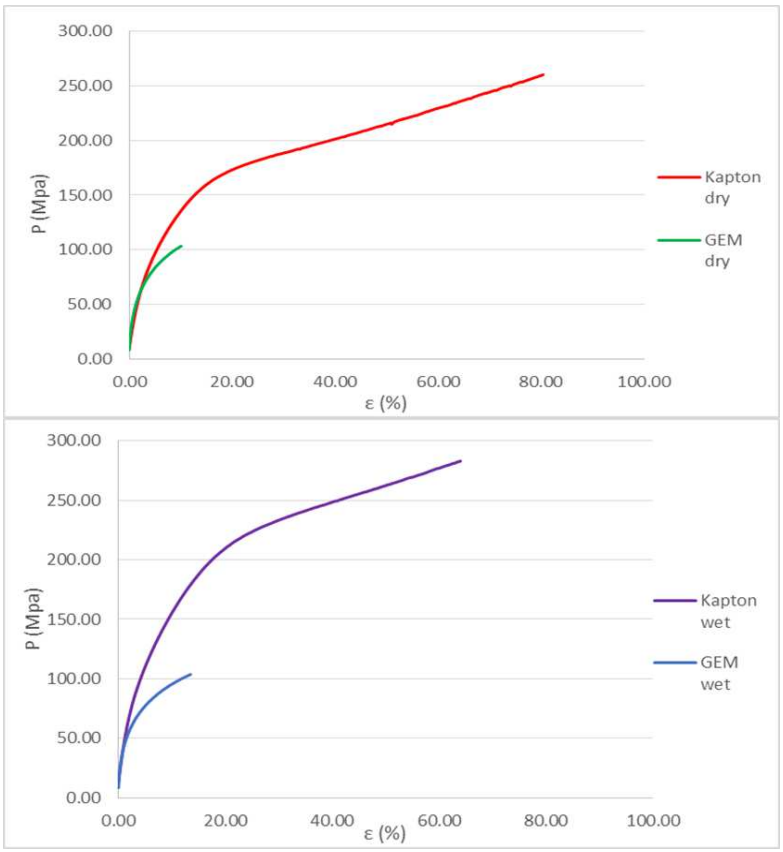

Figure 2.34: Behavior of dry (top) and "wet" (bottom) kapton and GEM foils during tensile stress test.

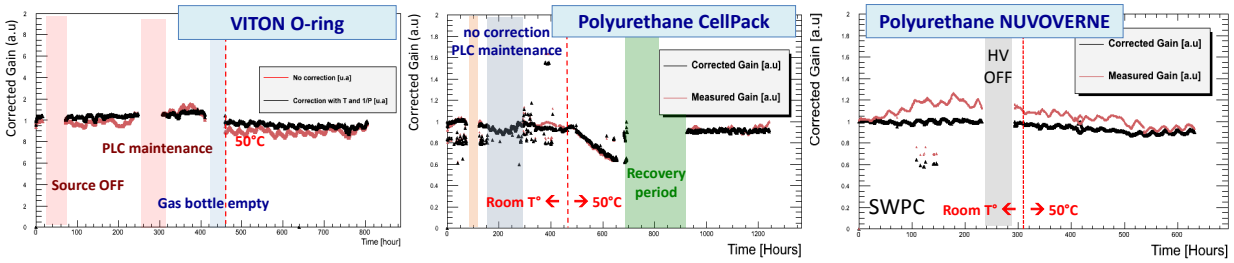

Figure 2.35: Results of outgassing studies of three GE1/1 candidate chamber materials: O-ring material Viton (left); polyurethane varnishes for inner and outer frames - Cellpack (center) and Nuvovern (right).

Aging test of GE1/1-IV prototype: A long-term aging test is performed at the Gamma Irradiation Facility (GIF) at CERN (see Figure 2.36). The GIF bunker contains a ^{137}Cs source of 566 GBq that emits gamma rays of 662 keV. A GE1/1-IV prototype detector is placed 30 cm from the source, where it receives an incident gamma rate on the order of 100 kHz/cm^2 with an observed pulse rate from gammas interacting in the detector of a few kHz/cm^2. Two sectors of the GEM chamber are irradiated by the ^{137}Cs source while two other sectors are shielded by lead blocks to provide a reference. Due to scattering and fluorescence effects, it is still possible to see a signal in these sectors; however, the rate is 15 times lower than in the irradiated parts. The detector is operated at a gas gain of 2×10^4 and is flushed with the standard $Ar/CO_2/CF_4$ 45:15:40 gas mixture at 0.5 liters/hr. The gas system for the test provides a dedicated gas line into the GIF irradiation bunker. The system is equiped with two SWPCs, one upstream and one downstream of the GE1/1 chamber. The SWPCs are particularly sensitive to the gas quality and can quickly indicate the presence of pollutants coming from the gas input (SWPC 1) or from the GE1/1 detector (SWPC 2). These counters monitor the cleanliness of the gas system.

By continuously monitoring the readout current of the GE1/1-IV detector, we can identify possible aging of the detector. A polymer deposit would affect the gas gain and the discharge probability. After corrections for fluctuations of the environmental parameters (T,P) are applied, the normalized gain of the irradiated sectors of the GE1/1-IV prototype shows no drop after accumulating about 10 mC/cm^2 of charge (see Figure 2.37). This charge is accumulated over a run period of 12 months and corresponds to about two years of GE1/1 operation at the HL-LHC (see also app. B). As the GIF has been shut down by now, the test setup is being moved to the new higher-intensity Gamma Irradiation Facility (GIF++) at CERN, where the aging test will continue with a goal of reaching $\geq$ 100 mC/cm^2.

2.3.3 Mechanical design

This section describes the mechanical design of the GE1/1 chambers in full detail.

2.3.3.1 Design Overview

An overview of the mechanical design of a single trapezoidal GE1/1 chamber is shown in Figure 2.38 and 2.39. The main components and materials of a single GE1/1 chamber are listed in Table 2.3. The assembly and sealing of the detector are entirely mechanical. No glue is applied during assembly, which makes it possible to open a detector again for repairs if needed. It also speeds up the assembly of the chamber since there are no wait times due to curing of glue.

The three GEM foils are sandwiched at their edges between four layers of a thin frame made from halogen-free glass epoxy (ISOLA DE156) that is composed of 8 individual pieces per layer (see Figure 2.40). The thicknesses of the different frame layers define the spacings between GEM foils as well as between GEM foils and drift/readout boards as follows: Drift gap / GEM1-GEM2 transfer gap / GEM2-GEM3 transfer gap / induction gap : 3/1/2/1 mm. The stack is held together by numerous small M2$\times$6 stainless steel screws. They penetrate all frame layers and foils about every centimeter and are tightened against small threaded M2 brass inserts (see Figure 2.40). Using inserts to counter the screws avoids loosening macroscopic and microscopic glass epoxy particulates from the frames as was observed in earlier prototypes where screws were threaded directly into the frame material. Frame pieces are coated with Nuvovern polyurethane varnish before assembly. Both those measures ensure that no glass epoxy particulates detach from the frames during assembly, fall onto GEM foils, and potentially produce electrical shorts in the GEM holes. The screw heads are conical with flat outer surfaces and are sunk into counterbores in the frames that surround the through-holes during

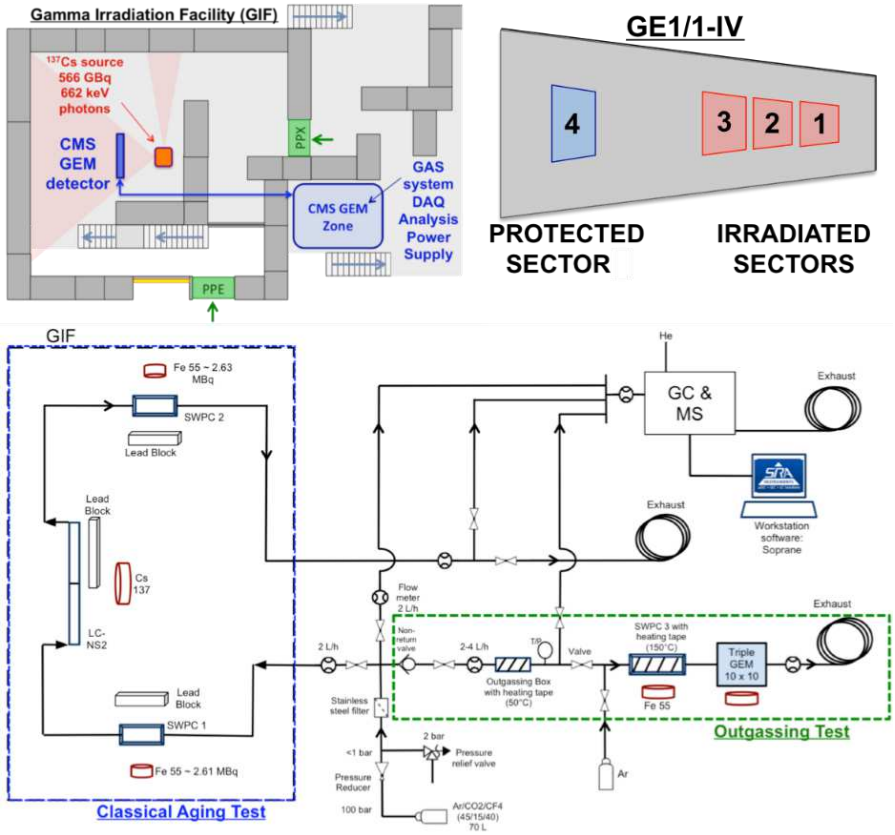

Figure 2.36: Schematic view of the aging test setup at the Gamma Irradiation Facility (GIF) at CERN and of the irradiated and shielded sections of the GE1/1 detector under test (top). Overview of the gas system for the classical aging test in blue and the outgassing studies in green (bottom).

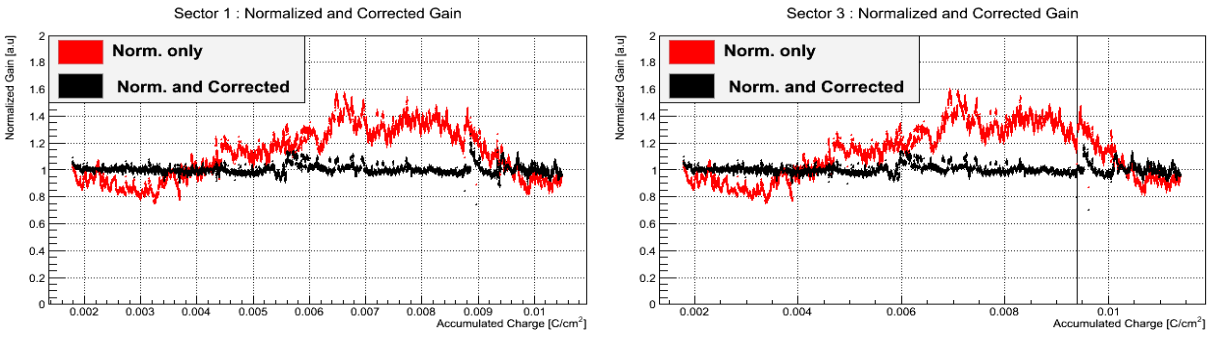

Figure 2.37: Corrected and normalized gain in irradiated GE1/1-IV sectors 1 (left) and 3 (right) as a function of the total charge accumulated in the detector during the GIF aging test. Note that the result for sector 2 (not shown) looks very similar. No aging effects have been observed after a total accumulated charge of about 10 mC/cm^2.

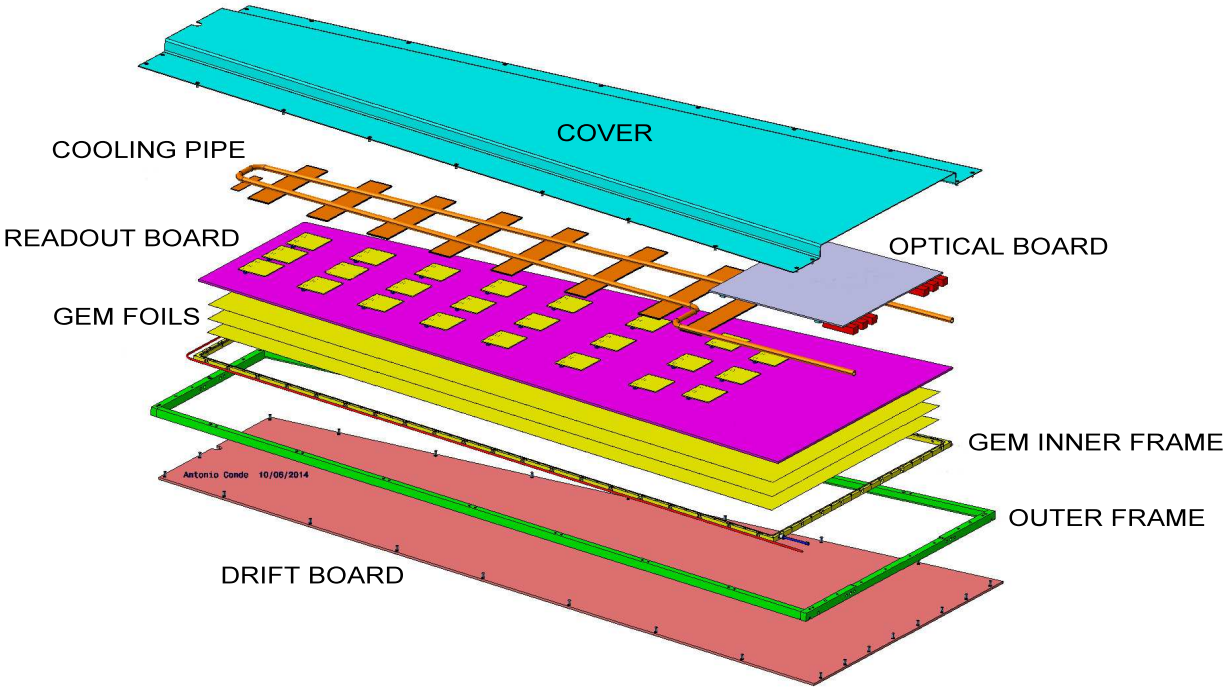

Figure 2.38: Exploded view of the mechanical design of a single GE1/1 chamber.

Table 2.3: Summary of layer structure and materials of a single GE1/1 chamber.

Layer	Material	Thickness [mm]
Protective cover	Al	1.0
Cooling pipe	Cu (filled with H_2O)	8 external ⌀, 6 inner ⌀
Cooling pads	Cu	1.0
GEB board	Cu/FR4	0.140/0.856
Readout board	Cu/FR4/Cu	0.035/3.2/0.035
Induction gap	$Ar/CO_2(/CF_4)$	1.0
GEM 3	Cu/polyimide/Cu	0.005/0.050/0.005
Transfer gap 2	$Ar/CO_2(/CF_4)$	2.0
GEM 2	Cu/polyimide/Cu	0.005/0.050/0.005
Transfer gap 1	$Ar/CO_2(/CF_4)$	1.0
GEM 1	Cu/polyimide/Cu	0.005/0.050/0.005
Drift gap	$Ar/CO_2(/CF_4)$	3.0
Drift board	Cu/FR4/Cu	0.035/3.2/0.035

tightening (see Figure 2.40 left). Similarly, the nuts are sunk into counterbores on the frames (see Figure 2.40 center), so that the screws and nuts are flush with the top and bottom surfaces of the inner frame after the stack is assembled.

Additional square stainless steel nuts are embedded into the frames every few centimeters with the axes of their threaded holes oriented perpendicular to the inner frame and GEM foil surfaces (see Figure 2.39, 2.40 right). These nuts counter M2.5 $\times$ 10/$\times$ 8 stainless steel screws that are inserted into small brass posts, so-called "pull-outs", which are located within the gas volume. When the pull-out screws are tightened manually, the GEM foils in the stack are tensioned as the inner frame is being pulled outwards towards the pull-outs. Due to the large number of screws, the GE1/1 can be assembled with good manual control over the GEM tension so that the foils can be tensioned as uniformly as possible. The relative large size of the square nuts and their large number ensure that the force on the frame at each pull-out is kept as low as possible to avoid any long-term local deformations of the frame due to the stress. The pull-outs are in turn bolted down onto the pcb that provides the drift cathode with two A2 stainless steel M2.5 $\times$ 4/$\times$ 8 screws that are sealed with polyamide washers against the drift board. With these nuts and screws, the GEM stack is attached to the drift pcb.

A large outer glass-epoxy frame machined from a single piece and placed around the tensioned GEM stack and the brass pull-outs provides the border of the gas volume (see Figure 2.41). The frame has numerous wide notches to accomodate the brass pull-outs. It is also coated with Nuvovern polyurethane varnish before assembly to seal in particulates. On both sides of the outer frame, a Viton O-ring is placed into a groove that runs around the entire outer frame to seal it. The anode readout board is placed on top of this outer frame and attached to the brass pull-outs with A2 stainless steel M2.5 $\times$ 4/$\times$ 8 screws which are sealed with polyamide washers against the readout board in the same way as the drift board screws. This sandwiches the outer frame tightly between the drift board and readout board and holds it in place essentially by friction. It provides a solid gas barrier that is only penetrated by two small holes in diagonally opposed corners to provide the gas inlet and outlet for the chamber.

The drift board features a single drift cathode on its inner side and a solid ground plane on the outside of the chamber for rf shielding purposes. It provides connections to external high voltage supply lines via HV noise filtering circuitry. The drift board routes a total of seven different potentials to the various GEM electrodes and to the drift cathode.

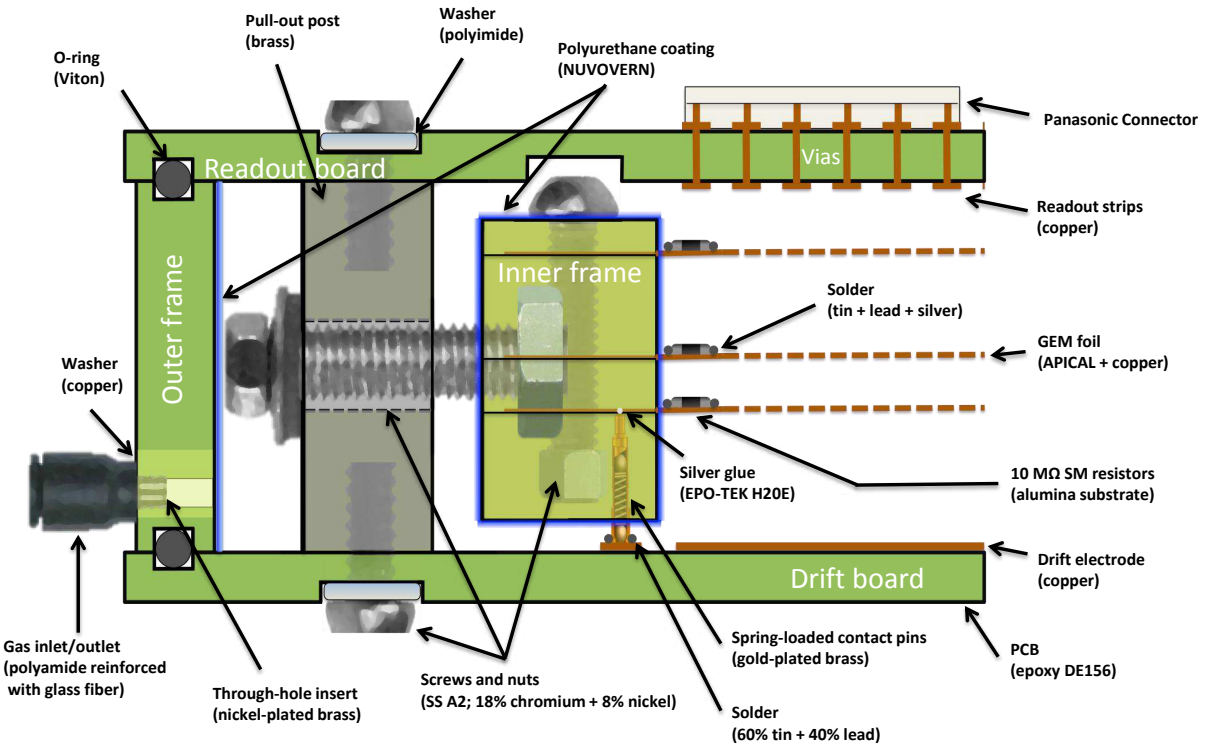

Figure 2.39: Cross section through inner and outer chamber frames and GEM foils that shows how the GEM foils are mounted within the GE1/1 chamber so that they can be mechanically tensioned against the brass pull-out posts without deforming the drift or readout boards. The materials of all chamber components are specified.

Figure 2.40: Section of the inner frame of a GEM stack with stainless steel screws and counterbores on one side (left) and embedded countering brass nuts on the other (center). The tabs on the frame are where vertically embedded square nuts (right) are located that are used for tensioning the GEM stack against brass pull-outs. The shiny frame surface (left) is due to its coating with Nuvovern polyurethane varnish.

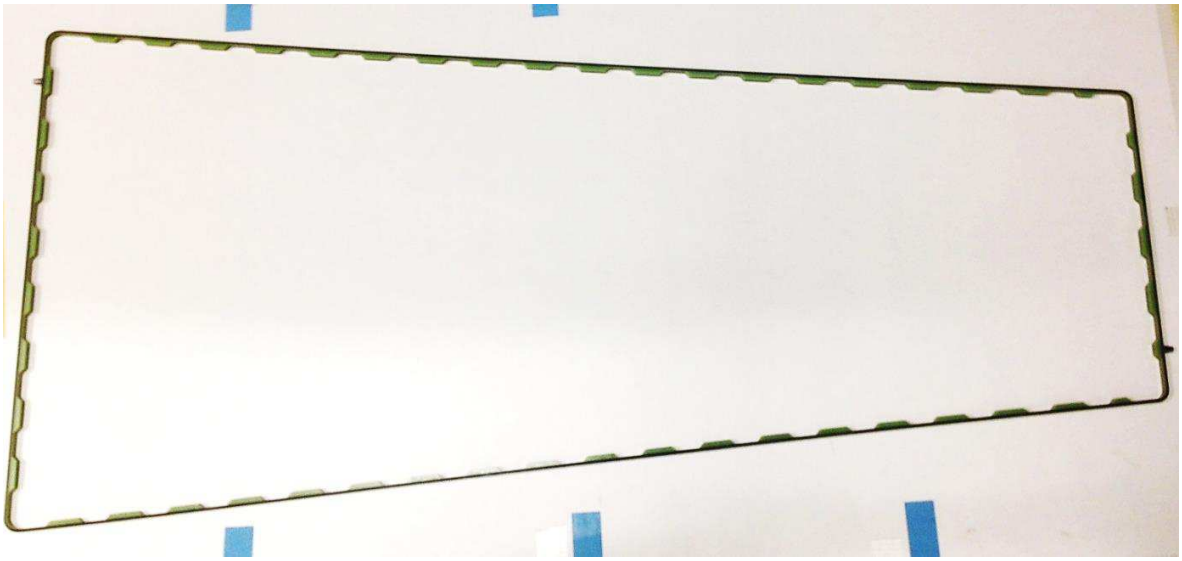

Figure 2.41: Outer gas frame of GE1/1-V with O-ring inserted. The frame is made from a single solid piece of halogen-free glass epoxy (ISOLA DE156). Gas inlet and outlet are visible in the top left and bottom right corners.

The readout board has 24 high-density header connectors (Panasonic part no. AXK6SA3677YGJ) with 130-pins on its outside to interface the radial readout strips on the inside to the VFAT2 hybrids that plug into the readout board from the outside. The connection is made with vias in the readout board that need to be sealed. A kapton coverlay attached with pure epoxy glue or alternatively prepreg material are being investigated by the CERN pcb workshop for that purpose. A third sealing method is to fill the vias with metal, which is the most expensive solution. The VFAT2 hybrids also plug into a second full-size pcb, the GEM Electronics Board (GEB), that is attached directly on top of the readout pcb. The GEB carries the digital output signals from all VFAT2 hybrids to the wide end of the chamber for processing and transporting to the Trigger/DAQ as described in detail in the chapter on electronics and DAQ. The GEB has cut-outs that allow the 130-pin connectors on the readout board to reach through. Copper pipes are routed on top of the GEB to provide coolant to the VFAT hybrids.

Finally, an aluminium frame is mounted on the drift board all around the outer edge (see Figure 2.38). An aluminium sheet with a thin central chimney along the long axis of the chamber is attached to that aluminium frame to cover the entire assembly from the readout side. Together, frame and cover provide solid protection for the on-chamber electronics and utilities.

2.3.3.2 Drift board design

Figure 2.42 shows the mechanical design and dimensions of the short and long drift boards of GE1/1-VI-L. A close-up view (see Figure 2.43) of the wide end of the drift board side that faces the chamber interior shows details of the on-board HV circuit traces for the HV noise filtering section, pads for a HV divider, and pads for the spring-loaded pins that make the electrical connections to the GEM foils. This design can be easily modified to allow for multi-channel HV supply lines instead of the HV divider. The design is asymmetric because the central section of the chamber needs to accomodate the on-chamber readout electronics.

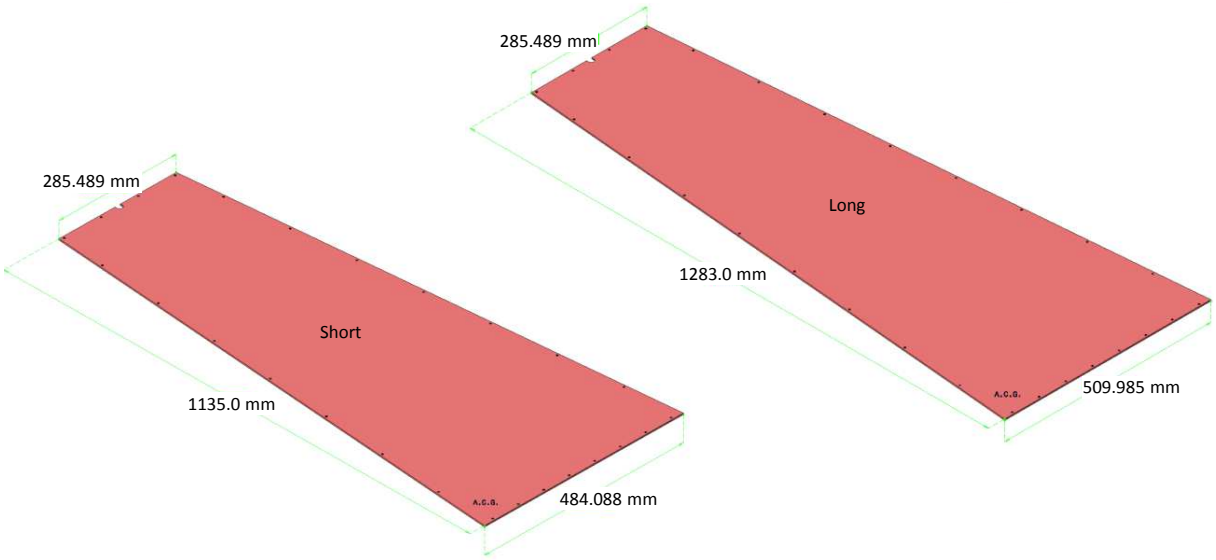

Figure 2.42: Design and dimensions of the drift boards for short (left) and long (right) GE1/1 chambers.

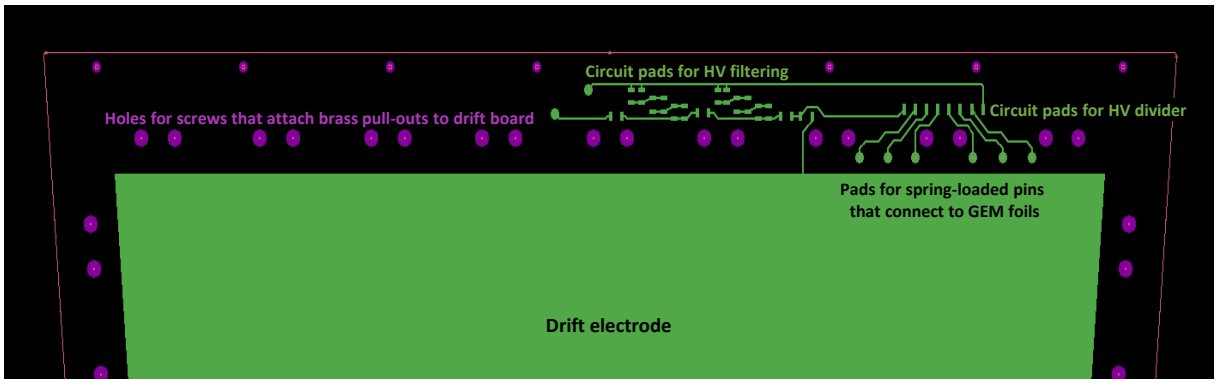

Figure 2.43: Close-up of the wide end of the GE1/1-VI-L drift board design with HV circuit traces.

2.3.3.3 Readout board design

The inner side of the readout board, i.e. the side that faces GEM3, features 3,072 truly radial readout strips arranged in eight η-sectors. The vertex of the strips coincides with the beam line. The active area covered by the strips subtends an angle of 10.15°, which allows for an overlap of 1.3 mrad (equivalent to 2.8 strips) between the active areas of adjacent chambers. The strips have a width of 230 μrad and are arranged with a pitch of 463 μrad. Each η-sector comprises 384 strips that in case of the long chamber vary in lengths from 11 cm at the short end (η-sector 1) to 19 cm at the wide end (η-sector 8). In addition, a couple of ground strips of the same dimensions are placed along the outer edges of the active area to prevent distortion of the electric field in the induction gap as the GEM foils cover a slightly larger area than the readout strips. The baseline design for the strip material is gold-plated copper produced in an electroless nickel / immersion gold (ENIG) process that is standard for pcb's. Figure 2.44 shows a close-up of the design of the short end of the readout board on that side. The smallest sector, i.e. η-sector 1, and a portion of η-sector 2 are shown. The view on the right of Figure 2.44 zooms in on the center of the strips in sector 1, where the vias are located that connect the strips to the outside of the readout board. On that outer side, traces are routed from the vias to 24 130-pin Panasonic connectors that the front-end VFAT3 hybrids plug into (see Figure 2.45). A set of three connectors serves each η-sector. Two of the pins on each Panasonic connector are connected to chamber common while the other 128 pins are connected to readout strips. The six tabs on the edges of the two long sides of the board allow attaching the GEB to the readout board (see Figure 2.46) after the chamber has been closed without compromising the active gas volume of the detector.

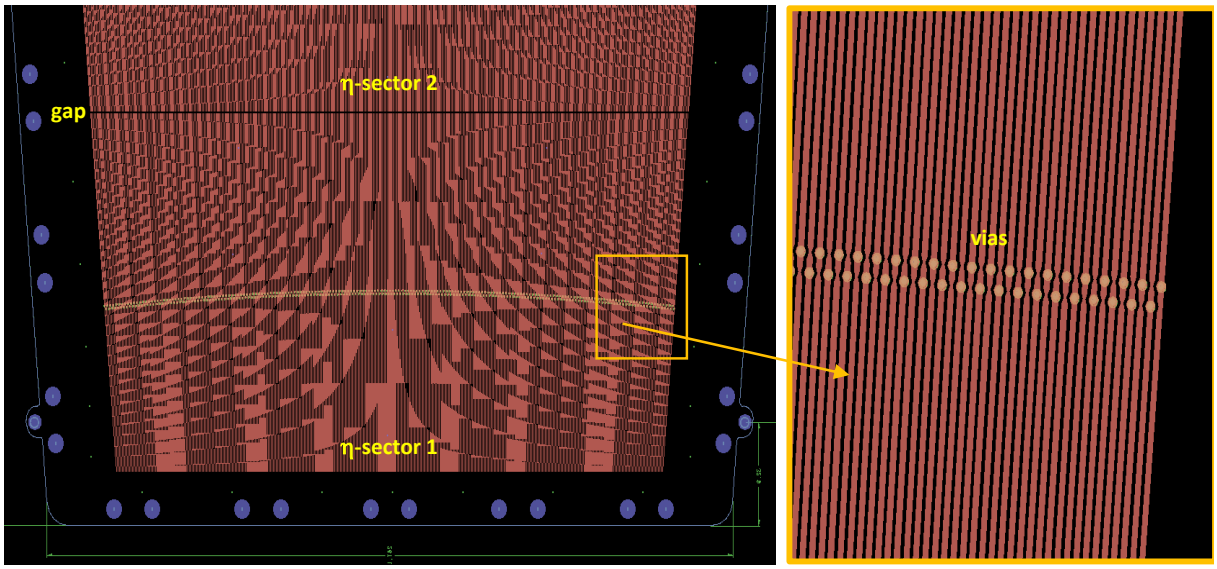

Figure 2.44: Design of the readout board for the long chamber GE1/1-VI-L (left). Shown is the inner side that faces into the gas volume opposite GEM3 at the short end of the board. Due to the high density of strips (384 readout strips in each sector), individual strips are not visible at this resolution. Note that the "hyperbolic" geometric pattern is an artifact of the display on a screen. Strips are visible when zooming in (right). The circular structures on each strip are vias that connect the strips to the outside of the board. The blue circles around the edge indicate positions of holes for screws that attach the readout board to the brass pull-outs.

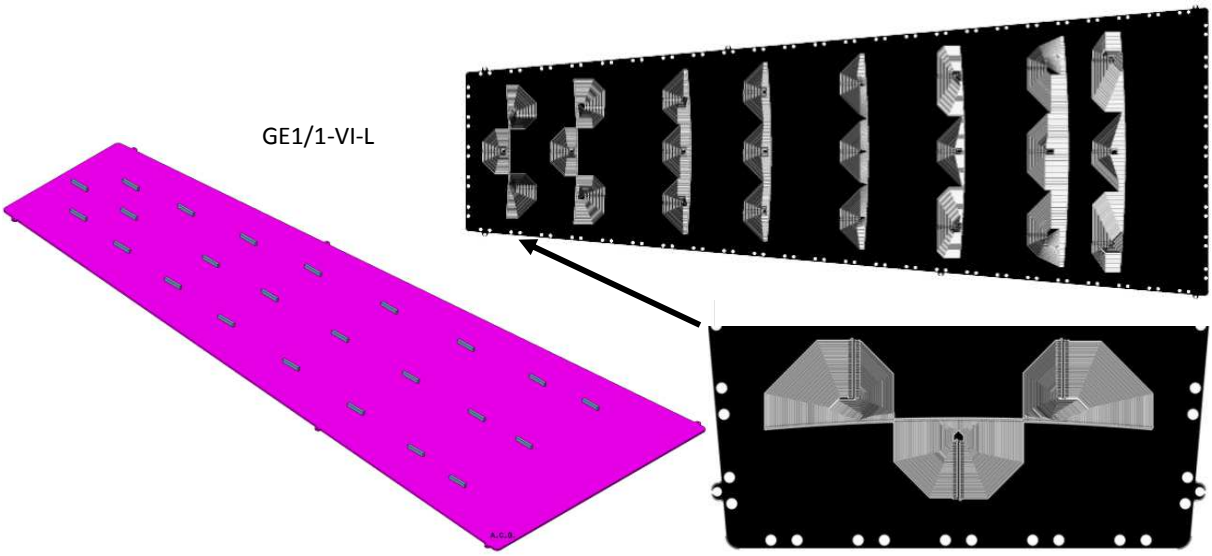

Figure 2.45: Design of the outer side of the readout board for the long chamber GE1/1-VI-L showing Panasonic connectors for VFAT2 hybrids (left) and traces from vias to Panasonic connectors (right).

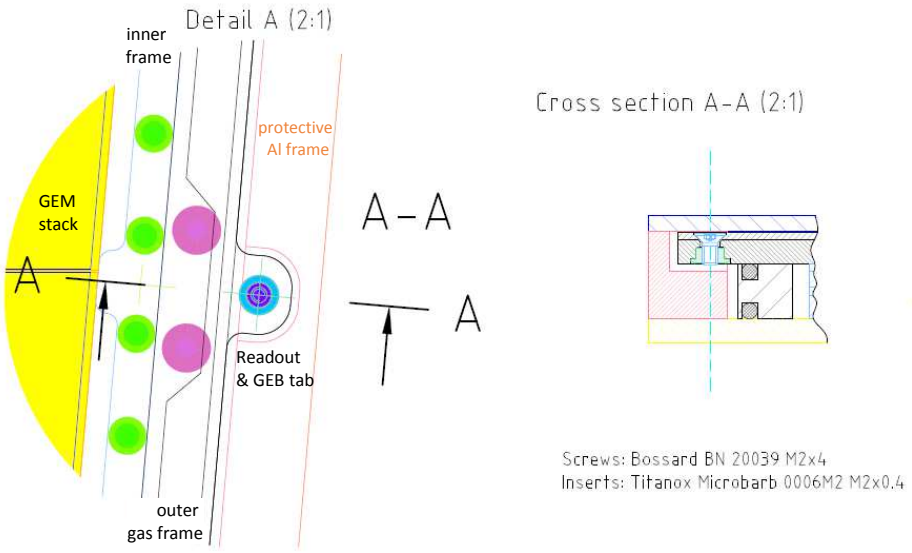

Figure 2.46: Design of tab for single screw (blue) that attaches GEB to readout board in top view (left) and cross section (right). The protective outer aluminium frame is notched to allow space for the tabs.

2.3.4 Foil stretching

The foils in the GEM stack are tensioned and made taut by uniformly pulling the stack outward against the brass pull-outs. This is achieved by manually tightening the screws that go through the holes in the brass pull-outs (see Figure 2.47) and that are countered by the nuts embedded in the inner frame that surrounds the GEM stack (see Figure 2.39). The screws are tightened to a torque of about 0.1 Nm. The end result are tautly stretched GEM foils closely surrounded by the outer gas frame (see Figure 2.48).

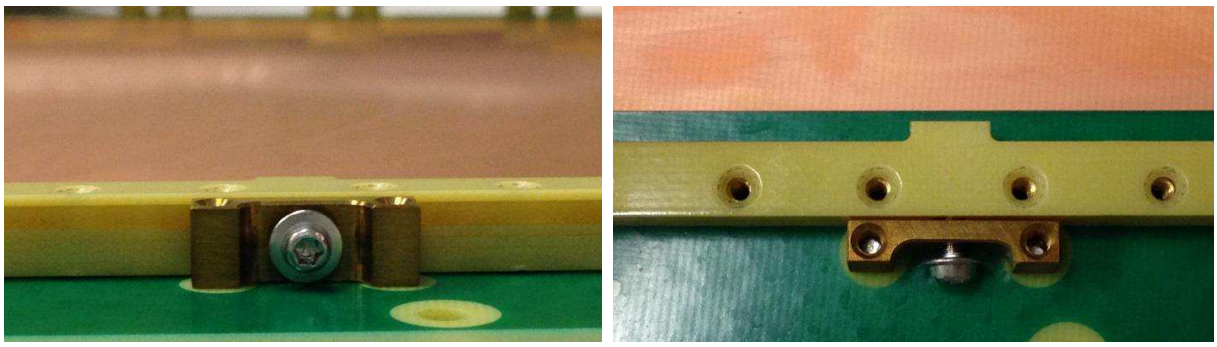

Figure 2.47: Brass pull-out with screw inserted into inner frame for tensioning the GEM foils in the stack in side view (left) and top view (right).

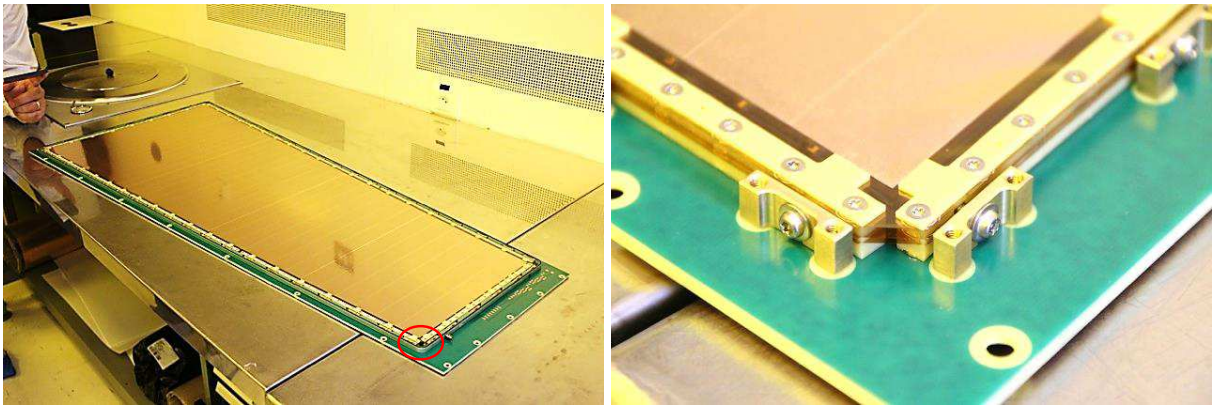

Figure 2.48: GE1/1-V prototype with GEM foil stack tensioned against brass pull-outs, mounted onto drift board, and surrounded by outer frame (left). The clear optical reflections in the top foil indicate that the stack is uniformly taut. The active chamber volume is now ready to be closed with the readout board. To help with scale reference, one of the editors (LB) of this chapter is lending a hand. A detail (red circle) of the stack is given that shows the gap between inner frame sections in one corner and the pull-outs (right).

Tolerances inherent in this method for stretching GEM foils and their relative positioning have an impact on the uniformity of gas gain and timing response. Previous studies on small GEM foils (by the LHCb experiment [42]) specify the required mechanical tolerances of gap dimensions and uniformity to $\pm 10\%$, e.g. $\pm 100 \mu$m for the 1 mm transfer and induction gaps, which corresponds to a 6% gain variation. In case of $Ar/CO_2/CF_4$ gas mixture, there is a slight dependence of the electron drift velocity on the electric field which translates into a small dependence of the timing performance on both mechanical precision and tension stability of the GEM foil stack.

Consequently, it is crucial to ensure precision during assembly, to determine reliable quality control (QC) procedures for mechanical tension, and to study the long-term stability of the mechanical foil tension. The assembly precision will be ensured by setting specifications on the torques applied to the pull-out screws during assembly. The specifications will be derived with a reference chamber for which the foil flatness will be monitored by Moirè interferometry (see below). We expect that interference patterns will assure flatness and uniformity to about 30μm in the plane orthogonal to the foil. Long-term stability will be guaranteed by optical strain gauges. The technique has been applied to several detectors in HEP for strain and deformations, temperature and humidity measurements, with a great deal of experience in the collaboration [43–45].

2.3.5 Gas distribution within chamber

The gas distribution inside the detector should not give rise to areas with very low gas flow that could result in pockets or regions where potentially harmful gas contaminants can accumulate. We evaluate the velocity field inside a GE1/1 detector design with a finite-element simulation using ANSYS, an engineering simulation software package for computer-aided engineering. A 3D CAD model of a (somewhat enlarged) GE1/1 detector geometry was developed and meshed by means of standard tetrahedrons using the ANSYS mesher package. The presence of the GEM foil stack is ignored in this basic model. The mesh is refined accurately in highly curved and sharp parts in order to control rounding errors arising from the discretized domain equations. Ultimately, the model is tuned with more than 500k elements.

The analysis is performed in a steady-state laminar regime with the ANSYS CFX module to solve the discretized Navier-Stokes equations [46–48] within the domain. The choice of laminar flow is based on the fact that the Reynolds number (Re) is very low in this case, $Re = \frac{\rho|\vec{v}|L}{\mu} \simeq 150$, where L is the characteristic linear dimension (length traveled by fluid), μ the dynamic viscosity of the fluid. Boundary conditions in terms of mass flow are applied to the inlets and outlets; the walls are considered as having no-slip flow.

We simulate the gas flow behaviour inside this (enlarged) GE1/1 chamber geometry with a

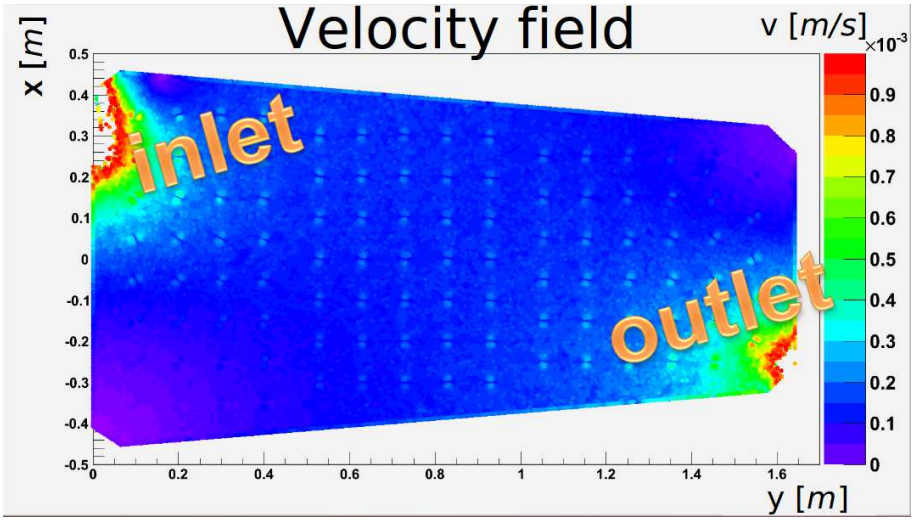

Figure 2.49: Gas flow distribution inside a (somewhat enlarged) GE1/1 detector volume with one inlet and one outlet according to ANSYS simulation. The effect of the GEM foil stack is ignored here. The butterfly-shaped regions of higher flow are an artifact in the simulation due to the overall very low gas flow velocity.

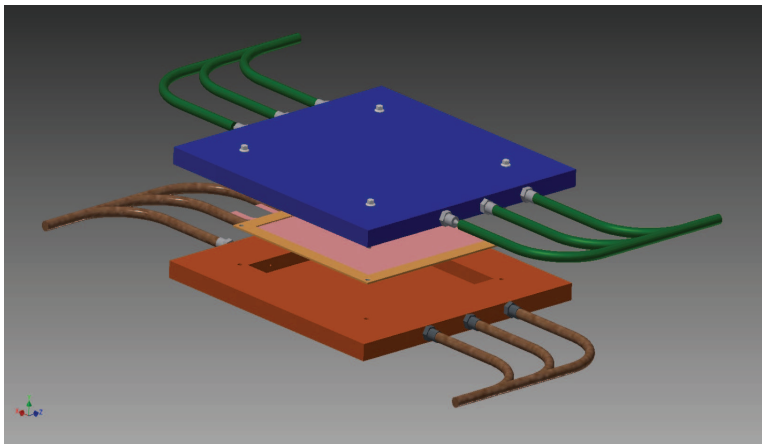

Figure 2.50: Setup for measuring the gas flow through the GEM holes.

single inlet and a single outlet on diagonally opposed corners (see Figure 2.49). The gas flows broadly diagonally and creates two areas with lower velocity fields near the corners without inlet or outlet. However, we still find laminar flow in those areas and we expect that the presence of the GEM stack will redirect more gas flow towards those corners. This justifies adopting this simplest possible internal gas distribution for the GE1/1 design.

The gas volumes inside the GEM stack, i.e. between GEM foils, are directly accessible to gas flow and gas diffusion via the gaps between the eight sections of the inner gas frame and through the GEM holes. Gas flow through GEM holes was verified experimentally with a simple test. The two halves of a $10 \times 10 \times 1$ cm^3 volume are separated by a septum made from a GEM foil (see Figure 2.50). The gas inlets are organised in such a way that it is possible to flush two different gases into the two halves. The gas outlets also collect the gases of the two halves separately. The two outgoing gases are sent to a gas chromatograph (GC) for analysis. With this arrangement, it is impossible that the two gases mix unless they flow or diffuse through the GEM holes. In the test Argon and CO_2 flowed into the chamber with a flow rate such that the volume had an overpressure of about 5 mbar, similar to the one expected in the GE1/1 chambers. The result of the GC gas analysis shows that the output gases in both halves are basically a perfect Ar/CO_2 50:50 gas mixture. This mixture is found right from the start of flushing, which indicates that the mixing is mainly due to flow and not due to diffusion. This demonstrates that the gas mixture can freely flush the whole GE1/1 gas volume with the GEM foils presenting no significant obstacle to the flow.

2.3.6 On-chamber HV distribution to GEM foils and drift electrode

The electrical HV connections to the GEM foils are made via spring-loaded pins (see Figure 2.51) that are soldered onto the drift board (see Figure 2.43) and that push against corresponding connection pads on the GEM foils (see Figure 2.31). For the HV pins to reach GEM foils 2 and 3, the corresponding connection pads are cut out of GEM foil(s) 1 and 2 during assembly. The drift electrode is powered directly off of the HV line that enters the drift board (see Figure 2.43). Below we discuss two basic schemes for powering all seven electrodes (drift electrode plus two sides of each of the three GEM foils) of the GE1/1 with HV.

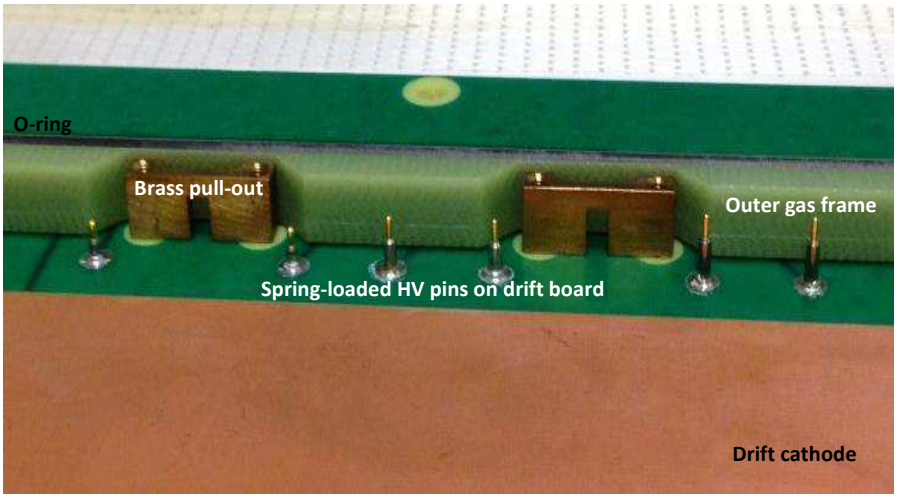

Figure 2.51: Six spring-loaded pins are soldered to the drift board for making electrical HV connections to corresponding contact pads on the GEM foils. Note that the three pairs of pins have different heights so they can properly reach the three GEM foils. Shown here is the arrangement for the GE1/1-V prototype.

2.3.6.1 Single-line HV input plus voltage divider

A simple voltage divider has been used very successfully during the R&D phase of the project to produce the seven needed potentials directly on the chamber (see Figure 2.52). The voltage is divided down from one HV input line that provides the drift potential, i.e. the most negative potential. The design of the voltage divider evolved from a large board with discrete resistors to a small ceramic device with single-inline pin (SIP) configuration that is soldered onto the drift board (see Figure 2.53). The current through the divider chain produces a voltage drop across every resistor which creates the electric potentials needed to power the elements of the detector. The electric fields produced with the HV divider in the various inter-electrode gaps of the triple-GEM detector can be easily calculated from $E_{gap} = \frac{I_{div}\,R}{x}$, where I_{div} is the divider current, R is the resistance across the gap in question, and x is the corresponding gap distance.

The advantage of this design is its simplicity. Only one channel of an HV power supply is needed to power the entire chamber via a single cable. The power supply has to supply about 800 μA of bias current I_{div} that flows through the HV divider. The strong disadvantage is that if a single HV segment on one of the GEM foils develops a short, e.g. due to a discharge, then the corresponding resistor on the HV divider and consequently the entire GEM foil is shorted out since all HV segments are connected to one pin on the HV divider. This kills the gain on that GEM foil and renders the entire chamber unusable. When such an incident occured during the R&D phase and the short on a GEM foil could not be fixed, then typically the protection resistor on the offending HV segment was removed to isolate that segment so that the rest of the chamber could still be operated. Obviously, this kind of a remedy is not practical for the full GE1/1 system as it required opening the chamber. Instead, the HV powering system must be designed so that it is robust enough to inherently tolerate single-segment HV shorts so that it can keep operating without any intervention. This can be achieved with multiple-line HV input to the chamber.

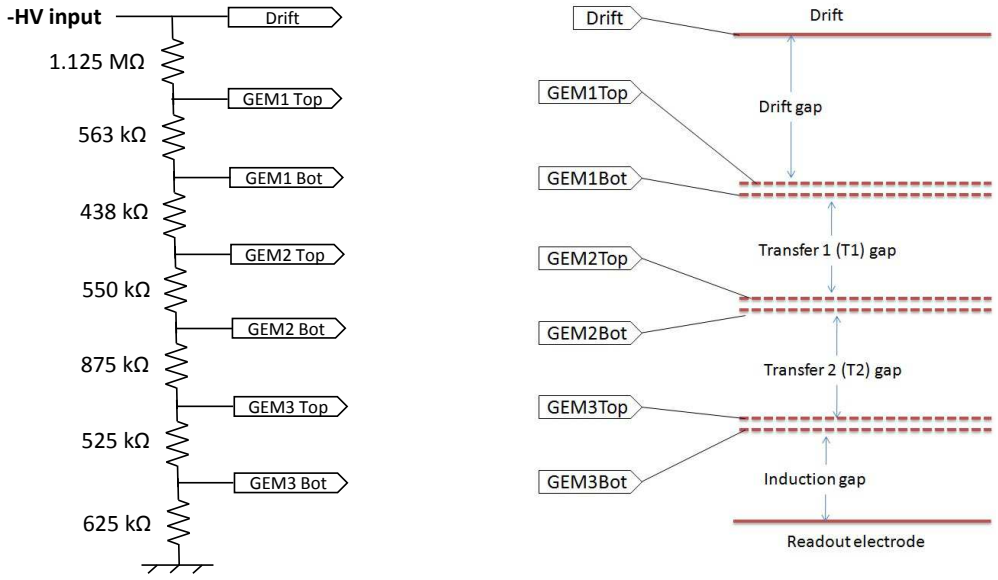

Figure 2.52: HV divider circuit diagram (left) for the 3/1/2/1 mm gap configuration and corresponding connections to GE1/1 chamber electrodes (right). Note that additional 10 MΩ protection resistors are located on the segmented sides of all GEM foils.

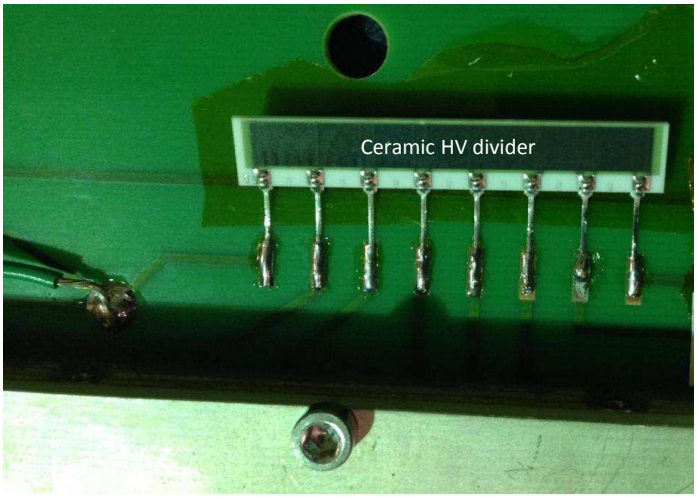

Figure 2.53: Miniaturized implementation of the HV divider on a ceramic substrate with single-inline pin configuration soldered onto the drift board of a GE1/1-III prototype.

2.3.6.2 Multiple-line HV input for production chambers

In this case, the seven required potentials are brought on individual HV lines to the drift board and routed on-board to the drift electrode and GEM foils (see Figure 2.54). This requires installation of an additional multi-pin HV connector on the drift board. Seven HV cables must be routed from each chamber to a HV distribution board.

This power configuration imposes two important requirements on the HV supply system. In case of a short in one HV segment of a GEM foil, the HV supply system must be able to sustain the voltage across that foil and simultaneously provide the current that is then flowing through the 10 MΩ protection resistor on the shorted HV segment. This will allow continued operation of the chamber despite the presence of a short in one (or more) segments. The second requirement is that the ramping (up or down) of the potentials on the two sides of all GEM foils that are now provided independently by different HV channels is very well synchronized, monitored, and safe-guarded so that the voltages across the GEM foils can never exceed a maximum given value (about 500V) – even for a very short time. Otherwise, even a brief temporary overvoltage could lead to sparking across the GEM foils that could destroy it. Designs of the HV supply and distribution system that address these concerns are discussed below in the section on power systems in Chapter 7.

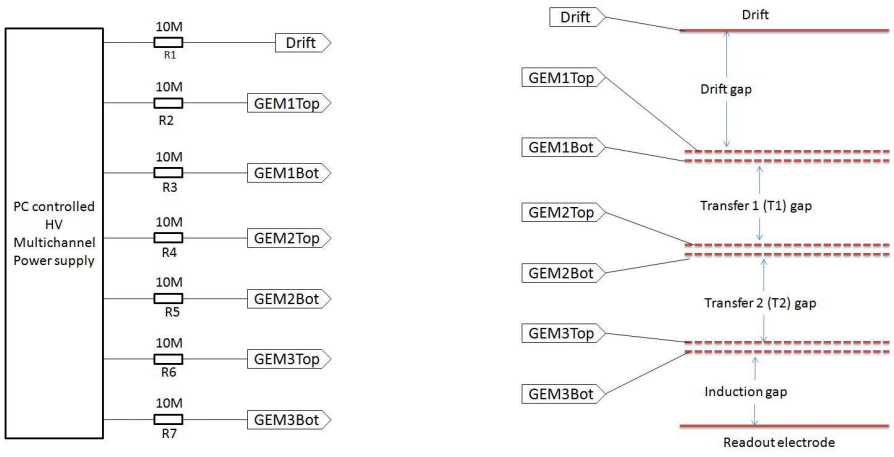

Figure 2.54: Multi-channel HV supply (left) and corresponding connections to chamber electrodes (right). Note that the 10 MΩ protection resistors are located directly on the GEM foils.

Chapter 3

Electronics

3.1 Electronics system overview

This chapter focuses on the hardware used for the treatment and readout of the detector signal from this starting point through the data acquisition system (DAQ) to the interface with CMS.

A block diagram of the main system components in the signal/control path is shown in Figure 3.1.

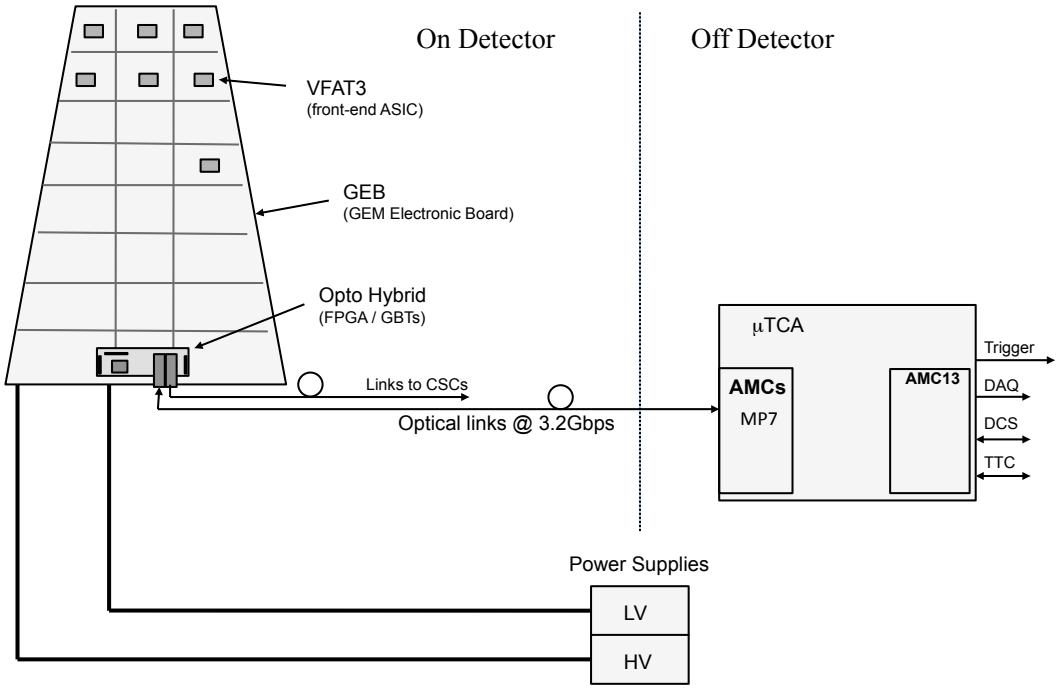

Figure 3.1: The GEM electronics readout system.

The block diagram illustrates the main system components for the readout of a single GEM chamber and is divided into 2 main regions, namely On-Detector and Off-Detector. Visible in the On-Detector part is the division of the GEM chamber into 24 sectors. The 128 strips from each sector are connected to the inputs of the front-end ASIC (VFAT3) via a connector on a

board known as the GEM readout board. The VFAT itself is mounted on a hybrid which plugs into the GEM Readout Board connector. The control, readout and power to/from the VFAT hybrid is delivered via electrical signals (E-links) running through a large flat PCB known as the GEM Electronic Board (GEB). An opto-hybrid board also plugs into the GEB which contains the GigaBit Transceiver (GBT) chip set, an Field Programmable Gate Array (FPGA), as well as optical receivers and transmitters to provide the link to the Off-Detector region.

There are two optical paths to the opto-hybrid. The first is bidirectional and runs between the micro-TCA crates located in the counting room and the opto-hybrid. This path is used for sending set-up and control signals to the front-end chips. The return path is used for the VFAT3 tracking and trigger data packets as well as to return slow control data. The second path is unidirectional and takes the VFAT3 fixed latency trigger data from the GEM system to the Cathode Strip Chamber (CSC) system.

The two data paths are illustrated in Figure 3.2.

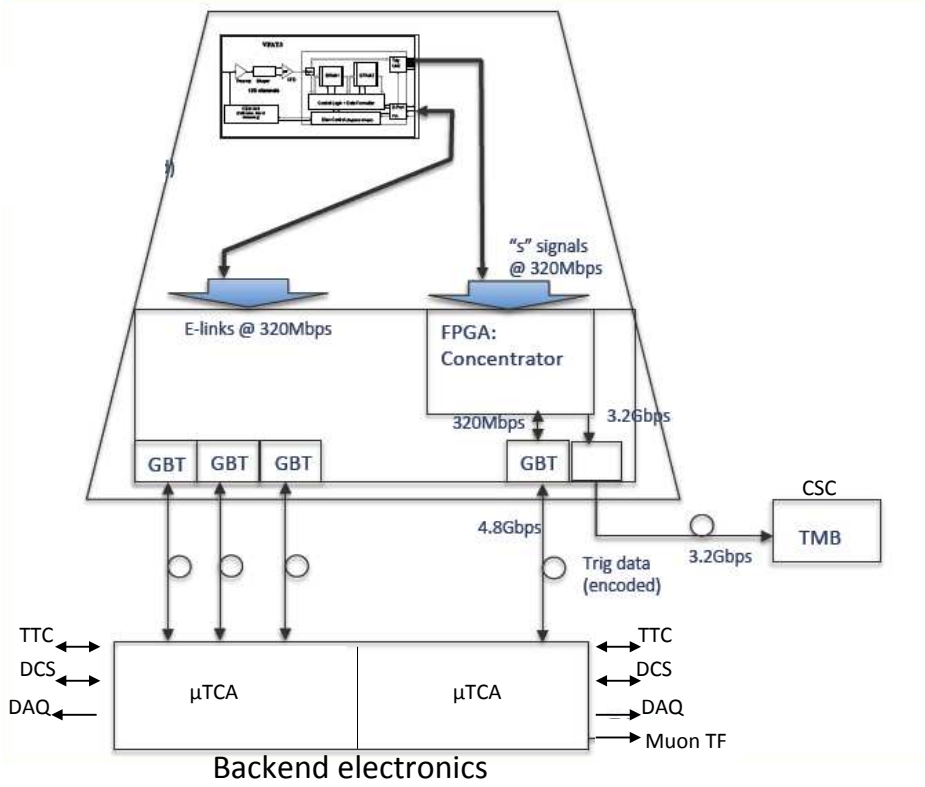

Figure 3.2: Block diagram of the system showing the tracking and trigger paths (detail of inset is given in Figure 3.3).

3.2 The VFAT3 front-end ASIC

The GEM detectors will be used to provide information relevant to triggering and tracking. The VFAT2 chip was used within the TOTEM experiment for the readout of GEM detectors. The requirements within TOTEM also necessitated tracking and triggering functionalities within the front-end chip. The VFAT2 architecture consisted of 128 channels continuously sampling the GEM strips. Its outputs provided "fast OR" fixed latency trigger information grouping together 16 channels at a time and also full granularity tracking information after the receipt of a level 1 trigger. The requirements of GE1/1 are similar, but there are some important differences that necessitate a new ASIC design. The most fundamental changes are the following:

- Charge readout: The signal charge delivered from a GEM detector on the passage of an ionising particle has a duration of $\approx$ tens of ns depending on the exact gas mixture used. The VFAT2 has a fixed shaping time of 25 ns which is much shorter than the duration of the signal. This results in a ballistic deficit. The VFAT3 is being designed with a programmable shaping time to be able to integrate all the signal charge. The result will be an increased signal to noise ratio compared to the VFAT2.
- Timing resolution: The timing resolution is dominated by the properties of the GEM detector. Since this is a very important parameter for optimal trigger performance; the electronics must process the charge delivered without degrading the intrinsic detector timing resolution. The VFAT2 achieves this by acting on the rising edge of the GEM charge signal with a short (25 ns) shaping time. The VFAT3 will have the option to operate in this mode or extend the shaping to integrate all of the charge and therefore boosting the signal to noise ratio. In this later case the timing resolution would normally be degraded due to time walk of a comparator. The VFAT3 is being designed to compensate for this effect and maintain the timing resolution at the level given by the detector itself.
- Trigger granularity: The VFAT2 had a trigger granularity of 16 channels. The specification for GE1/1 is a trigger granularity of 2 channels. The VFAT3 will hence be designed for this increased granularity specification.
- Level 1 Latency: The level 1 trigger latency within CMS will be increased. The VFAT2 was designed for a Level-1 accept (L1A) latency of 3.2 μs (with a maximum programmable latency up to 6.4 μs. The VFAT3 will increase the latency capability to beyond 12.5 μs. This complies with the requirements from the CMS trigger upgrades.
- Level 1 trigger rate: The trigger rate within CMS will be increased. The requirement being asked is possible L1A rates to a maximum of 1 MHz. The VFAT2 can cope with L1A rates up to 200 kHz. The important parameter here is the length of time needed for the readout of a data packet and the depth of the buffer for trigger data. The VFAT3 interface will run at 320 Mbps, which is a factor 8 faster than the VFAT2. In addition, the VFAT3 will have many programmable options to significantly reduce payload. This will result in a much increased data throughput going well beyond the CMS specification.
- VFAT3 is also being designed to be compatible with other system components foreseen for the CMS upgrades. Of particular importance is the GBT which communicates directly with the front-end chip. VFAT3 will have direct compatibility with the GBT interface.

The most basic requirements for the front-end ASIC are summarized here:

- 128 channel chip
- Read positive and negative charges from the sensor
- Provide tracking and trigger information
- Trigger information: Minimum fixed latency with granularity of 2 channels
- Tracking information: Full granularity after L1A.
- L1A capability: L1A latency beyond 12.5 μs
- Time resolution of less than 7.5 ns (with detector).
- Integrated calibration and monitoring functions
- Interface to and from the GBT at 320 Mbps
- Radiation resistant up to 100 MRads (radiation hardness of up to 1 MRad is sufficient for the GE1/1 application through Phase-II)
- Robust against single event effects

The block diagram for VFAT3 is shown in Figure 3.3.

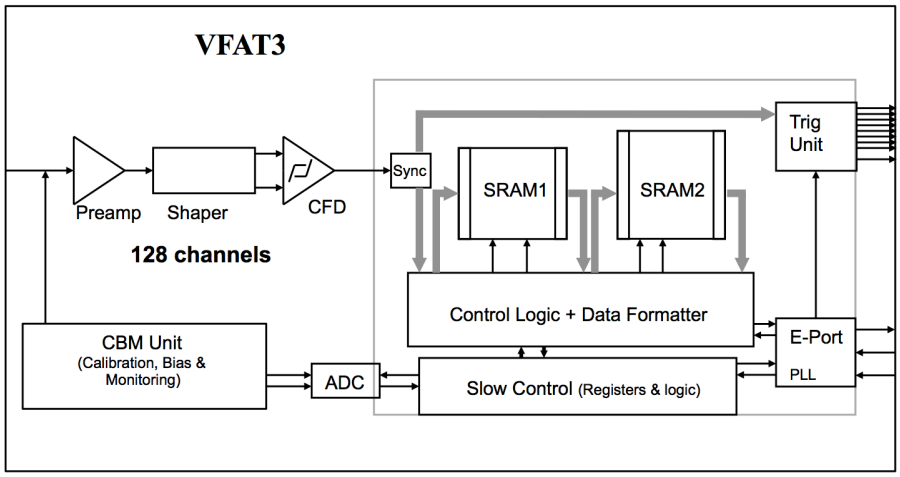

Figure 3.3: VFAT3 block diagram.

The VFAT3 architecture is composed of 128 channels, each comprising a charge sensitive preamplifier and shaper. This is followed by a constant fraction discriminator per channel. Following the discriminator is a synchronization unit which synchronises the comparator result with the 40 MHz clock. The data then splits into two paths, one with a fixed latency for trigger signals, and the second for tracking data which is non-synchronous. All communication with VFAT3 occurs through the E-port. This includes synchronisation to the LHC clock, slow control commands as well as fast trigger commands, data packets, calibration and monitoring. The chip is highly programmable to offer maximum flexibility. The sections below highlight the main characteristics and options.

3.2.1 The analog front-end

The analog front-end is optimized for the readout of gaseous detectors (and in particular GEM) but could also be used to read out silicon detectors. The front-end preamplifier and shaper are programmable to offer flexibility when connecting to detectors of different capacitances and charge characteristics. Each channel contains internal input protection to offer robustness to charge (discharge) spikes. The front-end specification is shown in Table 3.1 including a list of the programmable options.

Table 3.1: Main specifications of the analog front-end.

Key parameter	Comment
Detector charge polarity	Positive and Negative
Detector capacitance range	5 - 80 pF
Peaking times (T_p)	25, 50, 75, 100, 200 ns
Programmable gain	1.25 to 50 mV/fC
Max dynamic range (DR)	Up to 200 fC
Linearity	$<$ 1% of DR
Power consumption	2 mW/ch
Power supply	1.5 V
ENC	$\approx 1100e$ (with T_p=100 ns, $C_d = 30\ pF$)
Technology	130 nm CMOS

Signal charge from GEM detectors can last for approximately 60 ns or so depending on the gas mixture (see Figure 2.27). The shaping time of the front-end can be adjusted to fully integrate this charge and hence maximize the signal to noise ratio. Optimum timing resolution is maintained by the use of a CFD. Simulations show that the overall timing resolution can reach around 7 ns with shaping times of 50 ns or more. The spread from chip to chip will be very small, expected around the % level.

The calibration system provides internal charge pulses to the input of the front-end preamplifier. The magnitude, phase and polarity of the charge pulses are programmable. The channel to which the charge is injected is also programmable. This feature helps significantly in the production test and characterisation stage as well as the detector setup and commissioning stage. The functionality has two modes, one that injects a quick charge pulse (similar to a delta pulse) and another that injects charge via a constant current for a programmable length of time.

3.2.2 Variable latency data path

The block diagram for the variable latency data path is shown in Figure 3.4.

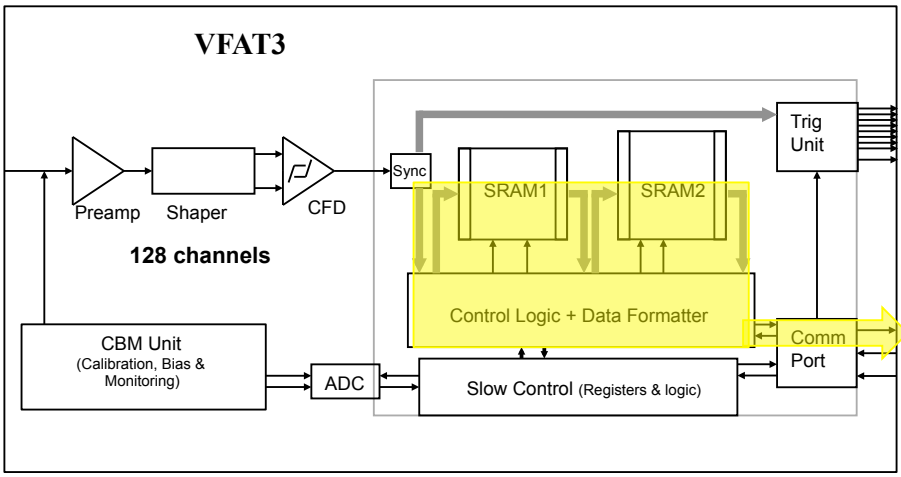

Figure 3.4: The VFAT3 block diagram with the variable data path highlighted.

This path is used for transmitting full granularity information via the E-port. The data rate is reduced by the application of a trigger arriving with a fixed latency. For operation in LHC for tracking data, this trigger is the L1A. The data transmitted therefore have to be accompanied via

a time-stamp to identify the bunch crossing (bx) associated with the data. The SRAM memories are sized to satisfy the L1A maximum latency and rate specifications.

3.2.2.1 Data formats

For the variable latency path there are two data types. The first is lossless and it is used to transmit full granularity information. The second is SPZS (sequential partition zero suppression) which has a reduced size.

An important concept for the data packet description is the use of control characters (CC) as headers. Encoding in the E-Port allows the use of unique CC that can act as data packet headers and inform the receiving DAQ system what type of data it is receiving.

The VFAT3 chip will be configurable in order to be able to switch between the two options. Lossless will be very important during the debugging and the commissioning stage. Another configurable setting of the VFAT3 chip is the number of time slots sent per L1A. This feature, also very important for timing and synchronization, can only be sustained with the SPZS mode when the CMS L1A will be increased beyond 100 kHz.

3.2.2.2 Data type: lossless

The lossless data packet style is derived from the VFAT2 data packet, but is optimized in terms of content.

Table 3.2: The VFAT3 lossless data packet.

Data packet	No. Bits
Header I/ Header IW	8
EC+BC/EC/BC	8-48
Data	128
CRC	16

The lossless data packet structure is shown in Table 3.2. A unique CC acts as a header identifying the start of the packet. The time-stamp is next in the form of an event counter (EC) and bunch counter (BC) numbers. This is followed by a data field which has 128 bits for the 128 channels. A logic 1 represents a hit in that channel. If 1 or more channels are hit, there is no further attempt to zero suppress the data. The final piece of information is the cyclic redundancy check (CRC) to confirm the integrity of the data packet.

The data packet size and content are programmable. Options exist to vary the number of bits in the time tags EC and BC. It is also possible to suppress the entire data field if no channels are hit. Indeed a further possibility is to suppress the entire data packet if no hits are registered and transmit only the header to acknowledge receipt of the trigger.

This data packet structure allows all VFAT3s to operate synchronously sending data packets regardless of their content or to have a data driven operation where data packets are sent only when registering hits. Since most of the chips will record nothing in any given bunch crossing, the latter option optimizes bandwidth enormously. Each chip, however, even in the minimum setting, will respond to an L1A trigger by sending at least a CC to acknowledge receipt of the trigger signal and also report that no hits corresponding to this trigger are present.

3.2.2.3 Data type: SPZS

The SPZS style incorporates zero suppression and is a variant on the CMS RPC data format. In this case the size of the data packet is a function of the number of hits in the chip. This enables very small data packets and hence the highest possible data transmission rate. This is very good for operation at high trigger rates.

The principle is as follows: The 128 channels are divided into 16 partitions, each containing eight channels. For each event, only the partitions containing data will be transmitted. If the overall occupancy is low, there will be a bandwidth saving on the payload transmitted per event.

Table 3.3: The SPZS Data Packet.

Data packet	No. Bits
Header I/ Header IW	8
EC+BC/EC/BC	8-48
Data	16-144
CRC	16

The SPZS data packet is shown in Table 3.3. It is the same form as the lossless data packet with the same programmable options relating to the time tags and the full suppression of the data field in the case of no hits. However, the data field follows the SPZS sequence. The SPZS sequence is shown in Figure 3.5. It starts with a partition list of 16 bits, each bit representing a partition. A 1 represents a hit in that partition. The partition list is then followed by the channel list. If 1 partition is hit then the channel list is 8 bits long, if 2 partitions are hit then it is 16 bits long, etc. The order of the sequence is always MSB first for both the partition list and the channel list.

The maximum number of partitions allowed is a programmable parameter.

3.2.3 Fixed latency trigger path

The fixed latency path is highlighted in Figure 3.6. The purpose is to provide fast hit information that is synchronous with the LHC 40 MHz clock. The hit information can then be put in coincidence with other detectors (such as the CSCs) to build CMS muon triggers. There are 8 SLVS (scalable low-voltage signaling) pairs, which are used to transmit 64 bits/bx . The format can be programmable to have trigger information based on a fast OR of channels or using the SPZS format. A bandwidth of 64 bits/bx allows the transmission of the fast OR signals of 2 channels or the full granularity information for up to 6 hit partitions with the SPZS data format.

3.2.4 Slow control

Slow control defines configuration of operational parameters permitting the writing and reading of internal registers which in turn provides the functions of programmability and monitoring.

VFAT3 uses the E-port for all data communication including the slow control. The use of CC in the E-port allows slow control commands and data to be distinct from all other commands and data fields. This is achieved by having two slow control CCs, one for communicating a slow control 0 and the other for writing a slow control 1.

Partition List	Channel Correspondence
p15	<127:120>
p14	<119:112>
p13	<111:104>
p12	<103:96>
p11	<95:88>
p10	<87:80>
p9	<79:72>
p8	<71:64>
p7	<63:56>
p6	<55:48>
p5	<47:40>
p4	<39:32>
p3	<31:24>
p2	<23:16>
p1	<15:8>
p0	<7:0>
Channel List of 1st partition in the partition list. 8b <msb:lsb>	
Channel List of 2nd partition in the partition list. 8b <msb:lsb>	
etc	

Figure 3.5: The SPZS data field sequence.

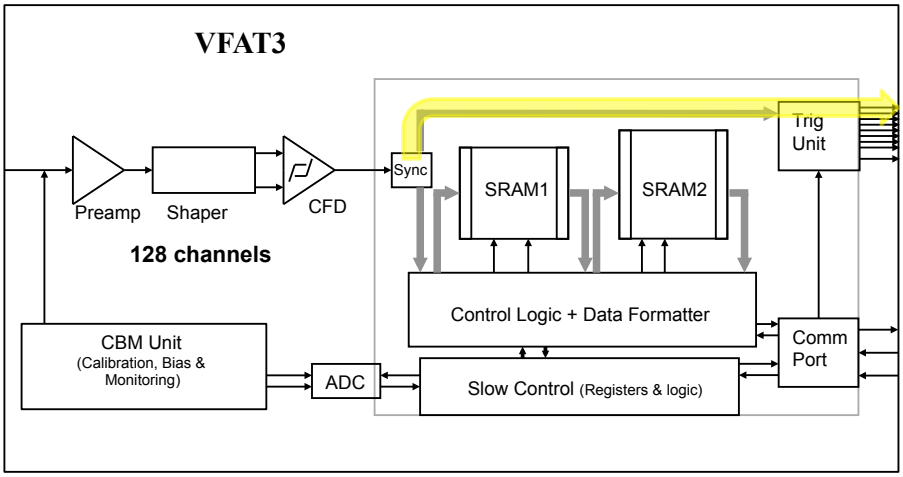

Figure 3.6: The VFAT3 block diagram with the fixed latency trigger path highlighted.

The slow control protocol adopts the IPbus protocol [49] (standard within CMS upgrades) and wraps this within the HDLC protocol. This ensures correct chip addressing and error checking of slow control packets. Reception and transmission of slow control commands/data must take *low* priority when compared to real data traffic. It is therefore possible to start and stop the slow control communication in mid-flow and resume when the E-port is free. The maximum allowable slow control communication rate is 40 Mbps.

3.3 The GEM electronic board

The GEM chamber (complete with readout electronics) fits into a very narrow slot where the mechanical constraints are very tight. The limited space means that running individual flat cables to each VFAT3 hybrid is not possible. As a result, the GEM electronic board (GEB) was designed to provide the electrical link between VFAT3 hybrids and the opto-hybrid within the limited space available.

Fabricated as a single large multilayer PCB, the GEB is a crucial element in the design of the GEM detector readout system. There are three main functions: (1) to carry electrical signals between the front-end chips and the opto-hybrid board; (2) distribute power; and (3) provide electrical shielding to the detector. The GEB is placed on top of the GEM readout board as shown in Figure 3.7.

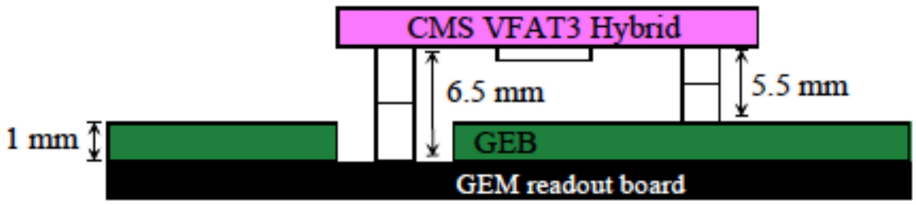

Figure 3.7: Schematic cross-section of the GEB placed on top of the GEM readout board. One VFAT3 hybrid and its connections to the GEB and the GEM readout board is also shown.

The GEB board is a 1 mm thick 6-layer PCB. The lowest layer is grounded and acts a shield preventing the EMI created by the switching of the digital electronics from interfering with the analog low-level signals on the GEM readout board. The top layer hosts the connectors and the SMD components. The other layers are used for the signal routing and powering.

A first version of the GEB board has been manufactured and tested. The prototype has the size of a long GE1/1 detector. Manufacturing with 6 layers was found to be feasible and cost effective. Electrical measurements have been done to characterize the signal integrity at 40 MHz and the functionality of the GEB board with the VFAT2 hybrids has been tested successfully. Figure 3.8 (left) shows the layout of the second version of the GEB board. For clarity only a few signal lines are shown. The first version-2 GEB boards have been delivered to CERN in January 2015. Figure 3.8 (right) shows a picture of the first version of the GEB board with a couple VFAT2 hybrids mounted on it.

3.4 The opto-hybrid and optical links

The opto-hybrid consists of a mezzanine board mounted along the large side of the GEB board, with typical dimensions of 10.0 cm $\times$ 20.0 cm $\times$ 1.1 cm. The tasks of the opto-hybrid board are to synchronize the data sent by the VFAT3 chips, zero-suppress the trigger data, encode the data and send them via optical links to the trigger electronics. The opto-hybrid, of which the

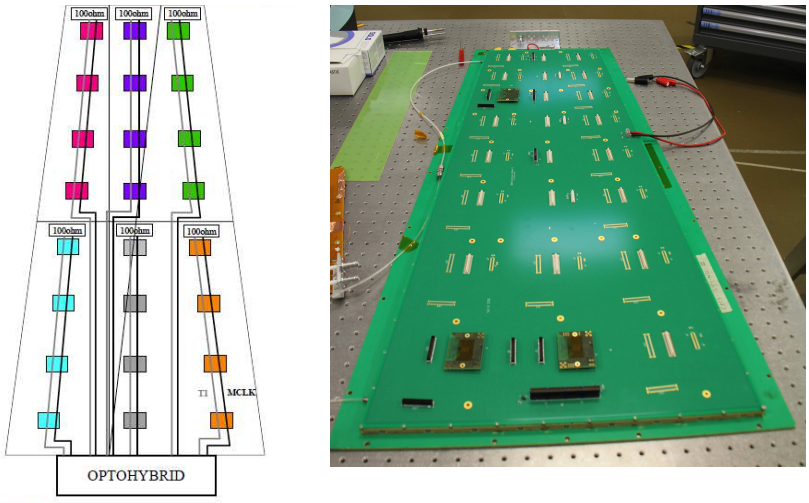

Figure 3.8: *Left:* Layout of the GEB board version 2. First boards have been delivered to CERN in January 2015. *Right:* A picture of the GEB board version 1.

schematic of a prototype is shown in Figure 3.9, is composed of an FPGA, 3 GBT chipsets and 2 optical connectors of type SFP+ (small form factor pluggable) or a Quad-SFP (QSFP).

3.4.1 The gigabit transceiver and the versatile link

The CMS GEM readout system includes the use of the GBT and Versatile Link technologies under development at CERN [50]. These technologies are tolerant to radiation up to 200 Mrad, which is several order of magnitude greater than the expected GE1/1 exposure levels. The GBT is an optical data link technology providing bidirectional 4.8 Gb/s serial communication with the capability to receive parallel data with an arbitrary phase at the 40 MHz LHC frequency, or at multiples of 2, 4, 8. Additionally, the GBT can recover the frame clock, reduce the jitter from an input clock, and distribute phase-controlled clock signals. The data rate (bandwidth) available is lower than the 4.8 Gb/s line rate, and depends on how the GBT is configured. For the CMS GEM project the data bandwidth will reach 3.2 Gbps.

The GBT Transceiver (GBTX) will work as a full link transceiver with bidirectional data communication with the front-ends and the counting room. The GBTX delivers the global system clock reference, which comes from the counting room, to all front-ends. The communication with the VFAT3 chips is made through sets of local Electrical Links (E-Links). Depending on the data rate and transmission media, the E-links connections can extend up to a few meters. E-Links use SLVS, with signal amplitudes that are programmable to suit different requirements in terms of transmission distances, bit rate, and power consumption. The E-links are driven by the E-Ports that are integrated into the front-end chips.

The optical link will simultaneously carry readout data, trigger data, timing information, trigger and control signals, and experimental control data that must be transferred with very high reliability. To ensure error free data transmission at high data rates in a harsh radiation environments, the GBT adopts a robust line coding and correction scheme that can correct bursts of bit errors caused by single event upsets (SEU).

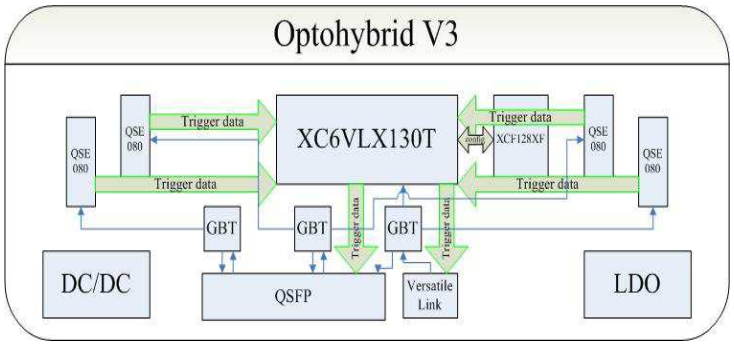

Figure 3.9: Schematic drawing of the opto-hybrid board. For the prototype the XC6VLX130T FPGA has been chosen.

This is important because a single bit error in the control path can affect many readout channels for many clock cycles. In this mode, the GBT system can be configured over the GBT link itself. The counting room electronics will use the LHC clock to transmit commands to the VFAT3 chips and the opto-hybrid; the GBTX will recover the LHC clock and provide it as a system clock for the entire front-end electronics.

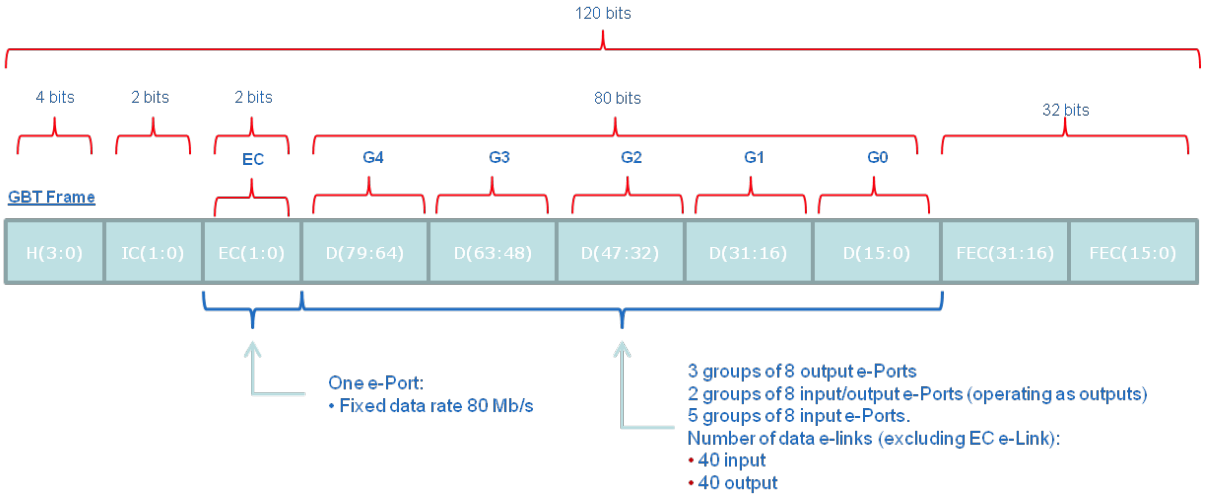

Figure 3.10: The GBT frame format.

Figure 3.10 represents the GBT frame format consisting of 120 bits transmitted during a single LHC bunch crossing interval (25 ns) resulting in a line rate of 4.8 Gbps. Four bits are used for the frame Header (H) and 32 are used for Forward Error Correction (FEC). This leaves a total of 84 bits for data transmission corresponding to a user bandwidth of 3.36 Gb/s. Of the 84 bits, 4 are always reserved for Slow Control information (Internal Control (IC) and External Control (EC) fields), leaving 80 bits for user Data (D) transmission. The D and EC fields are not

assigned, and can be used for DAQ, Timing Trigger & Control (TTC), or Experiment Control (EC) applications. DC-balance of the data being transmitted over the optical fiber is ensured by scrambling the data contained in the SC and D fields. For FEC, the scrambled data and the header are Reed-Solomon encoded before serialization. The 4-bit frame header is chosen to be DC-balanced.

3.4.2 Trigger path to the CSC

The trigger data will be sent in parallel to the CSC trigger mother board (TMB) and combined with the CSC data to improve the Level-1 trigger efficiency of the CSC system. To send the trigger data to the CSC TMB we will use the existing optical fibers currently used by the CSC detectors inside CMS. However, these fibers cannot sustain the GBT protocol so, the 8B/10B protocol will be used instead. The GEM-CSC data flow is described in section 4.3.

3.5 The back-end electronics

The back-end Electronics provides the interfaces from the detector (and front-end electronics) to the CMS DAQ, TTC and Trigger systems. The design foreseen for the CMS GEM off-detector electronics is based on FPGAs and Multi-GBit/s links that adhere to the micro-TCA (μTCA) standard. Micro-TCA is a recent standard that has been introduced for the Telecom industry and aims at high data throughput (2 Tbit/s) and high availability (with very low probability of interruption at $\approx 10^{-5}$). It is compact, hot swappable and has a high speed serial backplane. The μTCA is now a common standard for all the CMS upgrades and will replace the VME electronics.

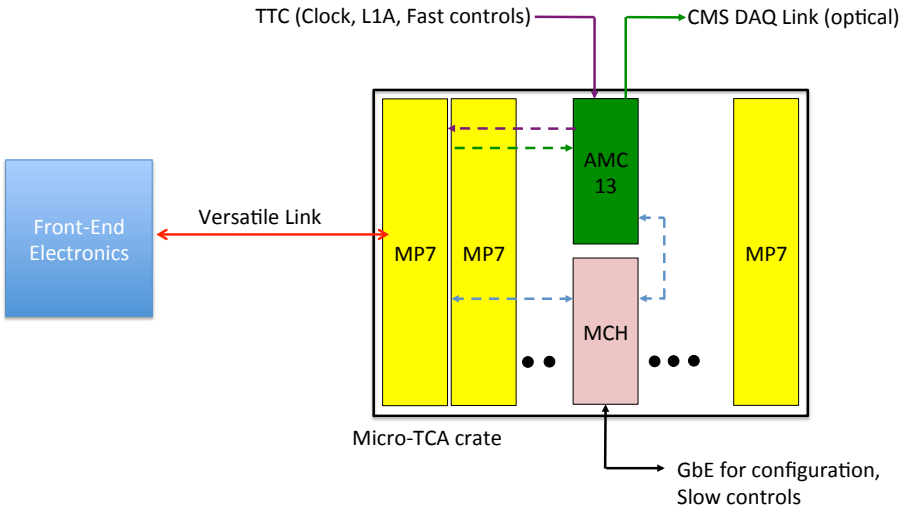

Figure 3.11: Layout of the back-end electronics μTCA crates.

The CMS GEM off-detector electronics, shown in Figure 3.11, consists of the preferred CMS μTCA crate, the VadaTech VT892, which supports 12 double-width, full-height AMC cards and two μTCA Carrier Hub (MCH) slots. The MCH1 slot houses a commercial MCH module, which provides gigabit Ethernet (GbE) communication and control using the IPMI protocol.

The MCH2 slot houses a custom MCH developed by Boston University and called AMC13. The AMC13 is the standard module within CMS to interface the μTCA crates to the CMS data acquisition system and to provide the CMS Trigger Timing and Control (TTC) signals downlink.

The AMC cards that will equip the μTCA crates will be the MP7 (Master Processor) card developed by Imperial College, London. The MP7, based on the Xilinx Virtex-7 FPGA and Avago MiniPOD optical modules, can provide 72 optical transceivers and 72 optical receivers, capable of operating above 10 Gbps. Eight MP7 boards, which are hosted within one micro-TCA crate, are needed to readout the entire GE1/1 system.

For the optical link between the opto-hybrid and the MP7 boards, the GBT protocol will be used for data transmission over (48 way) Mutlifiber Termination Push-On (MTP) cables.

Chapter 4

Data Acquisition and Trigger

4.1 Introduction

This chapter focuses on the trigger and tracking data flow from the front-end electronics to the muon trigger and the CMS DAQ system. This chapter also presents the expected data rate and latency on the different data paths. We also describe the firmware and software environment as well as the interface between the GEM readout system and the CMS DAQ.

4.2 Tracking data flow

Upon a Level-1 accept (L1A) signal, the full granularity data stored in the VFAT3 SRAM2 memories will be formatted by the Data Formatter and sent out by the chip through the E-port towards the GBT chipset. One GBT chipset will read out 8 VFAT3 chips. The format and content of the data packets has multiple options and are described in Section 3.2.2.1. In the case of the basic lossless data format, the data rate per optical link will amount to less than 200 Mbps at an L1A rate of 100 kHz (see Section 4.4).

Note that the GBT is fully transparent to the user data being transferred. In the GBT chip, after phase alignment, the data coming from the VFAT3 chips through the E-ports is first processed by the scrambler, a 4-bit header is then added, the Reed-Solomon (RS) encoding and interleaving takes place and finally the data are serialized. While the scrambler maintains the word size, the RS encoder adds the 32-bit Forward Error Correction (FEC) field adding up to a total frame length of 120 bits. This leads to an overall line code efficiency of 84/120 = 70%. At the receiver end the inverse operations are repeated in the reverse order. There the tasks will be performed by the AMCs located in the μTCA crates (see Section 3.5).

As described in Section 3.4.1, each GBT data link will carry 80 bits of user data for every LHC bunch crossing. Each GBT link will handle the data of 8 VFAT3 as shown in Table 4.1. The Control Character indicates which data format is being sent. The possible data formats are described in Section 3.2.2.1. BC0 indicates that this sample is from the bunch with number zero in the orbit. This bit is used for latency/alignment of the data links. The packet number indicates the sample number.

Figure 4.1 shows the mapping of the optical links from the GEM detectors to the back-end electronics. Each MP7 can receive up to 72 high speed optical links, that is 24 GE1/1 chambers or 12 superchambers tracking data. In total, one GE1/1 endcap require 3 MP7 boards to readout the tracking data and 1 MP7 for the trigger data. The full GE1/1 data can be hosted by one μTCA crate.

The rate of the incoming GEM data per MP7 card will be $\approx$ 12 (120) Gbps at 100 (1000) kHz

Table 4.1: GEM data format for the GBT. The control character indicates which data format is being sent. BC0 indicates that this sample is from the bunch with number zero in the orbit (used for latency/alignment of the data links). Packet Nbr indicates the sample number.

Byte	7	6	5	4	3	2	1	0
0	Control Character							
1	Packet Nbr [6:0]							BC0
2	VFAT 0							
3	VFAT 1							
4	VFAT 2							
5	VFAT 3							
6	VFAT 4							
7	VFAT 5							
8	VFAT 6							
9	VFAT 7							

for the lossless data format. After data reduction, the DAQ data will be sent through the μTCA backplane from each MP7 board to the AMC13 board which will then transmit the data fragments to the CMS DAQ system. The DAQ capacity of the AMC13 amounts to three 10 Gbps links. Data reduction on the MP7 boards can be easily achieved by requiring the matching of hits in the two GEM detectors making one superchamber.

4.3 Trigger data flow

Each VFAT3 chip will send the fixed latency data (see Section 3.2.3), also called trigger data, to the frontend FPGA on the opto-hybrid board through 8 SLVS pairs resulting in the transmision of 64 bits per LHC bunch crossing per VFAT3, where each bit represents the logical 'OR' of two adjacent strips, also called a GEM pad. At an average particle rate of 10 kHz/cm^2, we expect 1.2 hit/bx per GEM chamber, which means that most of the bits will be '0'. On the front-end FPGA a finite state machine will look for non-'0' bits and encode the pad position in the following way: 6 bits (padId) + 2 bits (ϕ column) + 3 bits (η-partition) = 11 bits.

These trigger data will be sent by the frontend FPGA, through the GBT chipset, to a dedicated MP7 board host in the μTCA crate. On this board coincidences will be searched for using the trigger data coming from the superchambers. This will allow the rejection of noise hits and reduce the data volume. Indeed, simulations (see chapter 6) show that the photon and neutron backrgounds hit the two GEM detectors of a superchamber only in a couple of % of the cases. The local GEM trigger algorithm will therefore search for pairs of hits in coincidence in space and time within each superchamber using a LUT. The data will then be sent to the upgraded Muon Track Finder board (MTF7) [2].

A copy of this trigger data will be sent from the frontend FPGA to the CSC Optical Trigger Mother Board (OTMB) over two optical fibers, where it will be combined with the CSC data to improve the Level-1 trigger efficiency of the CSC system (see Section 6.2.1). The fibers needed for the transmission of data to the OTMB already exist as part of the current CSC installation and are located along the CSC detectors inside CMS. Since the CSC OTMBs do not support the GBT protocol, the 8b/10b protocol will be used instead, providing 48 bits/bx per fiber for data. Consequently up to 8 trigger hits per GEM detector can be sent to the CSC OTMB at each LHC bunch crossing (bx).

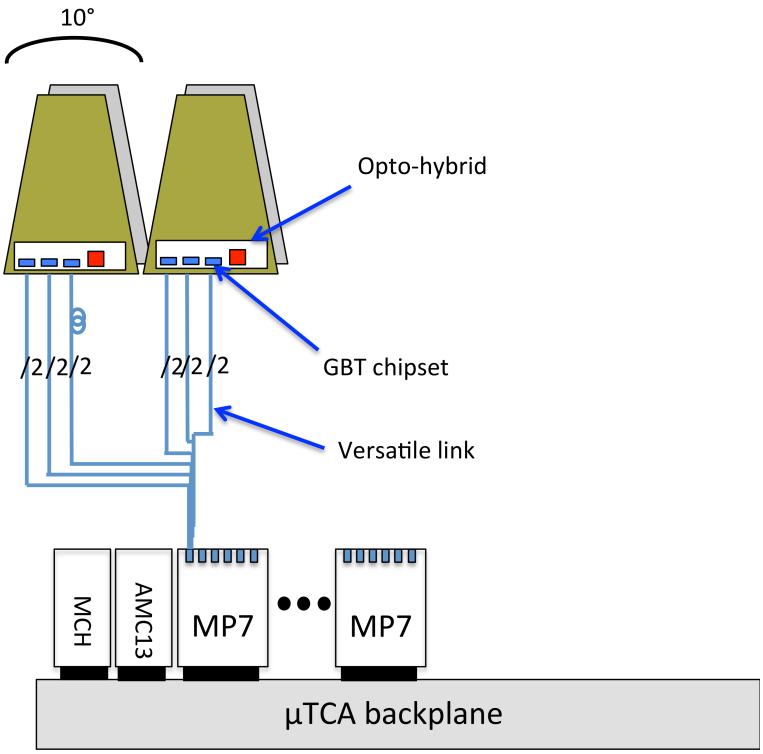

Figure 4.1: Mapping of the optical links for the tracking data. One MP7 can receive the data from 12 superchambers.

The GEM trigger data should arrive at the CSC OTMB within a latency of 17-18 bx. Table 4.2 shows the breakdown of the latency of the GEM-CSC trigger data path.

Table 4.2: Latency in bx of the GEM-CSC trigger data path.

Component	Latency (bx)
TOF	1 – 2
VFAT3	5
GEB	1
FPGA	2
SFP	5
Fiber (15 m)	3
Total	17 – 18

All Level 1 trigger primitives built in OTMB using GEM and CSC data will follow the usual CSC trigger path: from OTMB to the Muon Port Card (MPC) and further to CSC Track Finder (CSC TF).

4.4 Data rate simulations

In this section we present the estimation by simulation of the output trigger and tracking data rates of the opto-hybrid concentrator for several data formatting options and for LV1A rates of 100 kHz and 1 MHz. Those simulations are of importance to minimize data losses and compute the probability to reach the bandwidth limit of the optical links.

By design, the opto-hybrid is equipped with 3 tracking optical links, 1 trigger optical link, and

1 optical link which is connected to the CSCs OTMBs to communicate trigger information. Each link uses the GBT protocol with a maximum data bandwidth of 3.2 Gbps, except the link towards the CSC OTMBs, which has a maximum data bandwidth of 1.92 Gbps.

Using the averaged hit rate in the η-regions covered by GE1/1, dominated by the neutron and photon background (see Chapter 6), we simulate a number of hits, following a Poisson distribution, in the detectors and compute the size of the generated packet. For the trigger data packets, each hit pad (Fast OR of two neighboring strips) generates 11 bits of data (5 bits for the address of the VFAT3 on the GEB and 6 bits for padId in the VFAT3). For the tracking data packets, the VFAT3 flexibility allows the use of the lossless algorithm or the SPZS algorithm (see Section 3.2.2.1).

Table 4.3: Opto-hybrid output data rates in GE1/1 for L1A rates of 100 KHz and 1 MHz.

Algorithm	**Data rate (Gbps)**	**Probability of overcapacity**
Trigger Fast OR	0.05	$6x10^{-5}$ %
LV1A at 100 kHz		
Tracking Lossless	0.48	$< 10^{-7}$ %
Tracking SPZS	0.17	$< 10^{-7}$ %
LV1A at 1 MHz		
Tracking Lossless	4.8	$< 10^{-7}$ %
Tracking SPZS	1.73	$< 10^{-7}$ %

Table 4.3 lists the average data rates for GE1/1 for L1A rates of 100 kHz and 1 MHz. The probability that the links are used in overcapacity is defined as the fraction of L1A during which the transfered amount of data is larger than the allocated bandwidth, as calculated using the number of links described in the previous paragraphs.

The results show that in all cases the available bandwidth is sufficient to cope with the tracking data rates, while data losses on the trigger data might occur with a probability of 6 x 10^{-5} %. To recover those events, one could use the GBT in dual transmitter mode, thus doubling the bandwidth, or use a slightly more complex encoder.

To reduce the data losses, a modified trigger data encoder is also proposed where 1 bit is added to each packet to indicate the cluster size. With the unmodified algorithm, when two neighboring pads are hit, two packets are created. With the new encoder only one is formed. Using this new algorithm, the probability of overcapacity for the trigger links is lowered to $< 10^{-7}$ % for GE1/1.

4.5 DAQ firmware and software

4.5.1 MP7 and μTCA control

The μTCA standard does not specify any details of the communication between a control PC and an AMC beyond the low-level transport specification of gigabit Ethernet. The CMS Upgrade Working Group has adopted a standard protocol called IPBus [49] to provide a uniform solution for communication across all CMS upgrades which will use μTCA. The protocol defines a virtual A32/D32 bus on each Ethernet target and allows the programmer to pack multiple read, write, bit-set, and bit-clear operations into a single Ethernet packet. The base protocol uses the User Datagram Protocol (UDP) over the Internet Protocol (IP). The use of UDP rather than bare Ethernet allows development of control code with no specialized drivers or enhanced

machine access, i.e. standard user accounts and interfaces can be used for all purposes. The use of UDP/IP instead of TCP/IP greatly reduces the complexity of the implementation in the FPGA firmware of the AMC. Reliable delivery is ensured by a software server layer which manages multiple parallel requests for the same resources across multiple clients. The IPBus protocol and firmware module are supported by the Bristol University group.

4.5.2 Firmware

On each chamber, the front FPGA located on the opto-hybrid is responsible for synchronizing the trigger data from the 24 VFAT3, applying zero-suppression and transmitting the data to the CSC OTMB (see Section 6.2.1) and to the μTCA MP7 board. Once a Level 1 decision is issued the VFAT3 chips transmits the full granularity data associated to the event to the MP7 board through the GBT protocol. The FPGA of the MP7 boards will synchronize the data, apply the matching of pairs of hits in each superchamber for the trigger data, then transmit the trigger data to the Muon Track Finder or the full granularity data to the AMC13 through the μTCA backplane.

To handle the communication between the Detector Control System computer (DCS, see chapter 8) and the μTCA electronics, a dedicated IPBus slave will be implemented on the MP7 to translate the IPBus requests to a custom data format. The addresses used by IPBus to execute read/write operations will be mapped to the physical registers in the VFAT3 chips. Each IPBus slave will be connected to one optical link controller. The existence of firmware for the interface to the AMC13 as well as for the GBT core will allow the GEM developpers to focus on the GEM-specific firmware.

For the front FPGA located inside the CMS detector and therefore exposed to radiation, the firmware will require Single Event Upset (SEU) mitigation logic. We will follow the recommendation of the CSC group which uses the same FPGA on the ME1/1 CSC chamber and which has tested the radiation hardness of many commercial components, including the FPGA, up to several tens of krad [51]. The SEU mitigation in the FPGA will be provided by the use of triple-voting and with the embedded Virtex-6 Error Correction Checking (ECC) feature for the FPGA Block RAM.

4.5.3 Overview of the online software

The online software of the GEM readout system is designed according to the general scheme of the CMS online software. The implementation is based on the generic solutions provided by the CMS software framework: XDAQ, Trigger Supervisor, etc.

The direct steering of the hardware is performed on the computers controlling the μTCA crates. The central control over the hardware is split in two:

- the XDAQ applications providing access to the AMC boards receiving the GEM tracking data and the AMC13 are managed by the GEM node of the Function Manager,
- the XDAQ applications providing access to the AMC boards receiving the GEM trigger data and the opto-hybrid boards are managed by the GEM cell of the Trigger Supervisor.

The software is abstracted into several layers. The Hardware Access XDAQ application is a custom class derived from the *Application* class provided by the XDAQ package. At the lowest level are the interfaces to the IPBus protocol. Above this layer is the standard CMS μHAL layer which defines the access functions (Write, Read, ...). The next layer above becomes board

dependent. However since the boards receiving the GEM trigger or the tracking data are the same, the C++ classes will be essentially identical. Functions like Reset, Configue, Start, Finished, etc. are defined at this level.

4.5.4 Testing and integration

In 2014, a first GEM DAQ system has been developed to read-out VFAT2 chips, while the VFAT3 chip is being designed. The system is composed of new CMS VFAT2 hybrids mounted on the first version of the full size GEB board on which the first version of the opto-hybrid is placed. The layout of this first version of the opto-hybrid is shown in Figure 4.2. This version of the opto-hybrid can read-out a sub-set of 6 VFAT2 chips. The opto-hybrid is read-out by

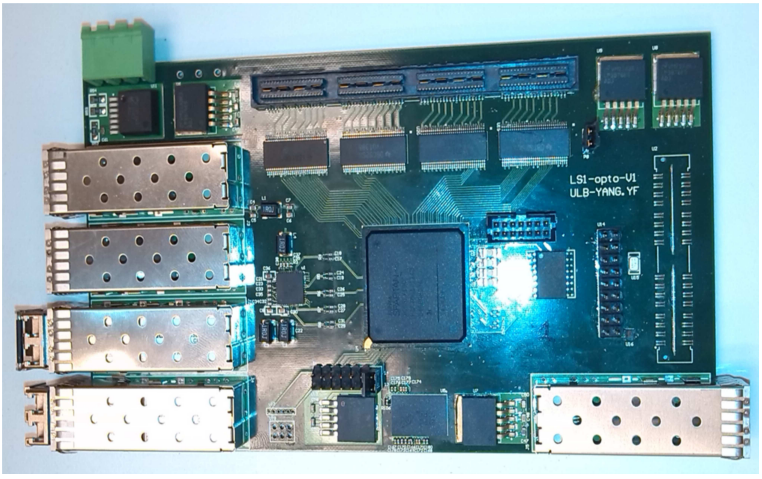

Figure 4.2: Layout of the opto-hybrid v1. It is equipped with a Spartan 6 FPGA.

a GLIB board [52] installed in a μTCA crate, controlled through IPBus. Since the Spartan 6 FPGA does not have high-speed transceivers that run faster than 3.2 Gbps, the GBT protocol can not been implemented, but a simpler 8b/10b encoding is possible. However, the GBT protocol has been successfully tested between a GLIB board and a Virtex 6 development board. This prototype is a proof of concept of the full GEM read-out chain that allows the test of the signal integrity in the GEB PCB as well as in the connection between the GEB and the opto-hybrid, and provides first measurements about the power consumption. The full read-out chain has been successfully tested in the lab as well as during a test beam at CERN in December 2014. During this test beam many of the functionalities needed for the final system have been tested, implying the implementation of the corresponding firmware and software: control of the VFAT2 chips and data readout through the bi-directional optical link, data integrity over the optical link, control from the DAQ PC through IPBus, etc.

Although the DAQ prototype differs from the final design in multiple ways, the firmware and software for the first version of the opto-hybrid and the GLIB are developed taking care to make them compatible with the later versions of the opto-hybrid with minimal changes. The current version of the system focuses on the control of the VFAT2 hybrids through I^2C which allows the software developers to test several functionalities of the chip as well as the communication between all the components of the DAQ chain.

In addition a GEM-CSC integration teststand is being built at CERN to test the full system. This facility is now composed of a GE1/1 prototype equiped with the first version of the GEB and of the opto-hybrid. The GE1/1 prototype is mounted on top of a ME1/1 CSC chamber and it is read-out by a GLIB and an AMC13 hosted in a μTCA crate controlled by a DAQ PC running

XDAQ. The opto-hybrid also transmits the trigger data to the CSC OTMB. While this facility is being commissioned the synchornization of both electronics systems has already been achieved and data sent from the GEM detector to the CSC OTMB.

The second version of the GEB board are already available and the design of the second version of the opto-hybrid will be finalized by the end of January 2015. These components will then be thoroughly tested by 5 laboratories in Europe and in the US, as well as in the GEM-CSC integration facility at CERN.

By the end of 2015, the design of the final versions of the GEB and opto-hybrid, compatible with the VFAT3 chip will start.

Chapter 5

Chamber Production, Quality Control and Quality Assurance

5.1 GE1/1 component production and assembly overview

In the last four years, the design of the full-size GE1/1 detectors has been optimized and now chambers are being prepared following the final production design. This has been possible given the excellent collaboration with various institutions with previous experience in building CMS muon detectors. A full length movie of the assembly of a GE1/1 detector can be seen here:

https://www.youtube.com/watch?v=Ssuqh5GAVZ4&feature=youtu.be

The philosophy of production is based on the experience gained during the construction phase of the CMS muon detector. Quality control (QC) and quality assurance (QA) are key factors to ensure the delivery of fully efficient detectors yielding their best performance when installed in CMS. The final chamber quality and performance depend on the production quality and on the accuracy of the chamber assembly operation, tracking, and documentation. In this chapter the QA and QC procedures of the complete cycle of the construction project of chambers for the GE1/1 station are described. Throughout the component procurement and production, and chamber assembly procedure, systematic inspections are also needed including verification of the QA and QC results. This will be done exploiting an extensive database that is used for reference throughout the life of the detector, from the moment of its assembly to its installation and operation inside CMS. Standardized procedures have been established that are identical as far as possible for all assembly sites which are described in Section 5.3.

The assembly and production workflow is presented in the process chart in Figure 5.1. The overall process is divided into three major parts:

- component production and quality control
- assembly and commissioning of single GE1/1 chambers at production sites
- assembly and commissioning of superchambers at CERN before delivery for installation at CMS P5.

The corresponding timeline is presented in Table 5.1. The tasks for QA, and QC procedures for components and chambers are described below. For each task, the average time is expressed. These numbers are generally estimated and additional delays may happen.

5.2 Component production and quality control

Components produced by industrial companies will be delivered to CERN where they will be visually inspected for defects and tested. Components passing this quality control, denoted

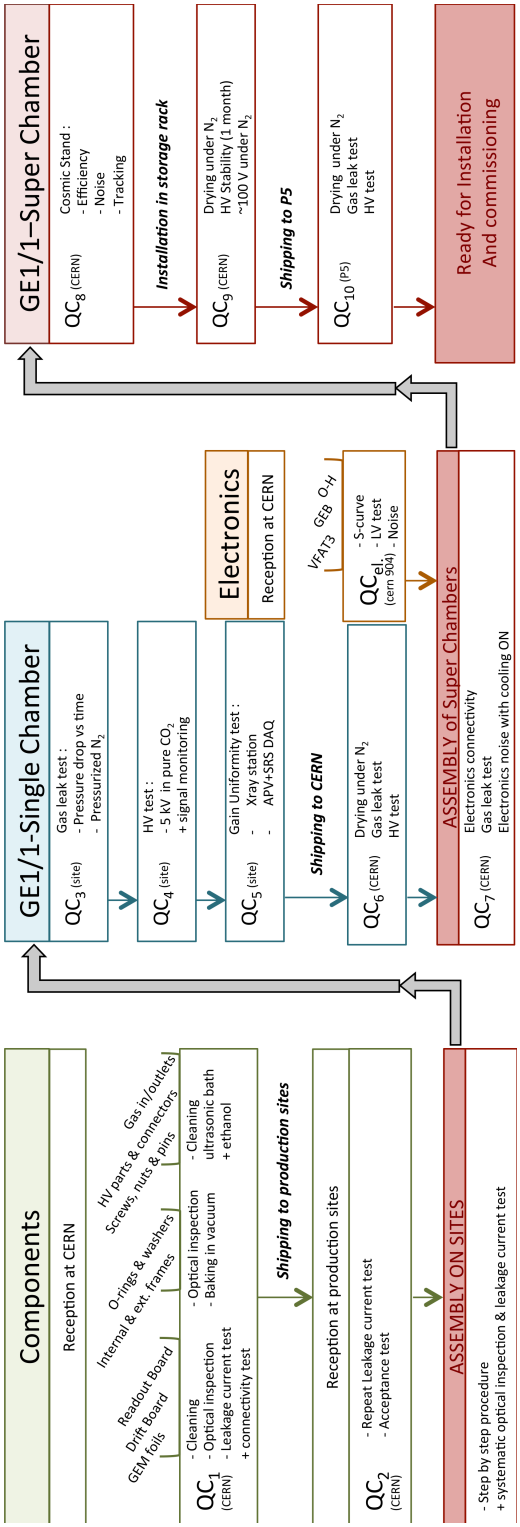

Figure 5.1: Process of GE1/1 chamber and superchamber assembly and construction from component production to final chamber commissioning.

Table 5.1: Timeline for the GE1/1 superchamber assembly.

QC	Expected time
QC_1	2 days (all components)
$QC_2 + assembly$	2 days
QC_3	1 day
QC_4	1 day
QC_5	1-2 days
QC_6	Until needed to assemble Superchamber
QC_7	2 days
QC_8	5 days
QC_9	Waiting for installation
QC_{10}	Quick test after transport

QC_1, will be shipped to the assembly sites. Some of the specific inspections and tests are described below.

Quality Control of HV divider. The HV divider is a chain of resistors used to deliver appropriate voltages to the drift plane and the three GEM foils (see Figure 2.1). A HV test is applied to the divider and the I-V curve is used to check the resistor value at each stage of the chain.

Drift PCB. An optical inspection is performed in a cleanroom to identify possible scratches and defects. A nitrogen gun is used to clean the drift plane for possible dust. The drift plane is then connected to HV and progressive HV ramping is used to check for possible sparks and/or changes in impedance.

PCB Readout. The PCB readout is inspected for possible shorts between strips or open strip-readout connections. A special connector is used to simultaneously check all the strips in one PCB readout.

GEM foil. The GEM foil must be handled and tested in a clean room. An optical inspection is first performed to identify defects, scratches, irregular hole sizes, and contact between top and bottom metalized surfaces. A leakage current test is part of the quality control of the GEM foils. Before and after the test, the GEM foils are stored in a safe and clean container with a maximum humidity of 35% and an ambieant temperature between 10 and 40 °C. High pressure nitrogen is used to remove possible dust. A microscope is also used when necessary to further investigate defects. The quality of the foil (leakage current and impedance) is checked using a picoammeter. With an applied potential difference of 500 V between the GEM metal sides, the GEM foil should draw a current of no more than 30 nA.

Other components needed for chamber assembly include O-rings, frames, gas in/outlets, and connectors. Once the acceptance criteria are fulfilled, complete assembly sets are shipped to the production sites after recording all QC and QA results in the database, as described in Section 5.5.

5.3 Chamber assembly at production sites

5.3.1 Assembly site requirements

The GE1/1 chamber assembly will take place at several sites. There is a minimum set of requirements for hardware and expertise for a site to be qualified. The site must have established a good track record of GEM chamber production and testing, including quality control checks

(QC_3 to QC_5 of Figure 5.1), gain measurements, successful operation in test beam campaigns of chambers produced from the center, and sufficiently skilled personnel. The following is a list of requirements for the production sites.

- Qualified personnel who are well trained in the assembly of GE1/1 chambers. The training will be done at CERN using dedicated final prototypes. The CERN group has already organized two weeks of intensive training with a total of 30 participants from 10 institutions. Personnel must be trained to work in a cleanroom and must understand the details of each step in the production process.
- Sufficient and appropriate space with dedicated areas for testing, assembly, storage, and logistics (reception and shipping of equipment).
- A certified cleanroom, rated at least at class 1000, equipped with at least one large bench to assemble full GE1/1 chambers. Auxiliary benches for assembly tools and spares are also required. Moreover, the cleanroom must be equipped with clean and dry nitrogen gas lines used to blow chamber parts during assembly. Storage cabinets are also required.
- A gas system, implemented with stainless steel pipes and leak proof. All components, such as valves, unions, and manometers, must be cleaned well to remove any oil residue from their production. The gas system must be capable of operation with CF_4-based gas mixtures, hence requiring components to be tolerant of fluorine. There must be filters to remove possible water contamination from the pipes. The use of oil bubblers or any oil-based devices is forbidden. Bubblers must be substituted with rotameters.
- Leakage current measurement station. There must be a nitrogen-flushed box of large enough size to comfortably house GE1/1 foils. A power supply must be available to provide 500 V at sufficient current for a single GEM foil. The nitrogen gas used for flushing in the leakage current box must be sufficiently dry and clean.
- X-ray setup to check the uniformity of the detector gain across the chamber surface.
- Gas leak measurement station. In this area the assembled chamber will be tested for gas leaks. The station must be equipped with a dry and clean nitrogen gas line and with a manometer to measure a pressure drop of the order of a few tens of a millibar per hour. The proposed method employs a U-shaped tube with millimeter scale. The U tube must be filled with water. No vaseline oil or other oil is allowed. Since the gas leak measurement will be done with dry and clean nitrogen, the piping can be done with clean plastic tubing.

5.3.2 Assembly site readiness present status

The GE1/1 collaboration has identified six possible assembly sites so far. The selection criteria are based on past experience at assembly sites in detector construction and on the support from their home institute given to the GE1/1 project. In the end, the final selection of assembly sites will be done after an assesment of their readiness for the final production six months before it starts. The site readiness will be judged following the criteria described in the previous section.

Following is a brief description of the six candidate sites and their present status.

- **Bhabha Atomic Research Center (BARC) Mumbai - India** BARC has actively participated in the RPC RE4 production, both in detector assembly (50 certified chambers) and in the chamber quality control using a cosmic-ray stand (see Figure 5.2(a)) instrumented with a gas system suitable also for GE1/1 chambers. The facility has a

large area for GE1/1 chamber storage and the present cleanroom (class 100) is being enlarged. The x-ray box for the gain uniformity test is under final design and will be completed by the end of 2014. BARC has successfully assembled and tested one GE1/1 full-size prototype demonstrating their full capability to participate to the final production.

- **INFN Sezione di Bari - Italy** INFN Bari participated to the RPC barrel chamber mass production and had a major role during the detector installation in CMS P5. The site has a wide cleanroom ($\sim 40m^2$) of class 10000 equipped with one optical table and one large marble table. The cleanroom contains a clean compressed-air line and a clean dry-nitrogen line. Assembly of an x-ray box and gas distribution system is complete. INFN Bari has already successfully assembled a GE1/1 prototype, which is presently under test in their x-ray facility (see Figure 5.2(b)).
- **CERN - Switzerland** The CERN site has the major responsibility for GE1/1 chamber construction and final validation. Assembly of GE1/1 chambers will take place in the Building 102 cleanroom. The chambers will then be moved to the tracker integration facility (TIF) cleanroom (see Figure 5.2(c)), where they will assembled into superchambers and tested on the cosmic stand, which is currenty under construction. At the TIF, all GE1/1 chambers assembled and validated from the different assembly sites will be delivered. The TIF has an operational x-ray setup for the gain uniformity QC of the chambers assembled at CERN. The GE1/1 superchambers will be placed in a storage area at the TIF before dispatch to CMS P5 for installation.
- **Ghent University (UGent) - Belgium** Ghent University previously produced 50 certified RPC RE4 chambers. It will take advantage of its present RPC lab (see Figure 5.2(d)), which has an operational cosmic stand. An x-ray station is assembled and ready with a movable gas mixing unit. A box for leakage current measurements on GEM foils is also ready. Options for installing a cleanroom near the Ghent GEM lab are being investigated. Using the Engineering Department cleanroom, one GE1/1 full-size prototype was successfully assembled.
- **Florida Institute of Technology (FIT) - USA** The FIT cleanroom (class 1000) is fully commissioned. It has a workspace for assembling up to two GE1/1 chambers in parallel (see Figure 5.2(e)). It is equipped with a clean gas line (nitrogen) and optical and marble tables for the GE1/1 assembly. A leakage current station and gas system are ready. A lead shielding box to accommodate GE1/1 detectors for x-ray tests was recently completed. FIT has successfully assembled and tested two GE1/1 full size prototypes.
- **INFN Laboratori Nazionali di Frascati (LNF) - Italy** The Frascati site already participated in "mass production" and will profit from the infrastructure and logistical capacity of the Frascati laboratory. The Frascati assembly site candidate has a large cleanroom (class 100) of about 20 m^2 with an adjacent large cleanroom (class 10000) of 42 m^2. The GE1/1 assembly will be done in the class 100 cleanroom, which is already equipped with marble and optical tables and cabinets, and was used to successfully assemble two GE1/1 full-size prototypes. The cleanroom (see Figure 5.2(f)) is equipped with clean gas lines (nitrogen and air). The x-ray facility is under construction and will be completed at the beginning of 2015. The site has an operational gas system with three (clean) gas lines for ternary gas mixtures instrumented with a gas chromatograph station for gas mixture quality control and monitoring.

Table 5.2 gives a list of production sites and the status in fulfilling the required characteristics described in the text.

Table 5.2: List of candidate production sites and current status of required characteristics.

	BARC	INFN-Bari	CERN	FIT	INFN-LNF	UGent
Cleanroom		X	X	X	X	
Leakage current setup		X	X	X	X	X
Gas system	X	X	X	X	X	X
X-ray setup	X	X	X	X	X	X
Shipping logistics	X	X	X	X	X	X
GE1/1 prototypes assembled	X	X	X	X	X	X
Past experience	X	X	X	X	X	X

5.3.3 Single GE1/1 chamber assembly

Upon receipt of the different components, the production site will start the QC_2 quality check procedure to identify possible damage that might have been incurred in transport.

As described before, visual inspection and leakage current measurements are the basis of the QC_2 process required to validate the components for assembly. The GEM foils will be tested for leakage current and the readout boards will be checked with a dedicated tool capable of identifying any possible bending damage.

The assembly procedure is well demonstrated in the video file:
https://www.youtube.com/watch?v=Ssuqh5GAVZ4&feature=youtu.be

The main steps are summarized below, as shown in Figure 5.3.

Step 1: preparation of the drift board

- The PCB is equiped with metallic inserts and HV contact probes.
- The outer frame is fixed to the PCB thanks to guiding pins.

Step 2: preparation of the GEM stack

- The first frame is placed on a rigid support.
- The first GEM and the second frame are then placed on top.
- The stretching nuts are inserted into the frames.
- The third GEM is installed and the last frame then close the stack.

Step 3: installation and stretching

- After removing the guiding pins the full stack is placed on the drift plane.
- The electrical contacts are checked for every GEM foil and the HV-divider.
- The chamber is closed with the readout PCB.
- Gas in/outlets are inserted in the outer frame.

The detector is now ready for the Quality Control.

5.3.4 Flatness and planarity check and monitoring

One of the critical steps in the assembly is to certify the tensile properties of GEM foils. This is accomplished using a Moiré interferometric system and a monitoring system that uses fiber Bragg grating (FBG) optical sensors. The required precision is 30 μm in order to measure the 100 μm maximum accepted deviation from planarity [53]. Long-term stability will be monitored by FBG optical strain gauges. This technique has been applied to several detectors in

HEP for strain and deformations, temperature and humidity measurements, with a great deal of experience in the collaboration [43–45]. The Moiré system under development in Frascati (see Figure 5.4) is composed of a projector equipped with an optical grating, a photographic camera equipped with an identical grating, the GEM foil mounted on optical slides, and a Laser Displacement System (LDS) to calibrate the Moiré fringes. The sensitivity of the LDS is 1 μm.

The systematic error of the LDS connected to the optical slits system was measured by performing back and forth scans on a flat reference surface. The residuals are limited to less than 5 μm (see Figure 5.6).

Preliminary results on a circular target scanned with the LDS (Figure 5.7a) have shown well separated fringes for a 100 μm displacement (see Figure 5.7b). A 30 μm resolution is expected with finer gratings and the implementation of a phase-shift algorithm.

A network of FBG sensors (see Figure 5.5) is used to validate the stretching procedure, to intercalibrate the Moiré interferometry, and to provide a continuous monitoring of stretching planarity. The stretching procedure is validated once by comparing uniformity response of FBG sensors installed in the active area of each GEM foil. A uniform stretching of three foils will be certified by identical response of the three FBG sensors. Intercalibration for Moiré interferometry and continuous monitoring will be provided by FBG sensors located on the edges of the upper GEM plane, in non-active areas.

Preliminary results have shown reliable gluing of FBG sensors on GEM and Apical films (see Figure 5.8), as well as excellent correlation between LDS and FBG displacement measurements (see Figure 5.9).

In Figure 5.10 are shown very preliminary results on how the response of FBG sensors installed on each GEM film, both parallel and perpendicular to the film bases as described in Figure 5.5, provide extremely similar strain pattern when subjected to a tensioning cycle. Once tensioned, the difference in their strain is less than 0.05 mstrain. This preliminarty result is a strong and solid indication that the three GEM foils are subject to the same tensile load during the assembly procedure.

5.3.5 Single GE1/1 chamber commissioning

Upon completion of the assembly, the chamber is tested for gas leaks with pure, dry, filtered nitrogen. A chamber is then pressurised up to 20 mbar (maybe even more) and kept under such pressure for some hours. Chambers not leaking will be flushed with Ar/CO_2 and turned on after 12 hours by applying a moderate HV. Thus they would have completed QC_{3-4}.

The next step is QC_5: the gas gain is the most important parameter to characterize GEM detectors. It reflects the good behavior of the GEM foils, the purity of the gas and in general the accuracy of the electric field configuration. The gain is also considered to be a basic measurement and a reference value associated with various properties of a GEM detector. It is therefore extremely important to perform the gain calibration with the greatest care and to follow common techniques at all chamber production sites to facilitate the comparison with other detectors or results from the literature.

The gain can be reliably measured from the pulse height spectrum of a radioactive source based on the amplitude of the collected signal compared to the electronic noise, the energy of the particles emitted by a radioactive source, and the way they interact with the detector.

5.4 Superchamber assembly and production at CERN

A superchamber (SC) is fabricated by coupling together two GE1/1 GEM single chambers. The mechanical assembly of a superchamber is shown in Figure 5.11 where one long and two short superchambers have been prototyped for integration studies purposes.

After gain calibration, at QC_5 a HV voltage scan is performed on the GE1/1 chambers and relevant parameters (gain, noise, and cluster size are measured) with final electronics, validated via QC_{el}. These measurements are performed with a cosmic stand and documented as QC_8

5.4.1 Cosmic ray tests

The goal of the cosmic ray test (QC_8) is to validate the performance of a chamber and its electronics. Figure 5.12 shows the cosmic stand setup built at CERN for this purpose. The setup allows several chambers (up to 15 superchambers) to be tested at the same time. The experimental setup includes the following features.

- Fully automatic HV scan, to allow measurement of the efficiency and spatial resolution.
- Measurement of cosmic muon tracks over a large area of the chamber.
- A DAQ system comparable to the one used in the CMS experiment, to test the on-chamber electronics.
- Data Storage and analysis. Raw data will be stored on disk for further offline processing. A central software will be developed to allow fast online data analysis.

Once this stage is completed, the superchamber is declared ready for final installation after documenting QC_{9-10} in the database.

5.5 Database

All QA and QC aspects of the assembly procedure and components are stored in a common database. The DB is based on Oracle and contains the following information.

- Main detector components: the chip FrontEnd, GEB board, GEM frames, and cooling. For each component the validation results will be recorded.
- Detector assembly: information about the assembly and quality check procedures of the chamber. It also includes preliminary validation tests: gas leak, channel connectivity, and electrical tests.
- Detector performance: includes results from x-ray and cosmic ray tests. It will contain plots from a full HV scan of cluster size, noise, and detector conditions including threshold, gain, environmental conditions, assembly site, date, location, and operator.

(a) BARC

(b) INFN-Bari

(c) CERN

(d) UGent

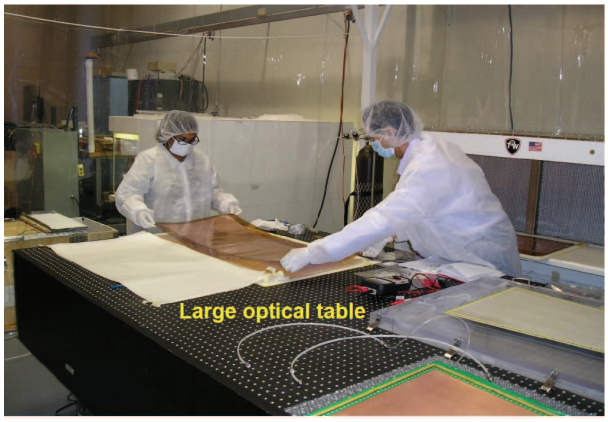

(e) FIT

(f) INFN-LNF

Figure 5.2: Pictures from different assembly site candidates.

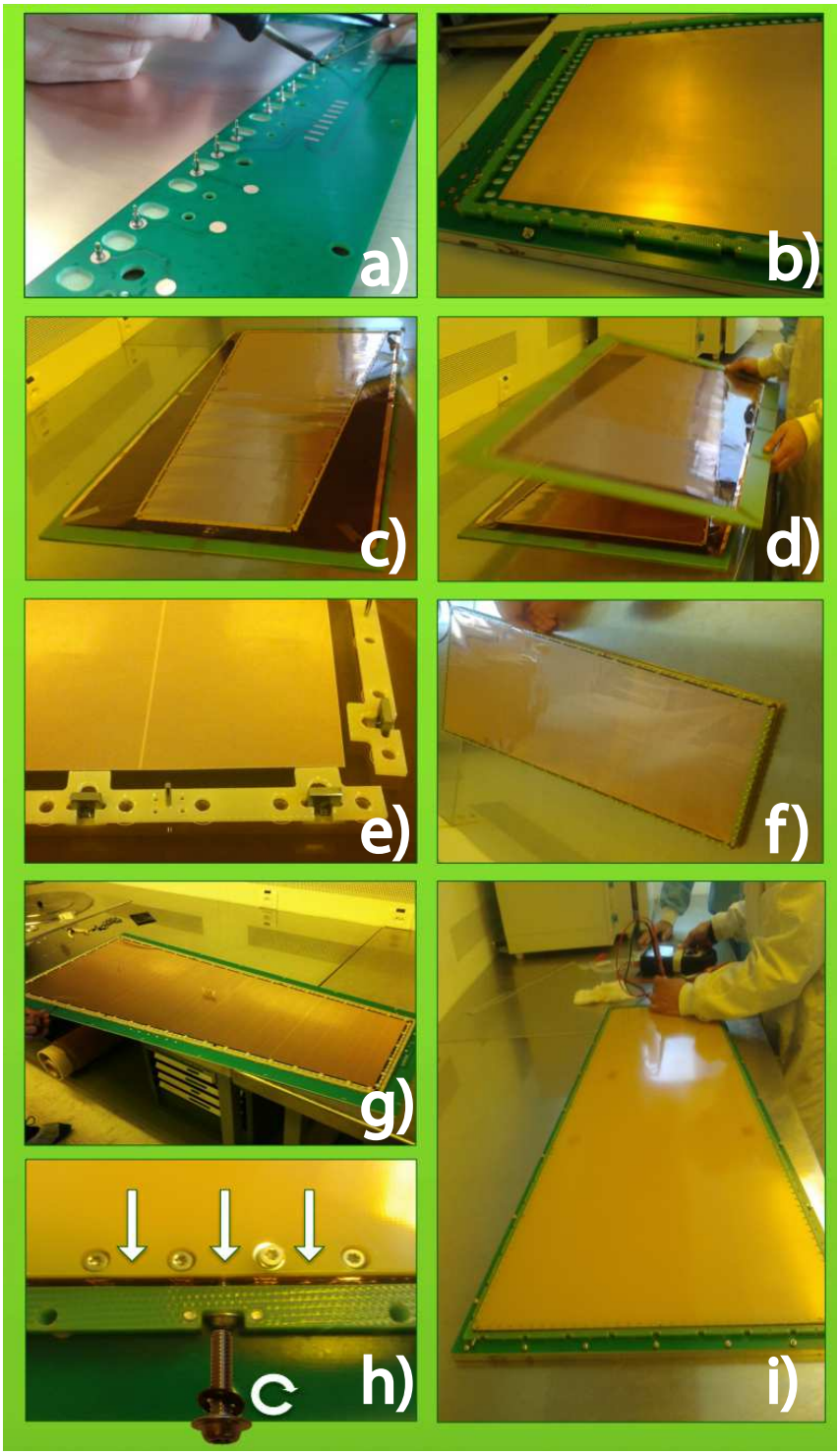

Figure 5.3: Main steps of the GE1/1 chamber construction. (a) Preparation of the drift board by soldering of the HV spring contacts and deep cleaning of the copper plane, (b) screwing of the brass pullouts needed for the foil stretching, (c)-(d) assembly of the of the GEM foil stack on a separated bench, (e) insertion of the pulling nuts into the stack frame, (f)-(g) the GEM foil stack is moved on the drift board, (h) the GEM foils are stretched with the dedicated screws, (i) The GE1/1 chamber is ready to be closed with the readout board.

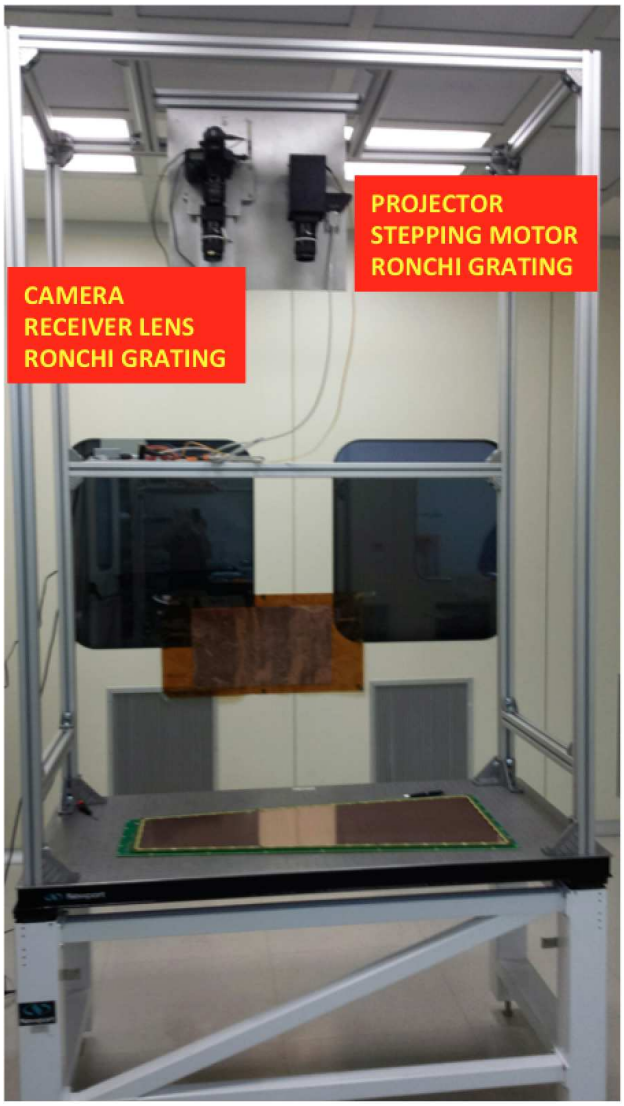

Figure 5.4: Moiré setup in Frascati clean room projecting fringes on a whole GE1/1 GEM chamber. The projector (mounted on a translational stage for phase-shift algorithm) illuminates the GE1/1 with a pattern generated via a Ronchi grating. The receiver lens is equipped with the same Ronchi grating. Moiré fringes are generated on the lens focal plane proportional to the GE1/1 non-planarity.

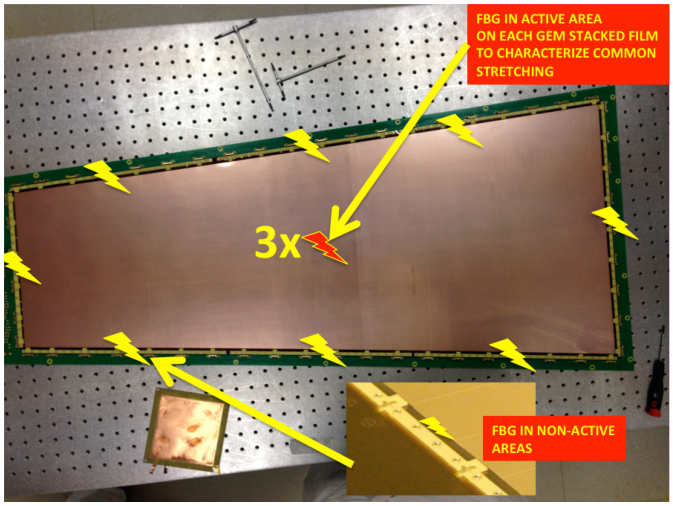

Figure 5.5: FBG sensors on GEM films in a GE1/1 chamber. The sensors in the middle of GEM planes are used once to certify the uniformity of stretching procedure over the three GEM planes. Sensors installed on the upper GEM plane only, provide intercalibration with Moiré and LDS systems, and deformation monitoring.

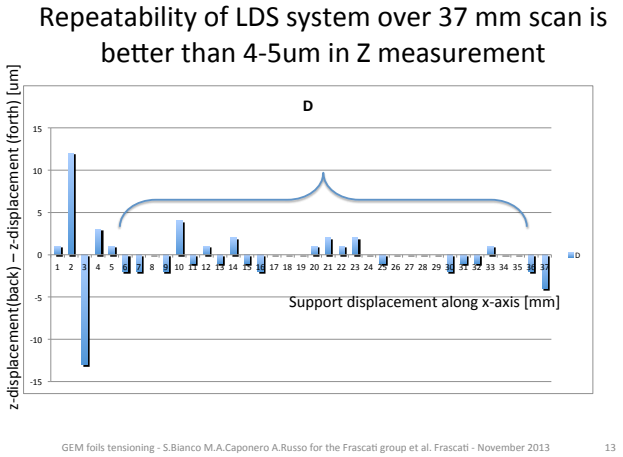

Figure 5.6: Residuals for a back-forth scanning of reference surface with the Laser Displacement System used to calibrate the Moiré fringes. Repeatability of LDS system over a 37-mm scan is better than about 4 μm in the measurement of z direction (transversal to scan) displacement.

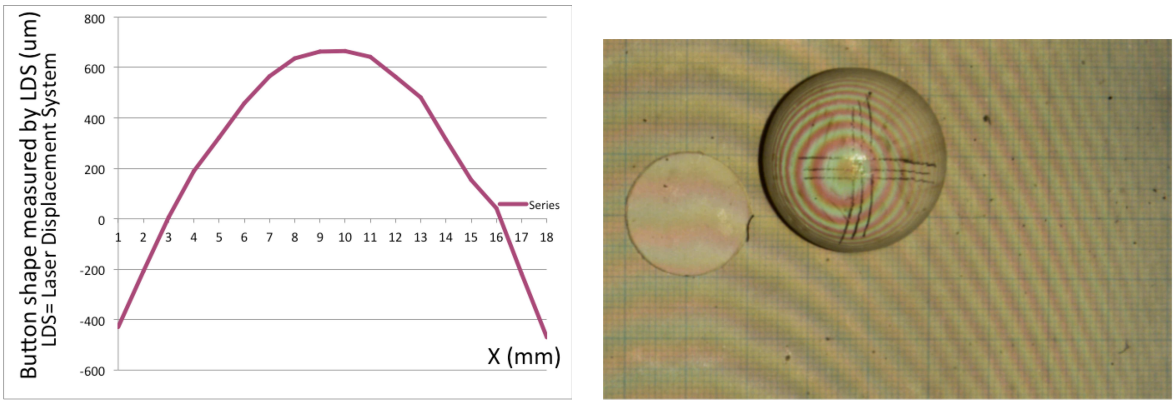

(a) (b)

Figure 5.7: Fringes on a circular object as scanned by LDS (a); Moiré fringes (b). One-fourth of period is easily visible, hence the estimate on resolution is 100 μm. Finer grating and phase-shift algorithm will improve resolution to better than 30 μm.

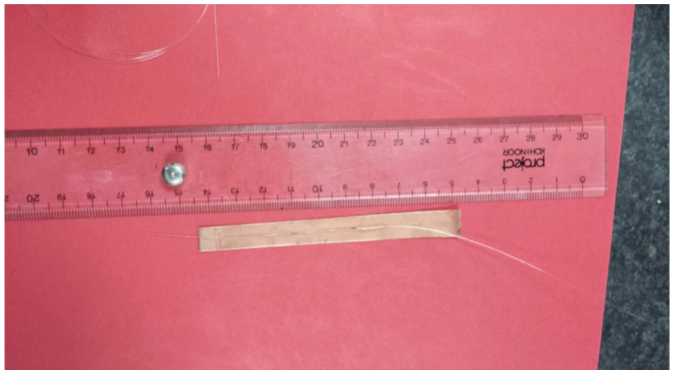

Figure 5.8: Gluing of a FBG sensor on GEM sample. Glues tested include UHU PWS 24h, 2011 ARALDITE HUNTSMAN, PATTEX PLASTIC HENKEL, UV-RAY WELLOMER UV4028. Glue selected was 2011 ARALDITE whose mechanical properties and radiation hardness are well known. A suitable set of tools and procedures was developed to assure reliable mechanical strength, while still retaining the requirement of minimal glue deposition.

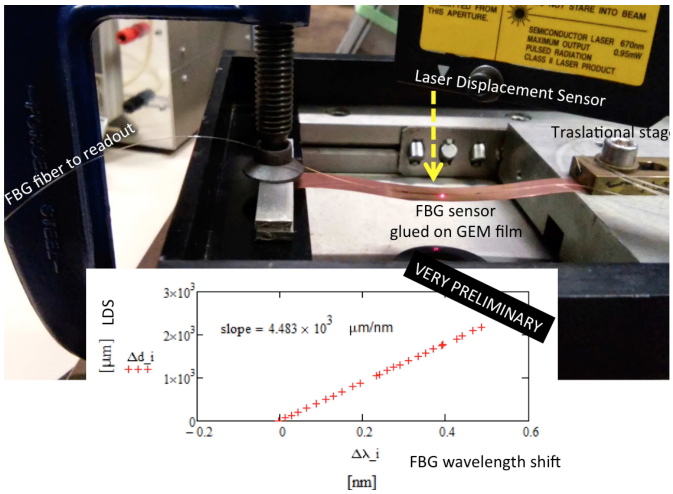

Figure 5.9: Test of gluing a FBG sensor on a GEM film strip. The FBG response is very well correlated with the gravitational sag as measured by LDS. Illustration shows the experimental setup with LDS (top), translational stage pulling the GEM film strip (right), FBG sensor glued on GEM film strip (centre) and optical fiber funnelling the laser light to interrogation system (left).

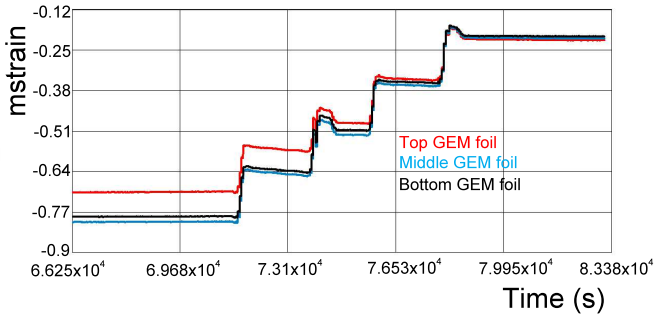

Figure 5.10: Preliminary data on the FBG sensors output during a tensioning cycle. The mechanical tension of the GEM film was varied over time from a non-tensioned state to a tensioned state. The sagitta as measured by LDS relative to the final (tensioned) state is shown (black curve). Two sets of sensors are used, i.e. perpendicular of parallel to the GEM film bases. Each set is composed of three sensors each glued on a GEM film. The sensors output (shown in strain units) is very consistent and uniform during the film tensioning, and, in the tensioned final state, is equal to better than 0.05mstrain.

Figure 5.11: GEM dummy superchambers.

Figure 5.12: Schematic view of the Cosmic Stand at CERN. In the picture the two mock-ups of a GE1/1 superchamber are visible. The cosmic stand can accomodate up to 15 superchambers.

Chapter 6

System Performance

The overarching goal of the proposed upgrade is to avert a potential significant deterioration of the CMS muon triggering capabilities in the range $1.6 < |\eta| < 2.2$ once the instantaneous luminosity approaches and exceeds 1.7×10^{34} cm^{-2} s^{-1}. As the affected range represents well over a quarter of the overall CMS muon coverage, such deterioration could significantly affect the CMS physics reach.

The forward region is the most challenging for muon triggering and reconstruction due to exceptionally high background rates and a much reduced magnetic field. These effects complicate pattern recognition and reduce momentum resolution. Despite being operated in the harshest environment, the forward part of the muon detector currently has the least redundancy in the entire muon system. While in the range $|\eta| < 1.6$ muon hits are reconstructed by at least two muon detector systems (either DT+RPC, or CSC+RPC), the region of $|\eta| > 1.6$ relies on the CSC system alone, as at the time of the CMS construction the available RPC technology did not meet the requirements for operating at such high rates. Figure 6.1 (left) illustrates these observations by showing the average number of muon layers with hits for a typical muon as a function of muon η overlaid with the flux of background particles.

Maintaining efficient muon triggering in the forward region at increased luminosity represents a particular challenge. With the current system, the inclusive muon trigger rate features a rapid growth with the increasing η, as illustrated in Figure 6.1 (right). Already at $\mathcal{L} = 1.7 \times 10^{34}$ cm^{-2} s^{-1}, maintaining the Level-1 trigger threshold of $p_{\mathrm{T}} > 15$ GeV, at which the efficiency for muons with $p_{\mathrm{T}} > 20$ GeV reaches the plateau, would generate a trigger rate of 10 kHz from this region alone. This is comparable to the single muon trigger rate for the entire muon trigger in Run 1 and is one tenth of the entire CMS Level-1 bandwidth of 100 kHz, which will not increase until after LS3. The upgrade of the CMS Level-1 trigger electronics capabilities [2] planned in anticipation of instantaneous luminosity increases following the LS2, muon track finders will simultaneously use hits from all available detector systems (DT, CSC, RPC) to reconstruct candidate tracks and measure their momenta. Efficient use of the available redundancy improves muon trigger efficiency and reduce rate driven by p_{T} mismeasurements in the region of $|\eta| < 1.6$, but not in the range $|\eta| > 1.6$, where no redundancy is available. Trigger threshold studies in [2] show that achieving an acceptable trigger rate for muons with $p_{\mathrm{T}} > 22 - 25$ GeV is not possible without substantial additional efficiency losses in the endcap region representing over a half of the overall CMS muon coverage.

The proposed GE1/1 upgrade addresses these concerns, both for the period between LS2 and LS3 and beyond into the HL-LHC era. First, it allows maintaining a robust muon trigger in essentially the full range of current muon coverage by reducing the contribution from $1.6 < |\eta| < 2.2$ by an order of magnitude. Second, strengthened redundancy of the system in the forward region adds to the robustness of the trigger and offline performance by provid-

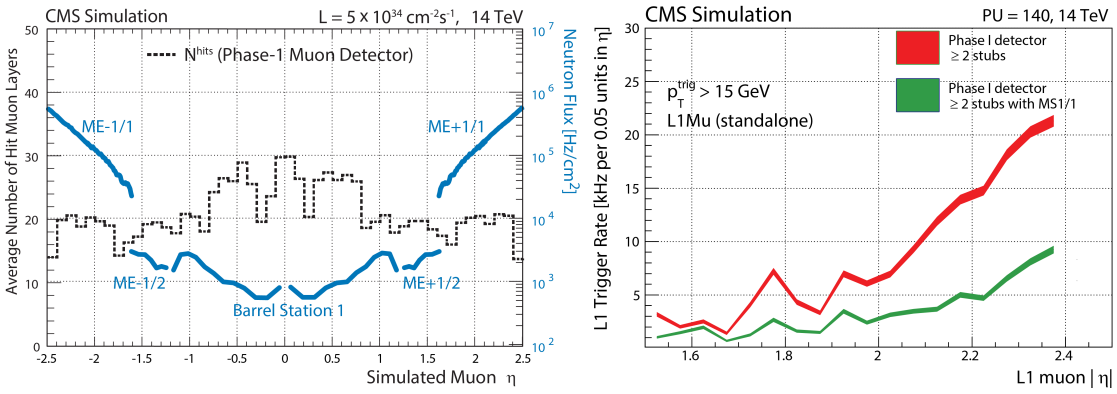

Figure 6.1: *Left:* The dashed line shows the average number of muon layers with reconstructed hits for a simulated muon as a function of η. It is compared to the flux of neutrons in Hz/cm^2 shown as colored curves (note the log scale on the right), which are the dominant cause of background hits, for the muon station first crossed by a muon with a given η. Forward region is exposed to the highest rates in the system, yet has the fewest muon layers needed for offline and trigger reconstruction and momentum measurement. Depending on the detector type the conversion factor can vary somewhat, but typically the hit rate is of the order of 0.2% of the neutron flux. *Right:* Trigger rate as a function of η shows a large increase towards high η due to the weakening magnetic field and increased particle rates. The two curves correspond to two configurations of the current muon trigger illustrating the special importance of the first station for the accuracy of momentum measurement: presence of reconstructed hits in the first station reduces momentum mismeasurements dominating the trigger rate.

ing means to reduce performance losses if parts of or entire CSC chambers become inoperable; these situations are unavoidable in real life operations and will become increasingly difficult to anticipate with the system aging. Third, the design of the GE1/1 system allows a seamless integration into the CMS muon offline reconstruction and identification adding to its robustness and performance. Maintaining reasonably low muon thresholds has an important impact on a broad range of physics scenarios relevant for the period of Phase-I LHC operation following the LS2, when large amounts of data are to be collected. Some of the examples of physics processes for which the sensitivity is dependent on low muon trigger thresholds include the so-called "compressed" scenarios, which can be realized in various flavors of SUSY, yielding low momenta leptons, SM Higgs measurements in $h \to \tau\tau \to \mu + X$, or resonant production of higgs boson pairs via $H \to hh \to \tau\tau bb$ predicted in models with extended Higgs sectors [8] relevant in many contexts including studies related to electroweak baryogenesis [9]. These considerations are not limited to the case of the inclusive muon trigger, as the reduction of the Level-1 rate in the most difficult region allows lower Level-1 thresholds across the board for inclusive muon trigger, di-muon trigger, and all of the muon+X triggers without increasing their rate.

The improvements in muon trigger and reconstruction brought by the GE1/1 upgrade will continue playing a critical role in maximizing the CMS physics reach in the post-LS3 HL-LHC environment. The GE1/1 detector has been designed in anticipation of future integration with other planned Phase-II CMS upgrades, of which the most notable for muon performance is the addition of the tracking trigger with its excellent momentum resolution. Preserving the high performance of the standalone muon trigger is essential in designing the ultra-high purity muon trigger, based on matching tracks from the tracking trigger with standalone muon candidates, and ensuring its stable performance. The latter is true not only for Level-1, but also for the High Level Trigger, which uses a variant of the offline standalone muon recon-

struction. The redundancy provided with the deployment of GE1/1 improves the quality of standalone muon reconstruction and can avert a deterioration in standalone muon momentum resolution if the performance of the aging ME1/1 system degrades. Standalone muon triggering and reconstruction capabilities will also remain of critical importance on its own due to its unique role in enabling sensitivity to new physics scenarios predicting new long lived particles via their decays to pairs of muons. Such displaced signatures frequently arise in models with hidden sectors [54], GMSB and R-parity violating SUSY [55], and other scenarios of new physics.

In this chapter, we discuss the impact of the new GE1/1 detector in improving the capabilities of the muon system and present a detailed evaluation of the projected performance of the upgraded detector. We also describe the tools and methods developed to perform these studies, trigger and reconstruction algorithms, and provide details of important intermediate measurements that our conclusions rely on.

6.1 Background evaluation and modeling the high luminosity environment

The high collision rates at the new energy and luminosity regime of the LHC gives rise to an extreme radiation environment. High background particle rates complicate signal identification and can have a significant impact on the performance of the detectors themselves, in extreme cases making them inoperable. These considerations put large emphasis on the accurate evaluation of the expected background rates in the region where a new detector will be installed; this is particularly true for the forward region where these background are especially high.

The dominant contribution to the CMS cavern backgrounds, which determines the hit rate and occupancy in the muon detectors, is due to neutrons and the secondary particles arising from neutron interactions with matter. This background has a long lifetime as neutrons can propagate for seconds without interacting. Neutrons arise from the interactions of hadrons produced in primary pp collisions with the material of the beam pipe and the structures positioned in the very forward region (very forward calorimeter (HF), beam collimator and shielding). The spectrum of these long-lived neutrons ranges between the thermal region and a few GeV. The slow neutron capture by nuclei with subsequent photon emission in the detector material yields photons and, consequently, electrons and positrons capable of producing detectable amounts of ionization in gas detectors.

The radiation environment is a key consideration in selecting the detector technology and the subsequent detector design. The high occupancy and hit rate can lead to inefficiencies in detector response, degraded resolutions and momentum mismeasurements, or can render the detector inoperable. It can also yield an unacceptably high rate of track misreconstructions which will contribute to the trigger rate. Moreover, the high flux of incident particles can lead to radiation damage of the electronics as interactions leading to anomalous local deposits of radiation can disrupt electronic signals (single event upsets), or destroy the components (single event damage). Therefore, evaluation of the background flux is an important prerequisite for correctly ascertaining its effects on the detector and trigger performance, and aging of the detectors and electronics.

Evaluation of the improvements in the overall CMS detector performance with the addition of the GE1/1 system relies on detailed simulation developed and integrated with the standard GEANT-based CMSSW framework. CMSSW includes GEANT-based propagation of particles through the detector material, digitization packages used for emulating detector and electron-

ics response, trigger simulation and event reconstruction. The standard CMSSW simulation workflow does not allow simulating the long-lived backgrounds in one go with the particles originating from a pp-collision. This is because of a cut-off implemented in CMSSW on the propagation time, which reduces significantly the CPU time required to generate events. Therefore, inclusion of the long-lived background contributions in CMSSW is performed by first evaluating the rate and the properties of the "hits" due to long-lived backgrounds followed by embedding hits emulating the contribution of the long-lived backgrounds into the CMSSW simulated data events. We use the CMS adaptation of the FLUKA package to calculate particle fluxes, which are then convoluted with the parameterization of the GE1/1 detector response obtained using a dedicated GEANT simulation study.

6.1.1 Evaluation of the backgrounds due to long-lived neutrons

The study of the long-lived component of the cavern background is performed using the FLUKA simulation tool. FLUKA allows the evaluation of the fluxes of long-lived neutrons and secondary particles produced in interactions of neutrons with the material of the detector (secondary particles capable of reaching GE1/1 chambers are typically produced at the edges of the volumes surrounding the enclosures where chambers are positioned). These fluxes are then convoluted with the chamber sensitivities in order to obtain the hit rates.

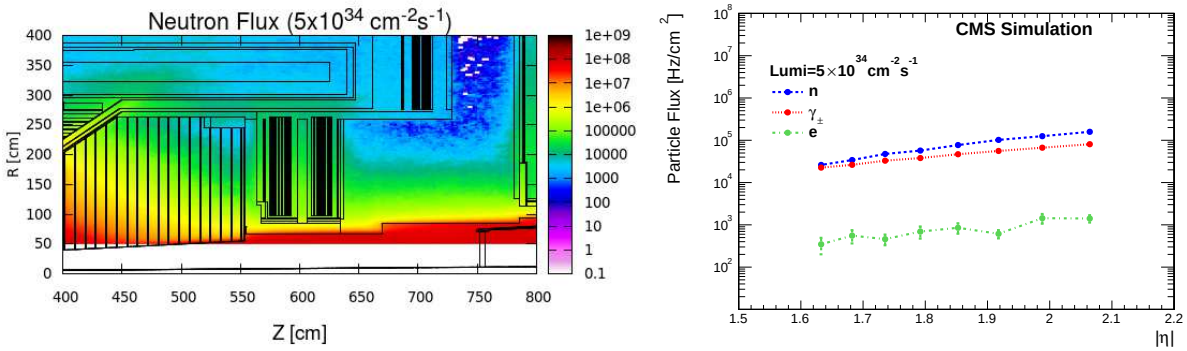

Figure 6.2: *Left:* The 2D flux map for neutrons normalized to an instantaneous luminosity of 5×10^{34} cm^{-2} s^{-1} and overlaid on the diagram showing the detector elements. *Right:* Particle flux for GE1/1 region as a function of the pseudorapidity range assuming an instantaneous luminosity of 5×10^{34} cm^{-2} s^{-1}.

The CMS adaptation of the FLUKA package contains a detailed description of the dimensions and material composition of each of the detector subsystems, i.e. tracking, calorimetry, muon system, etc. The validity of FLUKA predictions in the CMS environment is under study using Run 1 data and the first comparison is reported in [56]. To estimate the particle flux, we use the geometry corresponding to the Run 2 configuration of the CMS detector, which accounts for the planned improvements to the central beampipe and muon chamber shielding description in comparison with the version used for Run 1. FLUKA simulation has been setup with a beam energy of 7 TeV. The energy cut-off, below which the particles are no longer tracked, for neutrons has been set as 10^{-14} GeV. The corresponding cut-off values for photons, electrons and positrons vary between 10^{-5} and 10^{-3} GeV depending on the detector region. The results of the simulation are saved as a set of flux maps for each particle type, as illustrated in Figure 6.2 (left) showing the neutron flux map for the region surrounding the location of the future GE1/1 detector. Figure 6.2 (right) shows the predicted flux of neutrons through the volume corresponding to the location of the GE1/1 chambers as a function of pseudorapidity η.

The same figure shows the simulation prediction for the flux of photons and electrons arising from neutron interactions in the material surrounding the enclosure that the GE1/1 chambers will be installed in. Table 6.1 provides the numeric estimates of the particle flux through the top, middle and the bottom parts of the GE1/1 chambers for $\mathcal{L} = 1 \times 10^{34}$ cm^{-2} s^{-1} and $\mathcal{L} = 5 \times 10^{34}$ cm^{-2} s^{-1}.

Table 6.1: FLUKA predictions for the particle fluxes through the volume where the GE1/1 chambers are to be installed. Flux values are provided for each particle type and four points in the (R,z) coordinates corresponding to the bottom, lower middle, higher middle, and the top parts of the chamber.

Particle type	**R [cm]**	**z [cm]**	**Flux [Hz/cm^2] for $\mathcal{L} = 10^{34}$ cm^{-2} s^{-1}**	**Flux [Hz/cm^2] for $\mathcal{L} = 5 \times 10^{34}$ cm^{-2} s^{-1}**	**Flux uncertainty [%]**
Neutrons	150	560	2.9×10^4	1.5×10^5	1.5
	170	560	2.0×10^4	1.0×10^5	1.7
	190	560	1.3×10^4	0.6×10^5	1.9
	210	560	0.9×10^4	0.4×10^5	2.3
Photons	150	560	1.5×10^4	7.6×10^4	1.8
	170	560	1.1×10^4	5.6×10^4	2.0
	190	560	0.8×10^4	4.1×10^4	2.1
	210	560	0.6×10^4	3.0×10^4	2.3
Charged	150	560	2.8×10^2	1.4×10^3	16.4
	170	560	2.0×10^2	9.8×10^2	21.4
	190	560	1.2×10^2	6.2×10^2	24.0
	210	560	1.0×10^2	5.2×10^2	26.0

Results of the simulations can be used to calculate the total neutron fluence and the total irradiation dose accumulated by the GE1/1 chambers. After accumulating 3000 fb^{-1} of integrated luminosity, the total dose amounts to 1kGy (100 krad) at the highest eta region of GE1/1 chambers.

Evaluation of the rate of the hits generated in the chambers by the backgrounds induced by the long-lived neutrons requires knowledge of the flux for each particle type and the probability for a given type of particle to generate a spurious signal in the detector. The latter probability, referred to as the detector sensitivity, depends on the particle energy and the direction it crosses the outer surface of the chamber. When neutrons or photons enter a GEM chamber, their interactions with the material of the detector gives rise to secondary particles which can reach the gas gaps and generate signal. Electrons and positrons can generate signal directly by penetrating the chamber and ionizing the gas or can cause electromagnetic showers by interacting with the walls or the inner structures of the chamber, in which case the signal will be generated by secondary particles.

The sensitivity of the GE1/1 chambers to neutrons, photons, electrons and positrons is evaluated with a standalone simulation using Geant4.9.6.p02 and the FTFP_BERT_HP physics list [57] known to provide an accurate description of neutron interactions with matter down to thermal energies). The detector being modeled is the GE1/1 superchamber (two trapezoids with a height of 1283 mm and the lengths of the large and the small bases of 510 mm and 279 mm, respectively, stacked one on top of the other and separated by 3.7 mm) complete with a full material description (see Table 6.2). In the simulation, particles of fixed energy and given type cross the outer surfaces of the superchamber with uniform density over the outer surface of the chamber frame and with the incident angles distributed according to the angular distribution

Table 6.2: Layer structure of a single GE1/1 chamber as implemented in GEANT4.

Layer	Material	Thickness [mm]
Aluminum frame	Al	1.0
Cooling pipe	Cu (filled with H_2O)	8 external ⌀, 6 inner ⌀
Cooling pads	Cu	1.0
GEB board	Cu/FR4	0.140/0.856
Readout board	Cu/FR4/Cu	0.035/3.2/0.035
Induction gap	Ar:CO_2:CF_4 (45:15:40)	1.0
GEM 3	Cu/Kapton/Cu	0.005/0.050/0.005
Transfer gap 2	Ar:CO_2:CF_4 (45:15:40)	2.0
GEM 2	Cu/Kapton/Cu	0.005/0.050/0.005
Transfer gap 1	Ar:CO_2:CF_4 (45:15:40)	1.0
GEM 1	Cu/Kapton/Cu	0.005/0.050/0.005
Drift gap	Ar:CO_2:CF_4 (45:15:40)	3.0
Drift board	Cu/FR4/Cu	0.035/3.2/0.035

obtained in the FLUKA simulation study described earlier. The simulation is repeated for each particle type scanning over a broad range of energies. Events, in which at least one charged particle tracked by GEANT reaches the drift volume or the first transfer gas gap of either of the two stacked GEM chambers, are assumed to yield a valid signal in that chamber. The minimum energy thresholds for secondary particle production in GEANT has been set to about 1 keV for all types of particles except protons and nuclei, for which the threshold has been completely removed.

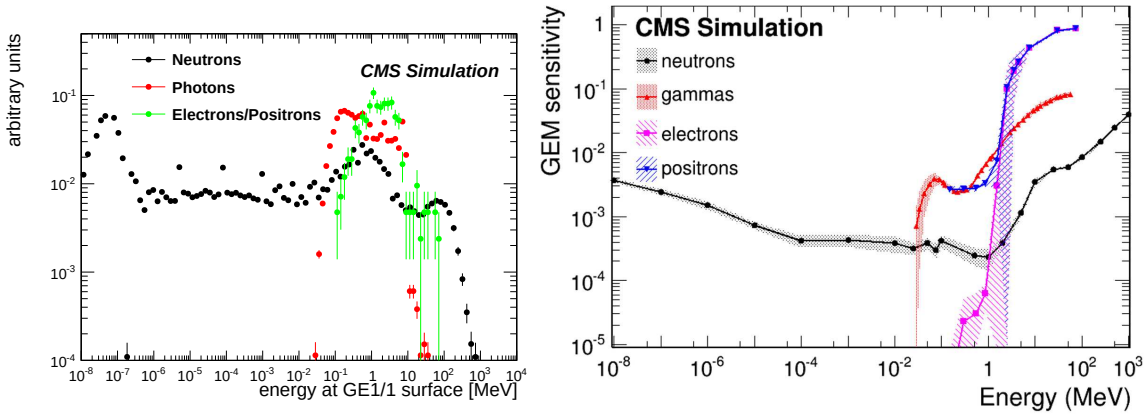

Figure 6.3: *Left:* The energy spectrum of incident particles crossing the GE-1/1 chambers predicted using FLUKA. *Right:* Energy-dependent sensitivity, defined as the probability to produce a measured hit in the chamber, of the GE-1/1 chamber to neutrons, photons, electrons, and positrons, as a function of the incident particle energy.

The final detector sensitivities we seek to obtain require averaging over both the angular and energy spectra of the background particles. While the averaging over particle directions is included at the generation stage, proper inclusion of the energy dependence is very important as particle energy spectra are changing by orders of magnitude in the range of interest, as illustrated in Figure 6.3 (left). Just as for angular distributions, the energy spectra are extracted from the FLUKA simulation. The sensitivity at a given particle energy is computed as the fraction of all generated events, in which a signal is observed, separately for each of the two detectors comprising a superchamber. The sensitivities obtained for the two chambers in a supercham-

ber are found to be very similar and the difference is taken as the systematic uncertainty. Thus obtained energy dependent sensitivities are shown in Figure 6.3 (right) with the bands indicating the total uncertainty. The final average sensitivities are computed as a convolution of the energy spectra with the energy dependent sensitivities for each particle type and are shown in Table 6.3. In the neutron case, the uncertainty includes an additional systematic uncertainty related to the Geant4 model used to simulate low energy neutron interactions.

Table 6.3: Sensitivity results for GE1/1. The uncertainties include both the statistic and the systematic uncertainty related to the different response of the two layers of chambers installed in an even and the odd configuration. In the neutron case, also a source of systematic uncertainty related to the GEANT4 model used to simulate low energy neutron interactions is included.

	Sensitivity [%]
neutrons	0.18 ± 0.05
photons	0.97 ± 0.04
electrons	8 ± 3
positrons	8 ± 3

Final computation of the detector hit rates induced by long-lived neutrons is performed by summing up the contributions from neutrons, photons and charged particles. Each contribution is calculated as the particle flux (see Figure 6.2 (right)) weighted by the corresponding average sensitivity (see Table 6.3). The combined hit rate as a function of η is shown in Figure 6.4 along with the individual contributions from neutrons, photons and charged particles.

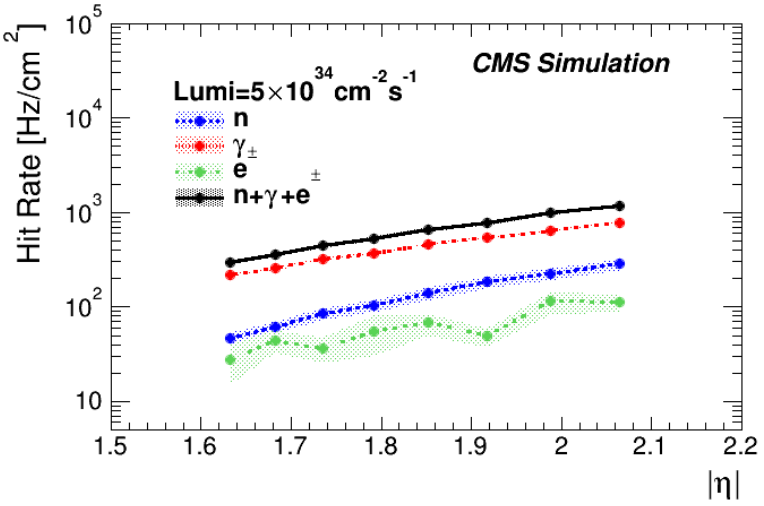

Figure 6.4: The expected contribution to the GE1/1 detector per-chamber hit rate associated with the backgrounds induced by long-lived neutrons for instantaneous luminosity of 5×10^{34} cm^{-2} s^{-1} as a function of pseudorapidity.

6.1.2 Software implementation and detailed simulation of the GE1/1 system

The integration of the GE1/1 detector into the full GEANT-based CMSSW framework has been a necessary step for the design of the algorithms and performance studies related to trigger, reconstruction and identification. As a first step, GEANT propagates particles through the GE1/1 detectors and generates energy deposits. A second required step is the digitization, which uses the ionization energy deposits generated by GEANT to emulate signals measured

in detector electronics according to an appropriate model. As discussed earlier, the long-lived backgrounds have not been simulated by GEANT and the digitization step has been used to embed the long-lived background hits. In the following, we describe the details of the model implemented in the digitization procedure.

Similar to the simulation of other CMS sub-detectors, the GE1/1 digitization uses a parametric model derived using a combination of test beam data analysis results and specialized simulation studies of the detector response. In the digitization process, energy deposits generated by GEANT for all particles crossing the detector are first individually converted into detector signals, i.e. signals induced on the detector readout strips or groups of strips. The digitization model takes into account the type of particle depositing energy as well as the time of the particle arrival, which is additionally smeared over the time resolution of the detector. In this step, hits due to electronics noise and due to long-lived background are embedded. Next, the overlapping signals are merged and assigned to the corresponding 25 ns clock window, which associates the signals to the correct bunch crossing. In the following, we describe the default parameters used in the GE1/1 digitization model.

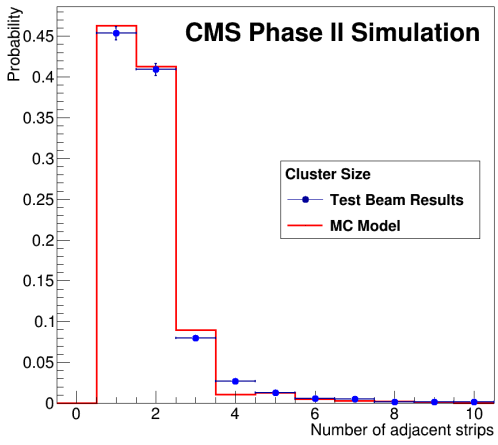

Figure 6.5: Comparison of the cluster size distribution obtained with the CMSSW simulation (line) compared with the test-beam measurements, which have been used to model the detector response in CMSSW.

- **Efficiency:** The registration efficiency is set to 98% for true muons crossing an individual chamber, which follows the results of the test beam studies [12]. The efficiency for all other particles crossing the chamber, e.g. photons from muon showering, follow the results of the sensitivity studies presented in the previous section.
- **Timing:** The true time at which the particle crosses the chamber is first adjusted by subtracting the time of flight for a muon from the nominal interaction point to the centre of the chamber to emulate the readout of detector t_0. Next, it is smeared according to the detector timing resolution (presented results use $\sigma = 5$ ns) following a Gaussian distribution. Finally, the time is corrected for the signal propagation time along the strip and the resulting time is used for assigning the corresponding time window (the bunch crossing) to the signal.
- **Cluster size:** The readout strips are "fired" (GE1/1 electronics readout is binary) according to the geometrical location of the hit and according to the signal shape measured in the test beam data for charged pions. The latter is implemented by

"firing" additional adjacent strips based on the probability function extracted from the test beam data. The mean value of the measured and simulated cluster size has been found to be $\sim$ 1.8. A validation of the procedure is illustrated in Figure 6.5 comparing the cluster size in the simulation using the digitization model with the test beam data.

- **Neutron-induced background and intrinsic noise:** modeling of the long-lived background is implemented following the results of the simulation-based hit rate estimation described in the previous section. The embedding of spurious signals due to photons, neutrons and charged particles follows the parameterized η-dependent functions obtained by fitting the distributions in Figure 6.4. The background hits and signal hits have the same model for generating clusters, but the time assignment follows a random (uniform) distribution. The intrinsic noise rate has been estimated as ~ 0.01 Hz/cm^2 and hence neglected.

The implementation of the GE1/1 digitization model with a realistic detector response and the inclusion of the neutron-induced backgrounds in the CMSSW framework allows the evaluation of the impact of GE1/1 upgrade on the overall performance of the CMS experiment. Simulation studies of muon trigger and offline reconstruction performance presented in the remainder of this chapter are carried out in the context of the common CMSSW framework.

6.1.3 Summary of the GE1/1 detector hit rates

The fully inclusive detector hit rate for the GE1/1 system is a sum of the hit rates due to the prompt and long-lived backgrounds. Figure 6.6 shows the contributions of each of these two components obtained using the simulation in the context of CMSSW for the instantaneous luminosity $\mathcal{L} = 5 \times 10^{34}$ cm^{-2}s^{-1}. Note that Figure 6.6 (left) compares the hit rate using a sample simulated in CMSSW with the FLUKA-based predictions used as input to the digitization model, which is essentially a closure test. The majority of the prompt component of the hit rate is due to the secondary electrons and positrons arising from Compton scattering, secondary ionization, conversions, and e^+e^- pair production. Secondary muon contributions arise from nuclear interactions of hadrons in the calorimeter and the absorber, heavy flavor, and decays in flight. The energy spectrum of secondary particles is dominated by very low energy particles. The prompt particle rates are evaluated using a sample of minimum bias events simulated with CMSSW. The integrated number of hits in a given η partition is normalized to the sensitive area of the partition and the time particles have been allowed to propagate following the pp interaction. The results are then scaled to the average number of interactions per bunch crossing corresponding to the instantaneous luminosity. All hits generated by particles within the window of 500 ns relative to the time of the primary interaction are counted. This procedure somewhat overestimates the hit rate due to prompt particles as the majority of energy deposits in the GE1/1 detection planes beyond the first 50 ns are due to the long-lived neutrons. We do not attempt to subtract that contribution as our goal is to verify that the contribution due to prompt particles is small rather than a precision measurement of the simulation predictions. The right plot in Figure 6.6 shows the obtained rates as a function of the distance from the center of the partition to the beam pipe. As expected, the contribution to the total rate due to the prompt particles is substantially smaller compared to that due to that arising from long-lived neutrons shown in the left plot in the same figure.

It is important to note that the estimated GE1/1 detector hit rate of up to a few kHz is much lower than the rates existing and successfully operating GEM detectors have been exposed in other working experiments. We therefore conclude that the background environment of the future GE1/1 detector is adequate for a safe and reliable long-term operation of a GEM-based

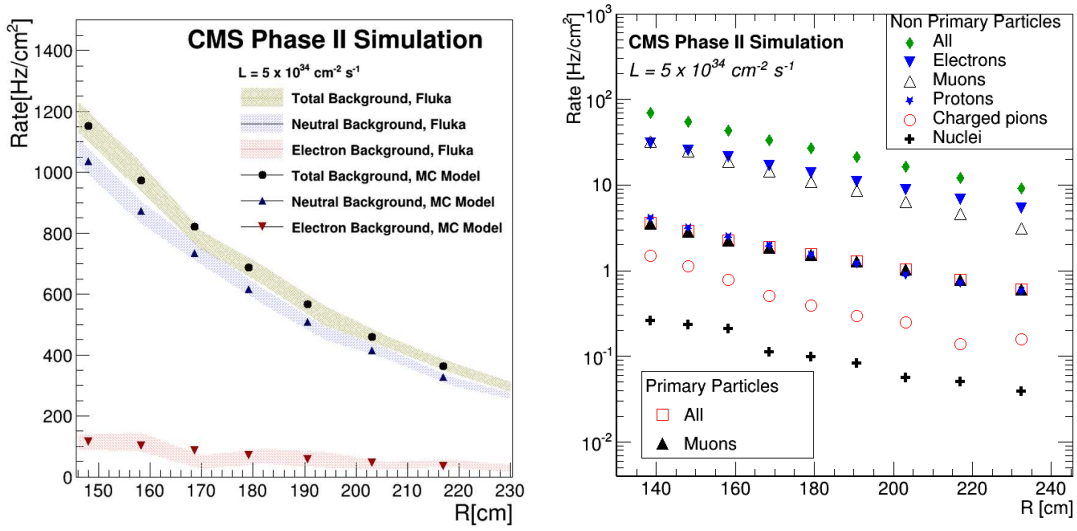

Figure 6.6: *Left:* The GE1/1 hit rate due to neutron-induced backgrounds obtained with the CMSSW simulation (data points) compared with the FLUKA prediction used to model these backgrounds in CMSSW (the width of the band indicates the uncertainty). *Right:* Rates of prompt particles reaching GEM detector planes in the first endcap station as a function of the radial distance to the beam pipe.

detector (see also Section 2.2.2.4).

6.2 Muon trigger performance

Maintaining efficient Level-1 muon triggering in the forward region $|\eta| > 1.6$ becomes progressively more difficult as the instantaneous luminosity increases. The forward region is inherently challenging due to low magnetic field and high background rates, which is further exacerbated by the lack of redundancy as the region is only instrumented by the CSC detector. As a result, the trigger rate shows a fast growth towards higher η illustrated in Figure 6.1 (right). In relative terms, the lack of redundancy in the region $|\eta| > 1.6$ will become even more apparent with the deployment of the upgraded muon trigger in 2016, capable of including hits from all available detectors in the track momentum fit. This new feature leads to essentially doubling the number of "guaranteed" points on tracks ensuring a good muon momentum measurement and a significant reduction of the trigger rate driven by soft muons with mismeasured momentum. However, the rate will be reduced only in the region of $|\eta| < 1.6$ where such redundancy is available.

The GE1/1 upgrade provides an effective solution to the trigger rate problem and allows CMS to preserve its excellent muon triggering capabilities in the range $|\eta| < 2.2$ until the LS3 and beyond. As it has been discussed earlier, GE1/1 allows preserving low muon trigger thresholds between LS2 and LS3, which has an important impact on CMS physics reach for Higgs precision measurements and new physics searches. With the deployment of the Level-1 tracking trigger in LS3, standalone muon trigger candidates will be matched to the inner tracks allowing for ultra-high purity muon triggering with low thresholds. At the same time, the high quality standalone muon trigger will remain important in maintaining efficiency for signatures with displaced muons, which the tracking trigger will be inefficient for. GE1/1 will also add to the

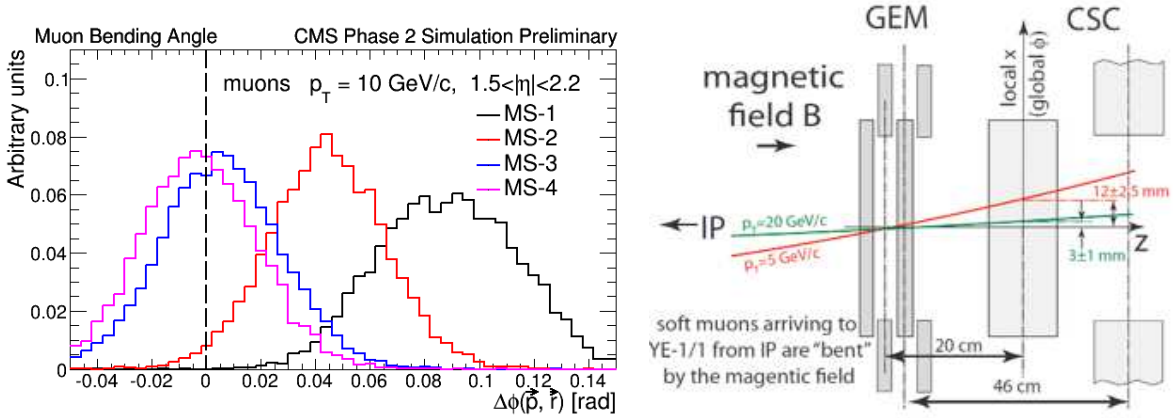

Figure 6.7: *Left:* Azimuthal bending angle of a simulated 10 GeV muon with respect to a normal vector to a CSC chamber, comparing the distributions for the four stations. *Right:* Sketch of a measurement of the bending angle with a pair of a CSC and a GEM chamber, illustrating discrimination between lower and higher momentum muons.

stability of the system as GE1/1 can partially offset the effects of possible decreased performance of the aging ME1/1 chambers.

6.2.1 Integrated local CSC-GEM L1 trigger

The challenge for triggering in the forward region, with $|\eta| \gtrsim 1.6$ arises from decreasing capabilities to discriminate low momentum muons from the high momentum ones. The rate is driven by muon momentum mis-measurements associated with the tails in the p_T resolution of the muon trigger. The CSC trigger measures muon p_T using the positions of stubs reconstructed in muon stations that the track crosses: if a soft muon undergoes a substantial scattering in the material of the absorber, it can sometimes be reconstructed as a high-p_T candidate.

Of the four muon stations in the CSC system, the first one (ME1/1) is of special importance for triggering. This is because the muon track's lateral displacement (along the direction of a change of the azimuthal angle), the main observable used by the CSC track finder for measuring the muon momentum, is the largest in the first station. As a result, presence of a reconstructed segment in the first station plays a key role in the precision of the CSC track finder momentum measurement. Inversely, any inefficiency in reconstructing segments in station ME1/1 reduces momentum resolution. The turning angle from the magnetic field also reaches the maximum in the first station ME1/1, as shown in Figure 6.7 (left). However, muon direction measurement cannot be utilized in the trigger because of low accuracy of a measurement within the ME1/1. It is limited by the low magnetic field in the forward region and, with the thickness of the CSC chambers of only about 11 cm, the lever arm is too small to compensate for it.

The achievable improvement in the trigger performance with the addition of GE1/1 is so significant because the proposed upgrade allows addressing both of the aforementioned points simultaneously. First, it creates a large enough lever arm between GE1/1 and ME1/1 chambers to enable a good measurement of the muon direction (the "bending angle") within the first station, as illustrated in Figure 6.7 (right). Second, the added redundancy allows reducing the fraction of muons with unreconstructed segments in the first station, which in turn reduces the fraction of poorly measured muon candidates.

The integrated CSC-GEM local trigger algorithm has been designed for implementation in the

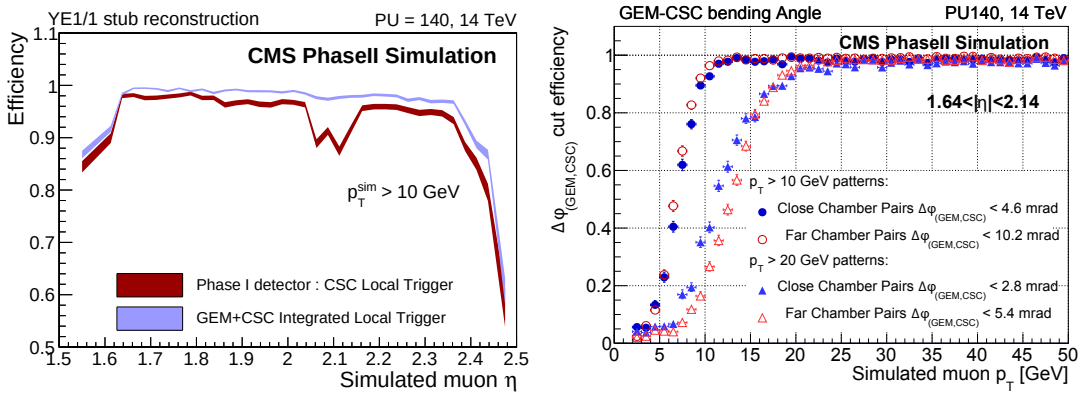

Figure 6.8: *Left:* Muon track segment (LCT) reconstruction efficiency of the integrated GEM-CSC trigger as a function of the simulated muon $|\eta|$, compared to the same for the Phase-I CSC-only algorithm. The upgrade allows for a large reduction in the number of muon candidates without a reconstructed segment in the first station, which have a reduced momentum resolution and make a disproportionally large contribution to the Level-1 trigger rate. *Right:* Simulated muon efficiency to pass a predetermined threshold high-efficiency pattern flag for even ("close") and odd ("far") GEM-CSC chamber pairs. The thresholds on the bending angle are selected to deliver a 98% efficiency for p_T values of 10 and 20 GeV. The bending angle selection effectively provides a second independent measurement of muon p_T , which is mostly uncorrelated with the measurement based on deflections of trajectory utilized in the current endcap Level-1 muon trigger.

ME1/1 Level-1 trigger board (OTMB). The OTMB reconstructs local charged track segments (LCT stubs) based on the inputs received from the CSC and GEM detectors. The CSC information is combined from the anode wire-group measurements in the polar angle (or radial position) change direction and from the cathode strip measurements in the azimuthal angle change direction. The anode measurements are combined in anode LCT stub component (ALCT) by the on-chamber electronics processor. The cathode LCT stub component (CLCT) is reconstructed by the OTMB based on data from on-chamber comparators which deliver per-layer strip information as binary hits with half a strip granularity achieved by using charge-sharing information in three neighboring strips. The wire-groups run at an angle along the length of an ME1/1 chamber. The strips are cut at a distance from a nominal beam line of 150 cm at $|\eta| \approx 2.1$, corresponding to ME1/1a and ME1/1b parts in the lower (higher $|\eta|$) and upper parts, respectively. A GE1/1 super-chamber extends over the entire η coverage of ME1/1b and the lowest partition of GE1/1 overlaps with the upper third part of ME1/1a. The GEM trigger pad information (a hit from two strips combined) arrives separately from each chamber in a super-chamber. A coincidence of pads between two chambers with some tolerance to allow non-normal incidence is treated as a co-pad bit.

In the existing version of the algorithm, an LCT is built by the integrated CSC-GEM algorithm for the following input cases in addition to the presence of an ALCT:

- There is a CLCT with at least four layers.
- There is a CLCT with only three layers and at least one matching GEM pad is found in the region of coverage by GEM; a three layer CLCT is used in ME1/1a region not covered by GEM.
- No CLCT is found and there is a GEM co-pad.

Except for the last case, the LCT data is built from the ALCT and CLCT. In the last case, an LCT is built from ALCT and GEM co-pad. Since an ALCT reconstruction efficiency is higher than 99% in the full range of ME1/1, the requirement of an ALCT for all LCT categories in the current algorithm yields only a small inefficiency, which can be further reduced if necessary.

The efficiency to reconstruct an LCT by the integrated CSC-GEM trigger, compared to the reconstruction based on the CSC chamber data alone is shown in Figure 6.8 (left). Additional redundancy provided by GE1/1 results in an increase in efficiency in the entire η range of the chamber. Additionally, a large drop in efficiency in the ME1/1a-ME1/1b transition region is recovered with help from GEM information. The bending angle is computed whenever both a GEM pad and a CLCT are available. The value of the bending angle is used to define high-efficiency angle pattern bits (98% used here), which are encoded in the modified LCT hardware data format. A modified track finder algorithm will use the bending angle in the definition of its track finding patterns. A simpler alternative is to reject muons if the momentum measured by the track finder is not compatible with the bending angle measurement at the cost of a small inefficiency. Results of this selection are illustrated in Figure 6.8 (right) where 10 and 20 GeV thresholds are used.

One further development of the integrated local trigger algorithm aims to extend matching of the CSC and GE1/1 data to ± 1 bunch crossing to account for GE1/1 hits reconstructed in the bunch crossing preceding or following the true bunch crossing due to the finite timing resolution of the detectors. The simulation used to design the existing algorithm and evaluate its performance has been tuned to reproduce the test beam data and predicts the rate of such misconstructions to be less than 5% of the time. However, if the use of a more eco-firiendly gas becomes a necessity, it is possible that GE1/1 will need to operate at a reduced timing resolution leading to an increased probability of GE1/1 hits having misreconstructed timing. The extension of the time matching window to ± 1 bunch crossing allows recovering correct timing assignment by comparing four independent time measurements (two GEM layers plus CSC anode and cathode stub timing measurements) for spatially matching combinations of hits. With the small spatial size of the search windows seeded by the CSC stubs, accidental matches are exceedingly rare and so the reduction in reconstruction efficiency and the increase in the rate of misidentified stubs are both negligible. The extended GE1/1-ME1/1 local trigger algorithm allows maintaining performance even in the event of significant degradation in timing resolution, e.g. in the conservative scenario in which GE1/1 switches to the $ArCO_2$ mix, which has been evaluated as part of the GE1/1 test beam studies. The implementation of such enhanced algorithm in the ME1/1 OTMB FPGA does not require any modifications to the hardware or electronics and is limited to firmware modifications only.

6.2.2 Muon trigger performance in Phase 1

Installation of the GE1/1 station in LS2 will allow for a reliable and efficient muon triggering with low thresholds in the entire range of $|\eta| < 2.2$ in the period of highest instantaneous luminosity of Phase-I operations. Figure 6.9 shows the large reduction in the muon trigger rate in the region of $1.6 < |\eta| < 2.2$ achievable with the deployment of the GE1/1 detector. The new trigger also provides for a non-negligible improvement in efficiency with the plateau efficiency of 96%. An important operational feature of the new trigger is that it eliminates the flatness seen in the curve for the CSC-only trigger, making reductions in the rate of the trigger achievable with only small increases in the threshold values. Even with the large rate suppression achievable with the deployment of GE1/1, the Level-1 rate shown in Figure 6.9 remains driven by mismeasurements of momenta of soft muons originating from heavy flavor, decays in flight and interactions in the material. As a reference, the contribution of muons

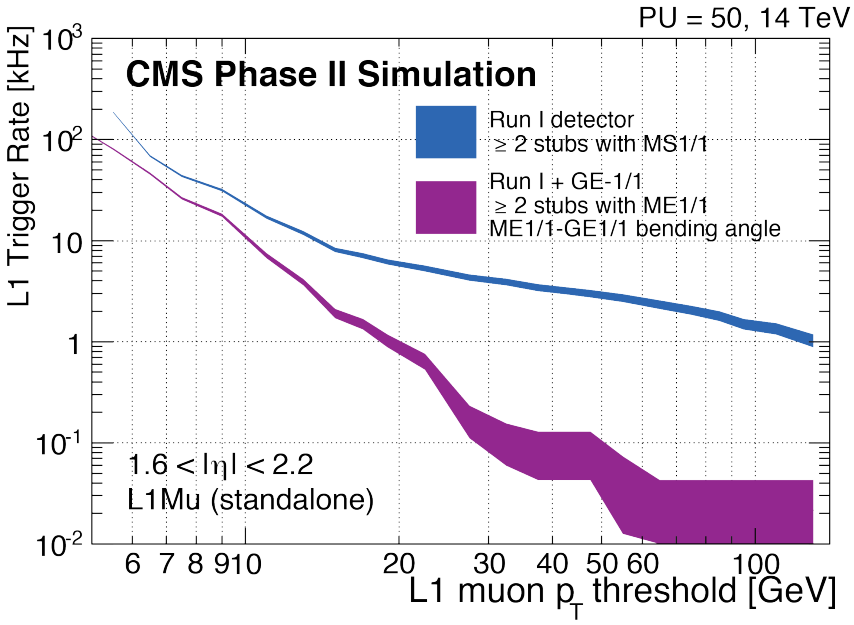

Figure 6.9: Level 1 muon trigger rates before and after the GE1/1 upgrade at a luminosity of 2×10^{34} cm^{-2} s^{-1}, for constant efficiency of 94%. MS1/1 denotes the first endcap muon station Level 1 trigger in both cases, i.e. with CSC-only or with the combination CSC and GEM trigger information. With the addition of GE1/1, the bending angle between the two stations can be used and the trigger rate is greatly reduced.

originating from W and Z decays to the trigger rate is at least an order of magnitude lower than the contribution due to momentum mismeasurements for Level-1 thresholds below $p_T \sim 20$ GeV, the range relevant for trigger operations. As the use of the bending angle effectively "unsmears" the trigger curve, the rate reduction for Level 1 thresholds below $p_T \sim 15$ GeV naturally diminishes. However, as the configuration shown in Figure 6.9 has been chosen to introduce essentially no additional trigger efficiency losses in the entire momentum range, the trigger rate at lower p_T thresholds can be further reduced as a result of additional optimization at some cost to efficiency in the lower p_T domain.

Improved performance of the Level-1 muon trigger allows for lower thresholds at a given rate not only for the inclusive Level-1 muon trigger, but also for the multi-object triggers involving muons in their selections. Lower trigger thresholds increase acceptance and enhance the CMS physics reach for a broad range of scenarios featuring relatively soft muons. In the SM Higgs case, even a modest reduction in muon trigger thresholds leads to a significant increase in the acceptance for $h \to \tau\tau \to \mu\tau_{had} + X$, which has the highest sensitivity among all $\tau\tau$ final states and in which muons, arising from the three body decays of tau leptons, are inherently soft. Processes with associated Higgs production where Higgs decays into a pair of taus provide another example. Other interesting scenarios to be explored with the dataset collected during Phase-I operations include models with the extended Higgs sector which can have an appreciable cross section, e.g. the production of a heavier Higgs H, followed by a decay $H \to hh \to \tau\tau bb$ strongly depends on muon trigger thresholds for $m(H)$ up to a few hundred GeV. Some striking examples include "compressed" SUSY scenarios, such as stop pair production where stop decays via $\tilde{t} \to \mu\chi^0 + X$ and the mass difference $m(\tilde{t}) - m(\chi_1^0)$ is small. Sensitivity to such signatures critically depends on the muon trigger threshold, as illustrated in Figure 6.10 showing the distribution of muon p_T. Other examples dependent on muon or muon+X triggers include

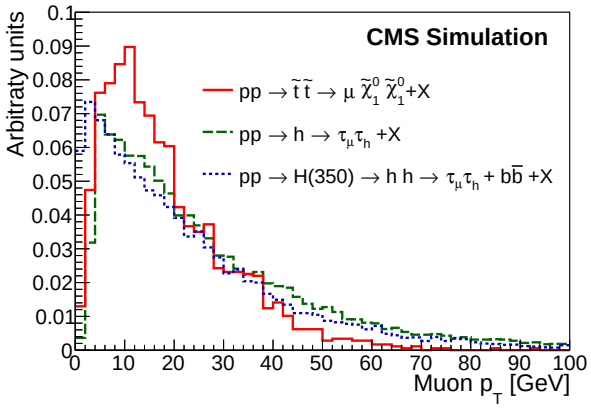

Figure 6.10: Distribution of muon p_{T} for several illustrative physics processes, for which acceptance strongly depends on low trigger thresholds for the single muon trigger: production of a SM-like higgs decaying via $\tau\tau \rightarrow \mu + X$, 2HDM type heavy higgs production $pp \rightarrow H \rightarrow hh \rightarrow \tau\tau bb$ with $m(H) = 350\,\mathrm{GeV}$, and SUSY stop production in a challenging for the LHC scenario with the "compressed" mass spectra (in this case $m(\tilde{t}) - m(\chi_1^0) = 40\,\mathrm{GeV}$).

challenging SUSY scenarios with heavy squarks and gluinos and small mass splittings among the lighter gauginos yielding soft leptons, e.g. via $\chi^+ \rightarrow \mu\chi^0 + X$.

A number of trigger paths targeting a range of physics signatures in Higgs, SUSY and "exotic" realms rely on muon selections at Level 1. Examples of such triggers include di-muon, tri-muon, muon+hadronic tau and muon+jet triggers, in which more exclusive selections allow lower thresholds and thus an increased acceptance for the targeted processes. Improvements in Level 1 muon trigger performance associated with the deployment of GE1/1 reduce the rates of these triggers, thus allowing lower thresholds on muon p_{T} or the momenta of other objects. This general illustration is relevant for a number of processes, e.g. the SUSY dilepton searches in scenarios with light $\tilde{\tau}$ and gauginos featuring very soft muons as the mass difference $m(\tilde{\tau}) - m(\chi_1^0)$ is small.

General considerations on the importance of maintaining lower muon trigger thresholds arising from signal kinematics at generator level remain valid in the environment with a substantially increased density of particles. We illustrate that using a sample of simulated $H \rightarrow 2\tau \rightarrow \mu\tau_h$ events, in which Higgs boson is produced via Vector Boson Fusion (VBF). The channel with one tau decaying to a muon and the other decaying hadronically is special in that it makes a very large contribution to the overall sensitivity of the $H \rightarrow \tau\tau$ measurement [58] due to the low backgrounds, with respect to the other decay channels, and a large branching fraction. The events are generated at $\sqrt{s} = 14$ TeV and overlaid with an average of 50 additional minimum bias events to emulate the high pile-up environment using standard CMS simulation tools.

Events are reconstructed with the common CMS techniques using the Particle Flow framework, followed by kinematic and particle identification selections closely resembling requirements in the CMS Run 1 H$\rightarrow 2\tau$ observation paper [58]. Selections include the same requirement of two jets separated by a large rapidity gap as in the original analysis, which greatly improves the ratio of signal to background dominated by $Z(\rightarrow \tau\tau)$+jets. Isolation selections used in muon and hadronic tau identification have been adjusted to loosen the requirements on the isolation energy deposited by neutral particles, as their contributions cannot be associated to vertices and the selection becomes too restrictive at high luminosity.

We evaluate the effect on the signal acceptance by varying the muon p_{T} threshold used in

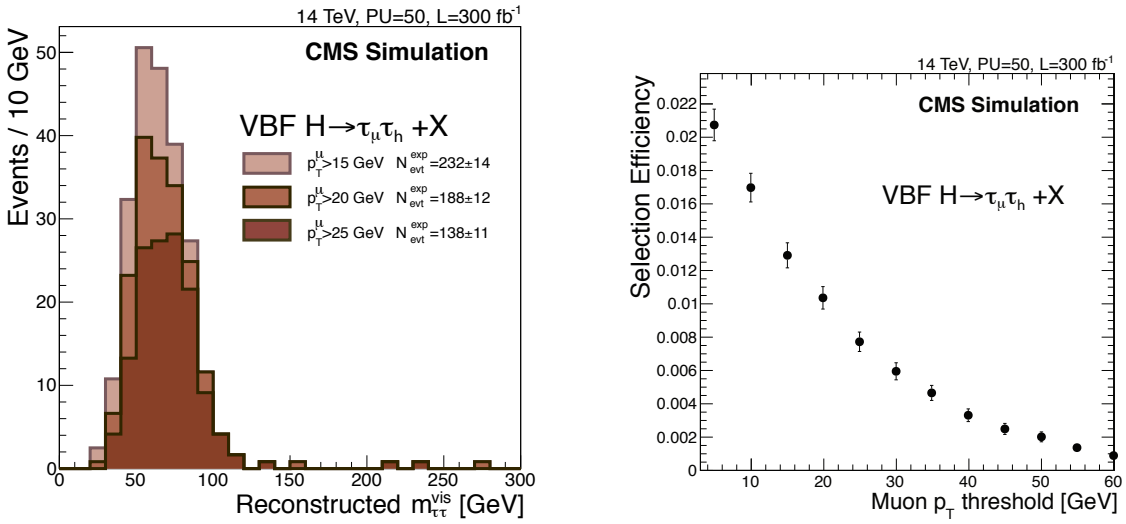

Figure 6.11: *Left:* The distribution of the visible mass of the μ, τ_h, met system for events surviving all analysis selections for the $H \to \tau\tau$ search in the VBF category in the $\mu\tau_h$ final state. The three distributions correspond to a sample with 300 fb^{-1} and the offline muon p_{T} threshold set to 15, 20, and 25 GeV, illustrating importance of maintaining low muon thresholds in the trigger and in the offline. *Right:* Full $h \to \tau\tau$ analysis selection efficiency for the $\mu\tau_h$ VBF category as a function of the chosen offline muon p_{T} threshold.

analysis selections in the range $5 < p_{\mathrm{T}}^{\mu} < 60$ GeV. Figure 6.11 (left) shows the distribution for the reconstructed visible mass of the $\mu + \tau_h$+MET system for p_{T}^{μ} thresholds of 15, 20, and 25 GeV along with the total number of reconstructed events passing all selections (in 23% of these events, muon candidate falls into the GE1/1, with this fraction being nearly independent of the p_{T}^{μ} threshold). Note that even with $L = 300$ fb^{-1} of data, the final sample remains fairly limited in statistics, emphasizing the importance of maintaining maximum possible acceptance. These results show that, on average, reducing muon threshold by 5 GeV, from 25 GeV to 20 GeV, yields a 35% increase in the number of signal events passing all analysis selections and an overall 68% increase if the thresholds are reduced from 25 GeV up to 15 GeV. Figure 6.11 (right) illustrates these observations by showing the gains in the acceptance associated with the reduction in the p_{T}^{μ} threshold used in the offline analysis.

6.2.3 HL-LHC trigger performance

Deployment of the tracking trigger by CMS in LS3 will allow an ultra-high purity and low-rate trigger targeting prompt muons by matching standalone muon candidates with the Tracker tracks. The excellent momentum resolution of the Tracker eliminates the flattening of trigger-rate curve owing to mismeasured low-p_{T} muons and yields a very sharp turn-on of the trigger efficiency. Using tracking isolation, which is less sensitive to PU than calorimeter isolation, and combining objects targeting exclusive final states allows very high purity and low trigger rates. The new combined trigger objects, referred to as L1TkMu, use track-trigger tracks extrapolated to the muon stations and matched with L1 standalone muon candidates. The GE1/1 information can contribute in resolution of ambiguities. More details about the Tracker part of the trigger can be found in [3].

Preserving the standalone muon triggering capabilities will continue being important in HL-LHC era. One particularly critical aspect is preserving the sensitivity to scenarios of new physics predicting displaced muons arising from decays of new particles with finite lifetime.

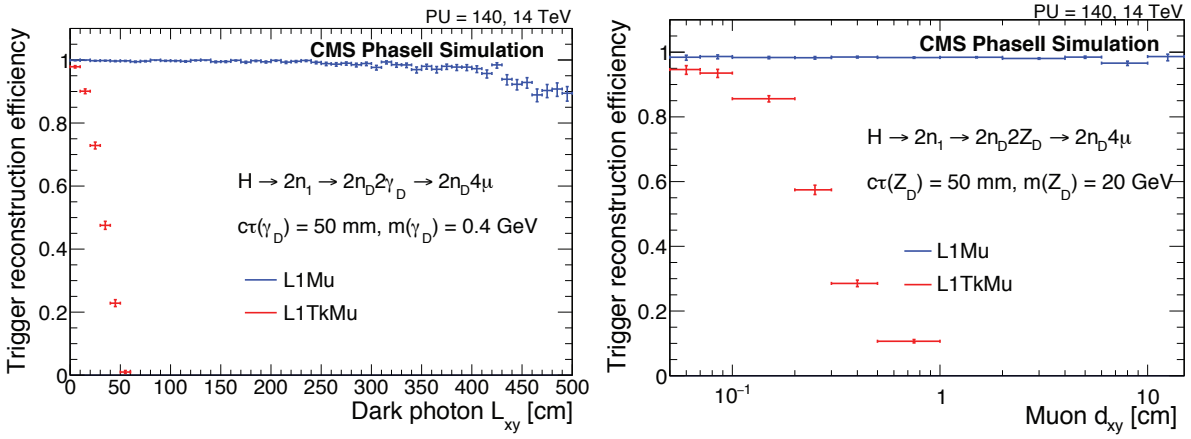

Figure 6.12: *Left:* The probability of reconstructing at least one muon candidate produced in the decay of a light long-lived light particle decaying to a pair of muons $\gamma_d \to \mu\mu$ as a function of L_{xy}, the distance between the γ_d decay vertex to the beamline in the transverse plane. Standalone muon trigger L1Mu performance is compared to that of L1TrkMu, a trigger based on matching muon and track trigger candidates with the CMS Phase-II detector simulation. Other parameters of the model are shown in the legend and are chosen to ensure that a typical muon transverse impact parameter d_{xy} is small to minimize any sources of inefficiency not associated with L_{xy}. *Right:* Probability to reconstruct a muon using L1Mu and L1TrkMu algorithms as a function of muon's true transverse impact parameter d_{xy}. The parameters of the model are chosen to provide a good coverage over the entire region of d_{xy} shown. Only muons with small true L_{xy} and $p_{\mathrm{T}} > 8\,\mathrm{GeV}$ are used in the measurement to minimize sources of inefficiency not related to d_{xy}.

Such models are motivated by a range of considerations spanning from the electroweak baryogenesis requiring additional singlet fields, models with hidden sectors, a number of SUSY scenarios etc. As the tracking trigger efficiency vanishes for tracks produced away from the beam spot, standalone muon triggering is the only viable option to trigger on such events, as triggering on displaced electrons or pions with energies at the electroweak scales is hardly conceivable in the high occupancy environment of the HL-LHC.

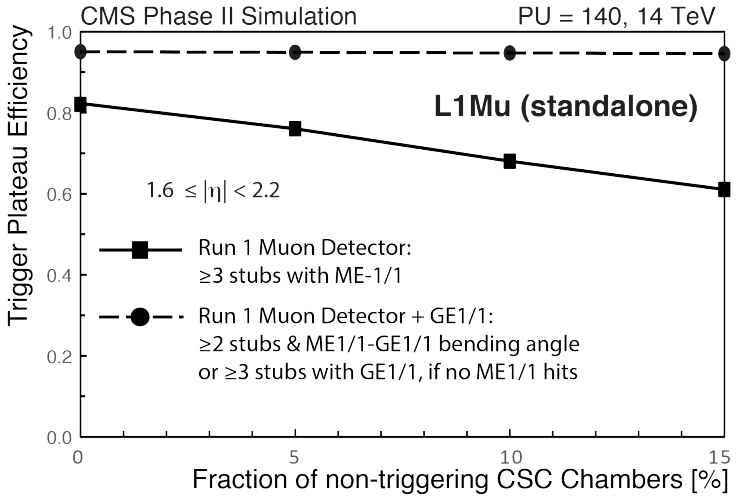

Figure 6.13: Single-muon trigger efficiency at the plateau in p_{T} as a function of the fraction of non-triggering CSC chambers, in Phase-I and Phase-II.

To illustrate the sensitivity of the standalone muon trigger to signatures with displaced leptons, we select two benchmark scenarios suitable for exploring a broad phase space of possible models predicting displaced muons. Both are implemented in the context of a SUSY with hidden sectors, in which new bosons are produced in the decays of a SM-like Higgs boson h with mass of 125 GeV into pairs of neutralinos n_1, which then decay into a stable dark sector neutralino n_d and a dark photon of mass $m(\gamma_d) = 0.4\,\mathrm{GeV}$ via $H \to 2n_1 \to 2n_d 2\gamma_d$. The second scenario $H \to 2n_1 \to 2n_d 2z_d$ differs only in replacing a low mass γ_d with a heavier "dark" Z boson with $m(z_d) = 20\,\mathrm{GeV}$. The new dark bosons are allowed to decay to pair of muons and each has $c\tau = 50\,\mathrm{mm}$. These two scenarios yield two very different topologies: in the first case a light γ_d decays into a collimated pair of muons produced away from the beamline and approximately pointing back to the beamspot, while in the second case muons are typically produced close to the beamspot, but have a substantial impact parameter. Figure 6.12 (left) compares the performance of the L1TrkMu and the standalone muon trigger L1Mu algorithms in reconstructing at least one of the two muons with no p_{T} thresholds required for the first model as a function of L_{xy}, the transverse displacement of the decay vertex from the beamspot. Figure 6.12 (right) shows the trigger reconstruction efficiency per muon as a function of its true impact parameter d_{xy} for the second model. In this case, only muons with small L_{xy} are chosen to factorize the inefficiency related to L_{xy}. It is apparent that the sensitivity to signatures with long-lived particles decaying to muons requires an efficient standalone muon trigger. These observations suggest a muon trigger based on two complementary flavors: the ultra-high purity L1TkMu featuring low thresholds and targeting prompt muons and a standalone L1Mu targeting muons reconstructed in the muon spectrometer but not the tracker in either pointing or explicitly not pointing topology. In the latter case, muon candidates will feature muon chamber stubs aligned along a straight line non-pointing back to the beamspot. Cosmic and beam halo muons featuring a similar unusual topology would be easy to remove already at the

trigger level.

Another important consideration for Phase-II detector operations is the aging of the CSC system that could increase the rate of hardware failures and/or degrade the performance of the chambers. ME1/1 chambers are a particular concern as they are subjected to by far the highest radiation levels among all muon detectors in CMS. To evaluate efficiency losses in the scenario with a fraction of ME1/1 chambers becoming inoperable, we choose the nominal L1Mu configuration for the existing Run 1 detector to require muon candidates to have 3 reconstructed stubs (out of 4 possible), one of which must be reconstructed in station ME1/1. While the rate of such trigger is too high for Phase-I operations, an increased bandwidth of the Phase-II L1 trigger could hypothetically allow such trigger. However, even such "loose" trigger would develop a significant deterioration in the trigger plateau efficiency with even a moderate fraction of non-triggering ME1/1 chambers in station ME1/1, as illustrated in Figure 6.13. The same plot shows that the inclusion of GE1/1 in the trigger allows designing a configuration capable of mitigating losses in trigger performance due to inoperable ME1/1 chambers. Furthermore, this trigger configuration yields an acceptable rate and noticeably higher plateau efficiency.

6.3 Muon reconstruction performance

Maintaining the high reconstruction efficiency and low misidentification rate of muon reconstruction at high luminosity is a high priority for CMS. The physics reach of the CMS experiment is dependent on the excellent performance of muon reconstruction, as evidenced by the role of the final states with muons in the recent Higgs discovery and abundance of searches for new physics relying on channels with muons. With the increase in luminosity, the relative importance of muons in analyses will grow, nonetheless the muon system will not be immune to an increase in background hit rate.

The high luminosity environment and the aging of the existing detector brings several challenges. The standard CMS muon reconstruction relies on matching the inner tracks propagated to the muon system with the standalone muon tracks reconstructed in the muon spectrometer. The small size of the matching windows, thanks to the accurate position measurement and good momentum resolution of standalone muons, prevents degradation in performance even with large increases of the inner track multiplicity. However, aging of the existing muon detector can accelerate the rate of detector failures and this will degrade the spatial and momentum resolution of the standalone muon reconstruction, which will force us to adopt larger matching windows. The increase in combinations by using larger matching windows can degrade the efficiency and increase the rate of misidentified muons. Failures in the first muon station, where the multiple scattering is the lowest and the bending of the tracks in the magnetic field is the largest, have a particularly strong impact on the quality of the standalone muon reconstruction. Furthermore, chambers in the first station of the forward muon region are the ones that will accumulate the highest doses of radiation.

Similar to the standalone muon trigger case, the standalone muon reconstruction has another important role in physics scenarios predicting long lived particles. If the lifetime of these new particles is significant, the bulk of the CMS acceptance to such signatures would be strongly dependent on the quality of the standalone muon reconstruction. In this case, the high performance of reconstruction in first muon station is especially critical as it drives the momentum resolution.

In the following, we demonstrate that the new GE1/1 system can be harmoniously integrated into the CMS muon reconstruction paradigm. We show that the addition of a new precision

muon detector in the strategically important first station adds to the robustness of the muon reconstruction by minimizing the degradation in performance if parts of the existing system become inoperable due to aging. The impact on the standalone muon reconstruction is particularly significant. The following results do not include effects such as miscalibration or alignment, but those are not expected to have a significant impact on our conclusions.

6.3.1 Integration of the GE1/1 detector into the common CMS muon reconstruction

The design of the GE1/1 detector facilitates its seamless integration into the common CMS muon reconstruction framework. In the following, we describe the details of how the information of the new detector is used for the muon reconstruction in the upgraded CMS experiment.

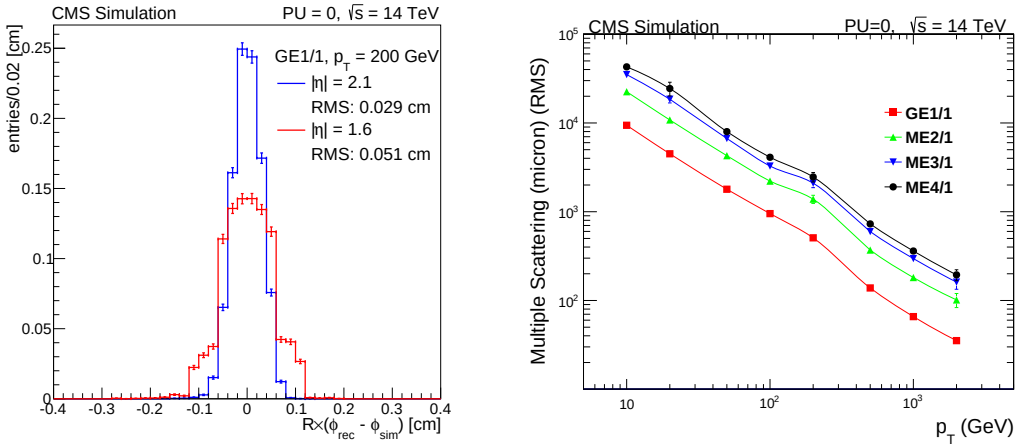

Figure 6.14: *Left:* The distributions of the differences between the reconstructed hit x-position and the true hit position in GE1/1 in the top and bottom parts of the chamber. The RMS of the distributions is the single hit resolution in the x-coordinate in the corresponding parts of the chamber, which is not constant as the GE1/1 strips are pointing radially (and the strip width varies accordingly). The distribution corresponds to a sample of muons with $p_{\mathrm{T}} = 200\,\mathrm{GeV}$. *Right:* The RMS of the multiple scattering displacement as a function of muon p_{T}, for GE1/1 and all the other forward muon stations, evaluated at $\eta = 2.0$. All electromagnetic processes such as bremsstrahlung and magnetic field effects are included in the simulation.

The local reconstruction of the GE1/1 system uses the digital readout data to combine the nearby hit strips to form clusters. The position of the clusters is determined as an average of the x-positions of the strips assigned to the cluster (GEM digital readout does not provide the information on the signal amplitude for the strips, so each strip is assigned the same weight). The uncertainty is calculated as the $N_{st} \times \delta x_p / \sqrt{12}$, where N_{st} is the number of strips in the cluster, $\delta x_p = 450\ \mu\mathrm{rad} \times R$ is the pitch size in local x-direction at the radius R, corresponding to the center of the partition, which the cluster belongs to (counted from the beam line). The reconstructed clusters become "GE1/1 RecHits"and are used in the standalone and global muon reconstruction. Figure 6.14 (left) shows the single hit resolution in the $R\phi$-coordinate, which runs in the plane of the chamber along a circumference centered at the beam position) and which the determines momentum resolution. The spatial resolution at two different η positions in the chamber are shown. The RMS ranges from 0.029 cm at higher η to 0.051 cm at lower η. The single hit resolutions can be compared to the RMS of the multiple scattering shown in Figure 6.14 (right) as a function of momentum. For muons with momenta $p_{\mathrm{T}} \simeq 200\,\mathrm{GeV}$ the uncertainty in the momentum fit due to the multiple scattering is $\simeq 0.05\,\mathrm{cm}$.

It is worth noting that the performance studies of the muon reconstruction do not include effects related to possible misalignment of the detectors, instead assuming a perfect alignment of the GE1/1 chambers. While this can never be true, effects of the misalignments are expected to become negligible after just a short period of operations with the upgraded detector. For comparison, alignment of muon chambers in station ME1/1 to the accuracy of 300 μm, comparable with the GE1/1 single hit spatial resolution, requires only about 20-30 pb^{-1} of collision data with the algorithm that extrapolates inner tracks to the plane of the ME1/1 chambers. GE1/1 and ME1/1 chambers are very comparable in the precision of the relative positioning of the readout strips, chamber size, and even the multiple scattering that muons undergo before reaching ME1/1 or GE1/1 is exactly the same. The only significant difference is a noticeably better single hit resolution of the ME1/1 chambers. However, for muons with $p_T > 20$ GeV used for alignment, multiple scattering is about 4 mm for both ME1/1 and GE1/1, which is much larger than the single hit resolution of either chamber, and so the alignment precision is proportional to (4 mm)/$\sqrt{L}$, where L is the integrated luminosity, in both cases below the point where the systematic effects can become significant.

6.3.2 GE1/1 impact on muon performance

The GE1/1 RecHits are used in the trajectory and momentum fits in both global and standalone muon reconstruction algorithms. In the following, we evaluate the degree to which the performance of muon reconstruction can be affected by degradation in the performance of the CSC chambers in the region $|\eta| > 1.6$. The specific figures of merit used are the standalone reconstruction efficiency and the transvere momentum resolution. The choice of standalone muon reconstruction is driven by its impact on a broad range of physics scenarios through the HLT performance, and by the unique access the standalone muons provide for models with new particles decaying meters away from the interaction point. We show that the redundancy provided with the installation of the GE1/1 detector significantly adds to the stability of the system and allows recovering of a significant fraction of the inefficiency even in very pessimistic scenarios.

Figure 6.15 (left) shows the standalone muon reconstruction efficiency at $\mathcal{L} = 5 \times 10^{34}$ cm^{-2}s^{-1} as a function of the pseudorapidity η of the simulated muon with high quality (the percentage of tracking reconstructed hits matches more than 50% of the simulated hits) and high purity (percentage of matched rechits with respect to the total number or rechits used for the muon reconstruction $> 75\%$). The reconstructed standalone muons used for this, and the subsequent studies have been previously selected by requiring a valid hit in at least two different muon stations, in order to ensure a decent p_T estimation. Moreover, since the contribution from out-of-time muons has been found to be very high, the reconstructed standalone muons have been filtered exploiting the muon timing measurement provided by the CSCs (requiring them to be compatible with a muon originating from the interaction point) and by requiring that all the muons were in the time window $\pm$12.5 ns w.r.t. a muon originating from a pp-collision. We will refer to all those standalone muons fullfilling all the above mentioned requirements as "high quality" muons. The recovery of the reduction in reconstruction efficiency with the addition of GE1/1 is particularly evident in the higher η region. The improvement is applicable to both the standalone muon reconstruction and the global muon reconstruction, since the latter is seeded by the standalone muons. Note that the efficiency recovery does not reduce the purity of standalone muon candidates, as is illustrated in Figure 6.15 (right), which shows the corresponding rate of reconstructing fake muons. The demonstrated recovery of the efficiency should be considered as a lower bound to the potential improvement, as the current implementation does not reconstruct GE1/1 segments, and therefore GE1/1 is not used in seeding the

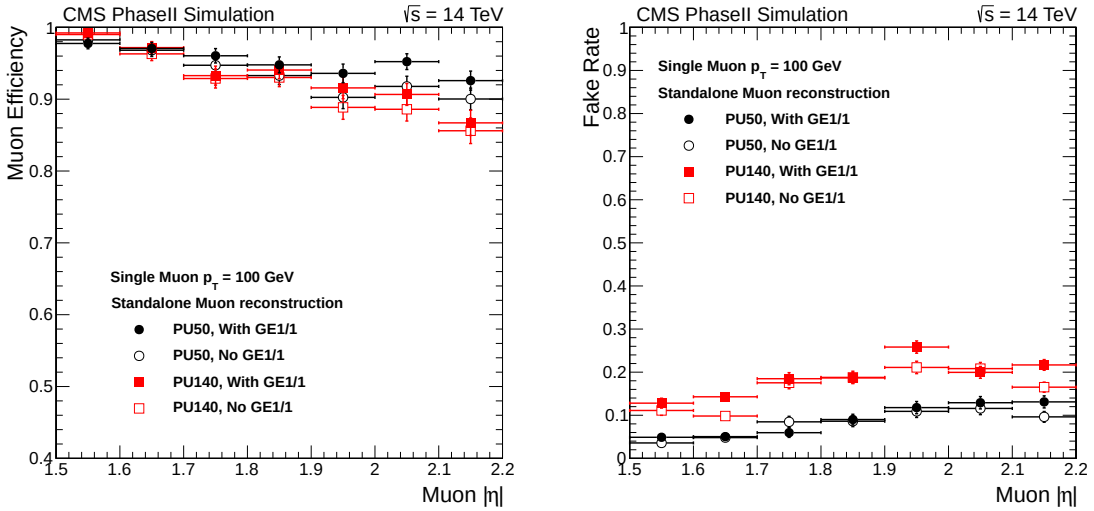

Figure 6.15: Standalone muon efficiency (left) and corresponding fake-rate level (right) as a function of η for the "2019" scenario using $\langle PU \rangle$ = 50 and 140 samples. Gain in the standalone muon efficiency is found adding the new GE1/1 detectors when the percentage of reconstructed hits matches the simulated one for more than 50% without any increase in the number of fake muons.

standalone reconstruction. While the directional accuracy of GE1/1 segments would be more coarse compared to that of ME1/1, the probability of reconstructing both hits in each of the two chambers in the super chamber is high and such segments could be used to seed standalone muon reconstruction.

The lack of redundancy of the system in the forward region $|\eta| > 1.6$, which relies solely on the CSC chambers that are seeing the highest radiation exposure in the entire muon system, is a concern that is not limited to the performance of the Level-1 trigger. The standalone muon reconstruction is not only used in the offline, where alternative algorithms such as the tracker muon reconstruction can be used to partially mitigate the reduction in performance. The very same standalone muon reconstruction and the global muon reconstruction, which directly relies on standalone muons, are also used in the HLT. Aging of the CSC chambers can not only reduce its performance, but lead to parts of entire chambers becoming inoperable for extended periods of time as repairs of the chambers and the onboard electronics can only be done during major shutdowns. Such scenarios can result in reduced momentum and spatial resolutions leading to degraded efficiency and increase in misidentification rates, and ultimately affecting the sensitivity of physics analyses and causing irreversible losses in data selection at the HLT.

Figures 6.16 and 6.17 show what happens to the standalone muon efficiency when ME1/1 is completely broken, with and without the help provided by the installation of GE1/1. As already discussed, the upgraded system shows a visible increase in the efficiency and a reduction in the rate of muon misidentification. However, the most important observation is that the additional redundancy associated with the GE1/1 system allows the recovery of most of the efficiency losses even in the most pessimistic scenario where the entire ME1/1 becomes inoperable. We consider different detector configurations at $\langle$ PU $\rangle$ = 50, which corresponds to the period between the LS2 and LS3 long shutdowns.

To quantify the impact of the CSC detector degradation on standalone muon momentum resolution and charge misidetification, we study the relative resolution of the muon curvature

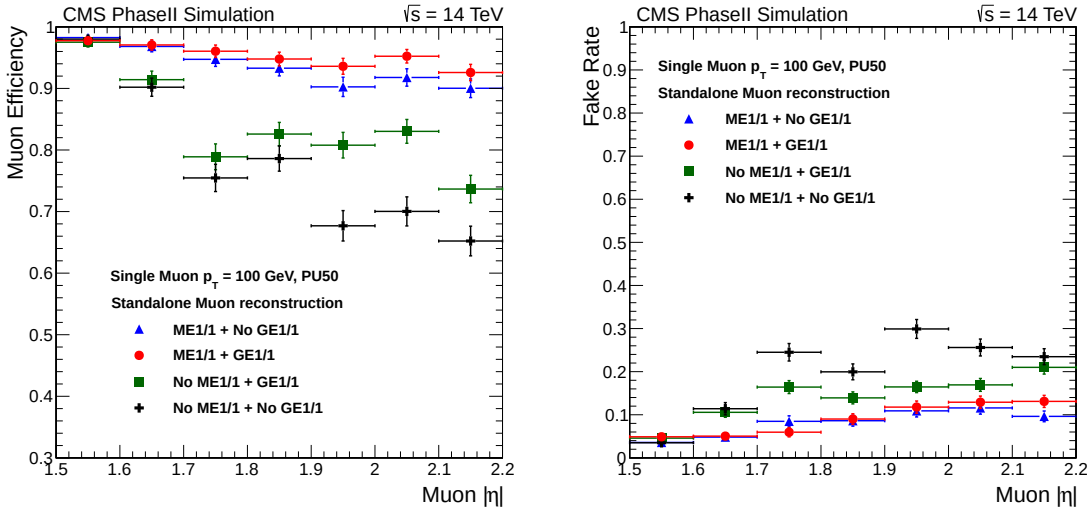

Figure 6.16: Standalone muon efficiency for high quality muons as a function of η in case of ME1/1 failure in the 2019 scenario at PU = 50 (left) and the corresponding level of fake-rate (right). The reconstruction efficiency is recovered by adding GE1/1 while the fake-rate level is kept as low as when ME1/1 is fully operative.

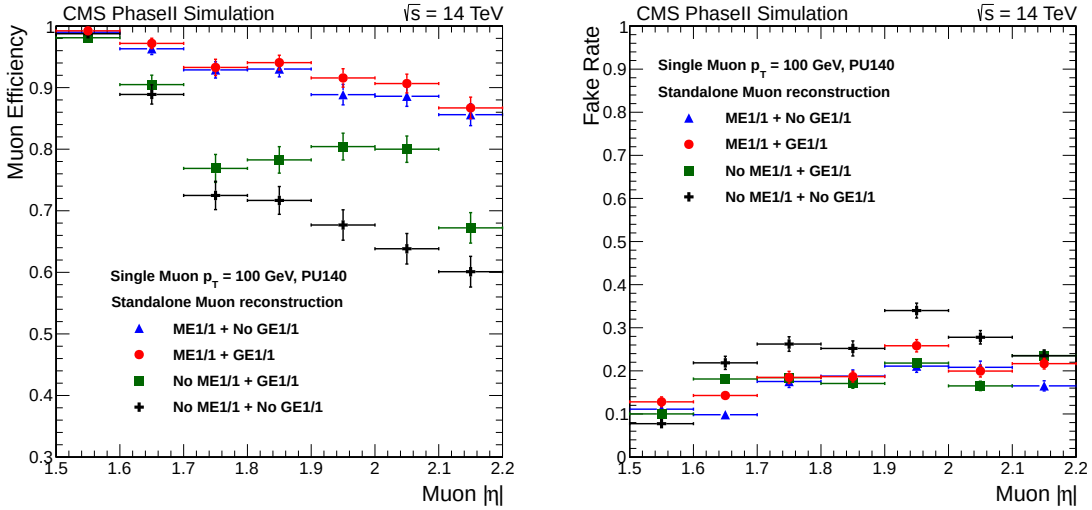

Figure 6.17: Standalone muon efficiency for high quality muons as a function of η in case of ME1/1 failure in the 2019 scenario at PU = 140 (left) and the corresponding level of fake-rate (right). The reconstruction efficiency is recovered by adding GE1/1 while the fake-rate level is kept as low as ME1/1 is fully operational.

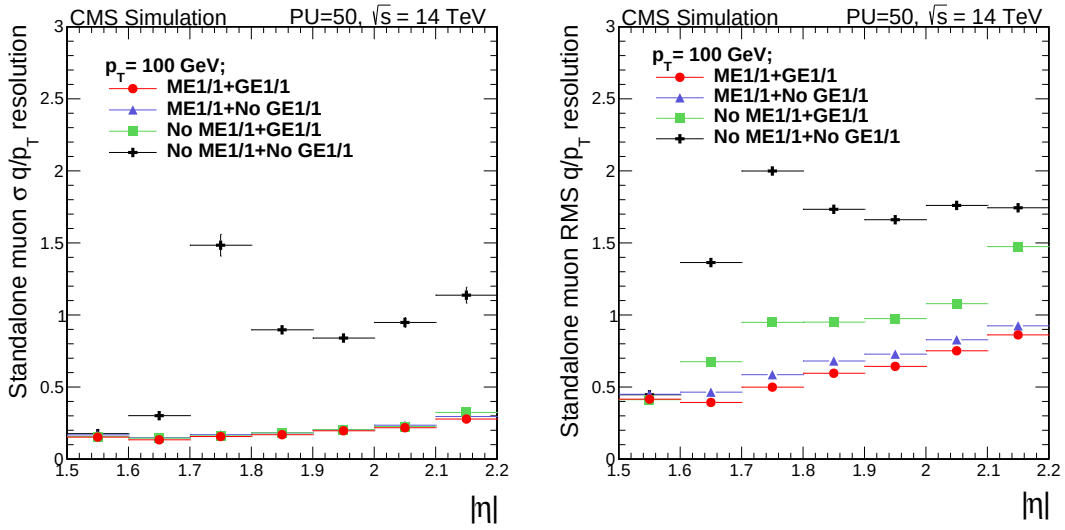

Figure 6.18: The dependency of the standard deviation (left) and relative RMS (right) of the $\delta(q/p_{\mathrm{T}})/(q/p_{\mathrm{T}})$ distribution as a function of the simulated muon pseudorapidity for several scenarios, illustrating the recovery of momentum resolution for standalone muons using hits in GE1/1 in the scenario where parts of the ME1/1 system become non-operational due to aging or other effects. The distributions are shown for muons with $p_{\mathrm{T}} = 100$ GeV reconstructed as standalone muons at PU= 50.

measurement. The specific figure of merit chosen is the residual distribution q/p_{T} defined as:

$$\frac{\delta(\frac{q}{p_{\mathrm{T}}})}{\frac{q}{p_{\mathrm{T}}}} = \frac{q^{Rec}/p_{\mathrm{T}}^{Rec} - q^{Sim}/p_{\mathrm{T}}^{Sim}}{q^{Sim}/p_{\mathrm{T}}^{Sim}}, \tag{6.1}$$

where q is the charge and p_{T}^{Sim} and p_{T}^{Rec} are the simulated and reconstructed transverse momenta. The standard deviation of the q/p_{T} residual distribution is obtained by fitting the distribution to the mean$\pm$RMS.

While the addition of GE1/1 does not change substantially the core resolution of the distribution, the presence of GE1/1 allows a significant reduction of otherwise unavoidable dramatic deterioration of momentum resolution in the scenario where ME1/1 becomes inoperable. Figure 6.18 makes this observation abundantly clear by showing the standard deviation σ (left) and RMS (right) distributions for several scenarios as a fuction of the simulated muon pseudorapidity.

Chapter 7

Integration and Installation in CMS

7.1 Introduction

The high-η part of the CMS detector can be seen in Figure 7.1 with a picture of one of the YE1 endcap disks on the right. The dark part (the black covers) of the endcap is the nose, which is physically the region of interest to install the new muon GE1/1 detectors covering the $1.6 < |\eta| < 2.2$ region. At present, this zone is partially vacant, with the CSC-ME1 station located there as only muon detector.

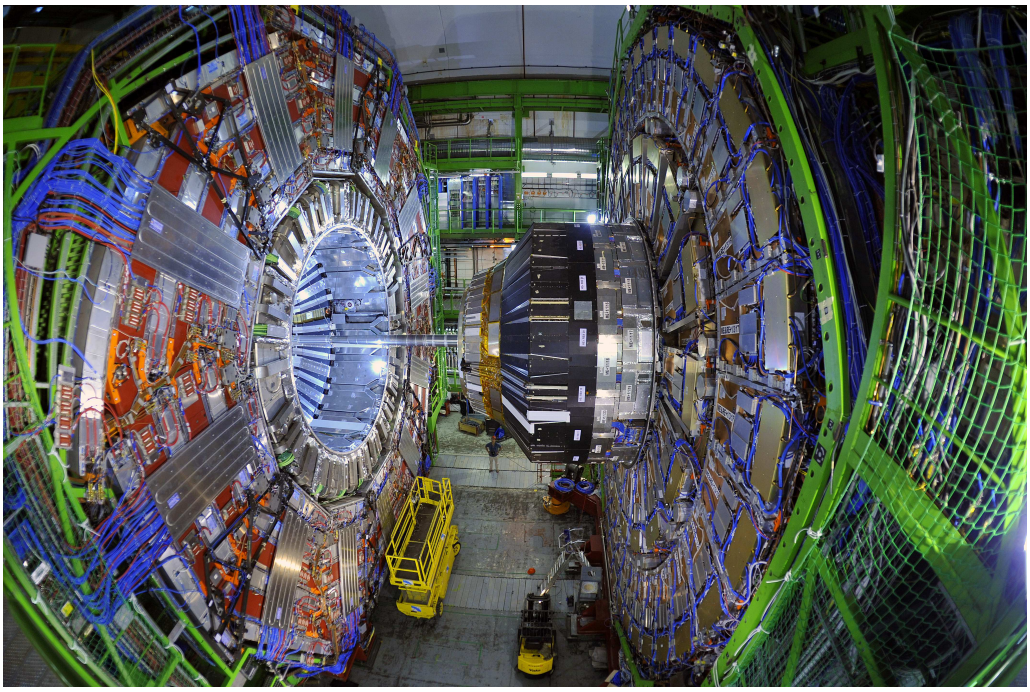

Figure 7.1: General view of the YE-1 endcap on the right.

Services to be integrated for the GE1/1 system are the high and low voltage power system in the underground service cavern (USC55) and corresponding power lines to the chambers in the experimental cavern (UXC55), the gas mixing system in the gas building on the surface, the gas and cooling circuit to the chambers in UXC55, and the optical fibers connecting the chambers to the off-detector electronics in UXC55.

7.2 Mechanical aspects and alignment

7.2.1 Description of the GE1/1 location

Figure 7.2 shows a quarter cut of the CMS detector. There, more details are shown of the GE1/1 zone, which is located just in front of the ME1/1 detectors. The GE1/1 are mounted using guide rails attached to the HE back-flange (see Figure 7.3) which is located 5674 mm away from the CMS interaction point. Mechanically, the GE1/1 chambers are not attached in any way to the CSC chambers. The back-flange is made of non-magnetic stainless steel, transparent to magnetic forces. This puts the GE1/1 chambers in a favorable location where the displacement of the chambers due to the CMS magnetic field is expected to be only a few millimeters along the Z direction (beam axis).

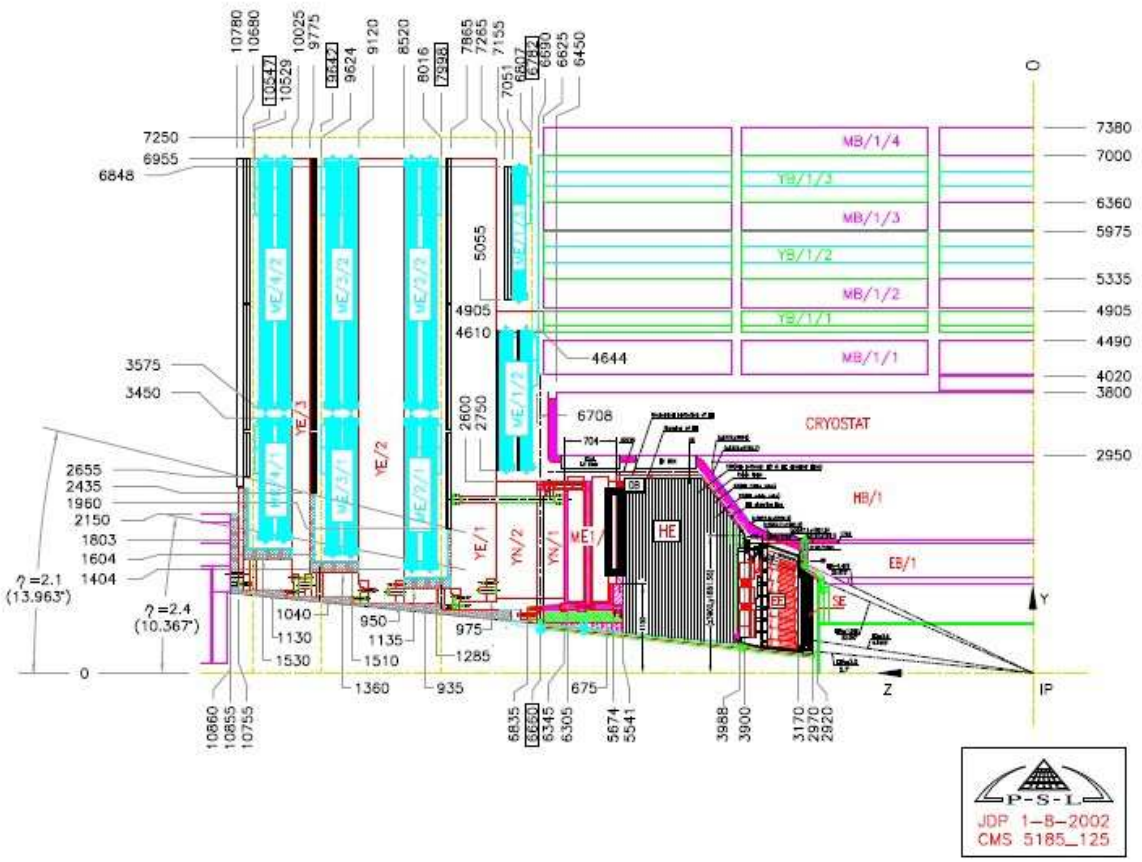

Figure 7.2: Quarter cut of the CMS detector. The GE1/1 superchambers will be installed on the HE back-flange, 5674 mm away from the interaction point, as indicated by the black box.

A general view of the GE1/1 installation slots is shown in Figure 7.4. In the figure one can see the ME1/1 detectors in position as well as their blue LV cables. The small pockets between the black covers of the nose and the ME1/1s are the actual installation slots for the GE1/1 superchambers. As is shown in the figure, the only accessible part of the GEM detectors after their installation will be their patch panel.

Figure 7.3: CMS HE back-flange showing GE1/1 chamber support rails.

Figure 7.4: General view of the GE1/1 installation slots (as indicated by the red box).

7.2.2 Position monitoring and alignment

7.2.2.1 Introduction

The GE1/1 detector on both sides of CMS can be considered as a double-layer disk (GE1/1-disk) formed by 36 superchambers mounted on the back-flange of the HE calorimeter. The determination of the chamber positions in the CMS coordinate system is split into two tasks: the positions of the chambers in the coordinate system of the GE1/1-disk and the location of the entire disk in CMS. The chambers themselves can be considered as rigid bodies.

The initial positions of the individual superchambers and the GE1/1-disk as a whole will change after closure: displacement of the chambers with respect to each other and their collective movement cannot be excluded due to magnetic field and temperature changes (though the thermal expansion of the individual chambers can be neglected). Therefore, a position monitoring system is necessary to determine the absolute chamber-positions and to follow these position changes.

The precision of the chamber positioning can be deduced from the physics requirements and consequently from detector design parameters. The most demanding direction is the azimuthal (R*phi) angle. The monitoring accuracy must be a fraction of the azimuthal resolution of the chambers (see Section 2.1) leading to $<$50 μrad requirement. The radial (R) position of the superchambers with respect to the GE1/1-disk and the X-Y position of the GE1/1-disk in CMS require the knowledge of the position with $<$100 μm precision. The position of the GE1/1-disk along CMS-Z has to be known with millimeter accuracy. The accuracy of the rest of the translations and rotations can be fulfilled by the installation accuracy for both the individual superchambers and the GE1/1-disk as a whole.

7.2.2.2 Alignment concept

Different methods to solve the task of alignment are applied in CMS for other subsystems [1, 59]. This experience has been used to work out the concept for the GE1/1-chambers.

As the readout strips that are relevant for the alignment cannot be observed after the assembly of the chambers, the first step is to transfer the strip positions during the construction to positioning elements to be mounted on the outside of the chamber body. These positioning elements can be used for monitoring at the installation and during the running period. Two types of elements are planned to be used: precision survey holes for removable survey targets and distance sensors permanently fixed on the chambers. The survey targets help to locate the chambers with moderate ($\sim$mm) precision during the installation.

The distance sensors measure the R*phi and the R distances between the adjacent chambers and are capable of defining the chamber positions in the GE1/1-disk coordinate system with the required precision. Following the layout of the GE1/1-disk the plan is to put distance-sensors on the long chambers: two on each phi-side and two in R-direction (see Figure 7.5). The total number of sensors planned to be used for the full project is 432 (6 per long chamber).

Finally, track-based alignment methods can define the entire GE1/1-disk in the CMS coordinate system, cross-check the results of the position monitoring system and further improve the precision of the alignment.

This concept that is based on three different, independent and complementary methods can guarantee the precise and robust solution of the alignment task.

The proposed scheme has been simulated using a simplified model of the GE1/1-disk contain-

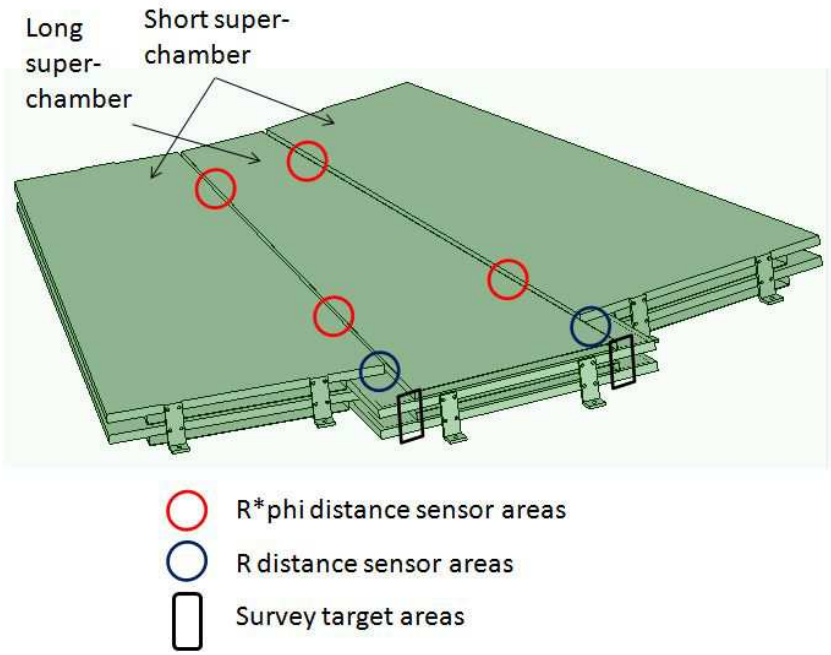

Figure 7.5: Locations of the distance sensors and survey targets.

ing six superchambers of 60 degree angular size and enlarged chamber distance (to 100 mm instead of the designed 38 mm). The larger angle and distance in the simulation could help us to detect possible problems that might occur during the position reconstruction from the measured data. The results have confirmed the correctness and completeness of the concept.

7.2.2.3 Distance sensors and calibration

Two different sensor types are studied as possible active elements of the position monitoring system: capacitive sensors and FBG-sensors (see e.g. [60]). The design dimensions of the sensor are $10 \times 10 \times 50\,\mathrm{mm}^3$, independent of the final solution. The measuring range is 0-10 mm.

As the task of the position monitor system is to provide the absolute positions of the chambers and the GE1/1-disk, the dimensions and locations of all the elements have to be known with the necessary precision. As the production cannot guarantee this accuracy these parameters have to be measured, in other words calibrated. Careful calibration is a key element of the accuracy that the system can obtain.

The first calibration step is the transfer of the strip positions of the readout board to its outer side using a 2D table (see Figure 7.6). This operation has to be done when the strips are still measurable (visible), i.e. before the chamber assembly.

First, the so-called sensor positioning plates are placed in the precisely machined holes of the base plate of the scanner table (see Figure 7.6A). Then, the readout board is put on the table with the strips upwards and the sensor positioning plates are glued to the back (connector) side of the readout board (see Figure 7.6B). Then, the upper surface is scanned and the images obtained by the camera are stored. This 2D scan -besides the alignment needs- is opening a possibility to check the quality of the strips and also to detect and measure their possible defects.

The fixations of the individually calibrated sensors are mounted on the chambers after the assembly of the GEM part. Then, those frame sections that are used as sensor targets on the

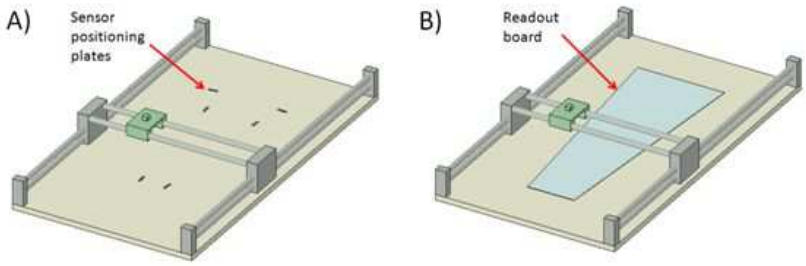

Figure 7.6: Principle of the chamber calibration: A) Measurement of the sensor positioning plates. B) Measurement of the strip positions and glueing of the plates to the connector side.

short chambers and the survey holes have to be measured with respect to the sensors (for the long chambers) or the sensor positioning plates (for the short chambers) by a coordinate measuring machine (CMM).

7.2.2.4 GE1/1-alignment R&D

There are still areas related to the distance sensors of the GE1/1-alignment hardware system where R&D work is required. Though both the capacitive and FBG options are based on known and used techniques, the conditions of the present application require further studies. For the capacitive solution the main concern is to develop a cost-effective but radiation-hard low-noise electronic transducer. For the FBG version the main problem is to find the best inner geometry and assembling technology of the sensor unit.

Besides the sensor R&D, considerable work is still required on the pattern recognition program for the scanning table to ensure fast, reliable and precise evaluation of the data. The simulation of the accuracy of the proposed system based on optogeometrical modeling is still being developed. Finally, the development of the software package providing the position reconstruction from the calibrated and measured data is still to be optimized.

7.3 Power system

7.3.1 HV power system

During the R&D phase of this project, a single-channel HV powering scheme based on a HV resistive divider circuit on the chamber was used (see Section 2.3.6.1). Unfortunately, this option has limits. For example, it is not possible to measure the currents of the individual GEM foils. The final system offers advanced multi-channel HV powering with the flexibility to provide the voltage levels to the GEM foils or sectors almost individually. This permits fine granularity in terms of HV settings for the GE1/1 detector, as well as GEM foil current measurements. Below, two options for such a multi-channel system are described; an engineering review will be organized early 2015 to determine the optimal solution.

The HV working point for the GE1/1 detectors with high gain and best time resolution is shown in Table 7.1. The potentials are shown for all detector electrodes as they are described in Section 2.3.6.1.

7.3.1.1 Multi-channel HV powering system

The HV system proposed by the University of Florida (UF) - Petersburg Nuclear Physics Institute (PNPI) team is based on an already existing design currently used in CMS to power the

Table 7.1: Expected HV working point of the GE1/1 detectors. The indicated voltage levels are actual voltage differences across the gaps or GEM foils.

Detector electrode	Voltage [V]	Dark current [nA]
Drift	900	0
GEM1	450	<35
T1	350	0
GEM2	440	<35
T2	700	0
GEM3	420	<35
Induction	500	0

CSC (except ME1/1) [61]. The design has been extensively tested over a few years of operation of these detectors. The system consists of two major components (see Figure 7.7):

- Primary HV power supplies and master boards, located in the Underground Service Cavern (USC55)
- HV distribution boards, located in Underground Experimental Cavern (UXC55), near the detector. These boards are designed to be radiation-hard and magnetic-field tolerant.

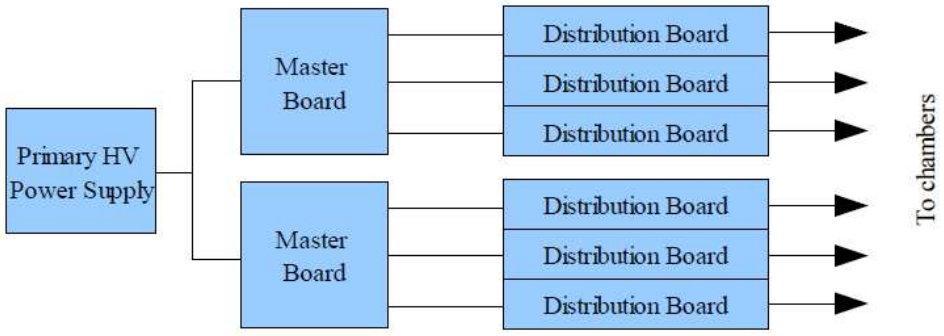

Figure 7.7: Multi-channel high voltage distribution structure.

The custom-designed GE1/1 HV system proposed here offers the following features:

- Each HV segment (or group of segments) in the GEM chamber is powered from its own HV regulator
- Each regulator is capable of adjusting the voltage, measuring the output current, detecting voltage deviations and over-current conditions. This is extremely convenient for tasks such as monitoring chamber aging, adjusting the gas gain, and detecting any abnormalities in the chamber behavior.
- In comparison to the single-line HV option, the UF/PNPI HV system does not use resistive dividers. Such dividers, consuming around 4W of power and being located in a small closed volume inside GE1/1 chamber with no air flow, lead to a significant local heat load. Also, in the presence of substantial leakage currents, passive HV dividers give rise to undesired biases in operating voltages across foils and gas gaps.

The GE1/1 chambers require several different voltage levels for proper operation. The UF/PNPI HV system is designed to power each chamber from several HV regulators, with at least one regulator per voltage level. This allows for greater flexibility during operation. Each voltage

Table 7.2: Specifications of the UF/PNPI GE1/1 HV system (baseline option).

Number of output channels in the system	144 chambers * 7 outputs = 1008 channels
Output channel organization	4 chambers per distribution board
Nominal output voltages	-3760 V Drift Catode
	-2860 V GEM1 TOP
	-2410 V GEM1 BOT
	-2060 V GEM2 TOP
	-1620 V GEM2 BOT
	-920 V GEM3 TOP
	-500 V GEM3 BOT
Absolute maximum voltage between top and bottom foil of the GEM	450 V
Absolute maximum voltage across drift, tranfer and induction regions	2000 V
Voltage settings, resolution, each output	1 V
Voltage adjustment, individually for each output	$V_{nominal}$ +/- 100 mV
Maximum output current per output, I_{max}	150 μA
GEM current leak tolerance	Up to two shorted segments per chamber, 100 μA leakage current
Individual output turn-off (trip) timeout	Programmable, with the step of 20 ms, up to 5 sec
Trip level software programmable	From 1 μA to 150 μA
Trip Level setting resolution	1 μA
Voltage measurement, individually for each ouput	Via software, resolution 1 V
Current measurement, individually for each output	Via software, resolution 1 μA
Rate of voltage change	2 to 100 V/s
Maximum HV ripple	20 mV p-p, bandwidth: 100 Hz to 20 MHz
Output control via software	Status: on/off, ramp, current limit/measurement, overcurrent trip, over/undervoltage trip

level can be individually adjusted for gas gain control, and the current and voltage can be measured on each output to prevent over-current conditions and voltage deviations. Additionally, complex chamber protection scenarios can be used, such as adjusting voltages on all chamber foils in case of over-current on one of the foils. In case of current leaks or complete shorts in some GEM segments, the individual regulators keep the voltages unchanged on all other segments, such that the chamber can still operate normally.

The GEM foils each have 47 sectors on the top side and a single common layer at the bottom. In addition, in each GE1/1 detector there are a drift electrode and readout plane (see Section 2.3). Powering each segment from its own HV regulator is impractical as it would require a huge HV output count (145 outputs per chamber, and 20880 outputs in the entire system). Several segment ganging options are being considered. The baseline option assumes that all segments on each segmented layer are ganged together. This requires only seven HV outputs per chamber, or 1008 outputs in the entire system.

Detailed specifications of the UF/PNPI GE1/1 HV system are listed in Table 7.2. A prototype of the HV distribution board was succesfully tested at CERN during November-December 2014. The test program included the following steps:

- Standalone parameter measurements and complete calibration of voltage measurement, voltage setting, and current measurement circuitry
- Tests with a GE1/1 chamber simulator circuit, including ramp-up, ramp-down, and behavior during simulated chamber over-current conditions and sparks
- Tests with an actual GE1/1 generation 3 chamber prototype using x-ray irradiation
- Tests with a tracking GEM chamber performed during beam test at the GIF facility

7.3.1.2 HV Complex-Channel powering system

INFN-Napoli and CAEN are designing a power system for the future RPC and GEM detectors, called HV Complex Channel system, that is back compatible with the present system and fulfills all CMS requirements. The HV power boards of the HV-CC system will be allocated directly in the new CAEN mainframe (SY1527) in order to reduce the number of crates, connections and the complexity of the present RPC system but with the caveat to be allocated in USC.

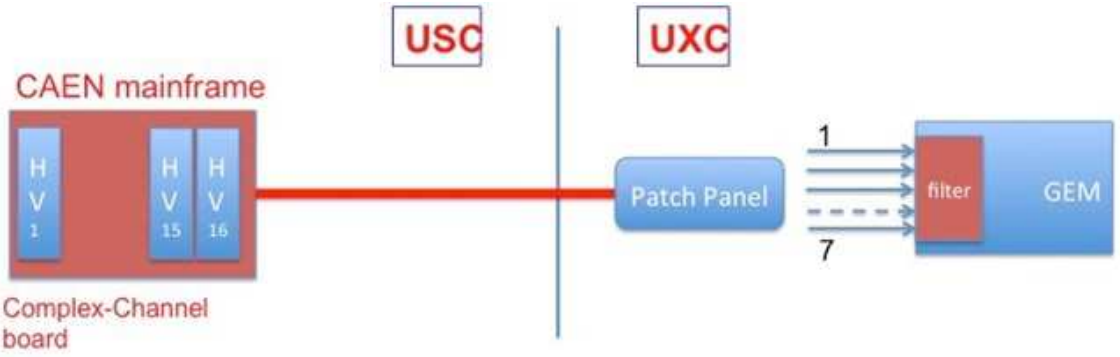

Figure 7.8: Schema of the complex-channel GEM power system. The entire power system hardware is placed in USC. A 80 meters multi-conductors cable will bring HV in UXC area.

The GEM version of the HV-CC (see Figure 7.8) is based on the following ideas:

- To power a GE1/1 chamber with 7 independent HV channels in order to be able to regulate and to change over time if needed the working point of each foil.
- To place the full power system in the USC area in order to have the core of the GEM system in an accessible area.
- To design a power system fully compatible with the hardware, firmware, DCS and DSS presently used by CMS.

The HV board for the GEM HV-CC is now under design. A first prototype will be delivered in the first part of 2015. It is a 1U board that can be allocated directly in the back of a CAEN SY1527 mainframe and is equipped with two independent complex channels, each providing 7 voltages that can be regulated and monitored independently. The main features of the HV board are:

- 7 stacked (serial) HV channels (up to 1000 V)
- Current monitor on each channel (resolution of 10 nA)

- Voltage setting/monitor on each channel (resolution of 1 V)
- Hardware Channel protections: maximum voltage, interlock
- Software Channel protections: overvoltage, overcurrent, overtemperature
- Very fast hardware feedback in case of discharge (local control)
- Ripple lower than few volts
- Floating at 5-10 V
- Back compatible with previous CAEN system

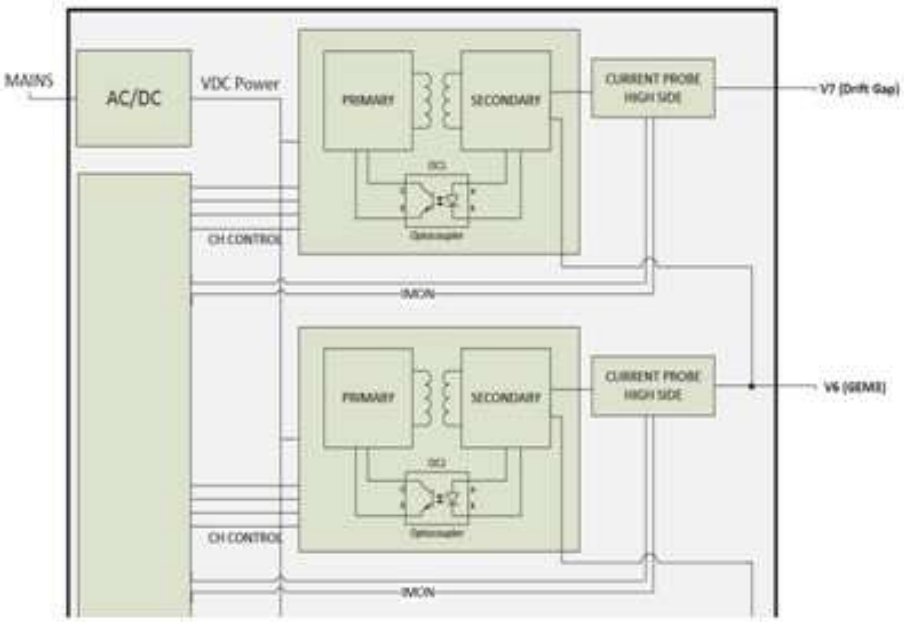

Figure 7.9: Schema of a voltage channel of the HV GEM board.

As shown in Figure 7.8, the full hardware system will be located in USC in order to reduce the number of inaccessible components and be able to access the system for maintenance and reparation anytime. This solution was strategic for the RPC project and was extremely useful to solve the problems encountered during the data taking. The USC (mainframe) and UXC (patch panel) will be connected through a multi-conductors cable (5 x 7 wires). Every set of 7 wires will be shielded and at same time one more shield will be added to the whole cable in order to protect it from external noise. The multi-conductors cable will run from the distributor in USC to the patch-panel in UXC. The USC distributor will be eventually used to join more chambers in one and reduce the number of HV boards needed but keeping the possibility to readout the absorbed current of every single chamber reading out the return line with a dedicated ADC.

7.3.2 LV power system

The LV power system will be based on CAEN EASY 3000, A3016 LV modules (see Figure 7.10).

The LV power requirements for a GE1/1 superchamber are shown in Table 7.3. For each superchamber there are three LV channels to power the on-detector electronics.

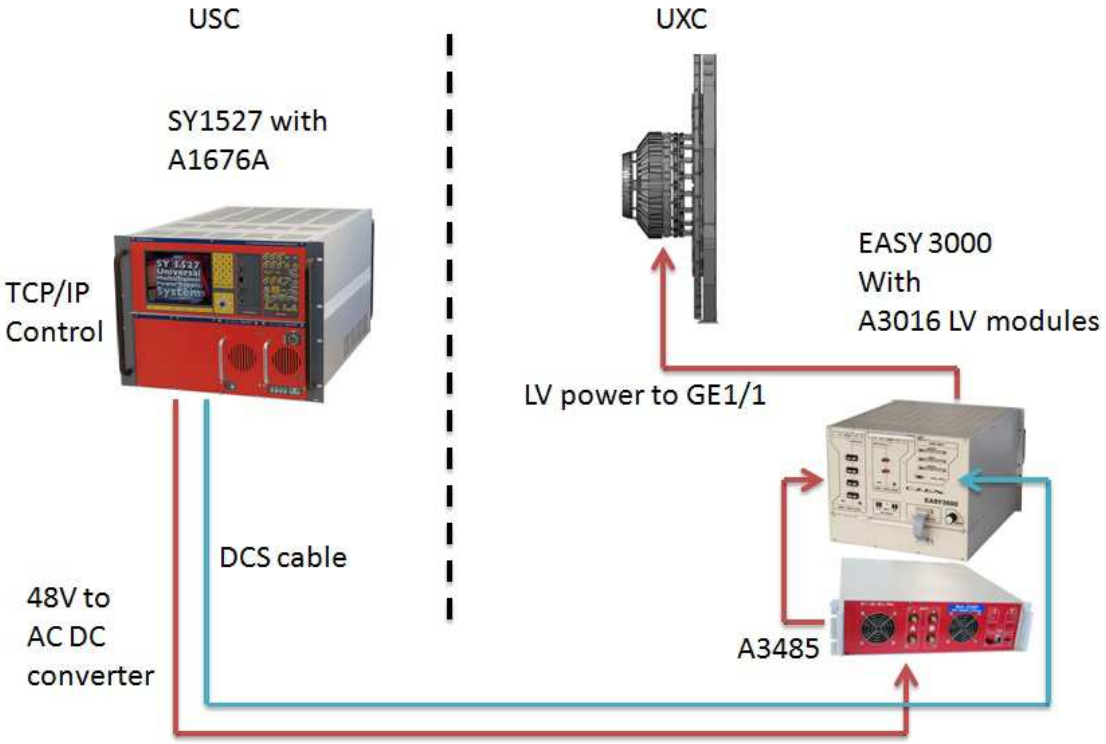

Figure 7.10: Architecture of the A3016 based LV power system.

Table 7.3: LV power requirements for a single GE1/1 detector and a GE1/1 superchamber.

	Voltage	Current consumption for single GE1/1 Detector	Current consumption for GE1/1 superchamber
VFAT	3.3 V	8 A	16 A
Opto-hybrid	4 V	6 A	12 A
Opto-hybrid	1.7 V	4 A	8 A

7.4 Readout, control and power lines

7.4.1 Optical links and architecture

The GE1/1 chambers require optical fibers for the data flow and control as described in Chapter 3. For a single GE1/1 detector, 8 single fibers are needed to connect the GE1/1 Opto-Hybrid with the μTCA crates located in the service cavern. In Figure 7.11 the general plan is shown with the number of fibers indicated for each endcap. Per endcap, there will be 36 GE1/1 superchambers installed, each requiring 16 fibers, i.e. a total of 576 fibers per endcap without considering spares.

The environmental conditions of the GE1/1 installation slots require the fibers located on the YE1 endcaps to be radiation hard. Radiation hard fibers will be used only on the nose and the disk periphery. For the rest of the connections normal telecommunication fiber cables will be used from the YE1 disks to the backend crates in the service cavern. The proposed radiation hard fiber is the DrakaEliteTM Super RadHard OM2 Multimode Optical Fiber, which permits lengths up to 300 m, with a bandwidth of 10 Gb/s, while the non-radhard fiber is the DrakaEliteTM OM3 Multimode Optical Fiber [62]. To implement this scheme, 2 patch panels are planned for each connection: one located on the GE1/1 superchambers and another on the

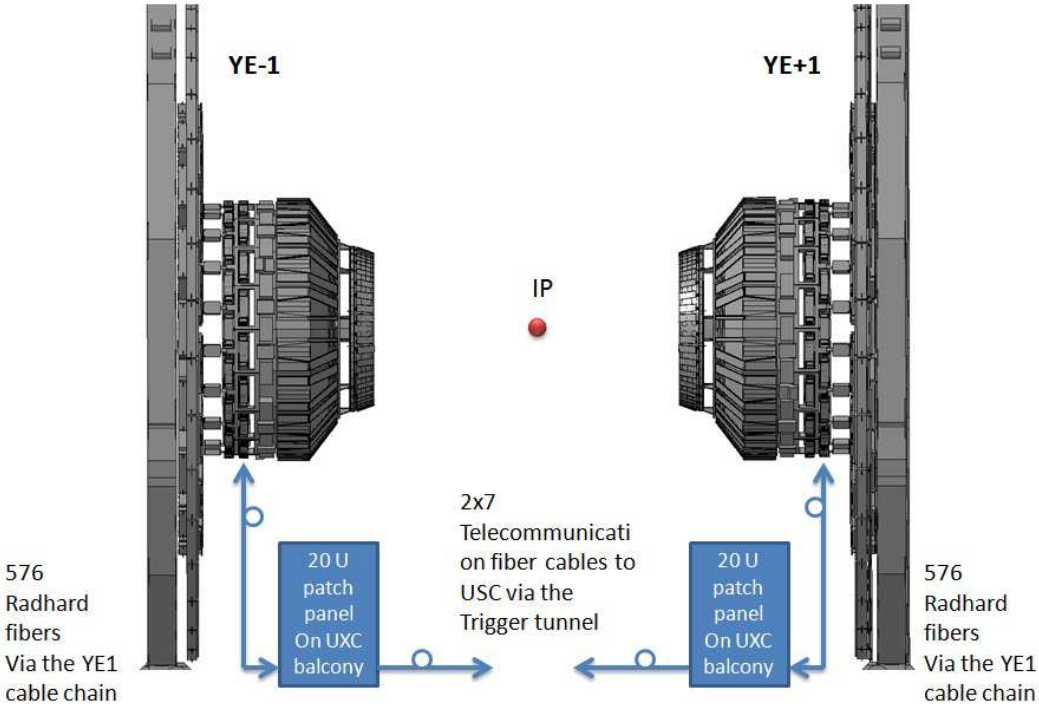

Figure 7.11: General scheme of the GE1/1 optical fibers.

YE1 periphery. To accommodate 576 lines a 20U space is required for each endcap for patch panels. This space has to be equally distributed across the disk periphery to permit efficient routing of the services. As is shown in Figure 7.11, from the 20U patch panels on, the fibers are grouped into 7 telecommunication optical cables per endcap, which go to the USC μTCA crates. To secure the connectivity of the GE1/1 superchambers, 20% of spare radhard fiber lines are foreseen to be distributed equaly to every installation slot.

7.5 Cable routing

The global routing plan of all cables for GE1/1 is shown in Figure 7.12. The bold red line shows schematically the path of all cables from the GE1/1 superchambers, indicated as orange rectangles, to the periphery of the YE1 disk. The cable routing on top of the ME1/2 and ME1/3 chambers is also shown, where dismounting of these detectors will be not necessary for the GE1/1 installation.

A complex issue to be faced in this upgrade project is the fact that all cable trays inside the nose are already completely filled with services for other sub-detectors. Hence, a strategy to avoid the standard paths was developed. Figure 7.13 shows the proposed routing of the cables inside the YE1 nose structure. This scheme is valid only when all cables for LV and HV and optical fibers are placed inside flexible ducts in order to secure and maintain the cable package volume. The GE1/1 cables will follow the paths of the ME1/1 cooling pipes which are marked in the figure as zig-zag blue dashed lines. In this way, the use of the nose cable trays is no longer needed. The cables will simply be routed close to the right side of the trays as seen from the interaction point.

Figure 7.14 shows the clearance available between the top of the small cable tray, placed in the ϕ direction and the YE1 nose covers. This represents the most critical point of the cable path

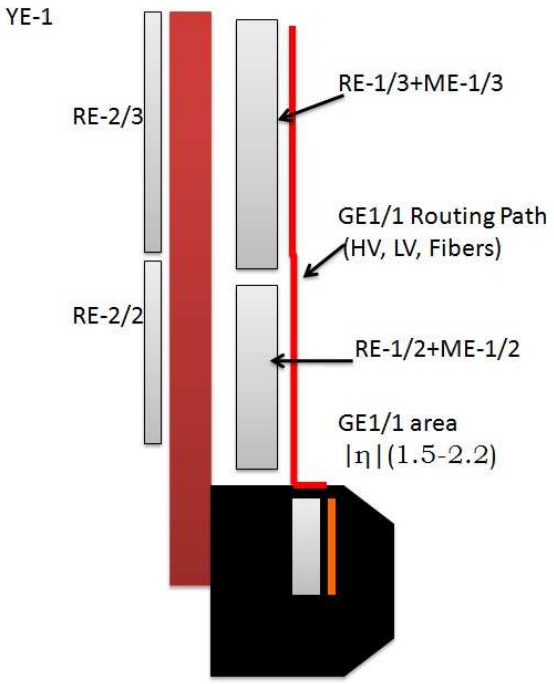

Figure 7.12: Diagram of the cable routing in the nose and on the YE1 disk.

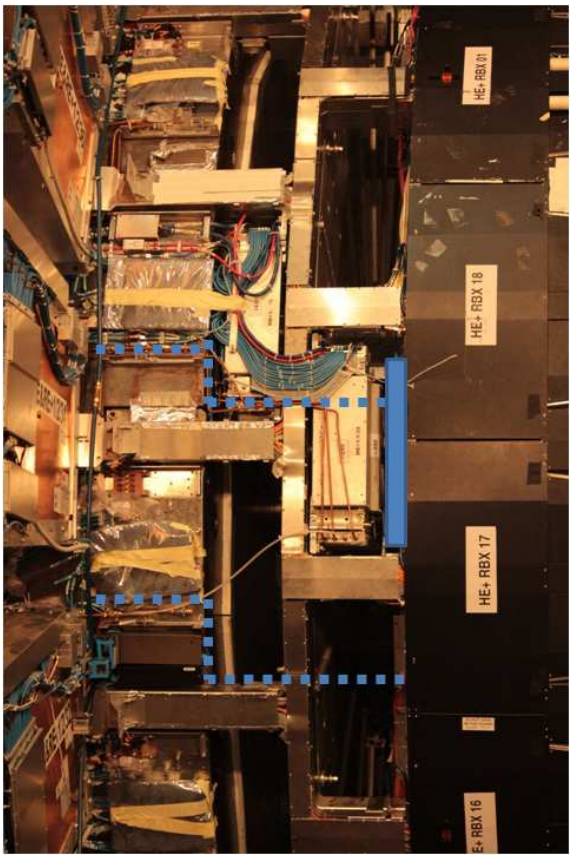

Figure 7.13: The cable routing inside the nose. The blue rectangle represents the patch panel of a GE1/1 chamber, while the blue dashed lines indicate the cable paths.

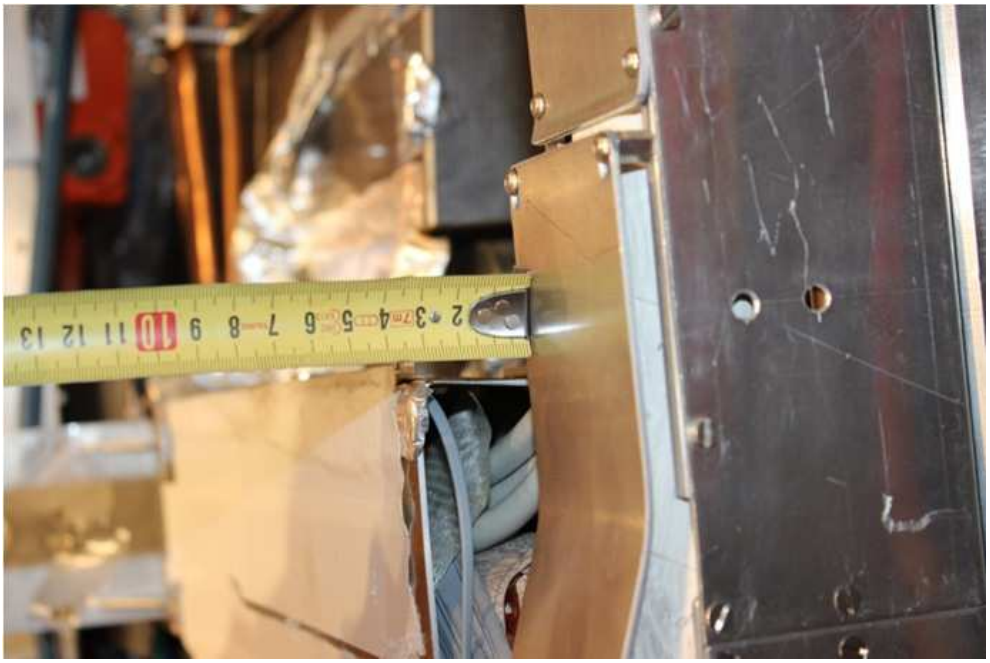

Figure 7.14: The maximum clearance available to install the cables between the CSC and the GE1/1 patch panel.

inside the nose. The picture shows this distance is about 30 mm, but for safety we are counting it as 20 mm.

Figure 7.15 shows several parts of the cable routing. The right picture shows the ME1/1 and the copper cooling pipes starting from the detectors. Just in front, towards the interaction point, the GE1/1 superchambers will be installed. The middle picture shows the overall path of the cable duct which will be exact as the copper cooling pipe seen in the picture. In the left picture one can see the breaking point which will go from the nose to the YE1 disk. On the endcap disks, the ducts will be placed on top of the ME1/2 and ME1/3 chambers, and will go all the way to the periphery of the disks where the crate racks are located.

7.6 Gas system

Table 7.4: General specifications of the GE1/1 gas system.

Detector gas volume	Volume [cm^3]	Gas flow [Volume/h]	Gas mixture
Single GE1/1 detector - Long	3120	1	$Ar/CO_2/CF_4$ 45:15:40
GE1/1 superchamber - Long	6240		
Endcap disk	224640		
Full installation	449280		

Table 7.4 shows the basic parameters of the gas system for the GE1/1 stations in CMS. The GE1/1 chambers are operated with a gas mixture of $Ar/CO_2/CF_4$ 45:15:40. It is similar to the CSC mixture, but with different fractions of the main gas compositions. The tetrafluoromethane (CF_4) in the mixture demands the use of only copper and stainless steel pipes in order to avoid water absorption and the formation of hydrofluoric acid, which is very dangerous for the detector electrodes. The GE1/1 gas system is partially using the existing RE1/1 gas infrastructure, in particular the previously installed copper pipes which run between the

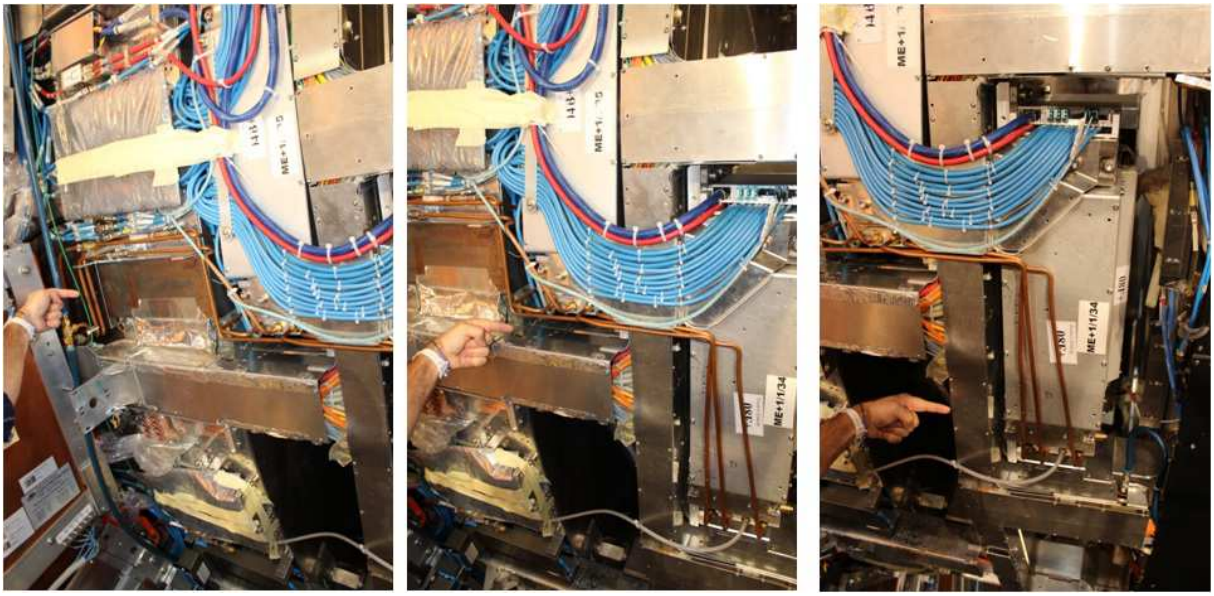

Figure 7.15: Cable routing inside the nose from GE1/1 to the YE1 disk.

GE1/1 installation zones and the gas distribution rack located on the YE±1 X1 towers at the far side.

Figure 7.16 shows the overview of the gas supply system for the GE1/1 stations. The main gas mixer with the supply cylinders is placed in the gas building located on the surface. The final $Ar/CO_2/CF_4$ mixture is transported to the detector cavern through a 254 m long stainless steel transfer pipe of 30 mm in diameter which runs in the PM54 shaft and connects the surface gas building with the gas racks in USC55.

The gas distribution for the GE1/1 installation slots is based on the existing pipe infrastructure foreseen initially for the RPC RE1/1 detectors. Tests are ongoing to validate the gas distribution circuit inside the YE1 nose.

7.7 Cooling system

The design of the GE1/1 cooling system is based on the calculations shown in Table 7.5 where the numbers are given for each heat power source on the detector side, i.e. the VFAT boards, the optical hybrid and the HV divider.

Table 7.5: Power calculations for a single GE1/1 chamber, a superchamber, and total power consumption per endcap and both GE1/1 stations together.

	Power consumption for GE1/1			
	Single chamber	**Superchamber**	**Endcap**	**Total**
HV Divider	4 W	8 W	288 W	576 W
VFAT boards	24 W	48 W	1.7 kW	3.5 kW
Opto-hybrid	50 W	100 W	3.6 kW	7.2 kW
Total	78 W	156 W	5.6 kW	11.2 kW

The GE1/1 on-detector cooling design is shown in Figure 7.17. The concept is based on the use of a u-shaped, 6 mm inner diameter copper pipe. The thermal contacts between the pipe and the heat sources are made with copper strip plates of 1 mm thickness.

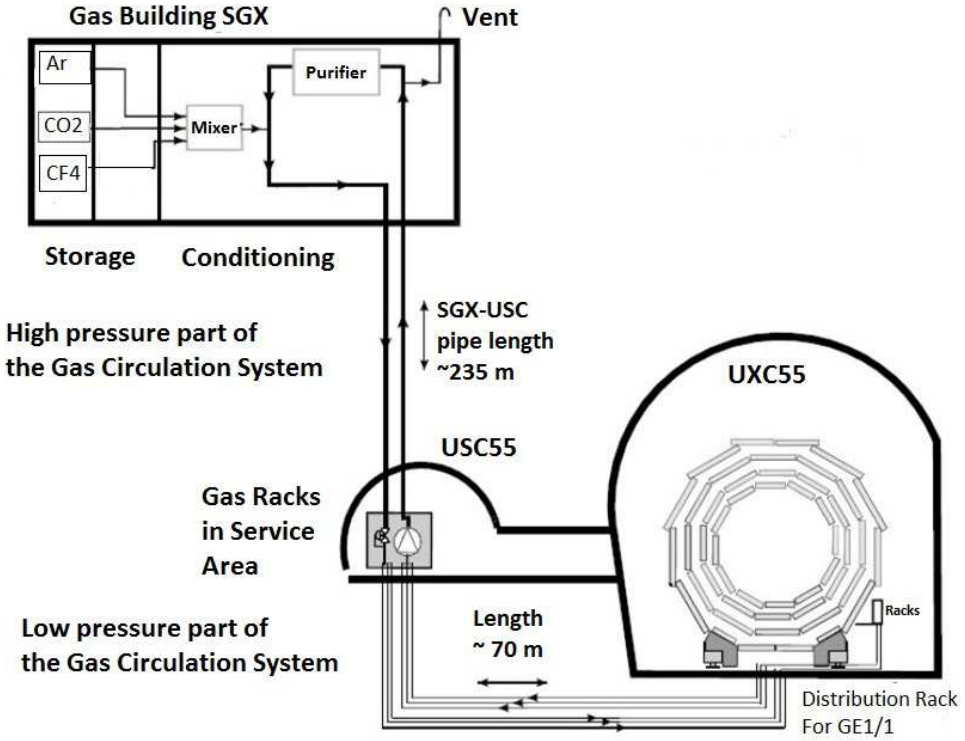

Figure 7.16: Overview of the GE1/1 gas system.

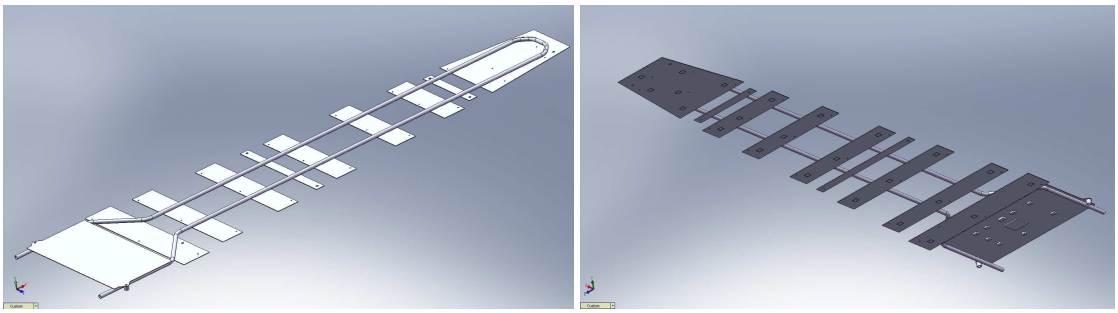

Figure 7.17: Top and bottom view of the GE1/1 cooling design.

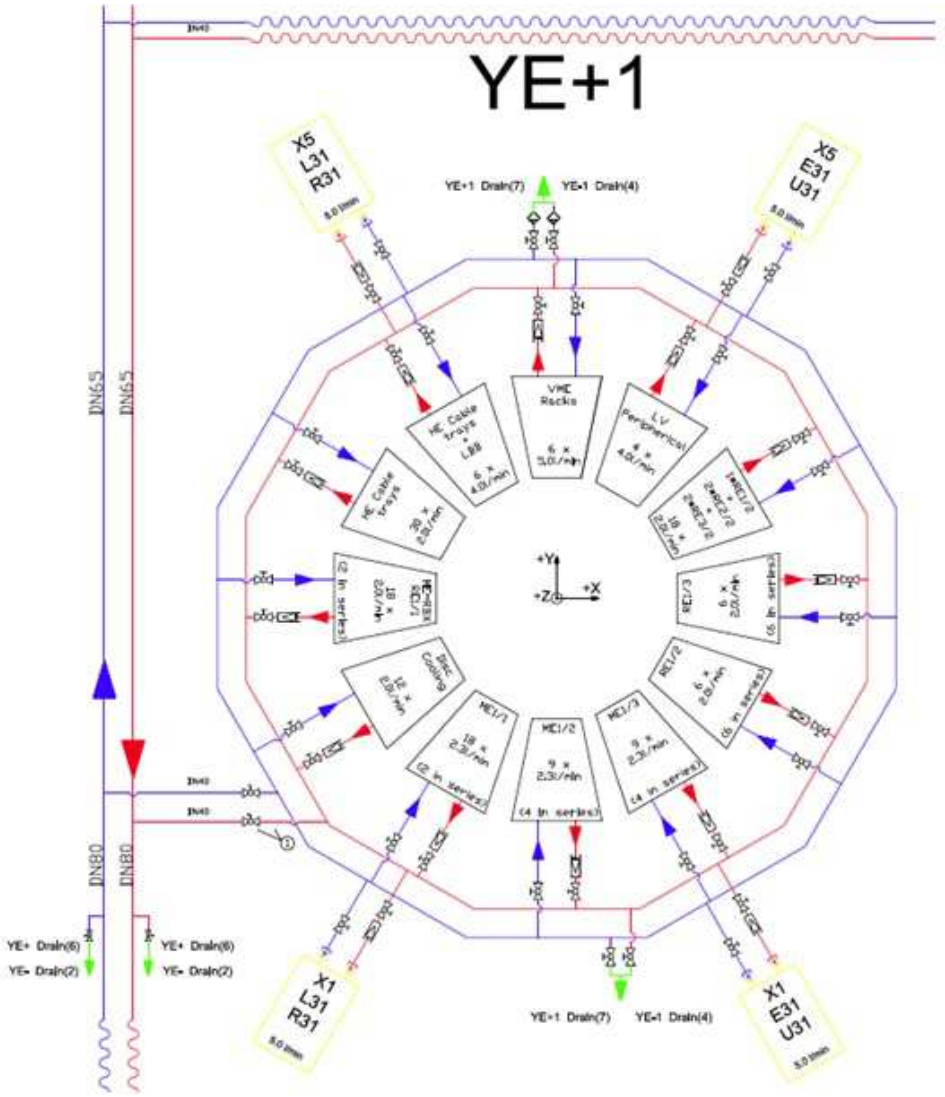

Figure 7.18: Overview of the YE1/1 cooling circuit.

The YE1/1 cooling circuit is shown in Figure 7.18 where one can see the 12 cooling loops for ME1/1, RE1/1 and the HCAL readout box (RBX). The GE1/1 chambers will use the cooling loops that were foreseen for RE1/1.

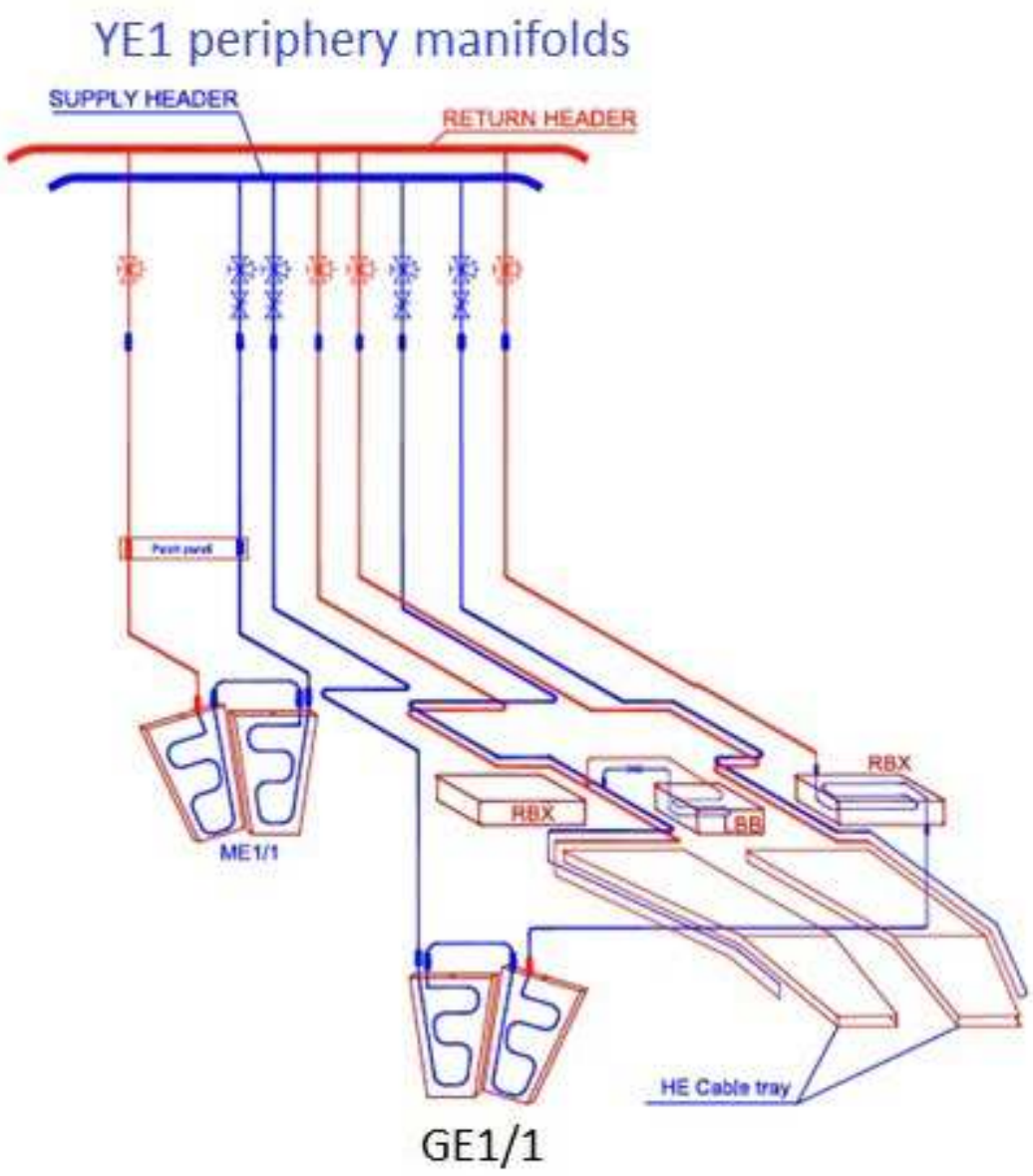

Figure 7.19: Overview of a single YE1/1 cooling loop.

Figure 7.19 shows one of the 12 cooling loops of the YE1/1 circuit. There, the GE1/1 superchambers are connected in series with the RBX. The amount of cooling power per superchamber is foreseen to be 156 W, including an extra safety margin. This will give a negligible impact on the present cooling system of the endcaps and will not lead to perturbation of the nearby subdetector systems.

7.8 Proposal for radiation monitoring with RADMONs

There is a proposal to monitor radiation on the GEMs with RADMONs [63]. RADMONs are solid-state dosimeters developed at CERN that can provide a quantitative measurement of the deposited dose and the exposed particle fluence in semiconductor devices. In one RADMON there are four detectors mounted: two radiation-sensitive field-effect transistors (RADFETs) for the photon dose and two p-i-n silicon diodes for the neutron and hadron dose measurement. For the RADFETs the range of the deposited dose is 0.001 Gy to tens of kGy (depending of required sensitivity). For p-i-n silicon diodes the range for neutrons is $10^8 - 2 \times 10^{12}$ cm^{-2} (all fluencies are quoted in terms of 1 MeVeq) and for fast hadrons (E $>$ 100 keV) and high energy neutrons (E$>$1 MeV) $2 \times 10^{12} - 4 \times 10^{14}$ cm^{-2}. The minimum setup is 12 RADMONs per GE1/1 disk, i.e. one RADMON for three GE1/1 superchambers. The inhomogeneity across superchambers as seen in FLUKA simulations (see Figure 7.20) justifies the number of RADMONs.

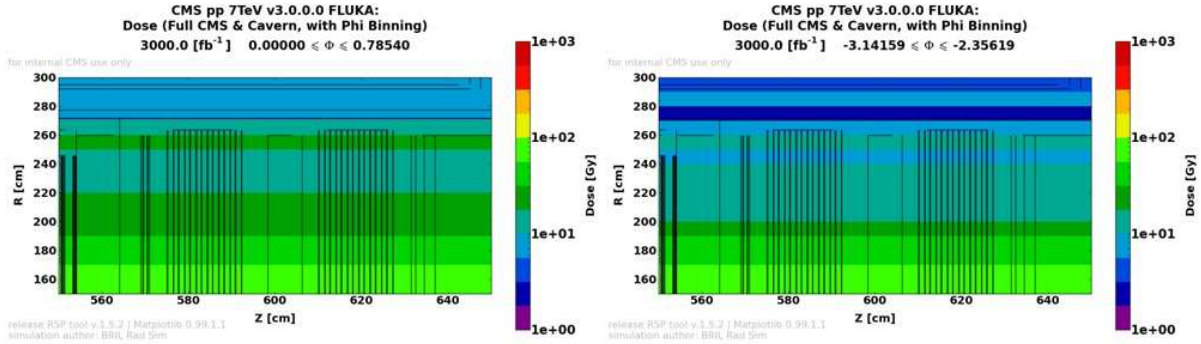

Figure 7.20: FLUKA simulation of the expected dose near the GE1/1 chambers, for $0 < \Phi < 0.78$ rad (left) and $-3.14 < \Phi < -2.36$ rad (right). Simulation performed for 3000 fb^{-}1 of 7 TeV pp-collissions.

The proposal made by the Sofia-INRNE group is to install and commission (at least) 2×12 RADMONs and controller boards for communication with the DCS (RS485, or CANBUS).

Chapter 8

Controls and Monitoring

8.1 Introduction

The complexity of the GEM system demands a high level of automation in operation in order to reduce human errors and optimize recovery procedures. In CMS the Detector Control System (DCS) [64] has two main tasks: the safe operation of the experiment and the monitoring of the status and performance of the detector. Data quality and certification of reconstructed data are tasks covered by the Data Quality Monitoring (DQM) system. These systems provide homogeneous environments across various subdetectors and trigger monitoring applications, allowing each subsystem to design and implement its own monitoring and control functions depending on its specific needs. Data from each subsystem are made available to central control system, which, in return, provides console hardware and software, archiving and other higher-level services.

This chapter presents the design and implementation of the DCS and DQM systems for the GEM subdetector. The Database management system, being developed for the GEM project, is also briefly described.

8.2 Detector control system

The CMS DCS system provides control over all subdetectors, all infrastructure, services, its active elements, the electronics on and off the detector, the environment in proximity of the experiment, as well as communications with the accelerator. All of these tasks are historically referred to as "slow controls".

The architecture of each subsystem can be divided into Front-End hardware components (i.e. sensors, power supplies, etc.) located in the experimental area, and a Back-End system, composed of the DCS computers, network, and software applications. Because of the large variety of equipment to be controlled, the standardization of the hardware and of the software interfaces is of primary importance for the homogeneous control of all different detector components. It aids the development of a uniform operator interface as well as minimizes the implementation and maintenance efforts. In accordance with CMS official guidelines, all back-end applications are developed using the commercial SIEMENS SCADA (Supervisory Control And Data Acquisition) [65] software, SIMATIC WinCC Open Architecture (WinCC OA) [66] and the Joint Control Project (JCOP) framework components [67] designed to enhance WinCC OA functionalities. JCOP includes components to control and monitor the most commonly used hardware at the LHC experiments, effectively reducing development effort and creating a homogeneous system at the same time. It also defines guidelines for alarm handling, control access, and partitioning to facilitate the coherent development of subdetector specific compo-

nents in view of their integration in the central system.

The DCS is integrated in the CMS DAQ system [68] as an independent partition and, during data taking, it is supervised by the Run Control and Monitoring System (RCMS) [69]. The RCMS controls the subdetector and the central data acquisition systems. It is based on the hierarchical control structure needed to control around O(10^4) applications, which in turn control electronics or handle event building and processing. The applications themselves are developed using the C++ based XDAQ [70] data acquisition framework, which provides hardware access, powerful data transport protocols and services. XDAQ is a software platform. It has been designed at CERN specifically for the development of distributed data acquisition systems.

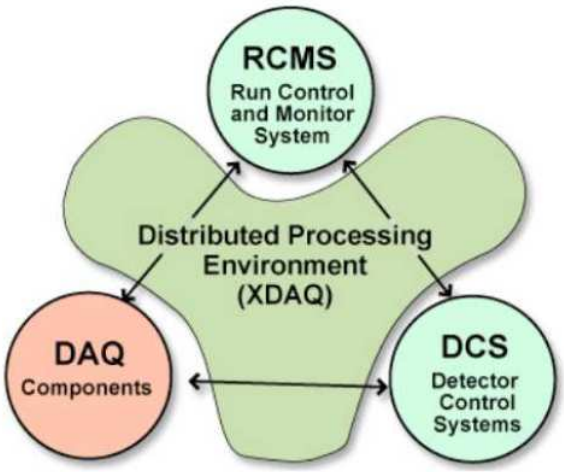

Figure 8.1: Schema of the interconnection among DCS, RCMS, DAQ, and XDAQ. [69]

The interconnection among DCS, RCMS, DAQ, and XDAQ is schematically shown in Figure 8.1. A general set of system requirements for DCS are: partitionability, modularity, homogeneity, scalability, automation and radiation tolerance. Furthermore, the high radiation and magnetic field make the experimental hall inaccessible during running conditions. Therefore, the control system must be fault-tolerant and must allow remote diagnostics. Many of its functionalities are needed at all time. To ensure this continuity, UPS and redundant software and hardware systems are implemented in critical areas. Besides these general requirements, each subdetector has specific ones resulting from its unique design and implementation. Requirements specific to the GEM subdetector are discussed in the following section.

8.2.1 GEM detector control system

The GEM DCS provides continuous control and monitoring of the subdetector, the trigger, and all ancillary subsystems. It takes appropriate corrective and automatic actions when pathological conditions are detected to maintain operational stability and ensure high quality data. It monitors and controls the environment in proximity of the experiment, handling electricity supply, cooling facilities, environmental parameters, crates, and racks. Safety related functions, such as detector interlock, are provided by the GEM DCS in collaboration with the Detector Safety System (DSS) [71]. The DSS, in fact, delivers uninterrupted and autonomous detector protection in case of major hazards such as fire, gas leakage, or oxygen deficiency. The GEM DCS is not designed to be a personnel safety system.

The GEM DCS is hierarchically organized in a tree-like structure and divided in subcomponents: high voltage (HV), low voltage (LV), environmental (humidity, temperature, and pres-

sure), frontend electronics, gas, and cooling. Each component can work standalone, or in parallel distributed over different machines. A supervisor level is required in order to gather and summarize all information, and to present it in a simplified but coherent interface to the operators.

All the information regarding running conditions and logging, referred to as conditions data, needs to be stored in order to monitor system behaviour over time and to perform off-line analysis. The GEM DCS stores conditions data in the CMS Online Master Data Storage, used by all the online subsystems. In its final configuration, the amount of GEM DCS data stored will be $\sim$5 GBytes/year.

These data are not easily searchable and viewable from outside the CMS site due to security restrictions. A natural method to convey and display this information is through a web server. Thus, a Web Based Monitoring (WBM) tool [72], which uses Apache Tomcat application container [73, 74] and Java Servlet technology, is in place and accessible via web browsers for collaborators locally and remotely, anywhere and anytime. Among all monitoring services provided by WBM and focused on real-time or historical status of the detector, two are of particular interest for the GEM subdetector: the LastValue and the ConditionBrowser. The LastValue service consists of interactive schematic representation of the detector and a browsable tree. The last recorded values of the detector quantities (detector status, voltages, currents, gas flow, and thresholds) and environmental quantities (temperature and humidity levels) are displayed for each of the 144 GEM chambers. The ConditionBrowser allows the access to all values stored in the database for visualization. The aforementioned quantities can be plotted for any given time interval or range of run numbers or luminosity sections. Thus, patterns in behaviour and performance of the system, as well as reoccurring problems, can be easily spotted and analysed. In addition, via the GEM specific WBM service, more detailed and refined plots may be produced and visualized. Via custom written queries, different parameters can be displayed and correlated for monitoring purposes. As an example, operating voltages may be displayed only when the detector status is "ON" and only when proton-proton collisions were present. All WBM plots and their underlying data are downloadable for further offline analyses.

8.2.2 GEM finite state machine

Detector controls are organized in a tree-like Finite State Machine (FSM) hierarchy representing the logical structure of the detector, where commands flow down and states and alarms are propagated upwards. FSMs offer an easy and powerful way to model detector behaviour through the definition of a finite number of states, transitions, and actions. All the subdetector control systems are integrated in a single control tree headed by the central DCS to ensure a homogeneous and coherency throughout the experiment. Therefore, states and commands for top and the conjunction nodes are fixed by CMS. The states are: ON, OFF, STANDBY, and ERROR and the commands are: ON, OFF, and STANDBY. This ensures uniformity and compatibility with the central DCS, permitting adequate transitions between the states. During a transition between states, the FSM takes care of loading the correct parameter values and alarm settings from the configuration database. Figure 8.2 describes the FSM schema for a high voltage channel. The "transitional" states, RAMPING UP and RAMPING DOWN, describe the situation in which one or more HV channels are ramping in voltage towards the values have been set.

8.2.3 Electronic controls and monitoring

The GEM electronic chain is described in Section 3 and 4. Monitoring the state of the electronics, while taking data, is critically important. The trigger throttling system (TTS) provides the

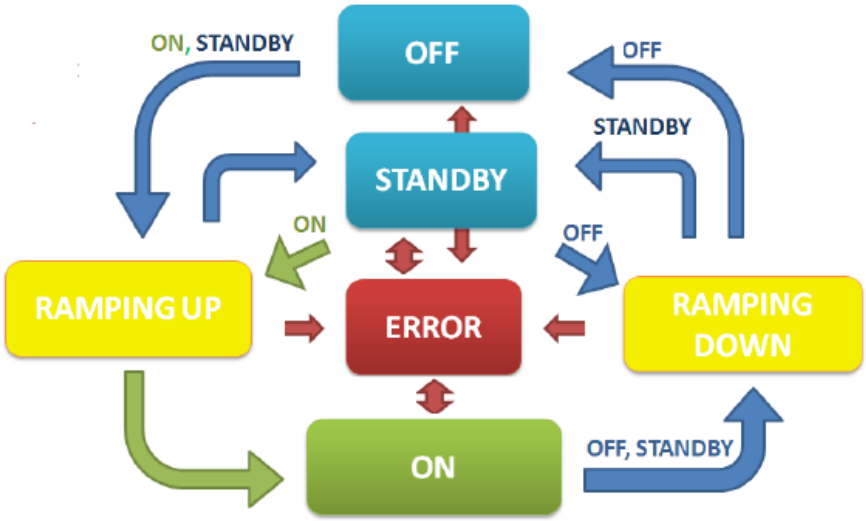

Figure 8.2: FSM schema for a high voltage (HV) channel.

feedback loop between the readout system and the trigger system. It functions by temporarily reducing the L1A rate if it receives feedback that the readout system data buffers will begin to overflow, resulting in a loss of data and possibly data corruption or readout system instability. The system is designed in order to be able to cope with highest foreseen trigger rate. If a bottleneck arises due to a malfunctioning piece of the system, it will be logged and an automatic recovery will be attempted without sending the system into an error state. If the state stays in a "warning" state for too long, and it can't be automatically recovered, then an expert intervention is required. If the system is sending bad or corrupted data, this will also be detected and, whenever possible, recovered automatically without requiring a reconfiguration, possibly by resetting and re-synching the links. Data formatting status (errors, event counters, etc.), system buffer status, link buffer status, and link status will also be monitored, as they all provide key information in the case of system malfunction.

During normal running conditions of CMS, the electronics will undergo two steps: configuration and run. The configuration has to be a very quick operation, consequently all the procedures for the electronic readiness must be happening in the initialization step, when it is switched on, and automated.

In fact, when the system is powered on, the VFAT chips will each have their parameters set to values determined from calibration tests. The main operational parameters will be hit count mode, the trigger mode, the mono-stable pulse length, the cycle time of the hit counter, voltage thresholds on the comparator, and the chip latency with respect to the L1A. Additionally, for each channel the threshold can be tuned by means of a trim DAC, and whether a particular channel is masked or not. The optimal values will be set automatically at power on and checked during configuration to verify that they have been properly set. All internal counters are also reset to zero and the data buffer emptied. Calibration routines to determine the latency and threshold of the chips (as well as the trim DACs) for the individual channels have been defined. These need to be run few times in a year in order to ensure that the detector is operating optimally. The calibration values will be stored in the configuration database that will serve the system in the initialization step. The configuration step is then simply translated in setting into "run mode" from "sleep mode" each chip, after which they will send data packets to the opto-hybrid on a received L1A.

The opto-hybrid will process the data received from the VFAT chips. S-bits will be sent to the GE1/1-CSC trigger link, as well as the GE1/1 backend electronics. The full tracking data will be sent to the backend electronics to be checked, packaged, and sent to the readout system. The opto-hybrid will receive the fast commands and distribute them to the VFAT chips. On initializing the hardware, a check is done to ensure that the optical links are all active and error free. On configuring the device, counters will be reset (L1A, events received from each VFAT, events sent to the backend electronics, events sent to the trigger link, and any error counts on the links or in the data packets), and during normal running condition the link with the CSC OTMB will be enabled. During running, the opto-hybrid can format the data from all VFAT chips into a common block and send it to the backend for further processing. Counters to check the integrity of the data passing through the system can be used to track the number of CRC errors and other problems in the stream.

The backend electronics boards (MP7) will process the data received from several opto-hybrids and format it to be sent to the central DAQ system via AMC13. In addition, the central trigger and timing commands will be received by the backend electronics to be sent to the detector frontend. On starting the system, the communication with the frontend will be established. Depending on the run mode (global or local), a connection to the central system as well is required. Configuration will involve resetting the counters of all fast commands received, as well as error counters and event processing counters. The GE1/1 run mode will be programmed into the MP7 cards, specifying the data readout path (whether to perform a local readout or not), the trigger source (central TTC system or possibly a local trigger source for certain types of calibration runs), and other running information common for the whole GE1/1 system. Monitoring the system will involve checking errors during the formatting of the data received from the opto-hybrid, monitoring the status of the specific MP7 with regard to the TTC/TTS system to ensure that the whole system is in sync.

GBT optical links connect the frontend electronics with the GE1/1 backend electronics and provide a trigger link with the CSC subsystem (OTMB). Fast commands (TTC/TTS signals, L1A, etc.,) as well as the DAQ link to the central CMS are provided to the GE1/1 μTCA crate through the CMS standard AMC13 card. Signals coming from the central system are delivered to the MP7 boards over the μTCA Fabric B connections. These signals are transmitted to the frontend electronics over the same bi-directional optical links that receive the tracking and trigger data from the from the frontend electronics. During the configuration step, the status of the various optical links will be established, and, in the case of one of the links being inactive (opto-hybrid to OTMB for triggers, opto-hybrid to MP7 for readout, or AMC13 to cDAQ for DAQ) the system will attempt to establish the link. If it is unable to do so at this stage, the system will attempt a recovery via a resynchronization or reset in the firmware. If this is unsuccessful, the configuration step must fail and the faulty link be specified waiting for expert intervention. During running, the quality of the data being transmitted on the optical links between the opto-hybrid and the OTMB, as well as the path to the backend will be monitored for problems. If errors are detected on the optical links, this may necessitate a reset issued by the firmware, or in extreme cases, a reconfiguration of the hardware.

8.3 Data quality monitoring system

The CMS Data Quality Monitoring (DQM) framework [75] provides, within the more general CMS framework, common tools for creation, filling, storage, and visualization of histograms and scalar elements. It offers standardized algorithms for statistical tests and automated data certification. It is a set of user-defined algorithms. It is intended to be used both online, during

data taking, and offline, during reconstruction and re-reconstruction stages. Its final purpose is to monitor and certify the quality of recorded data.

Online DQM applications are an integral part of the event data processing. Each application, usually one per subsystem, receives event data through a dedicated Storage Manager event server. A special stream of events is used to perform DQM operations [76]. The stream contains detector and trigger raw data, Level-1 and High Level Trigger (HLT) summary results, in addition to HLT byproducts essential for monitoring trigger algorithms. There is neither event sorting nor handling, and no guarantee that parallel applications receive the same events. Starting and stopping DQM online applications is centrally managed by the RCMS.

On the other hand, Offline DQM runs as part of the reconstruction process at Tier-0, of the re-reconstruction at the Tier-1s, and of the validation of software releases, simulated data, and alignment and calibration results. Despite the difference in location, data content and timing of these activities, offline monitoring is unique and formally divided into two steps. First, histograms are created and filled while data are processed event by event. The second step is the harvesting when histograms and monitoring information, produced in step one, are extracted and merged to yield full statistics. Efficiencies are calculated, summary plots are produced, and quality tests are performed. The automated data certification decision is taken here. The disadvantage of offline monitoring is the latency of reconstructed to raw data, which can be as long as several days. On the other hand, the advantages are substantial. All reconstructed events can be monitored and high-level quantities are available. This allows the identification of rare or slowly developing problems.

8.3.1 Architecture of the GEM DQM system

The GEM DQM system is developed within the compass of the CMS reconstruction and physics analysis software framework, CMSSW, and is based on object-oriented programming languages: C++ and Python. It has been designed to be flexible and easily customizable, since it needs to be used within different monitoring environments: online/offline DQM and standalone programs for private analyses. Every data analysis and monitoring algorithm is implemented in a separate module, completely independent from the others. Each module inherits from the parent classes DQMEDAnalyzer and DQMEDHarvester [77] specifically designed for monitoring purposes. Modules may be added or eliminated from the monitoring sequence as needed. Different parameter configuration files allow the modules to run on both detector and simulated date without requiring code changes and so re-compilation. The modules have been organized in a source/client structure.

Source modules access information on an event-to-event basis, define the quantities to be monitored, and fill histograms. Event selection is performed at this level using specific trigger paths. Offline applications instead run on muon enriched samples during the event-reconstruction stage. Client modules perform the actual analyses by accessing periodically the histograms with a frequency that depends on the monitored quantity, varying from every luminosity section to once a run. Clients have the tasks of: creating summary histograms, performing quality tests, calculating alarm levels, saving the output in ROOT files, and taking a preliminary data certification decision.

Histograms are organized in a hierarchical tree-like folder structure reproducing detector geometry. The parameters monitored are: single hit multiplicity, bunch crossing, number of reconstructed hits, cluster size, occupancy, detection efficiency, detector noise, and data integrity. These parameters are monitored for each of the 144 GEM chambers individually. This sums to $\sim$thousand histograms and navigating through them is complicated for non-experts. There-

fore, special layouts containing only summary histograms are prepared for both GEM and central DQM shifters, thus allowing the shift crew to quickly identify problems and take action. These histograms are meaningful, not overburdened with information and equipped with a clear set of instructions for interpreting them. Reference histograms may be superimposed and Quality Tests (QT) are applied. QTs are standardized and integrated within the CMS DQM framework. They include among others: comparison with reference histogram using ROOT χ^2 algorithm and ROOT Kolmogorov algorithm, check that histogram contents are between (Xmin,Xmax)/(Ymin,Ymax).

8.3.2 Data certification

The overall certification of data collected during operation is based on the online and offline DQM, and on the DCS monitored information.

A preliminary data certification is performed automatically within the GEM offline DQM algorithms. This automatic certification is based on the results of standard quality tests applied to the occupancy, cluster size, noise, data integrity distributions, as well as on the GEM DCS status. The application is flexible enough to allow the expert to modify the algorithm in case of need. The automatic certification is bound to provide as a result a number that has to range between 0 and 1 reflecting detector performance and a quality flag, i.e. good, bad. The CMS specification requires the quality flag to be set to bad when such a number is less than 0.95. Such a case requires expert intervention. Results are visually displayed in a summary histogram as shown in Figure 8.3. The plot uses dummy data and it is presented for illustrative purpose only.

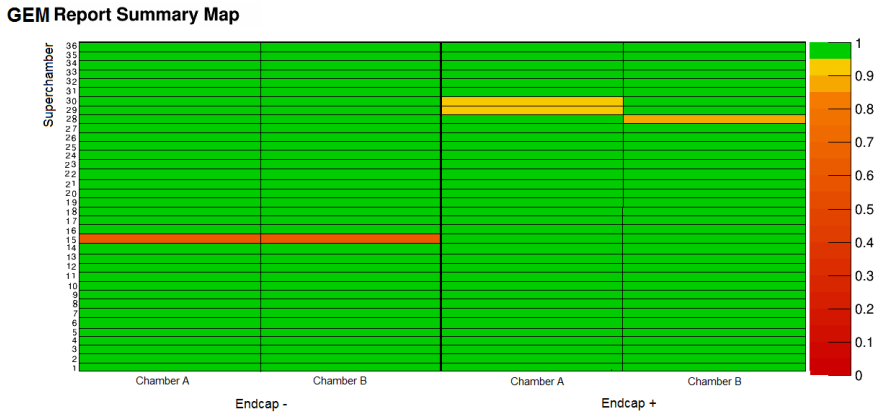

Figure 8.3: Automatic data certification results displayed in a summary report histogram. Color convention follow CMS specifications. Dummy data has been used for this plots that is here presented for illustrative purpose only.

A more accurate certification is performed by both online and offline by central DQM shifters. During the first running period Online DQM shifts took place 24/7, during detector operation at the CMS "on-detector" control room in Cessy, France. Offline DQM shifts were carried out, only in daytime, at the CMS control center, on the main CERN site. Shift activities are supported by regular remote shifts; two shifts per day at Fermilab (USA) and one shift per day at DESY (Germany). Shifters analyse a limited number of summary histograms with an exhaustive set of instructions to facilitate this task. The final list of "good" and "bad" run flags is inserted in the CMS Run Registry (RR) [78] and must be signed-off by a GEM Data Manager expert, as a final certification step, and copied to the offline condition database. The RR is the official workflow management and tracking tool used to certify collected data, to keep track of

the certification results, and to make them available to the entire collaboration via a web-based user interface.

8.3.3 DQM graphical user interfaces

DQM output, which includes histograms, alarm states, and quality test results, is made available in real time via a central graphical user interface (GUI) [79], accessible from the web. Being web-based, this central GUI permits users all over the world to access the data and check results without installing experiment specific software. Monitoring data is also stored to ROOT files periodically during the run. At the end of the run, final result files are uploaded to a large disk pool accessible from the central GUI. Subsequently, files are merged to larger size and backed up to tape. Recent monitoring data (several months worth) are cached on disk for easy access. The GUI was custom built to fulfil the need of shifters and experts for efficient visualization and navigation of DQM results and not meant as a physics analysis tool.

The GEM Data Manager expert can access all the real-time and historical information using any browsing system delivering prompt feedback on demand.

8.4 Database management system for the GEM project

The GEM project will rely on a dedicated Database management system (DB) within the official CMS Online Master Database System (OMDS) [80] based on ORACLE technology [81]. The GEM DB will be in charge of four different logical functionalities:

- The Equipment Management DB, in charge to store all information of all the basic components of the GEM system and will comply with the traceability requirements imposed by the French Agency of Nuclear Security law concerning the nuclear installations, being CERN classified as an “Installation Nucleaire de Base”.
- The Construction DB will support the GEM Chamber and Electronics construction on all the phases storing the Quality Controls test result. Data will be kept to be able to trace back all possible problems appearing in the system. A dedicated web based user interface will be deployed to allow the operators to upload and retrieve all relevant information of the construction processes.
- The Configuration DB will be used to store all the parameters needed to set up the system into any running mode. They will include voltage settings of power supplies and the programmable parameters of the electronics.
- The Condition DB will store data that describe the state of the GEM during operation. Those data are used in the studies of the detector performance and for post mortem analysis for malfunctioning detectors.

The DB architecture will be designed to account for the different usage and access of the different data. It will use the same database schema as that used for construction and online operations of other CMS subdetectors. The GEM DB will consist of multiple tables that are used to map and track the detector components, and to store detector test, configuration, and monitor data. The development process involves the use of 4 instances of the database, Template DB instance (current phase), Development DB, Integration DB, and Production DB.

Chapter 9

Project Organization, Responsibilities, Planning and Costs

9.1 Participating institutes

The CMS GEM Collaboration is currently comprised of 37 institutions in 18 countries with a total of 192 physicists, engineers, and doctoral students.

The collaboration membership by country and institute follows.

1. Univ. Libre de Bruxelles, Brussels, **BELGIUM**
   P. Barria, G. De Lentdecker, M. Korntheuer, T. Lenzi, T. Maerschalk, E. Verhagen, Y. Yang, R. Yonamine, F. Zenoni
2. Ghent Univ., Gent, **BELGIUM**
   S. Cauwenbergh, A. Cimmino, S. Salva, M. Tytgat, N. Zaganidis
3. Inst. for Nuclear Research and Nuclear Energy, Sofia, **BULGARIA**
   A. Aleksandrov, R. M. Hadjiiska, P. Iaydjiev, G. Rashevski, M. Rodozov, M. Shopova, G. Sultanov
4. Sofia Univ., Sofia, **BULGARIA**
   L. Litov, B. Pavlov
5. Peking Univ., Beijing, **CHINA**
   C. Asawatangtrakuldee, Y. Ban, D. Wang, M. Wang
6. Univ. de Los Andes, Bogota, **COLOMBIA**
   C. Avila, B. Gomez, C. F. Gonzalez, J.C. Sanabria
7. Academy of Scientific Research and Technology - ENHEP, Cairo, **EGYPT**
   A.A. Abdelalim, O. Aboamer, W. Ahmed, R. Aly, Y. Assran, W. Elmetenawee, A. Hassan, R. Masod, S. Mohamed, A. Radi
8. Lappeenranta Univ. of Technology, Lappeenranta, **FINLAND**
   M.T. Kupiainen, J.P. Talvitie, T. Tuuva
9. Atomic Energy and Alternative Energies Commission, Saclay, and Inst. of Research into the Fundamental Laws of the Universe, Saclay, **FRANCE**
   G. Fabrice
10. Hubert Curien Multidisciplinary Inst. , Strasbourg, **FRANCE**
    J.-M. Brom, U. Goerlach, J.A. Merlin

11. RWTH Aachen Univ., III. Phys. Inst. A, Aachen, **GERMANY**
K. Hoepfner, B. Philipps, F.-P. Zantis

12. Inst. for Particle and Nuclear Physics, Budapest, **HUNGARY**
G. Bencze, G. Endroczi

13. Inst. for Nuclear Research, Debrecen, **HUNGARY**
N. Beni, S. Czellar, A. Fenyvesi, J. Molnar, Z. Szillasi

14. National Inst. of Science Education and Research, Bhubaneswar, **INDIA**
K. Mandal, P.K. Mal, S.K. Swain

15. Panjab Univ., Chandigarh, **INDIA**
V. Bhatnagar, R. Kumar, P. Kumari, A. Mehta, J. Singh

16. Delhi Univ., Delhi, **INDIA**
A. Bhardwaj, A. Kumar, M. Naimuddin, S. Ramkrishna, K. Ranjan, A.H. Shah, R.K. Shivpuri

17. Saha Inst. of Nuclear Physics, Kolkata, **INDIA**
S. Banerjee, S. Bhattacharya, N. Majumdar, S. Mukhopadhyay, S. Roy Chowdhury

18. Bhabha Atomic Research Center, Mumbai, **INDIA**
A.K. Mohanty, L.M. Pant

19. National Inst. of Nuclear Physics, Univ. of Bari, and Polytechnic of Bari, Bari, **ITALY**
M. Abbrescia, P. Altieri, C. Calabria, C. Caputo, A. Colaleo, N. De Filippis, G. De Robertis, F. Loddo, M. Maggi, S. My, S. Nuzzo, G. Pugliese, R. Radogna, A. Ranieri, C. Tamma, R. Venditti, P. Verwilligen

20. National Inst. of Nuclear Physics and Univ. of Bologna, Bologna, **ITALY**
S. Braibant, F.R. Cavallo, M. Dallavalle, P. Giacomelli, L. Guiducci

21. National Laboratory of Frascati, National Inst. of Nuclear Physics, Frascati, **ITALY**
L. Benussi, S. Bianco, M. Caponero, D. Piccolo, G. Raffone, G. Saviano

22. National Inst. of Nuclear Physics, Napoli, **ITALY**
S. Buontempo, S. Meola, P. Paolucci, F. Thyssen

23. National Inst. of Nuclear Physics and Univ. of Pavia, Pavia, **ITALY**
A. Braghieri, A. Magnani, P. Montagna, C. Riccardi, P. Salvini, I. Vai, P. Vitulo

24. Chonbuk National Univ., Jeonju, **KOREA**
H.S. Kim, M.S. Ryu, Y.G. Jeng

25. Korea Univ., Seoul, **KOREA**
S. Choi

26. Seoul National Univ., Seoul, **KOREA**
U. Yang, J. Almond, G.B. Yu

27. Univ. of Seoul, Seoul, **KOREA**
K. Choi, M. Choi, H. Kim, J. Lee, J. Lee, I.C. Park, G. Ryu

28. National Center for Physics, Islamabad, **PAKISTAN**
W. Ahmed, I. Awan, A. Ahmad, M.I. Asghar, H. Hoorani, S. Khan, S. Muhammad, A. Sultan

29. Texas A&M Univ. - Qatar (associated with Texas A&M Univ., USA), Doha, **QATAR**
M. Abi Akl, O. Bouhali, A. Castaneda, Y. Maghrbi

30. Petersburg Nuclear Physics Inst., Gatchina, **Russia**
A. Vorobyev

31. CERN, Geneva, **SWITZERLAND**
D. Abbaneo, M. Abbas, P. Aspell, S. Bally, J. Bos, J. Christiansen, S. Colafranceschi, A. Conde Garcia, M.M. Dabrowski, R. De Oliveira, B. Dorney, S. Ferry, A. Marchioro, A. Marinov, J.A. Merlin, E. Oliveri, H. Postema, A. Puig Baranac, A. Rodrigues, L. Ropelewski, A. Sharma, M. van Stenis

32. Texas A&M Univ., College Station, **UNITED STATES OF AMERICA**
A. Celik, S. Dildick, W. Flanagan, J. Gilmore, T. Huang, T. Kamon, V. Khotilovich, S. Krutelyov, A. Safonov, A. Tatarinov

33. Wayne State University, Detroit, **UNITED STATES OF AMERICA**
A. Gutierrez, P.E. Karchin, J. Sturdy, P. Thapa, S. Zaleski

34. Univ. of Florida, Gainesville, **UNITED STATES OF AMERICA**
D. Acosta, I. Furic, A. Korytov, A. Madorsky, G. Mitselmakher

35. Univ. of California, Los Angeles, **UNITED STATES OF AMERICA**
C. Bravo, J. Hauser, A. Peck, X. Yang

36. Univ. of Wisconsin, Madison, **UNITED STATES OF AMERICA**
A. Sakharov

37. Florida Inst. of Technology, Melbourne, **UNITED STATES OF AMERICA**
V. Bhopatkar, M. Hohlmann, A. Mohapatra, E. Starling, A. Zhang

9.2 Project organization

The CMS GE1/1 muon upgrade is a project of the CMS GEM Collaboration in the CMS Muon Collaboration. An overview of the CMS GEM organizational structure is shown in the organigram of Figure 9.1. This organizational chart has evolved from 2009-2010 when the proto-collaboration was constituted from CMS-SLHC-RD-2010.02. It was comprised of active collaborators in detector R&D and studies for physics motivation. During 2011-2012 a revision was made with the addition of several new institutions when aspects of trigger exploitation using the detector were introduced. Finally, during 2013-2014 the collaboration increased with participation in every aspect from all institutions outlined above.

The GEM Management Board (MB) supervises, reviews progress, and defines planning and strategy for the GEM project. It defines and manages the scope, budget, and milestones of the project, and the sharing of responsibilities among the collaborating institutions. This is shown in Figure 9.9 and is discussed in Section 9.8.

The GEM MB meets several times a year, typically during CMS and CMS upgrade/physics weeks. In important areas where expertise lies outside the project (for example sophisticated

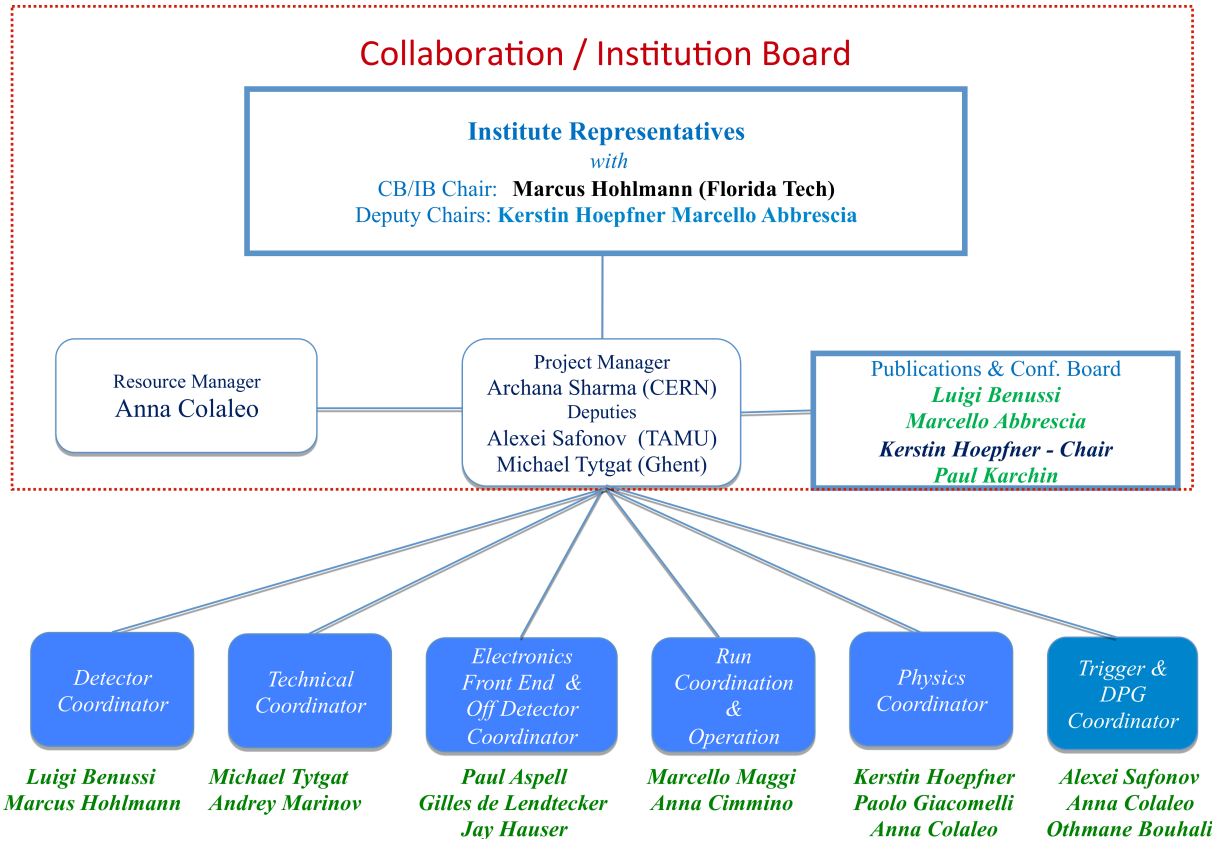

Figure 9.1: GEM Collaboration management organigram.

micro-electronics) matters of concern are brought to the attention of experts in the field and solutions are sought.

Overall direction of the project is provided by the GEM Institution Board (IB), composed of representatives from each of the collaborating institutes and led by a chair and deputies. The GEM IB meets periodically to provide guidance on technical and organizational matters. The GEM IB provides a means of communication between the project management and the institutes.

The GEM Project Manager (PM) and deputies provide the leadership to implement the goals of the collaboration and coordinate activities with CMS Muon IB and CMS Upgrade management. The management team includes a Resource Manager who maintains detailed records of cost estimates, actual expenditures, and coordinates the assignment of experimental physics responsibilities with the institute representatives. The project will be organized in tandem with the new Muon Organization.

9.3 Role of the Project Manager and Management Team

The Project Manager and the management team are selected by the institution leaders and endorsed by the collaboration Chairperson, who, along with the PM, represent the project to the CMS upgrade project office. The roles of the Project Manager and Chairperson are characterized by the following charge and deliverables.

- To lead the MB to define and manage the scope, cost and budget for the GEM upgrades, taking into account the LHC shutdown and schedules, available resources, and interests of the groups involved. In particular, this TDR reflects the management

of the GE1/1 project to be installed during LS2.

- To lead the MB to define a set of project milestones and then steer the project to meet them, assuring the necessary flow of resources and information exchange throughout the project.
- To work closely in the project with the other coordinators to review technical progress,to manage the planning and strategy to deal well with problems and opportunities, to establish and maintain appropriate documentation with reliable archiving for all relevant technical specifications of parts and interfaces to ensure, QA procedures, QC procedures and logistics.
- To prepare for reviews of important technical, engineering and procurement decisions, normally chaired by CMS Upgrade and Technical Coordination.
- To chair the MB, organize meetings, agendas, objectives and follow-up with reports to the GEM and Muon Institution Boards.
- To work in partnership with the Upgrade and Muon teams to assure proper consideration of all decisions, including their impact on the Muon project as a whole, with appropriate preparation of points for endorsement by the Muon IB.
- To work closely with the GEM Resource Manager on all resource-related matters.
- To represent the GEM Upgrade in the CMS Upgrade Project Office as well as in CMS Management and LHCC meetings.
- Last but not least, the GEM MB Chairperson and Project Leader have been responsible for assembling an editorial team and publishing this TDR.

The PM and RM work to ensure that the sharing of effort is equitable across the collaboration. This assists in keeping track of the staffing of the project along with the necessary flexibility of injecting resources when needed in relevant areas.

The publications and conference committee promotes the publication of results from the CMS GEM project and their presentation in conferences. The committee assists in the review and approval of publications, conference abstracts, talk slides, posters, and conference proceedings. The committee also maintains a list of CMS GEM collaborators and authors.

The project management is assisted by coordinators in six key areas of the project: detector chambers, Technical Coordination, electronics, DAQ, operation, physics, and trigger/DPG. The detector coordinators manage the construction and testing of the GEM chambers. The technical coordinators are responsible for the planning and installation of chambers, electronics, and services at P5 and at test and preparation areas such as B904, TIF, GIF++, and test beams. The electronics coordinators manage the design and construction of on- and off-detector electronics including the front-end VFAT chips, GEBs, opto-hybrids, μTCA readout system, trigger interface, firmware and DAQ software. Run and operations coordination includes irradiation and beam testing as well as operation at P5. The physics coordinators lead the simulation effort to assess the impact of the GE1/1 system on the physics performance of CMS in key channels in sync with ongoing CMS Upgrade as a whole. The trigger and DPG coordinators lead the development of software to simulate the GEM detectors, predict the trigger performance, and monitor the performance of the system during operation.

9.4 GEM Technical Coordination Team

This team is composed of two detector construction Coordinators, that lead the technical activities within the project. The Coordinators act as a team to ensure the following items.

- Realistic and detailed plans are prepared.
- Adequate resources and supervision are committed to the different activity lines.
- The planning is consistent with the project milestones, quality objectives and budget.
- Progress is properly monitored across the technical activities in all centres and potential production sites at national institutes.
- Technical specifications for parts and interfaces between parts of the system are established, well defined, documented and followed.
- QA/QC procedures are established, well defined, documented and followed.
- Information flows properly within the project, to/from the GEM MB and within the Technical Coordination Team, and that there is a central repository used to organize and archive project documents. The Coordinators convene technical steering groups of experts as necessary.

9.5 Role of the Resource Manager

The Resource Manager of the GEM project has the following tasks:

- Maintaining and updating the subproject CostBook, starting initially from estimates of costs and funding, and evolving towards a detailed bookkeeping of actual expenses and contributions from the participating FAs
- Elaborating and updating the cost time profile and the cost sharing among FAs.
- Taking care, together with the Technical Coordinators and/or with the heads of Working Groups and/or the people responsible at the Production Centres, of procurements for the construction of the upgraded detector. Specifically, the Resource Manager is responsible along with the Project Manager, for the tendering process involved in common procurements performed centrally.
- Reporting regularly on construction expenditures to the GEM MB, to the CMS FB, and preparing regular reports for the LHC RRB and the RRB Scrutiny Group as required.

9.6 Construction schedule

An overview of the construction schedule, up to installation, is shown in Figure 9.2. The major milestones of the project are shown in Table 9.1. The construction is aimed for completion in time for installation during LS2, currently scheduled for the first quarter of 2018.

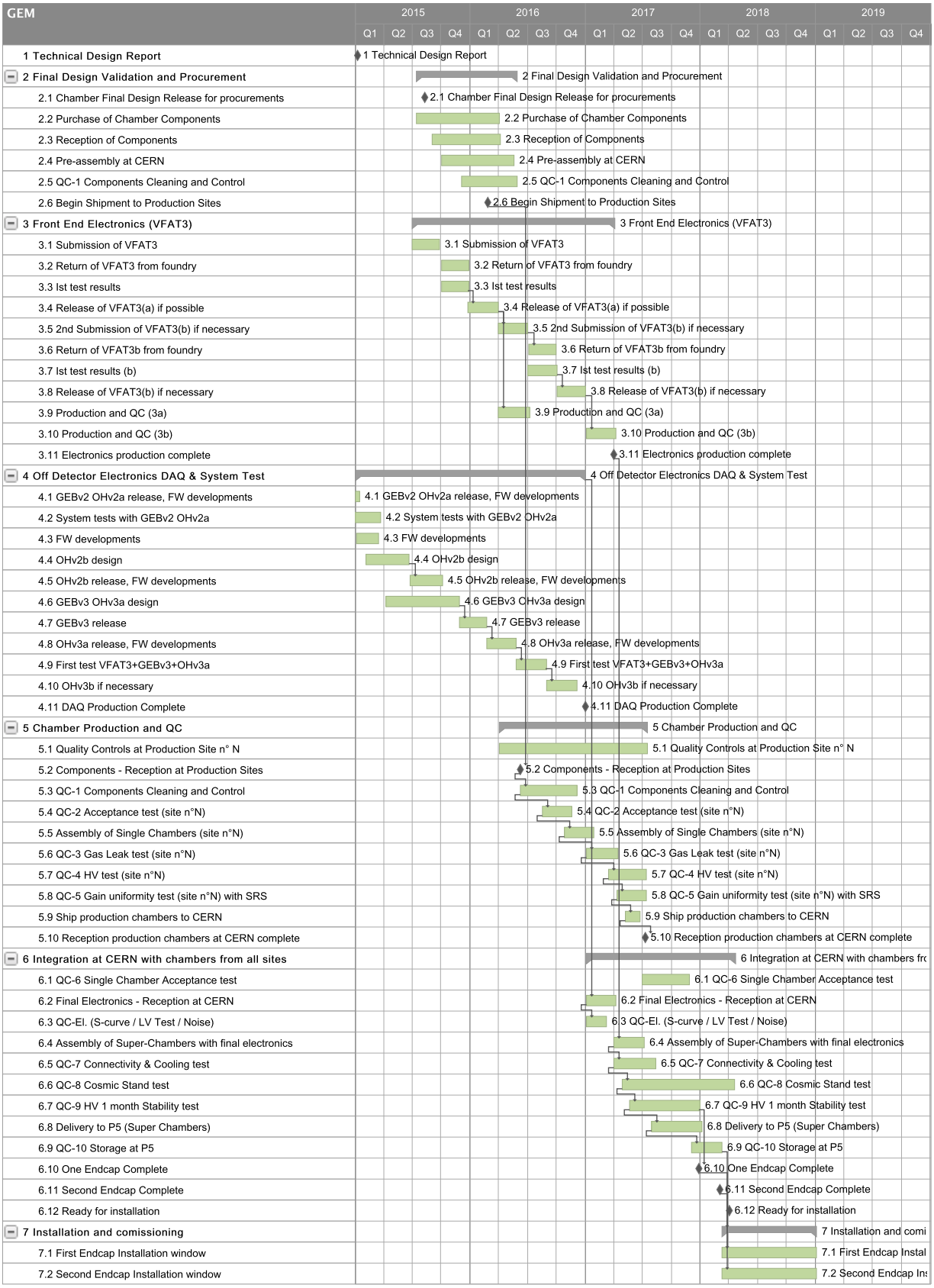

Figure 9.2: GEM GE1/1 LS2 project schedule.

Table 9.1: Major milestones of the GE1/1 LS2 construction project.

Milestone	Date
Technical Design Report	01/2015
Chamber Final Design Release for procurements	08/2015
Begin Shipment to Production Sites	02/2016
Components Reception at Production Sites	06/2016
DAQ production complete	01/2017
Electronics production complete	03/2017
Reception production chambers at CERN complete	06/2017
One endcap complete	01/2018
Second endcap complete	03/2018
Ready for installation	03/2018

9.7 Costs

The detailed cost estimate of the GEM GE1/1 detector has been established, with several individual items in the Cost Book, on different levels of a Work Breakdown Structure (WBS).

The estimated costs are expressed as CORE cost, according to the definition developed for the CMS Construction Project MoU and LHCC Cost Review Committee. CORE costs are defined as M&S (materials and services) costs for the production phase of the project and include only those items which fall into the allowed expense group according to the following guidelines:

- final prototype or pre-production fabrication required to validate a final design or product quality, prior to production;
- engineering costs incurred during production at a vendor or contractor, not at a CMS member Institution;
- production fabrication and construction costs, including QA and system testing during the assembly process;
- transportation costs, integration and installation.

CORE costs do not include:

- *R&D* and prototype costs associated with developing the design;
- costs for purchasing or building infrastructure and facilities at the CMS institutions;
- any labor costs at CMS institutions or support for physicists at CERN;
- travel costs for institution personnel.

In addition, following CMS guidelines for CORE costs, neither general contingency (for unexpected or unforeseen technical flaws or major accidents) nor financial contingency (for inflation, exchange rate variations, or general evolution of economy or market conditions which may alter the cost of procured materials and components) have been included in the estimates.

For manufactured or assembled components the yield is defined to account for any costed parts that will not meet specification. Spare parts to cover production losses and to ensure successful commissioning are included in the CORE estimates, while spares to support long term maintenance and operation (*M&O*) are not. In many cases, in order to deliver assembled or produced components additional costs are borne by institutions and funding agencies, including (*R&D*), design engineering and other institution labor. In addition to the systems installed in the experiment, the estimates include costs for test stand needed for commissioning, beam studies

Item name	Total KCHF
GE11 Project total	**3746**
Chambers	**853**
Electronics On-Detector Total	**1435**
Test bench	40
GE11	1395
Electronics Off-Detector Total	**334**
Test bench	34
GE11	300
Power total	**711**
Test bench	42
GE11	669
Services	**283**
Integration	**130**

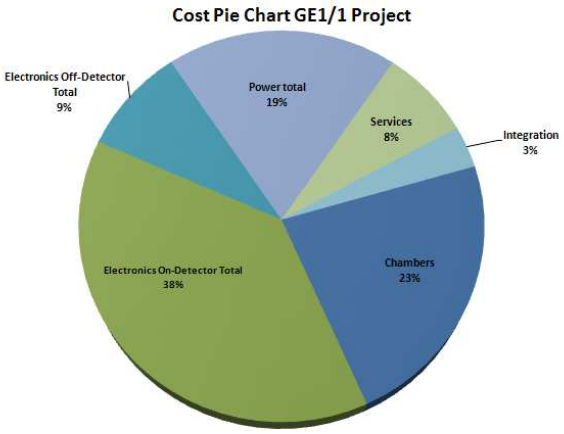

Figure 9.3: GEM GE1/1 LS2 project - CORE cost table (left) and pie chart (right).

and firmware development.

Tables are built from the tasks and component level with the basis of estimate described for both unit cost and unit quantity.

The quantities included in the tables are therefore:

- the number of units to be installed in CMS;
- the number required for commissioning test benches;
- construction and commissioning spares.

The cost estimates have a firm basis in industrial offers or similar parts already purchased, about 85%, and in the experience gained during the prototype work or private information from vendors, about 15%. It is expected that the cost uncertainty is less than 10%. Quotes and estimates have been provided in CHF, EUR, or USD, depending on the geographical location of institutes, companies, vendors, or suppliers. In this section, all monetary values are expressed in CHF. The following conventional exchange rates have been used to convert EUR and USD to CHF:

1 USD = 0.92 CHF, 1 EUR = 1.23 CHF

An breakdown of the CORE cost estimate in main categories is shown in Figure 9.3 (left) with a pie chart showing the main contributions in Figure 9.3 (right).

The detailed costs per categories are presented in the following sections.

9.7.1 Detector cost estimate

The total detector cost, described in details in Table 9.2, includes the costs of the chamber and the superchamber, mechanical components for assembly, the storage, the test stands and the shipping. The cost of an individual item is estimated using a unit cost and an estimate of the quantity needed.

For each item the quantity needed is the sum of the actual quantity of material for production of the 144 single chambers to be mounted on the detector, plus 2% of material needed to compen-

Table 9.2: GEM GE1/1 LS2 project - Detector cost details.

Item name	Total cost (kCHF)	Unit Cost (CHF)	Quantity of Units in CMS	Quantity of Units for Test Stands	Quantity of Production spares	Quantity of Units	Item Cost (CHF)
GE1/1 Detector total	**853**						
Chamber components	**807**						
Drift electrods	63	400	144	3	10	157	62832
GEM	581	3600	144	3	14	161	581040
Readout boards	126	800	144	3	10	157	125664
Cooling circuit	31	200	144	3	10	157	31416
Chamber assembly components	5	35	144	3	10	157	5498
Superchamber Assembly	**6**	80	72			72	5760
Storage and test stand at CERN	**20**	20000	1			1	20000
Shipping	**20**	20000	1			1	20000

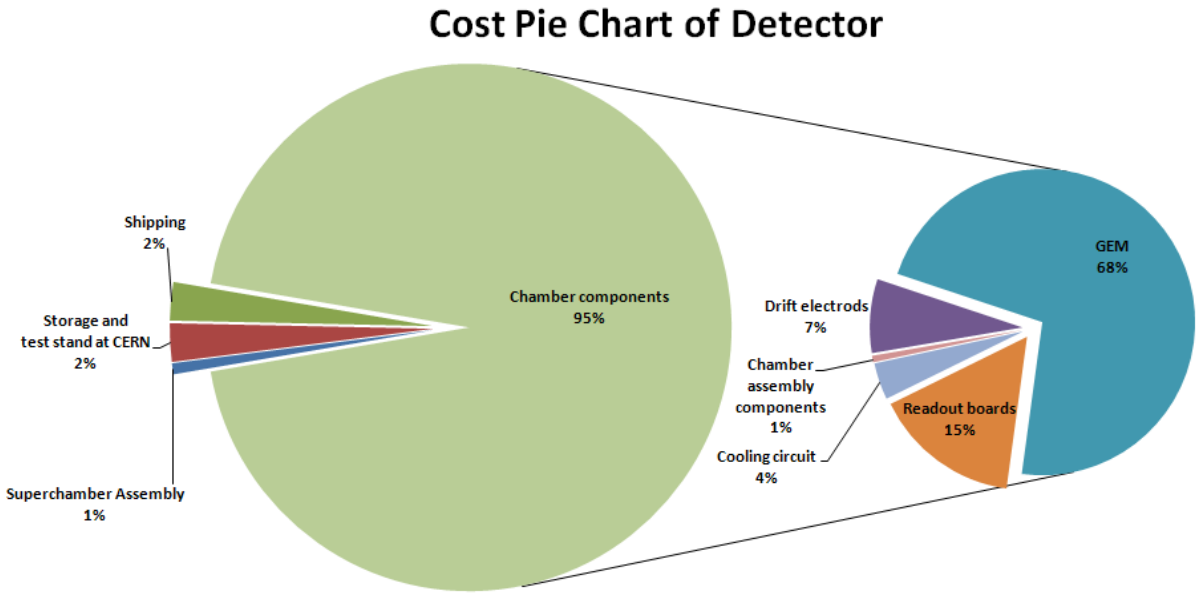

Figure 9.4: Main contributions to the detector cost estimation (left), with details of the chambers cost (right).

Table 9.3: GEM GE1/1 LS2 project - Electronics cost details.

Item name	Total cost kCHF	Unit Cost (CHF)	Quantity of Units in CMS	Quantity of Production spares	Quantity of Units	Item Cost (CHF)
GE1/1 Electronics	**2364**					
On Detector Total	**1395**					
VFAT3 Eng Run	450	450000	1	0	1	450000
VFAT3 Production	58	10	3456	2304	5760	57600
VFAT3 additional Wafer costs	22	319268	1	0	1	21600
VFAT3 Hybrid	350	81	3456	864	4320	349529
GEB	303	1683	144	36	180	302964
Opto Hybrid	213	1184	144	36	180	213098
Off Detector Total	**300**					
MP7 (Crate incl)	115	12780	8	1	9	115020
Link Inter Crate	0.4	72	4	1	5	360
Bi Links	184	256	576	144	720	184320
Power Total	**669**					
cables LV	16	100	144	16	160	16000
cables HV	80	500	144	16	160	80000
LV supply	220	8130	24	3	27	219518
HV Supply	265	9829	24	3	27	265383
LV Easy crates	11	1535	6	1	7	10745
HV Easy crates	8	1535	4	1	5	7675
AC/DC converter	33	4723	6	1	7	33062
mainframe	32	10627	2	1	3	31882
Controller	5	1476	2	1	3	4428

sate for expected yields during fabrication operations (GEM foils, PCB, pipes, connectors, etc), plus material for additional 5% of spare chambers. The spare chambers are needed to safely overcome the assembly, integration, commissioning, and installation stages, when handling of parts may result in their accidental damage, thus needing immediate replacement. We have included the cost for three additional complete chambers for long term test at the irradiation facilities and test beam. The pie chart for the cost of the detector is shown in Figure 9.4, where the wedge for the single detector component, which represents the largest contribution to the cost, is detailed in a separate pie chart.

9.7.2 Electronics cost estimate

The electronics costs, shown in detail in Table 9.3, include the costs of the front-end, off-detector and power system electronics. The cost estimate of the three major components is summarised in Figure 9.5, while the major contribution to the cost of the each of the four components is shown in the Figure 9.6.

The main contribution is due to the on-dectector electronics, in particular driven by the cost of the two pre-production submission with final mask set of VFAT3. The second major cost is due to the power system, where standard CAEN system and vendor quotes have been assumed.

For the electronics as general guidance the following production yields have been considered:

- 0.6 for an analogue packaged ASIC;
- 0.9 a digital packaged ASIC;
- 0.9 for a standard (off-detector) electronics module;
- 0.8 for a complex (front-end) electronics module.

A test bench has been prepared, for a total cost of 116 kCHF, in the CERN Building 904, where

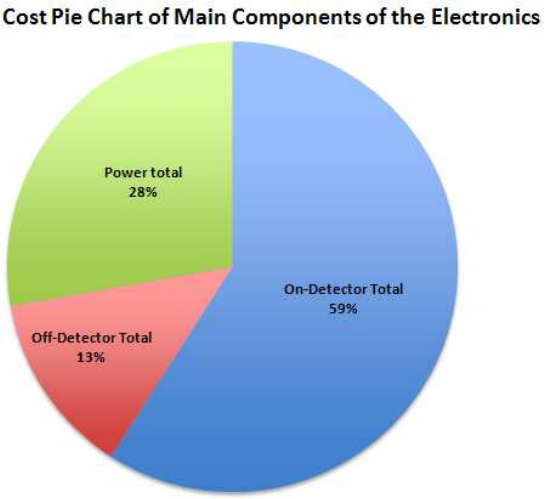

Figure 9.5: The breakdown of the electronics cost estimate.

Table 9.4: GEM GE1/1 test bench in Building 904 cost details.

Item name	Total cost (kCHF)	Unit Cost (CHF)	Quantity of Units for Test Stands	Quantity of Units	Item Cost (CHF)
GE1/1 Test bench	**116**				
On Detector Total	**40**				
VFAT3 Production	2	10	144	240	2400
VFAT3 Hybrid	15	81	144	180	14564
GEB	14	1683	6	8	13465
Opto Hybrid	10	1184	6	8	9471
Off Detector Total	**34**				
MP7 (Crate incl)	26	12780	1	2	25560
Link Inter Crate	0.3	72	2	3	216
Bi Links	8	256	24	30	7680
Power Total	**42**				
Cables LV	1	100	6	6	600
Cables HV	3	500	6	6	3000
LV supply	8	8130	1	1	8130
HV Supply	10	9829	1	1	9829
LV Easy crates	2	1535	1	1	1535
HV Easy crates	2	1535	1	1	1535
AC/DC converter	5	4723	1	1	4723
Mainframe	11	10627	1	1	10627
Controller	2	1476	1	1	1476

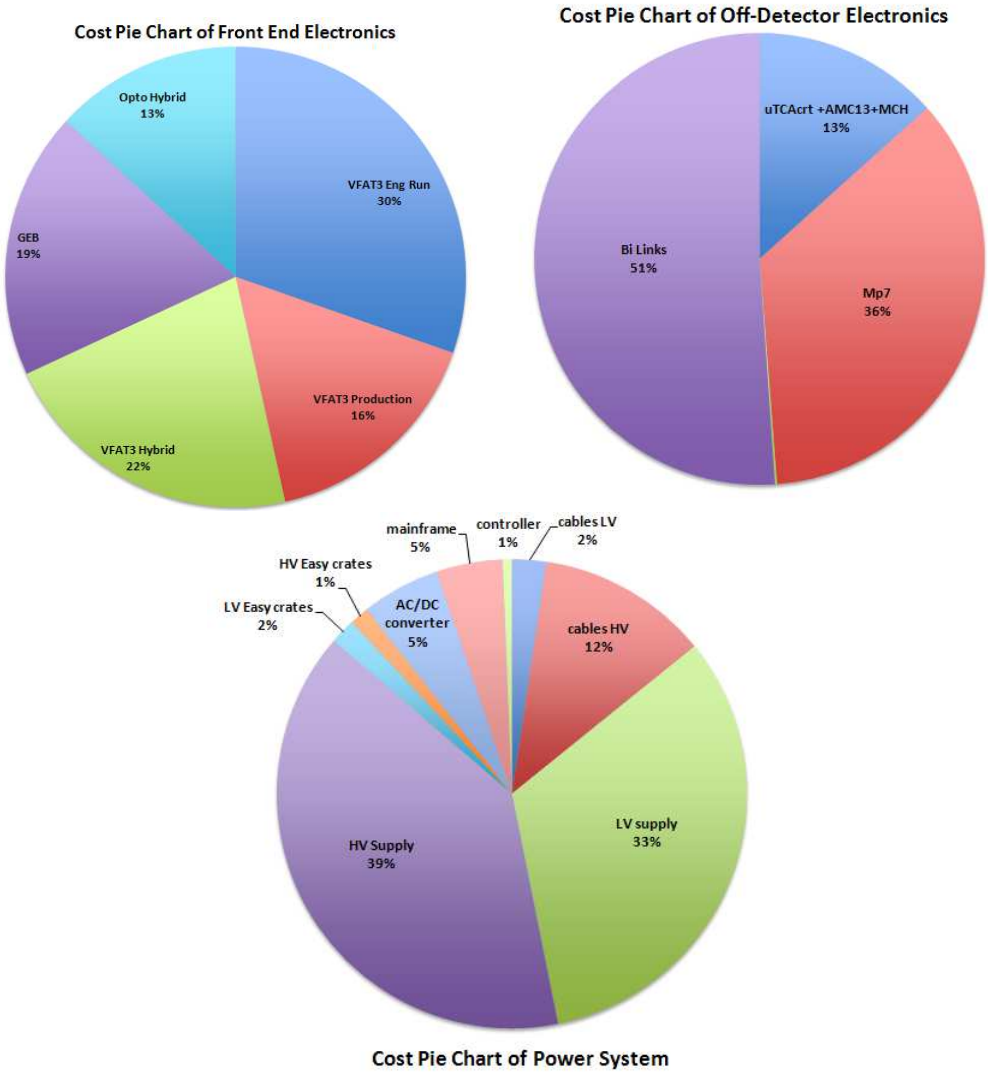

Figure 9.6: The breakdown of the on-detector, off detector and power system electronics cost estimates.

up to six fully equipped chamber electronics plus read-out chain and trigger will be setup for the quality control of the final electronics, as described in Figure 5.1. The cost details are shown in Table 9.4.

9.7.3 Services and infrastructure cost estimate

The main services to be integrated are the gas, the cooling system, and the Detector Control System computers and sensors to monitor the enviromental parameters (temperature, humidity) which can affect the detector performances. Table 9.5 shows the costs of services needed to complete the installation, commissioning and operation of the GE1/1 system during LS2.

The main contribution to the service cost are listed in are summarised in Figure 9.7 (left). The major cost here is due to the gas system, for which the details are provided in Figure 9.7 (right).

For the gas system the standard installation as for all the gas systems for the LHC experiments is foreseen.

In Figure 7.16 the overview of the gas supply system for the GE1/1 stations was presented. The main gas mixer with the supply cylinders is placed in the gas building located on the surface. The final $Ar/CO_2/CF_4$ mixture is transported to the detector cavern through a 254 m long stainless steel transfer pipe of 30 mm in diameter which runs in the PM54 shaft and connects the surface gas building with the gas racks in USC55.

All primary gases are the same ones used by other CMS detector, therefore all the required components for the primary gas supplies in SGX5 are already installed. The gas distribution for the GE1/1 installation slots is based on the existing pipe infrastructure installed initially for the RPC RE1/1 detectors.

Therefore the remaining elements contributing to the costs of the gas system are:

- Control rack: the gas system is controlled by an industrial Programmable Logic Controller (PLC), which is located in a control rack with the crates corresponding to all functional modules. All measured values (pressure, flows, mixing ratios, temperatures, etc.) are processed in the PLC and used to control the process as well as to generate alarms or interlocks to the gas system operation. A user interface has been developed using standard DCS software, which allows to monitor the status of each gas system device, control active components, transfer to the PLC regulation set points and alarm thresholds.
- Mixer module: the primary task of the mixer module is to provide the suitable gas mixture. The mixer module has up to four gas input lines equipped with Mass Flow Controller (MFC)2, which are controlled via software.
- Chamber pre-distribution system: once the gas mixture is prepared by the MFCs, it is sent to several pre-distribution modules located in the UGC, where several gas parameters (as pressure, gas flow, etc.) can still be modified via online software during LHC runs. The cost foreseens the installation in UGC of two new racks (one per endcap) with dedicated pneumatic valves and pressure regulation valves.
- Chamber distribution manifold: one manifold (12 supply and return channels and flowmeters) is available in each distribution racks in UXC. At the moment the controls are integrated in the RPC gas system. It is required to decouple the two systems and re-calibrate the flow-meters.
- Pump: The gas mixture coming out from the detectors is sent, by means of a pump module, to the USG building, to the purifier system (see below). Then a small per-

Table 9.5: GEM GE1/1 LS2 project - Services cost details.

Item name	Total cost kCHF	Unit Cost (CHF)	Quantity of Units in CMS	Quantity of Production spares	Quantity of Units	Item Cost (CHF)
GE1/1 Services total	**283**					
DCS	**68**					
DCS computers	10	5000	2		2	10000
Monitoring sensors	58	300	144	14	158	47520
Gas System	**165**					
Control rack	15	15000	1		1	15000
Circulation pump	30	30000	1		1	30000
Mixer	30	30000	1		1	30000
Purifier	60	60000	1		1	60000
Exhaust	10	10000	1		1	10000
Distribution manifolds	5	210	24		24	5040
Connection to SGX5 supply	5	5000	1		1	5000
Connection to UGC	10	10000	1		1	10000
Cooling	**50**					
On disks infrastructure	50	50000	1		1	50000

centage of gas, which depends on detector and system constraints, is sent to the exhaust line (see below) while most fraction is dispatched to the pre-distribution modules.

- Purifier: the gas mixture collected through the pump is sent to a set of cartridges, which can be filled with different cleaning agents, allows purification of the gas mixture from possible pollutants. The purified gas is then sent back to the detector and a small fraction of fresh mixture can be re-injected.
- Exhaust: The fraction of gas mixture sent to the exhaust is automatically replaced with fresh mixture coming from the mixer module.
- Connection to UGC supply: supply and return gas pipes from SGX to UGC. At least two pipes are needed to supply the pre-distribution and to collect the return gas from the detectors.
- Connection to SGX5 supply: the pipes from the gas distribution racks to the periphery of the disks should be also already installed and arranged in patch panel.

The cooling infrastructure needed for GE1/1 is presented in Figure 7.18 where one can see the 12 cooling loops for ME1/1, RE1/1 and the HCAL readout box (RBX). The GE1/1 chambers will be included in the cooling loops for the RBX and will use the pipes foreseen for RE1/1, therefore the major cost contribution comes from the purchase of connectors, flowmeters, flexible hoses and labor from external firms. The quotations for gas and cooling system are provided by the CERN Physics Dectector Technology Department (CERN-PH-DT).

The DCS hardware architecture consists of multiprocessors computers which provide access to all of the DCS services. A network of Fiber Bragg Grating (FBG) optical sensors will be installed on the detector for the temperature and humidity measurements. The FBG technique has already been applied to several detectors in CMS and the readout system stability and reliability has been demonstrated, with continuous data taking under severe and complex operation conditions (high radiation and magnetic field). The cost estimate is based on a recent similar order for detectors installed during LS1.

Included in the cost are the infrastructure needed for the installation: mecchanical supports for transportation from the CERN assembly and commissioning area to the CMS cavern; specially

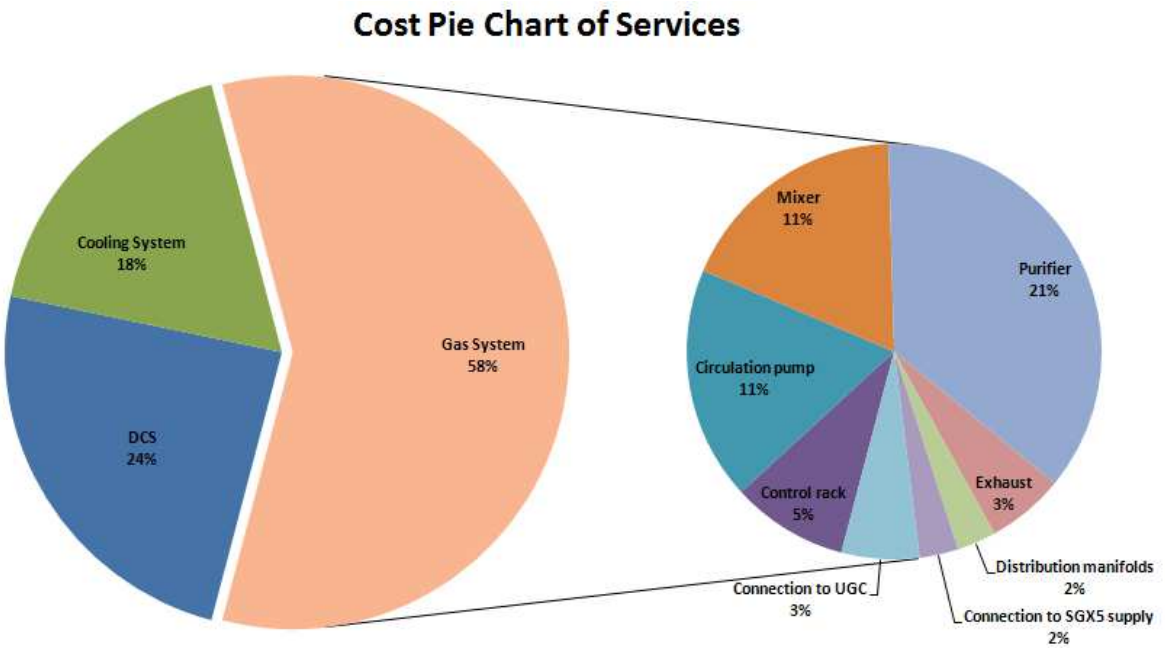

Figure 9.7: The main contributions to the cost of services (left), and details of the cost estimate for the gas system (right).

designed installation tools will be required to insert the chambers in the YE1 nose. The same tools will also be used for maintenance or repair.

9.7.4 Expected funding, cost sharing and profile

The global cost of the GE1/1 construction project, 3.7 MCHF, is expected to be borne by all institutions participating in the project as shown in Section 9.1. Discussions with the Funding Agencies are ongoing to define the sharing of the total project cost. It is expected that the commitments will be formally made by all funding agencies when signing the Memorandum of Understanding.

It should be noted that for most institutes the total funding has already been accepted and/or approved by the corresponding funding agencies. Indeed in order to be ready for installation in LS2, the construction of chamber prototype and electronics for test purposes and the preliminary procurements for test bench at building 904 and setting up of test facilities at the TIF (which are part of the core cost) has already started, thanks to some funding agencies which are already started their contributions.

Following the project schedule in Figure 9.2 and the Cost Book presented in previous sections a preliminary cost profile is presented in Figure 9.8.

This exercise has only begun. The full realisation of this planning exercise requires a good knowledge of the funding profile. After approval, the integrated total funds available from each of the countries participating in the project will be committed by linking the cost profile to the composite funding profile, as requested by LHCC CORE rules.

This is a work in progress and will evolve when the TDR project is approved.

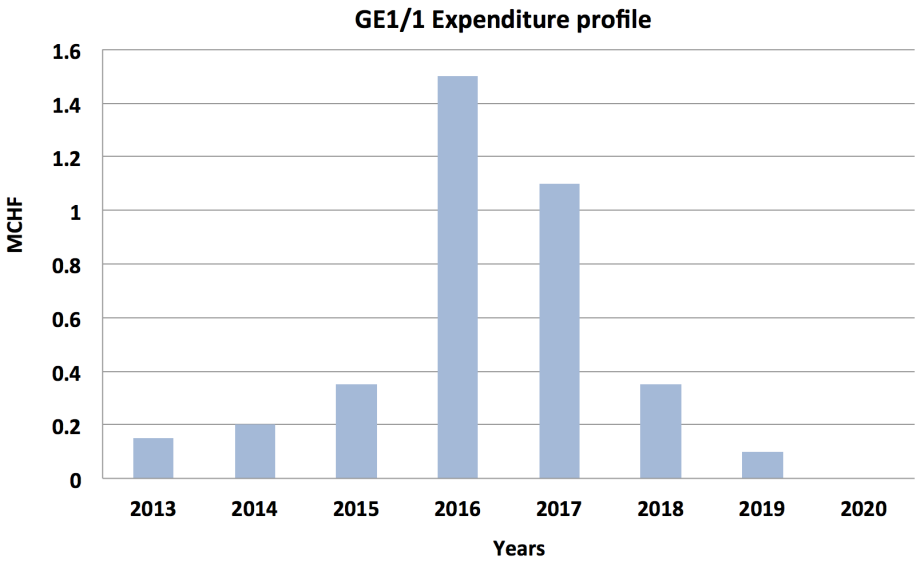

Figure 9.8: GEM GE1/1 LS2 project - expenditure profile.

9.8 Organization of the construction work

A preliminary sharing of the areas of work is shown in Figure 9.9. The horizontal rows describe the major tasks undertaken for five key areas:

Detector Hardware - Comprising GEM foil production, chamber component procurement and QA/QC for construction and assembly of the full detector

Technical Coordination - Comprising integration, installation and services design and commissioning to deliver a completed operational detector at the CMS P5 cavern, with a database that tracks production and operation

Electronics and DAQ - Comprising the development of the front-end readout (VFAT), the electronic board (GEB), the opto-hybrid (OH) with GBTs, and the uTCA-based DAQ, with trigger software and firmware development

Detector Operation - Comprising the Detector Control System (DCS), Data Quality Monitoring (DQM), Web-based monitoring (WBM), and Physics validation tools (PVT)

Trigger and Detector Physics - Comprising detector stand-alone simulation, physics studies and simulation, reconstruction, muon and trigger performance, test beam activities and data analysis

The Slice Test - Consisting of the test described in Appendix A.

The full collaboration has been and will actively participate in all activities listed above as can be seen in the table. The tasks have been discussed extensively with the institution leaders and commitments are reflected in the resource sharing matrix, presented in Figure 9.9.

The full project for GE1/1 installed in LS2, needs about 70 FTE in total for construction and installation with a distribution as follows: 72% Physicists, 12% Technicians and 16% Engineers.

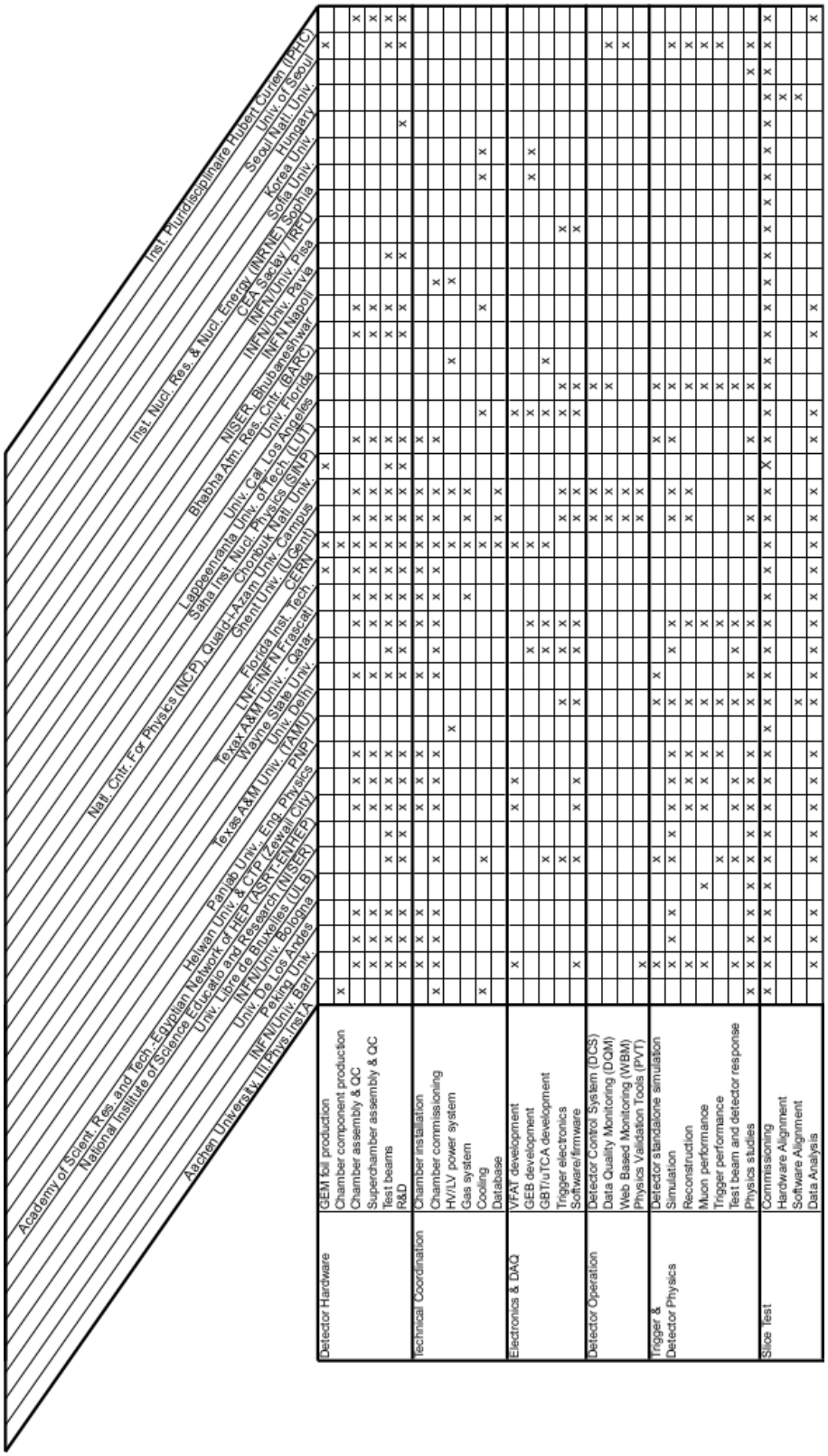

Figure 9.9: Task Matrix of institutional areas of work.

Appendix A

The GE1/1 Slice Test

A.1 Introduction

In June 2013, CMS approved the installation of a limited number of GE1/1 chambers into the muon endcaps, in order to gain first operational experience with this new subsystem and also to demonstrate the integration of the GE1/1 chambers into the trigger. During the 2016-2017 Year-End Technical Stop, 4 GE1/1 superchambers covering a 40° sector will be installed in YE1/1, at the location depicted in Figure A.1.

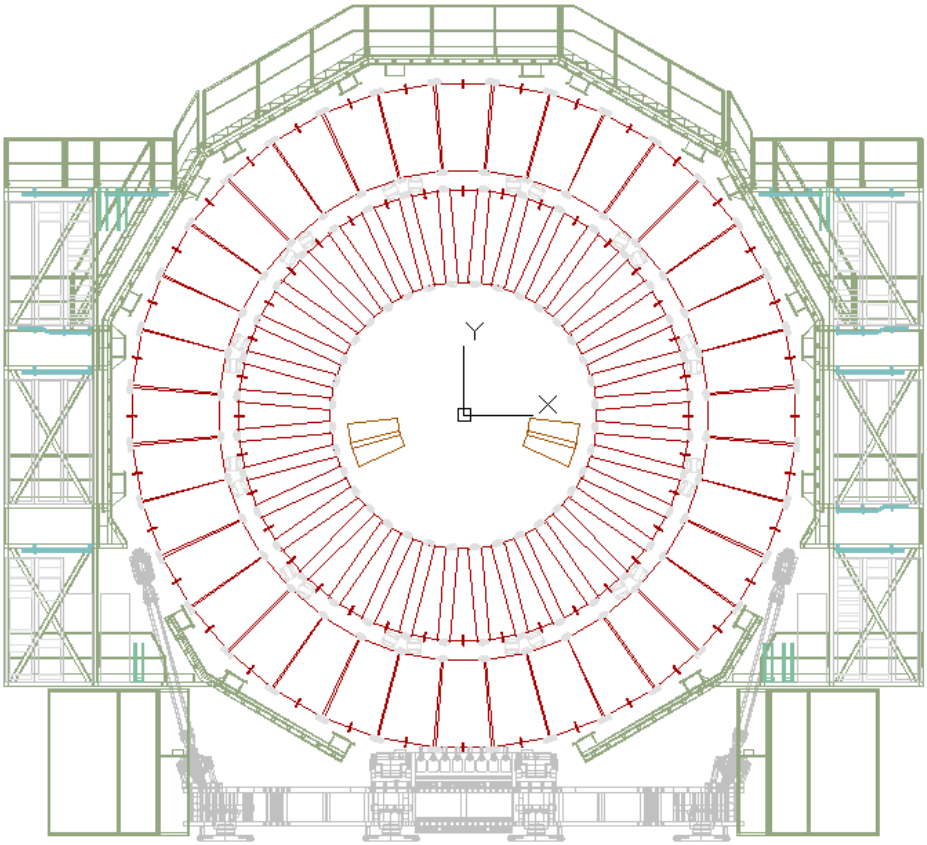

Figure A.1: Location of the Slice Test GE1/1 superchambers in YE1.

A.2 Detector configuration

As described in Chapter 7, during LS1, most of the required services and cabling for the GE1/1 station will be in place and tested. With few exceptions, the final GE1/1 services and cabling configuration will be used for the Slice Test chambers as well.

The HV power for the slice test chambers will be based on the single-channel HV divider option as was used during the R&D phase of the project (see Section 2.3.6.1). In this case, only one HV channel is required per GE1/1 chamber, or two channels per GE1/1 super-chamber. Note here the already installed HV cables meant for a RPC RE1/1 station that so far has not been built. These cables run from the UXC X0 HV patch panel to the GE1/1 installation slots for both the positive and negative endcap.

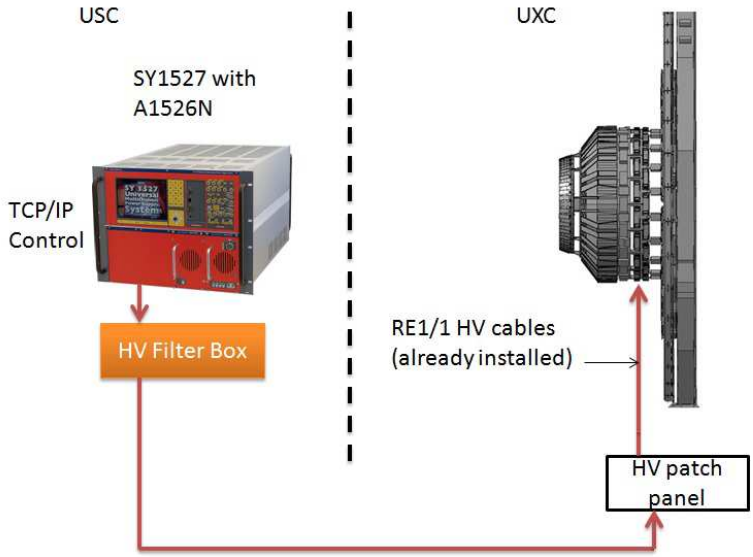

Figure A.2: Diagram of the GE1/1 powering configuration based on the HV divider.

The general view of the single-channel HV powering configuration is shown in Figure A.2. It represents a standard system based on commercial HV modules made by CAEN. As is shown in the figure, all the HV power modules are located in the USC S1 level where the CAEN main frame SY1527 is installed. The A1526N HV powering modules are used, which are able to provide up to 15 kV/1mA with negative polarity. This power supply has been used in the GE1/1 project since the beginning, both in lab measurements and beam tests. The A1526N board has a certain noise level from its output, which needs to be cut off using a HV filter box located close to the module.

To transport the power from A1526N to the GE1/1 chambers, a multi-core HV cable of about 150 m is required between the USC and UXC caverns, which has to follow all the routing procedures adopted by CMS.

Given the installation of the Slice Test chambers at the end of 2016, the construction and commissioning of the GEM gas mixer will be completed latest after the Summer in 2016. For the Slice Test, a gas flow of about 10 l/h is foreseen, for a total detector volume of about 20 l.

The front-end electronics power dissipation for the Slice Test detectors is assumed to be less than 250 W in total for the 2 superchambers. This will have a negligible impact on the presently available YE1 cooling system.

A.3 Front-end electronics and data-acquisition

Due to the still ongoing developments of the front-end chip and GBT chip set in the coming years, it is foreseen that the readout of the chambers during the Slice Test will be close to but nonetheless slightly different from the final system that is described in Chapter 3. The on-detector electronics will be based on the VFAT2 instead of VFAT3 ASIC, and on the 2nd instead of the final (3rd) version of the GEB and opto-hybrid. The latter will already include the GBT chip set.

Since the VFAT2 design is not compatible with the GBT chipset all the data (trigger and tracking data) will transit through the front-end FPGA (Virtex 6) located on the opto-hybrid. The number of optical links per detector and the trigger data link towards the CSC TMB will be the same as in the GE1/1 system that will be installed during LS2.

For the back-end electronics, the system should be the same as for the LS2 installation but with fewer components : one μTCA crate hosting one MP7 board and one AMC13 board.

Since the VFAT2 will be used for the Slice Test, the trigger data granularity will be lower than for the LS2 system: 16 channels instead of 2. Nevertheless, the system will be operated as the LS2 system, emulating the GBT. The Slice Test will therefore offer a unique opportunity to gain experience in the integration of the GE1/1 system in CMS, its commissioning and the integration of the GE1/1 data to the CMS trigger and DAQ system.

Appendix B

Integrated Charge Estimation

Here we briefly detail the estimation of the charge per area that will be integrated in the GE1/1 chambers over a lifetime of 20 years at the HL-LHC as stated under the design requirements in section 2.1.1. The integrated charge Q_{int} per area is given by:

$$Q_{int} = R_{max} \times n_{tot}^{ion} \times g \times e \times t_{HL-LHC}\,, \tag{B.1}$$

where R_{max} is the maximum charged-particle hit rate per area produced by all particles incident on the chamber, n_{tot}^{ion} is the total number of ion-electron pairs produced by charged particles traversing the drift gap in the chamber, g is the gas gain of the GE1/1, e is the electron charge, and t_{HL-LHC} is the total time in seconds that the HL-LHC will be providing collisions over 20 years.

We use R_{max} = 5 kHz/cm^2 as the rate estimate in the hottest area of the GE1/1 and $g = 2 \times 10^4$ as the typical gas gain value for a Triple-GEM. In an Ar/CO_2 70:30 gas mixture, on the average 93 ion-electron pairs are produced per cm. The largest path length l in the GEM drift gap that occurs for ionizing particles when they traverse the GE1/1 is $l = d/\cos\theta$. Here $d = 0.3$ cm is the drift gap of the Triple-GEM and $\theta \approx 25^o$, which corresponds to $\eta = 1.5$, is the largest angle relative to the normal onto the chamber under which particles are incident on the GE1/1. This gives l =0.33 cm and $n_{tot}^{ion} = 31$ ion-electron pairs in the GE1/1. Assuming that the HL-LHC will have an annual duty factor of $\approx 1/3$ as is typical for collider operations, we estimate that the chambers will be exposed to charged particles for $\approx 10^7$ seconds each year.

Multiplying these factors together, we find an estimated integrated charge per area for a projected GE1/1 lifetime of 20 years of:

$$\mathbf{Q_{int}} \approx 5 \cdot 10^3\, s^{-1} cm^{-2} \times 31 \times 2 \cdot 10^4 \times 1.6 \cdot 10^{-19}\, C \times 20 \cdot 10^7\, s = \mathbf{99\ mC/cm^2} \tag{B.2}$$

Gas mixtures containing in addition CF_4 in any percentage will produce very similar integrated charges because the total ionization of CF_4 (100 pairs/cm) is quite close to that of Ar (94 pairs/cm) and CO_2 (91 pairs/cm). Specifically, for $Ar/CO_2/CF_4$ 45 : 15 : 40 the total ionization is 96 pairs/cm which gives Q_{int} = 101 mC/cm^2 for the GE1/1.

Appendix C

GE1/1 Project 3D Views

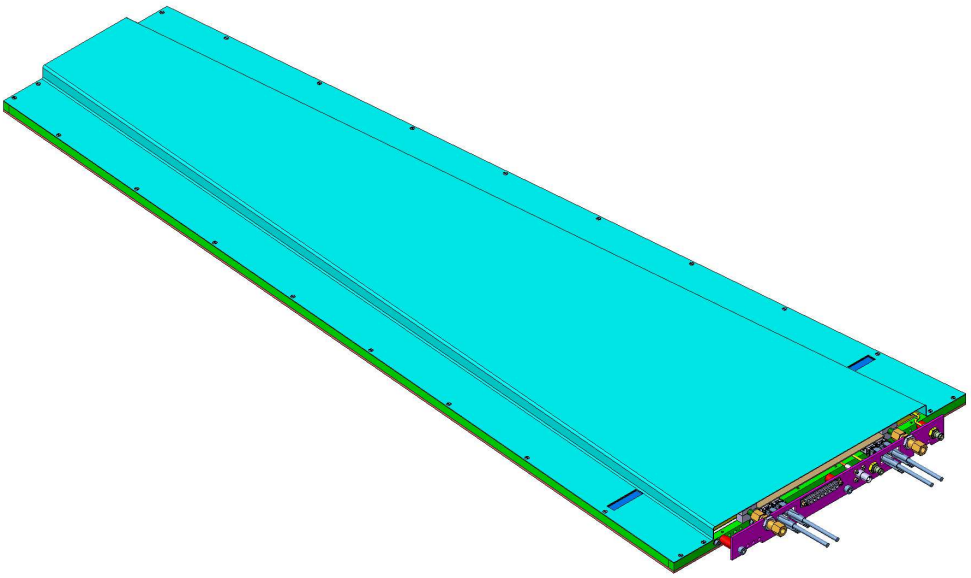

Figure C.1: GE1/1 mechanical chambers.

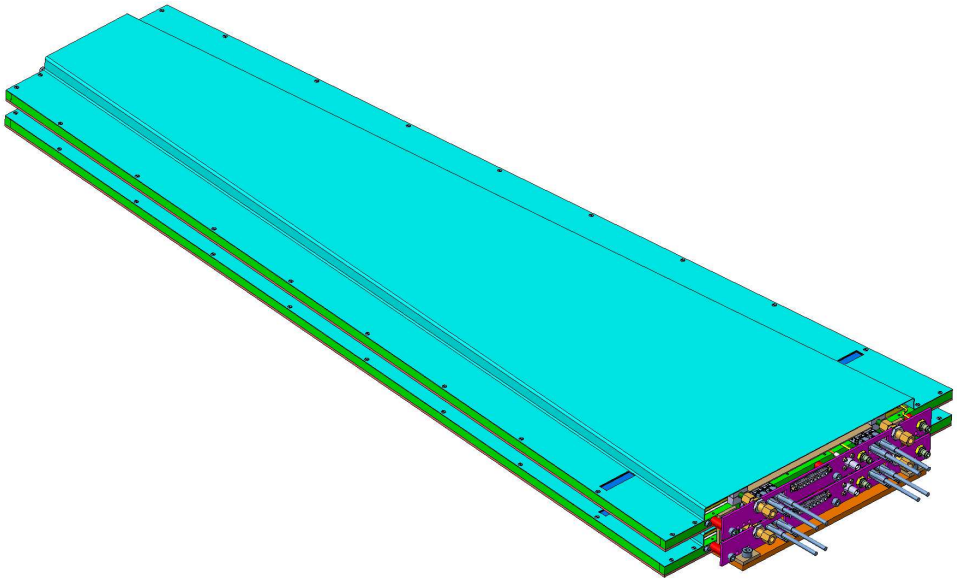

Figure C.2: GE1/1 super-chamber.

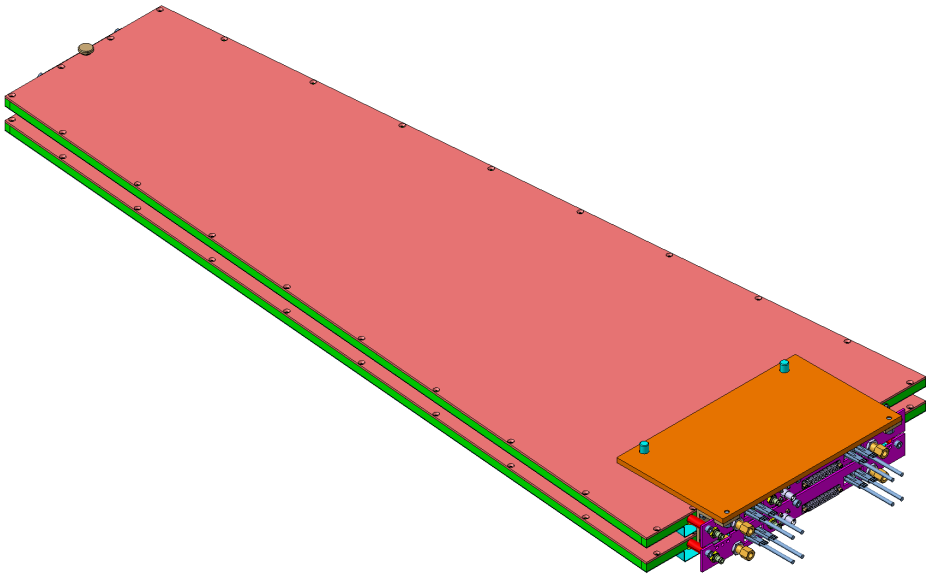

Figure C.3: GE1/1 fixations.

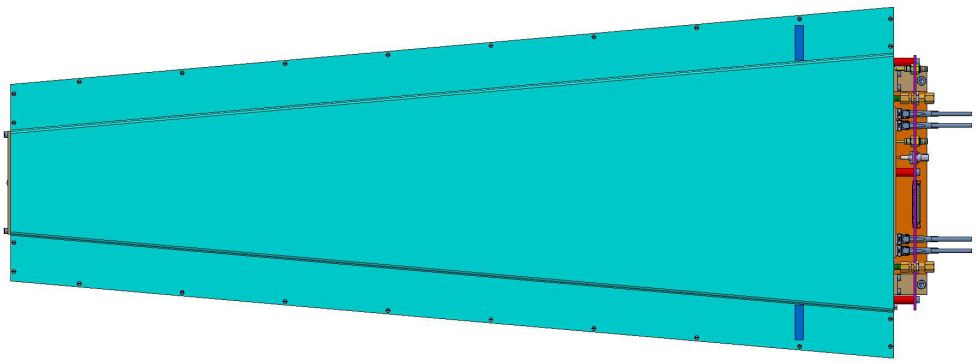

Figure C.4: GE1/1 chimney.

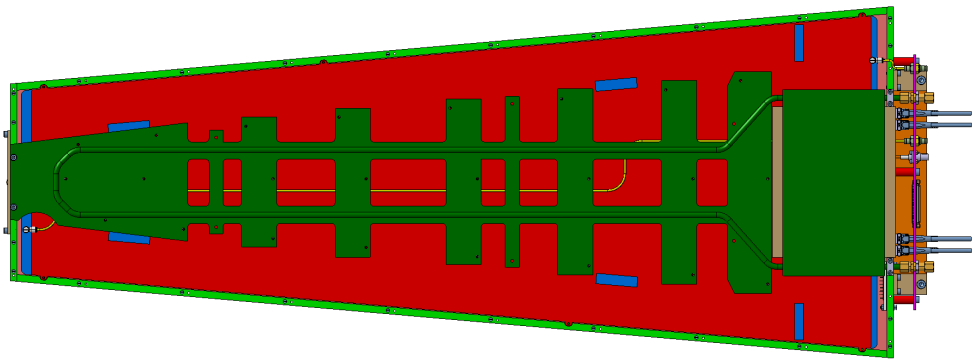

Figure C.5: GE1/1 cooling circuit.

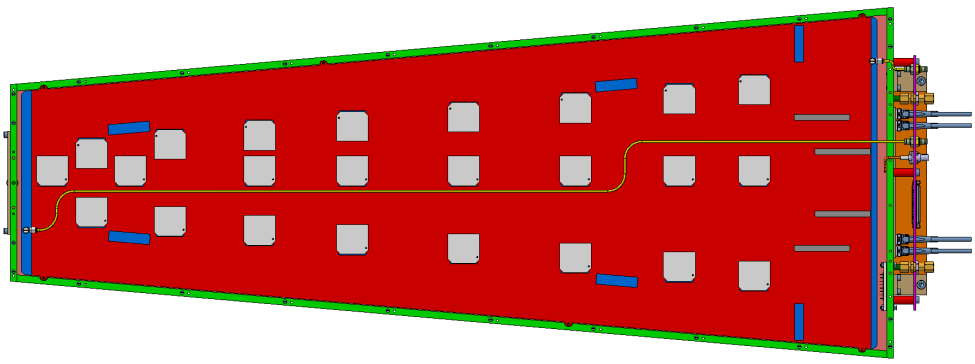

Figure C.6: GE1/1 hybrid gas pipes.

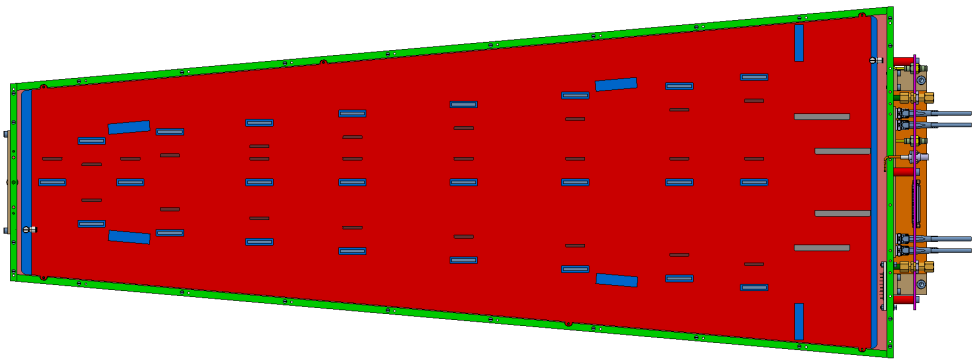

Figure C.7: GE1/1 GEB.

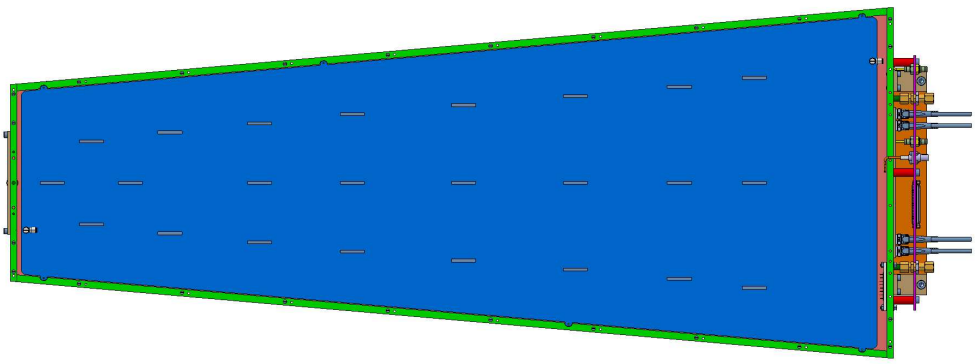

Figure C.8: GE1/1 readout board.

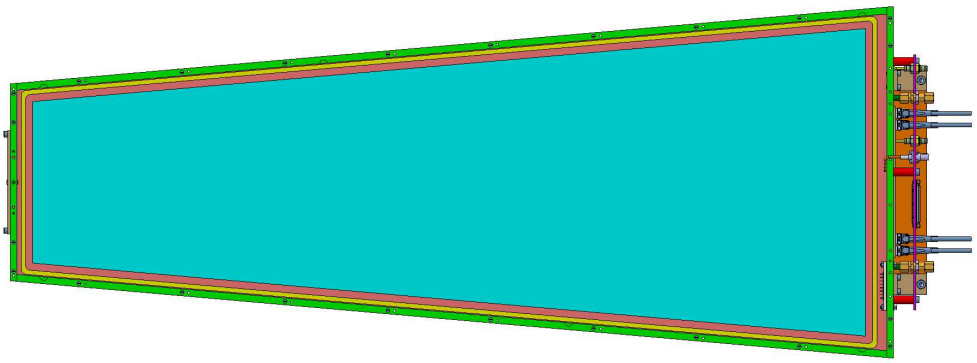

Figure C.9: GE1/1 active surface.

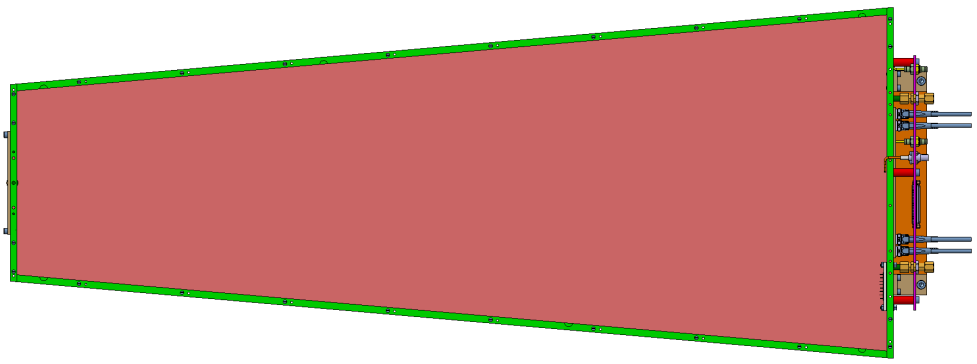

Figure C.10: GE1/1 drift board.

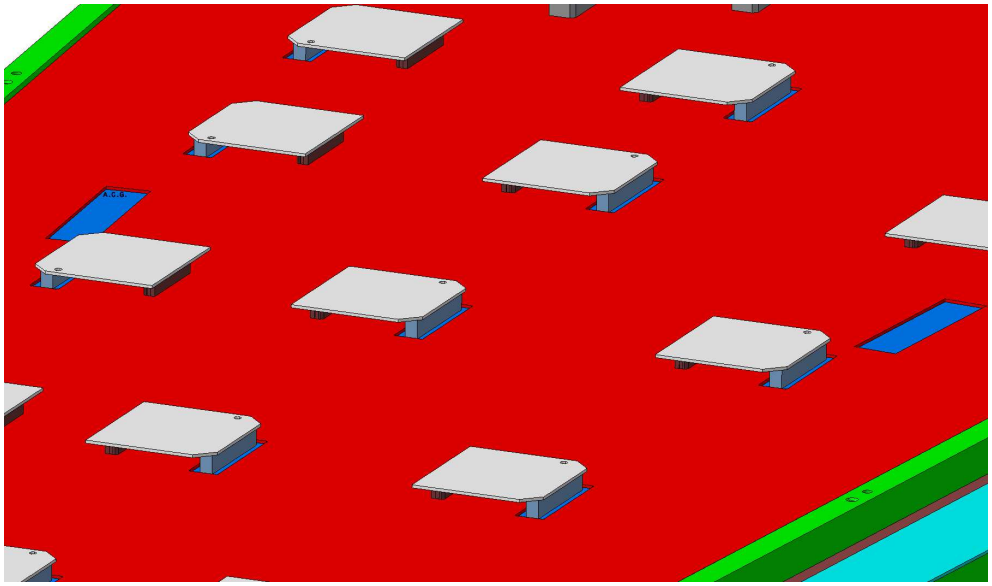

Figure C.11: GE1/1 hybrids detail.

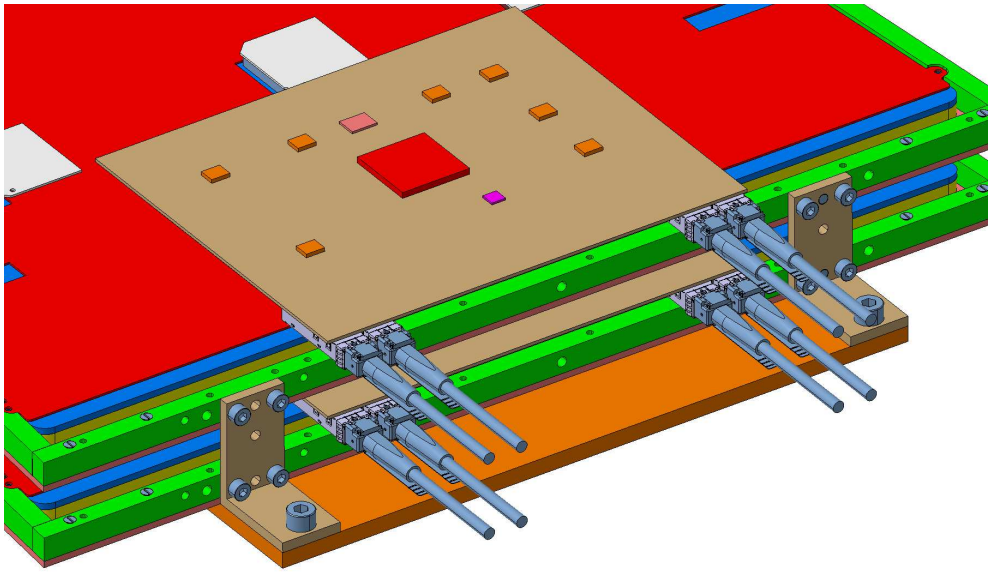

Figure C.12: GE1/1 optohybrid and fibres.

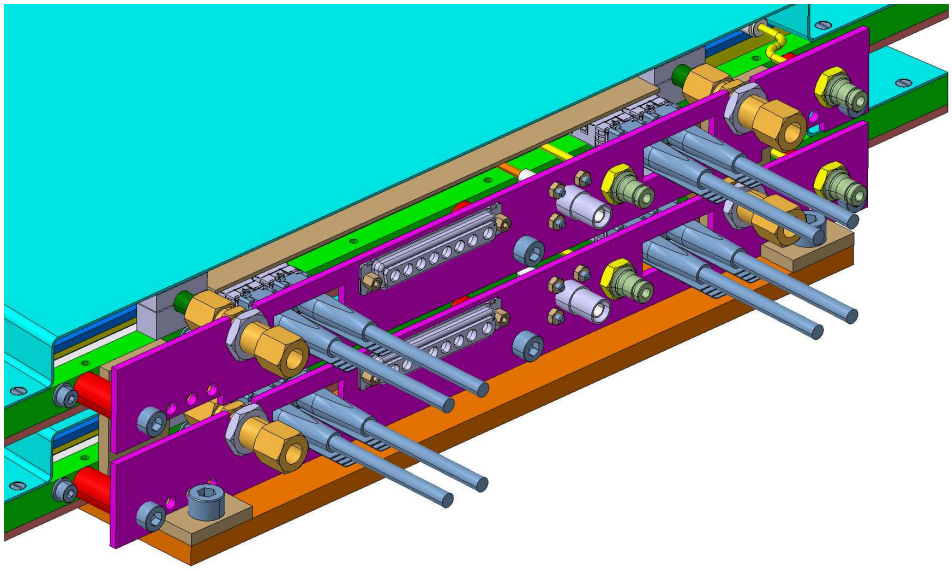

Figure C.13: GE1/1 patch-panel.

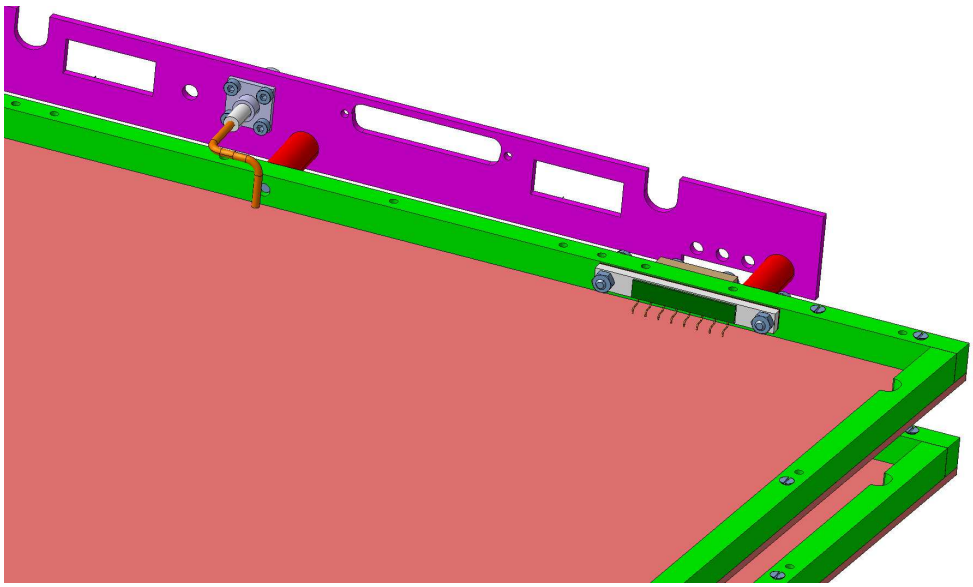

Figure C.14: GE1/1 HV divider and connectors.

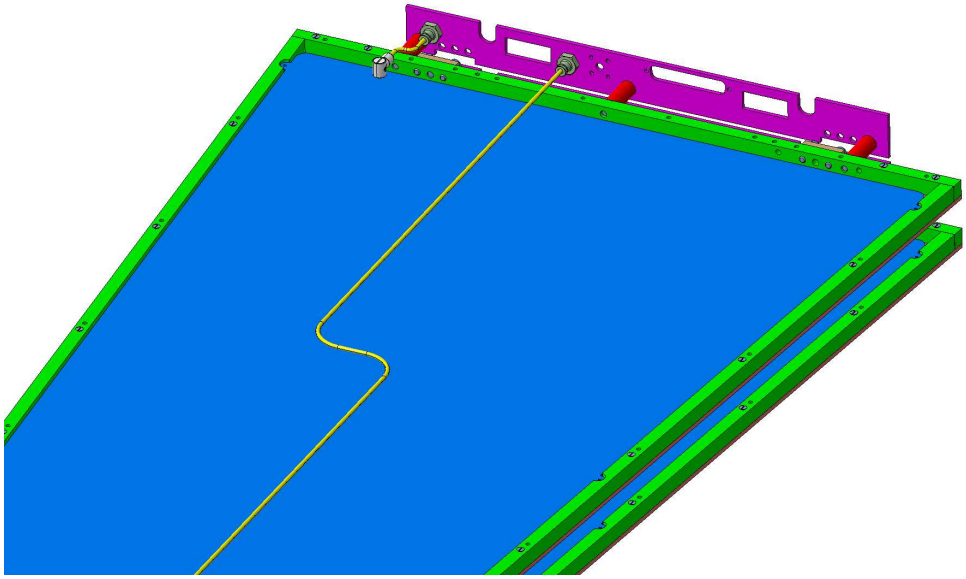

Figure C.15: GE1/1 gas conduits.

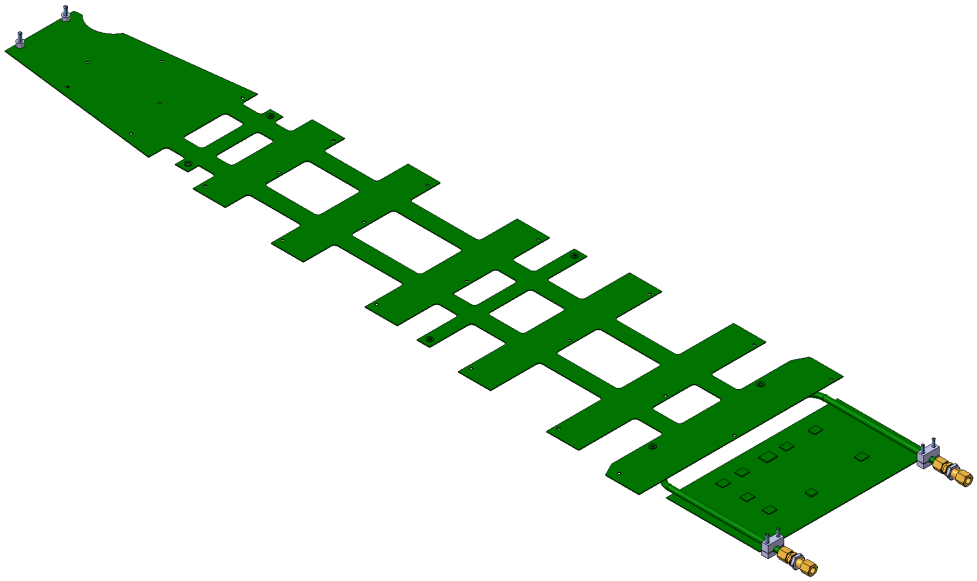

Figure C.16: GE1/1 thermal screen.

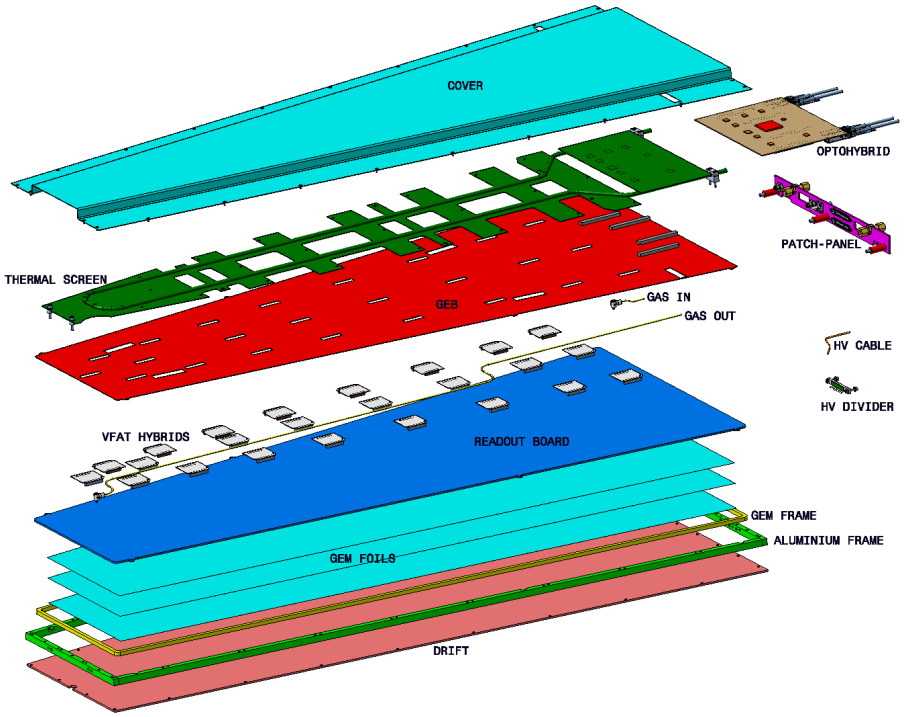

Figure C.17: GE1/1 exploded view.

Appendix D

Glossary

List of acronyms used in this document:

- AC = Alternating Current
- ALCT = Anode Local Charged Track segment, theta view, part of the CSC system
- ADC = Analog-to-Digital Converter
- AMC13 = A μTCA data concentration and clock distribution card specifically designed for the CMS experiment
- APV25 = Analogue Pipeline Voltage 0.25 (micron process)
- ASIC = Application Specific Integrated Circuit
- CAD = Computer Aided Design
- CFD = Constant Fraction Discriminator
- CERN = European Organization for Nuclear Research
- CCU = Communication and Control Unit
- CHF = Swiss Franc
- CLCT = Cathode Local Charged Track (cathode view muon stub), part of the CSC system
- CMS = Compact Muon Solenoid
- CMSSW = Compact Muon Solenoid Software, is the CMS experiment software package
- CNC = Computerized Numerical Control
- CSC = Cathode Strip Chamber
- CORE = (LHCC) COst REview committee
- CPU = Central Processing Unit
- DAC = Digital-to-Analog Converter
- DAQ = Data AcQuisition
- DB = Database
- DC = Direct Current
- DCS = Detector Control System
- DDR = Double Data Rate (RAM)
- DOH = Digital Opto-Hybrid
- DQM = Data Quality Monitoring
- DR = Digital Receiver

- DSS = Detector Safety System
- ENIG = Electroless Nickel / Immersion Gold
- EMC = ElectroMagnetic Cmpatibility
- EUR = Euro
- FA = Funding Agency
- FB = Finance Board
- FBG = Fiber Bragg grating
- FE = Front End
- FPGA = Field Programmable Gate Array
- FSM = Finite State Machine
- FTE = Full Time Equivalent
- GBT = Gigabit Transceiver
- GC = Gas Chromatograph
- GE1/1 = GEM Endcap Station 1 Ring 1
- GEB = GEM Electronics Board
- GEM = Gas Electron Multiplier
- GIF = Gamma Irradiation Facility
- GWP = Global Warming Potential
- HAL = Hardware Access Library
- HE = Hadron Endcap
- HF = Hadron Forward (Calorimeter)
- HL = High Luminosity
- HLT = High Level Trigger
- HL-LHC = High-Luminosity Large Hadron Collider
- HV = High Voltage
- HV-CC = Complex Channel
- IP = Interaction Point
- JCOP = Joint Control Project
- L1A = Level-1 (Trigger) Accept
- LDS = Laser Displacement System
- LED = Light-Emitting Diode
- LHC = Large Hadron Collider
- LHCC = Large Hadron Collider Committee
- LPGBT = Low Power GigaBit Transceiver
- LS1 = Long Shutdown 1
- LS2 = Long Shutdown 2
- LS3 = Long Shutdown 3
- LV = Low Voltage
- MB = Management Board

- ME1/1 = Muon Endcap Station 1 Ring 1
- MIP = Minimum Ionizing Particle
- MoU = Memorandum of Understanding
- MPGD = Micro pattern gas detector
- MP7 = Master Processor board, Virtex-7
- μTCA = Micro Telecommunications Computing Architecture
- OH = Opto-Hybrid
- OMDS = Online Master Database System
- OTMB = Optical Trigger Motherboard
- P5 = LHC Access Point n. 5
- PC = Personal Computer
- PCB = Printed Circuit Board
- PEEK = Poly-Ether Ether Ketone
- PFN = Physical File Name
- PLC = Programmable Logic Controller
- PM = Project Manager
- PROM = Programmable Read-Only Memory
- PU = Pile-up
- QA = Quality Assurance
- QC = Quality Control
- R&D = Research and Development
- RAM = Random-Access Memory
- RCMS = Run Control and Monitoring System
- RH = Relative Humidity
- RHIC = Relativistic Heavy Ion Collider
- RMS = Root Mean Square
- RPC = Resistive Plate Chamber
- RRB = Resource Review Board
- S/N = Signal-to-Noise (ratio)
- SC = GE1/1 SuperChamber
- SIP = Single Inline Pin
- SEM-EDS = Scanning Electron Microscopy Energy Dispersive Spectrometry
- SPS = Super Proton Synchrotron
- SS = Stainless Steel
- SWPC = Single-Wire Proportional Counter
- TBD = To Be Determined
- TDC = Time-to-Digital Converter
- TDR = Technical Design Report
- TE = Technology (Department at CERN)

- TEC = Tracker End Cap
- TIF = Tracker Integration Facility
- TOT = Time over threshold
- TTC = Trigger Timing and Control
- TTS = Trigger Throttling System
- USB = Universal Serial Bus
- USC = Underground Service Cavern
- USD = United States of America Dollar
- UV = Ultraviolet
- UXC = Underground eXperimental Cavern
- VBF = Vector Boson Fusion
- VFAT = Very Forward Atlas and Totem
- YE1 = Yoke Endcap 1
- YETS = Year-End Technical Stop
- WBM = Web Based Monitoring

References

[1] CMS Collaboration, "CMS The Muon Project Technical Design Report", Technical Report CERN-LHCC-1997-032, CMS-TDR-3, CERN, 1997.

[2] CMS Collaboration, "CMS Technical Design Report for the Level-1 Trigger Upgrade", Technical Report CERN-LHCC-2013-011, CMS-TDR-012, CERN, 2013.

[3] F. Palla, "Tracking Triggers for the High Luminosity LHC", *PoS Vertex2013* (2013) 034.

[4] N. Arkani-Hamed and S. Dimopoulos, "Supersymmetric unification without low energy supersymmetry and signatures for fine-tuning at the LHC", *J. High Energy Phys.* **0506** (2005) 073, doi:10.1088/1126-6708/2005/06/073.

[5] G. Giudice and A. Romanino, "Split supersymmetry", *Nucl. Phys.* **B699** (2004) 65–89, doi:10.1016/j.nuclphysb.2004.11.048.

[6] G. Giudice, M. Luty, H. Murayama, and R. Rattazzi, "Gaugino mass without singlets", *J. High Energy Phys.* **9812** (1998) 027, doi:10.1088/1126-6708/1998/12/027.

[7] L. Randall and R. Sundrum, "Out of this world supersymmetry breaking", *Nucl. Phys.* **B557** (1999) 79–118, doi:10.1016/S0550-3213(99)00359-4.

[8] C.-Y. Chen and S. Dawson, "Exploring two Higgs doublet models through Higgs production", *Phys. Rev.* **D87** (2010) 055016, doi:10.1103/PhysRevD.87.055016.

[9] J. Z. Neil Turok, "Electroweak baryogenesis in the two doublet model", *Nucl. Phys.* **B358** (1991) 471–473, doi:10.1016/0550-3213(91)90356-3.

[10] F. Sauli, "GEM: A new concept for electron amplification in gas detectors", *Nucl. Instrum. Meth.* **A386** (1997) 531 – 534, doi:10.1016/S0168-9002(96)01172-2.

[11] D. Abbaneo et al., "Test beam results of the GE1/1 prototype for a future upgrade of the CMS high-η muon system", *IEEE Nucl. Sci. Symp. Med. Imag. Conf. Rec.* (2011) 1806–1810, doi:10.1109/NSSMIC.2011.6154688, arXiv:1111.4883.

[12] D. Abbaneo et al., "Beam Test Results for New Full-scale GEM Prototypes for a Future Upgrade of the CMS High-eta Muon System", *IEEE Nucl. Sci. Symp. Med. Imag. Conf. Rec.* (2012) 1172 – 1176, doi:10.1109/NSSMIC.2012.6551293, arXiv:1211.3939.

[13] D. Abbaneo et al., "Performance of a Large-Area GEM Detector Prototype for the Upgrade of the CMS Muon Endcap System", *IEEE Nucl. Sci. Symp. Med. Imag. Conf. Rec.* (2014) arXiv:1412.0228.

[14] A. Cardini, G. Bencivenni, and P. De Simone, "The Operational Experience of the Triple-GEM Detectors of the LHCb Muon System: Summary of 2 Years of Data Taking", *IEEE Nucl. Sci. Symp. Med. Imag. Conf. Rec.* (2012) 759–762, doi:10.1109/NSSMIC.2012.6551204.

[15] S. Bachmann et al., "Charge amplification and transfer processes in the gas electron multiplier", *Nucl. Instrum. Meth.* **A438** (1999) 376–408, doi:10.1016/S0168-9002(99)00820-7.

[16] TOTEM Collaboration, "Performance of the TOTEM Detectors at the LHC", *Int. J. Mod. Phys.* **A28** (2013) 1330046, doi:10.1142/S0217751X13300469.

[17] A. Sharma, "Properties of some gas mixtures used in tracking detectors", *SLAC-JOURNAL-ICFA* **16** (1998).

[18] R. Veenhof, "Garfield, a drift chamber simulation program", *Conf. Proc.* **C9306149** (1993) 66–71.

[19] COMPASS Collaboration, "The COMPASS experiment at CERN", *Nucl. Instrum. Meth.* **A577** (2007) 455–518, doi:10.1016/j.nima.2007.03.026.

[20] M. French et al., "Design and results from the APV25, a deep sub-micron CMOS front-end chip for the CMS tracker", *Nucl. Instrum. Meth.* **A466** (2001) 359–365, doi:10.1016/S0168-9002(01)00589-7.

[21] B. Ketzer et al., "A triple-GEM Detector with pixel readout for high-rate beam tracking in COMPASS", *IEEE Nucl. Sci. Symp. Conf. Rec.* (2007) 242–244, doi:10.1109/NSSMIC.2007.4436323.

[22] W. Anderson et al., "Design, Construction, Operation and Performance of a Hadron Blind Detector for the PHENIX Experiment", *Nucl. Instrum. Meth.* **A646** (2011) 35–58, doi:10.1016/j.nima.2011.04.015.

[23] B. Surrow, "The STAR forward GEM tracker", *Nucl. Instrum. Meth.* **A617** (2010) 196–198, doi:10.1016/j.nima.2009.09.012.

[24] P. Aspell et al., "VFAT2: A front-end system on chip providing fast trigger information, digitized data storage and formatting for the charge sensitive readout of multi-channel silicon and gas particle detectors", in *Topical Workshop on Electronics for Particle Physics, Praque, Czech Republic, 03-07 Sept.*, pp. 292–296. 2007. doi:10.5170/CERN-2007-007.292.

[25] D. Abbaneo et al., "Characterization of GEM Detectors for Application in the CMS Muon Detection System", *IEEE Nucl. Sci. Symp. Med. Imag. Conf. Rec.* (2010) 1416–1422, doi:10.1109/NSSMIC.2010.5874006, arXiv:1012.3675.

[26] D. Abbaneo et al., "The status of the GEM project for CMS high-η muon system", *Nucl. Instrum. Meth.* **A732** (2013) 203–207, doi:10.1016/j.nima.2013.08.015.

[27] K. Gnanvo et al., "Detection and Imaging of High-Z Materials with a Muon Tomography Station Using GEM Detectors", *IEEE Nucl. Sci. Symp. Med. Imag. Conf. Rec.* (2010) 552–559, doi:10.1109/NSSMIC.2010.5873822, arXiv:1011.3231.

[28] S. Martoiu, H. Muller, A. Tarazona, and J. Toledo, "Development of the scalable readout system for micro-pattern gas detectors and other applications", *J. Instrum.* **8** (2013) C03015, doi:10.1088/1748-0221/8/03/C03015.

[29] R. Carnegie et al., "Resolution studies of cosmic ray tracks in a TPC with GEM readout", *Nucl. Instrum. Meth.* **A538** (2005) 372–383, doi:10.1016/j.nima.2004.08.132.

[30] T. Alexopoulos et al., "Examining the Geometric Mean Method for the Extraction of Spatial Resolution", *J. Instrum.* **9** (2013) P01003, doi:10.1088/1748-0221/9/01/P01003.

[31] M. Tytgat et al., "Construction and Performance of Large-Area Triple-GEM Prototypes for Future Upgrades of the CMS Forward Muon System", *IEEE Nucl. Sci. Symp. Med. Imag. Conf. Rec.* (2011) 1019–1025, doi:10.1109/NSSMIC.2011.6154312, arXiv:1111.7249.

[32] "ANSYS®Academic Research, Release 14.0". http://www.ansys.com.

[33] "Garfield++ - simulation of tracking detectors". http://garfieldpp.web.cern.ch/garfieldpp.

[34] J. A. Kadyk, "Wire chamber aging", *Nucl. Instrum. Meth.* **A300** (1991) 436–479, doi:10.1016/0168-9002(91)90381-Y.

[35] J. Va'vra, "Review of Wire Chamber Aging", *Nucl. Instrum. Meth.* **A252** (1986) 547–563, doi:10.1016/0168-9002(86)91239-8.

[36] M. Hohlmann, C. Padilla, N. Tesch, and M. Titov, "Aging phenomena in gaseous detectors – perspectives from the 2001 workshop", *Nucl. Instrum. Meth.* **A494** (2002) 179–193, doi:10.1016/S0168-9002(02)01463-8.

[37] S. Bianco, G. Saviano, and A. Franchi, "Test for the Measurement of Diffusion Coefficient of Water in Kapton Foils for the Gem Detector of the Upgraded High-Pseudorapidity Muon Detection in CMS", *LNF Preprint INFN-13-09/LNF* (2013).

[38] R. Guido, "CMS Trapezoidal GEM Foils Structural Analysis", *LNF Preprint LNF-10/20(IR)* (2010).

[39] R. Guido, "CHE and Related Stresses in GEM Foils", *LNF Preprint INFN-13-11/LNF* (2013).

[40] ASTM-International, "D570-98 Standard Test Method for Water Absorption of Plastics". http://www.astm.org/DATABASE.CART/HISTORICAL/D570-98R05.htm.

[41] ASTM-International, "D882-02 Standard Test Method for Tensile properties of Thin Plastic Sheeting". http://www.astm.org/Standards/D882.htm.

[42] M. Poli-Lener and G. Bencivenni, "Triple-GEM detectors for the innermost region of the muon apparatus at the LHCb experiment". PhD thesis, Roma U., Roma, 2005. Presented on 01 Dec 2005.

[43] L. Benussi et al., "The Omega-like: A novel device using FBG sensors to position vertex detectors with micrometric precision", *Nucl. Phys. Proc. Suppl.* **172** (2007) 263–265, doi:10.1016/j.nuclphysbps.2007.08.138.

[44] M. A. Caponero et al., "Use of fiber optic technology for relative humidity monitoring in RPC detectors", *PoS RPC2012* (2012) 073, doi:10.1088/1748-0221/8/03/T03003.

[45] S. Grassini et al., "SiOx coated plastic fiber optic sensor for gas monitoring in RPC", *PoS RPC2012* (2012) 072.

[46] D. J. Achenson, "Elementary Fluid Dynamics, ", *Oxford Applied Mathematics and Computing Science Series, Oxford University Press* (1990).

[47] L. D. Landau and E. M. Lifshitz, "Fluid mechanics, Course of Theoretical Physics, 6 (2nd revised ed.), ", *Pergamon Press* (1987).

[48] I. G. Currie, "Fundamental Mechanics of Fluids, ", *McGraw-Hill* (1974).

[49] "The IPbus protocol". https://svnweb.cern.ch/trac/cactus/wiki.

[50] P. Moreira et al., "The GBT-SerDes ASIC prototype", *J. Instrum.* **5** (2010) C11022, doi:10.1088/1748-0221/5/11/C11022.

[51] J. Gilmore et al., "Very forward muon trigger and data acquisition electronics for CMS: design and radiation testing", *J. Instrum.* **8** (2013) C02040, doi:10.1088/1748-0221/8/02/C02040.

[52] P. Vichoudis et al., "The Gigabit Link Interface Board (GLIB) ecosystem", *J. Instrum.* **8** (2013) C03012, doi:10.1088/1748-0221/8/03/C03012.

[53] D. Abbaneo et al., "A study of film and foil materials for the GEM detector proposed for the CMS muon system upgrade", *J. Instrum.* **9** (2014) C04022, doi:10.1088/1748-0221/9/04/C04022.

[54] N. Arkani-Hamed, D. Finkbeiner, T. Slatyer, and N. Weiner, "A Theory of Dark Matter", *Phys. Rev.* **D79** (2009) 015014, doi:10.1103/PhysRevD.79.015014.

[55] P. Graham, D. Kaplan, S. Rajendran, and P. Saraswati, "Displaced Supersymmetry", *J. High Energy Phys.* **1207** (2012) 149, doi:10.1007/JHEP07(2012)149.

[56] CMS Collaboration, "The performance of the CMS muon detector in proton-proton collisions at sqrt(s)=7 TeV at the LHC", *J. Instrum.* **7** (2013) P10002, doi:10.1088/1748-0221/8/11/P11002.

[57] "Geant4 Physics Reference Manual". http://geant4.web.cern.ch/geant4/UserDocumentation/UsersGuides/PhysicsReferenceManual/fo/PhysicsReferenceManual.pdf.

[58] CMS Collaboration, "Evidence for the 125 GeV Higgs boson decaying to a pair of τ leptons", *J. High Energy Phys.* **104** (2014) doi:10.1007/JHEP05(2014)104.

[59] CMS Collaboration, "The CMS tracker system project: Technical Design Report", Technical Report CERN-LHCC-98-006, CMS-TDR-5, CERN, 1998.

[60] Z. Szillási et al., "One year of FOS measurements in CMS experiment at CERN", *Physics Procedia* **37** (2012) 79–84, doi:10.1016/j.phpro.2012.02.360.

[61] V. Barashko et al., "Commissioning of Muon Endcap Cathode Strip Chamber High-Voltage System", Technical Report CMS-IN-2010/032, CERN, 2010.

[62] "Specialty fibers - DrakaElite". http://prysmiangroup.com/en/business_markets/markets/fibre/products/speciality-drakaelite.

[63] F. Ravotti, M. Glaser, and M. Moll, "Sensor Catalogue", Technical Report TS-NOTE-2005-02, CERN, 2005.

[64] R. Arcidiacono et al., "CMS DCS design concepts", in *Proceedings of the 10th International Conference on Accelerator and large experimental physics control systems, ICALEPCS 2005, Geneva, Switzerland, Oct. 10-14*, pp. PO1.062–6. 2005.

[65] A. Daneels and W. Salter, "What is SCADA?", *Conf. Proc.* **C991004** (1999) 339–343.

[66] "SIMATIC WinCC Open Architecture". http://www.automation.siemens.com/mcms/human-machine-interface/en/visualization-software/simatic-wincc-open-architecture/pages/default.aspx.

[67] M. Gonzalez-Berges, "The Joint COntrols project framework", *eConf* **C0303241** (2003) THGT006, arXiv:physics/0305128.

[68] G. Bauer et al., "The run control and monitoring system of the CMS experiment", *PoS ACAT* (2007) 026, doi:10.1088/1742-6596/119/2/022010.

[69] CMS Collaboration, "CMS: The TriDAS project. Technical design report, Vol. 2: Data acquisition and high-level trigger", Technical Report CERN-LHCC-2002-026, CMS-TDR-6, CERN, 2002.

[70] V. Brigljevic et al., "Using XDAQ in application scenarios of the CMS experiment", *eConf* **C0303241** (2003) MOGT008, arXiv:hep-ex/0305076.

[71] S. Schmeling, B. Flockhart, S. Luders, and G. Morpurgo, "The detector safety system for LHC experiments", *IEEE Trans. Nucl. Sci.* **51** (2004) 521–525, doi:10.1109/TNS.2004.828631.

[72] W. Badgett et al., "Web Based Monitoring in the CMS Experiment at CERN", arXiv:1409.1133.

[73] "Axis is an XML based Web Service Framework". http://ws.apache.org/axis.

[74] "The Apache Tomcat Servlet container". http://tomcat.apache.org.

[75] L. Tuura, A. Meyer, I. Segoni, and G. Della Ricca, "CMS data quality monitoring: Systems and experiences", *J. Phys. Conf. Ser.* **219** (2010) 072020, doi:10.1088/1742-6596/219/7/072020.

[76] CMS Collaboration, "Commissioning of the CMS High-Level Trigger with Cosmic Rays", *J. Instrum.* **5** (2010) T03005, doi:10.1088/1748-0221/5/03/T03005.

[77] "Migration of the DQM and Validation code to be Thread Safe". https://twiki.cern.ch/twiki/bin/viewauth/CMS/ThreadedDQM.

[78] CMS Collaboration, "CMS Run Registry: Data Certification Bookkeeping and Publication System", Technical Report CMS-CR-2011-020, CERN, Geneva, Jan, 2011.

[79] L. Tuura, G. Eulisse, and A. Meyer, "CMS data quality monitoring web service", *J. Phys. Conf. Ser.* **219** (2010) 072055, doi:10.1088/1742-6596/219/7/072055.

[80] M. De Gruttola et al., "Persistent Storage of non-event Data in the CMS Databases", *J. Instrum.* **5** (2010) P04003, doi:10.1088/1748-0221/5/04/P04003.

[81] B. Bryla and K. Loney, "Oracle Database 12c: the Complete Reference". McGraw-Hill Education, 2013.